NUMERICAL SIMULATIONS OF THE LUBRICATING OIL AND AIR FLOWS IN THE CRANKCASE OF AN INTERNAL COMBUSTION ENGINE

DOCTORAL THESIS

DI Wilfried EDELBAUER

Supervised by:

Univ.-Prof. Dipl.-Ing. Dr.-Ing. habil. Günter Brenn

Univ.-Prof. Dipl.-Ing. Dr.techn. Friedrich Franek

GRAZ UNIVERSITY of TECHNOLOGY

2007

ABSTRACT

Due to the increasing demand for high efficiency of Internal Combustion (IC) engines, engineers are compelled to pay attention to the complex two-phase flow of oil and air in the crankcase. Reduction of the ventilation losses and limitation of the oil consumption due to oil droplets leaving the crankcase are the targets of optimization.

The aim of this thesis is to provide a better understanding of the complex flow phenomena in the crankcase and to model formation and transport processes of the two-phase flow. Therefore model correlations have been implemented into a multi-phase CFD code using the Eulerian-Eulerian approach. Due to the complexity of the moving crank drive and the multi-phase flow, CFD has been so far rarely used for the simulation of the lubricating oil and air flows in the crankcase. Up to now performed CFD simulations have dealt with very simple geometry conditions for the computational mesh. Either non-moving meshes have been used, or the movement has been strongly simplified, disregarding the whole crank drive and performing piston motion only.

In this work the time scales of the different flow phenomena are estimated to determine the most relevant processes. Oil disintegration at the crank drive and oil atomisation due to the blow-by at the piston rings are pointed out as the major sources for the oil droplets. Therefore existing models are combined and adapted for the application in crankcase simulations. Droplet formation due to condensation of evaporated oil components is a further source for the oil mist. But due to negligible contribution in the short time of a few engine cycles, it is not considered in the simulations. Separate simulations of the blow-by gas flow and the oil disintegration at the crankweb have been performed. The moments of droplet size distribution functions are transported to obtain the spatial Sauter mean diameter distribution of the oil droplets. To enable the simulation of several engine cycles, the blow-by flow simulation is performed on a simple crankcase geometry including the moving pistons and neglecting the crank drive. The simulation of the oil disintegration at the crankweb is done on an advanced computational mesh with a moving piston and a rotating crankshaft. Although the conrod is not modelled, the two-phase flow simulations on a mesh with a moving crank drive lead the way to further investigations in that field. Besides the oil droplet propagation in the three-dimensional gas flow field, the simulations show that blow-by generates small droplets with diameters of a few micrometers, while large droplets are generated by the oil disintegration at the crankweb.

Keywords: blow-by; CFD; crankcase; droplet size distribution; engine oil; liquid disintegration; multi-phase flow; rotary atomisation; simulation.

TABLE OF CONTENTS

NOMENCLATURE

Latin symbols

a	Long half-axis of an ellipse; liquid rim thickness;	[m], [m]
	coefficient in algebraic equation	[~]
A	Surface area	[m²]
$\mathbf{A}$	Surface area vector	[m²]
b	Short half-axis of an ellipse; width	[m], [m]
B	Collision impact parameter	[-]
B_M	Spalding's mass transfer number	[-]
B_T	Spalding's heat transfer number	[-]
c_m	Mean piston velocity	[m/s]
c_D	Drag coefficient	[-]
c_P	Specific heat capacity	[J/(kgK)]
c_T	Turbulent dispersion coefficient	[-]
C	Model constant, Convection term	[-], [~]
d	Diameter	[m]
dm	Probability of occurrence	[-]
D	Diffusion term	[~]
D	Turbulent dissipation inter-phase exchange	[W/(m³s)]
D_Y	Diffusion coefficient	[m²/s]
$\mathbf{e}$	Unit vector	[m]
E	Aspect ratio of an ellipse	[-]
f	Arbitrary function	[~]
$\tilde{f}$	Droplet number probability density function	[1/(m³ms)]
$\mathbf{F}$	Force vector; general vector	[N]
Fr	Froude number	[-]
g	Gravitational acceleration	[m/s²]
h	Specific enthalpy	[J/kg]
$\overset{\circ}{H}$	Heat transfer rate	[J]
H	Interfacial heat exchange term	[W/m³]
k	Turbulent kinetic energy;	[J/kg]
	derivative in Runge-Kutta solution procedure	[~]
K_C	Flow coefficient	[-]
K	Turbulent kinetic energy inter-phase exchange term	[W/m³]
K_F	Fluid number	[-]
l	Length	[m]

L	Specific latent heat	[J/kg]
Le	Lewis number	[-]
m	Mass	[kg]
M	Molecular weight	[kg/kmol]
$\mathbf{M}$	Momentum inter-phase exchange term	[N/m³]
Mo	Morton number	[-]
n	Rotational speed	[1/s] or [rpm]
$\mathbf{n}$	Normal vector	[m]
n	Droplet size probability density function (number based)	[1/m]
n_b	Number of boundary faces in the computational grid	[-]
n_{cell}	Number of cells in the computational grid	[-]
n_{cham}	Number of chambers in blow-by model	[-]
n_{dat}	Number of datasets	[-]
n_f	Number of internal faces in the computational grid	[-]
n_{ph}	Number of phases	[-]
n_{ring}	Number of piston rings	[-]
n_ϕ	Number of flow variables solved for by the CFD solver	[-]
N	Multiple of n	[1/(m³m)]
$\tilde{N}$	Droplet number distribution function	[-]
N'''	Particle number density	[1/m³]
N_{coll}	Droplet collision probability per unit volume per time	[1/(m³s)]
Oh	Ohnesorge number	[-]
p	Pressure	[Pa]
P	Shear production term	[W/m³]
P	Probability; point in cell centre of computational cell	[-], [-]
Pr	Prandtl number	[-]
q	Heat flux	[W/m²]
Q_0	Zeroth moment of the droplet size distribution	[1/m³]
Q_1	1st moment of the droplet size distribution	[1/m²]
Q_2	2nd moment of the droplet size distribution	[1/m]
Q_3	3rd moment of the droplet size distribution	[-]
r	Radial coordinate; disc radius	[m]; [m]
$\dot{r}$	Dimensionless droplet radius	[-]
R	Gas constant; rate of change	[J/(kgK)], [~]
$R_{blow-by}$	Percental blow-by mass flow rate (volume flow rate)	[-]
Re	Reynolds number	[-]

s	Stroke of the engine	[m]
S	Saturation ratio; source term	[-], [~]
S_Q	Source of the moment transport equations	[~]
S_U	Source of the moment-average velocity equations	[~]
Sc	Schmidt number	[-]
Sh^*	Modified Sherwood number according to [2], [3]	[-]
t	Time	[s]
T	Temperature	[K]
$\mathbf{U}$	Velocity vector	[m/s]
U	Velocity component	[m/s]
V	Volume	[m³]
v	Droplet size probability density function (volume based)	[$1/m^3$]
We	Weber number	[-]
x	Space; place holder; dimensionless coordinate	[m], [-], [-]
y	Space; dimensionless distortion of an ellipsoid	[m], [-]
Y	Vapour mass fraction	[-]
Z	Ohnesorge number squared Oh^2	[-]

Greek symbols

α	Volume fraction	[-]
β	Exponent for calculating drag as function of α	[-]
γ	Wetting angle	[rad]
γ_C	Model constant in atomisation model	[$m^{½}$]
$\not{y}_A, \not{y}_m$	Diffusive source and volumetric (mass) source of ϕ	[~]
Γ	Mass inter-phase exchange term; diffusion coefficient	[kg/(m³s)], [~]
δ	Film height; thickness	[m]
δ_{ij}	Kronecker symbol	[-]
ε	Turbulent energy dissipation	[m²/s³]
θ	Energy source	[W/kg]
κ	Thermal conductivity; adiabatic exponent	[W/(mK)], [-]
κ_{lam}	Lamella number	[-]
κ_{RR}	Rosin-Rammler exponent	[-]
κ_{U_I}	Velocity ratio	[-]
λ	Wave length	[m]
λ_l	Volumetric efficiency of the engine	[m]
μ	Dynamic viscosity	[Ns/m²]

ν	Kinematic viscosity	[m²/s]
ρ	Density	[kg/m³]
σ	Surface tension	[N/m]
σ_T	Coefficient of turbulent heat flux	[-]
σ_k	Coefficient of turbulent kinetic energy	[-]
σ_ε	Coefficient of turbulent dissipation	[-]
σ_ν	Coefficient of turbulent diffusion	[-]
τ	Dimensionless time scale	[-]
$\boldsymbol{\tau}$	Shear stress tensor	[N/m²]
ϕ	Dependent flow variable	[~]
ϕ_{BT}	Exponent for calculation of B_T	[-]
φ	Realisation in event space	[-]
χ	Phase indicator or component indicator	[-]
ψ	General scalar	[~]
ω	Angular velocity	[rad/s]
Ω	Event space	[-]

Symbols

$\dot{x}$	Time derivative of variable x	
$\bar{x}$	Average value of variable x; ensemble average or any other mean value	
x'	Turbulent fluctuating component of x	
x^*	Dimensionless value of x	
Δx	Discrete variation of x	
$\mathbf{x}$	Vector or tensor x	

Subscripts

0	Initial value	
32	Sauter mean diameter/radius	
amb	Ambient	
ax	Axis	
A	Surface area	
b, bn	Boundary face value and normalised boundary face value	
blw	Blow-by	
br	Break-up	
c	Continuous phase	
coal	Coalescence	

coll	Collision
cond	Condensation
crit	Critical conditions in smallest cross section at choked flow
crnk	Crankcase
cycl	Engine cycle
cyl	Cylinder
d	Dispersed phase
drop	Droplet
D	Drag
evap	Evaporation
exp	Thermal expansion
E	Aspect ratio
f	Cell face index, Value at cell face
gas	Gas
gr	Grid
i, j, m, p, q	Index notation
k ,l	Phase indices
lig	Ligament
liq	Liquid
max, min	Maximum, minimum
P	Value at the cell centre
P_f	Value at the cell centre of neighbouring cell
r	Radial component
red	Reduced value on reference radius
ref	Reference
rot-det	Droplet detachment from rotating crank drive
RT	Rayleigh-Taylor (e.g. wave length)
s	Smaller
sat	Saturation
sheet	Sheet
sep	Separation
strip	Strip (thickness)
S	Surface
t	Tangential or circumferential component
tot	Total number
T	Turbulent dispersion force

vap	Vapour
ϕ	Flow variable

Superscripts

A	Diffusive part of a source in general transport equation
t	Turbulence
V	Volumetric part of a source

Abbreviations

BDC	Bottom Dead Centre
CA	Crank Angle
CCV	Closed Crankcase Ventilation
CFD	Computational Fluid Dynamics
CV	Control Volume
DDM	Discrete Droplet Model
ELPI	Electrical Low-Pressure Impactor
GUI	Graphical User Interface
HC	Hydro Carbon
HVLA	Hydraulic Valve Lash Adjuster
IC	Internal Combustion
ITDC	Ignition Top Dead Centre
MPI	Message Passing Interface
ODE	Ordinary Differential Equation
PCV	Positive Crankcase Ventilation
	Pressure Control Valve
PDF	Probability Density Function
RR	Rosin-Rammler
SMD	Sauter Mean Diameter
SMR	Sauter Mean Radius
TAB	Taylor Analogy Breakup
TDC	Top Dead Centre
TED	Turbulent Energy Dissipation
TKE	Turbulent Kinetic Energy
VOF	Volume-Of-Fluid method

Foreword

About four years ago I decided to do a PhD in the field of fluid dynamics. But the attraction of moving fluids to me is even older. Since my childhood I have been fascinated by the beauty of the dabbling brook beyond the house of my aunt. Every time I visited that place I played there. I waded through the water and observed the beauty of the splashing droplets. It seems that those experiences have left a permanent impression in my life.

During my master study in Graz I learnt that the motion of fluids can be described by only a few equations. I was surprised that such a complex phenomenon like the motion of a flowing river can be modelled so easily. Then I learned that there are almost no flow problems, where an exact solution of the equations describing the fluid flow can be obtained. That confirmed my original opinion that fluid flow is too complex for general prediction. Some time later I got in touch with CFD. I saw that for many applications exact solutions are not essential, if one can find an approximate solution covering the core of the problem. I was eager to learn more about that approach, and so I performed my master thesis in the field of CFD and multi-phase flows. After my degree in mechanical engineering I got the opportunity of getting involved as research assistant at the Austrian Center of Competence for Tribology (AC²T research GmbH). They offered a job which had to do with CFD simulation of the air and oil flows inside the crankcase of an IC engine. That job should be done in close co-operation with the AST department at AVL List GmbH, who is the developer of the CFD code FIRE. Furthermore, this work could be the framework for doing a PhD. On the one hand I did not know if I should dare to do the PhD on such a topic. I had not come across similar investigations in that field, but I knew that there are a lot of complex phenomena in the crankcase. I did not know if I could handle that topic. On the other hand I saw the challenge and I decided to do it.

Now more than three years have passed. I am sitting in my room and I am finishing my thesis by writing this foreword. A lot of things have happened in the past three years and I have made a lot of experiences. It has been a very fruitful and interesting time for me. But it has also been a hard time with thinking and writing far into the night at several times. I am happy that a long and interesting work will be finalised soon. Further I would like to say THANK YOU:

I wish to thank my supervisor, Prof. Günter Brenn at the Institute of Fluid Mechanics and Heat Transfer of Graz University of Technology, for his excellent ongoing support and for so many fruitful discussions. At several times he directed me with his great expertise. I also wish to thank my co-supervisor, Prof. Friedrich Franek at AC²T research GmbH, for his

advice and for being the initiator of AC²T where I have been working for more than three years.

Special thanks to Heinrich Kratochwill for the good teamwork, for being a very good colleague and for creating the well working computational meshes. Furthermore, I must mention De Ming Wang, who advised me so often in numerical issues. He is a great expert in CFD and he is an excellent colleague. Also special thanks to my sister Irmi Edelbauer for correcting grammar and spelling of this thesis. I appreciate her work of reading and correcting a thesis of almost 200 pages without any engineering background. Thanks to Eberhard von Berg and Branislav Basara at AVL and Nicole Dörr at AC²T for their help. I would also like to mention the others, who have contributed to a good time the past three years at AC²T and AVL: Gerd Rabenstein, Susanne Kutschi, Valdas Caika, Sasa Bukovnik, Georg Hager, Peter Sampl, Klaus Pachler, Michael Bogensperger, Peter Priesching, and Reinhard Tatschl.

I wish to thank my whole family, in particular my parents, who have encouraged me during the years of study. They gave me advice at any time. Special thanks to Birgit, now my fiancée, whom I met six months after I had started working on this thesis. She has been the greatest and most wonderful change of my life during the time of this project. Her support, her love and her great patience have been indispensable for coming to that stage of this work. She has encouraged and endured me, when I was down.

Thanks to the University of Technology of Graz, especially to the Institute of Fluid Mechanics and Heat Transfer, for providing the opportunity of doing this PhD. Furthermore, the Austrian K*plus* Kompetenzzentrenprogramm (governmental technology and research funding initiative) should be thankfully acknowledged for the financial support for the project that I have been involved.

At last, and by no means least, I would like to thank my God for His continual guidance over the past years. He has been with me all the time.

1 Introduction

The crankcase is the space underneath the pistons in an Internal Combustion (IC) engine. The understanding of the effects and phenomena in the crankcase is becoming more and more important. Sufficient lubrication of the cylinder walls, minimising the ventilation losses and an effective cooling of the piston bottom are very important requirements on a modern crankcase design. The aim of this thesis is to provide a better understanding of the gas and oil flows in the crankcase and to model the formation and transport processes of the oil mist and the splash oil. This is important, since the complex three-dimensional gas flow in the crankcase determines the ventilation losses. Furthermore, the crankcase gas is returned to the combustion process to prevent pressurising of the crankcase. An oil mist separator has to clean the crankcase gas from the oil mist. This thesis presents a tool for simulating the formation and transport processes of the oil mist and the splash oil in the crankcase.

The main tasks of the crankcase are to cover the reservoir of the lubricating oil and to provide the space for the crank drive. Driven by the gas forces resulting from the combustion, the pistons move up and down. The conrod transmits the translational piston motion into rotation of the crankshaft. Due to the motion of the crank drive, the gas in the crankcase is set into motion. The gas flow carries the oil mist and causes ventilation losses. The crankcase gas originates from exhaust gases that leak from the combustion chamber down to the crankcase via gaps between the piston rings and the liner wall. This gas is called blow-by gas. In order to prevent pressurising the crankcase, there must be a continuous flow of the ventilated gas out of the crankcase. This is controlled by the crankcase ventilation system. There are different types of ventilation systems. One can distinguish between closed and open crankcase ventilation systems. A further difference is the operating pressure, which can be positive or negative in reference to the atmospheric pressure.

The lubricating oil moves in a closed loop. In most combustion engines the oil reservoir is placed at the bottom of the crankcase in the oil pan. In sophisticated automotive engines, a windage tray is integrated. This is designed to keep oil from splashing up from the bottom of the pan and back onto the crankshaft. The windage tray also helps to minimise aeration of the engine oil and consequently helps to eliminate oil foaming. From the oil reservoir the oil is sucked through the pick up filter screen and through the pick up tube before it enters the oil pump. This pump pushes the oil through the filter, and, via galleries and oil delivery holes, to the different lubrication points and oil consumers in the engine. The main oil consumers are the bearings of crankshaft, conrod and camshaft, the piston cooling nozzles, the cylinder head, the turbocharger and the Hydraulic Valve Lash Adjusters (HVLA). After passing the lubrication points, the oil flows back to the oil reservoir of the crankcase. The oil

from the crankshaft bearings and the conrod bearings flows as a film on the moving parts, retains at the edges of the bodies, and detaches due to the centrifugal forces. The oil disintegrates into ligaments and droplets which impact on the wall of the crankcase and the liner. The splash oil on the liner wall guarantees the lubrication between liner and piston. From the wall the oil flows down to the oil pan driven by the gravity force, closing the loop. The oil from the cylinder head flows back through large dimensioned holes, which ensure an unobstructed flow to the oil reservoir.

In general one can distinguish between coarse fractions of oil droplets and fine fractions of droplets and particles in the crankcase. The splash oil from the piston cooling jets and the detachment from the moving crank drive produce the coarse fractions of the oil droplets in the crankcase. Condensation of evaporated oil components and oil atomisation due to blow-by in the small gaps between liner and piston rings create very small oil particles. These represent the fine fractions of droplets, the oil mist. Apart from engine oil, there are also fractions of unburnt fuel, condensed water, solid particles and combustion residues as dispersed phase in the crankcase.

In engines with closed ventilation system the crankcase gas is drawn from the crankcase into the intake manifold. That means the crankcase gas is returned to the combustion process, similar to the exhaust gas recirculation. An oil mist separator is required to clean the crankcase gas from oil droplets and soot, because the amount of oil components participating in the combustion should be as small as possible. Especially the crankcase gases of turbocharged Diesel engines have to be cleaned very carefully. Remaining oil droplets drop the efficiency of the turbocharger due to coke deposition on the turbocharger turbine. Furthermore, the droplets would damage the blades of the turbocharger and reduce its durability. Also the performance of the air cooler would be reduced due to oil accumulation, if the crankcase gas was not cleaned from the oil mist.

One can see that there is a complex multi-phase flow in the crankcase. The phases are crankcase gas and liquid oil as the main components, as well as small fractions of water, fuel and soot. The crankcase gas consists of air, combustion products, fuel vapour, and oil vapour. The composition varies with engine load and rotational speed.

A great deal of attention of today's engine developers is paid on the crankcase ventilation system and the oil mist separator. Less attention is paid on the generation of the blow-by gas and the oil mist. Although the splash oil is essential for the lubrication between the liner and the piston, the generation of the splash oil was almost disregarded in the past. Due to the ever increasing requirements on engine efficiency and engine performance, there is a demand for optimising the crankcase design. On the one hand minimising the ventilation losses and the

losses due to blow-by, reducing the space of the crankcase and optimal efficiency of the oil mist separator are important demands on a modern crankcase design. On the other hand there has to be an oil supply system of highest reliability, which has to ensure sufficient lubrication at all operation points. Furthermore, oil foaming has to be prevented, since it would disturb the oil flow in the closed loop. For investigations of the flow in the crankcase with the aim to fulfil the requirements from the design, an appropriate simulation tool is necessary.

Computational Fluid Dynamics (CFD) is a powerful tool for flow investigations in engineering applications. Since the early nineties, CFD simulations have been used very intensively for the development of mixture formation and the combustion process. Anyway, for crankcase applications, CFD was almost unused so far. Due to the complexity of the moving geometry and the multi-phase flow, the use of CFD for simulation in a real crankcase was inhibited. Although CFD was applied in gear box simulations [61] and for crankcase simulations with moving piston, but without modelled crank drive [84], CFD simulations of the two-phase flow in moving crankcase geometries including the crank drive were not found in the literature.

Continuing revolution in numerical simulation techniques, better physical models and the possibility of simulating multi-phase flow pave the way for more advanced simulations. The permanent increase of CPU performance and the possibility of powerful parallelisation (MPI) enable complex calculations within reasonable time. Hence CFD is becoming interesting for simulations of the crankcase flow. A useful code must be able to calculate multi-phase problems for at least two phases, the gas phase and the oil phase. To deal with the complex geometry, the code has to handle moving computational grids. The commercial CFD code FIRE [6] fulfils many of the requirements. FIRE can calculate multi-phase flows in two different ways.

The Discrete Droplet Method (DDM) is an Eulerian-Lagrangian approach. The dispersed phase consists of spray parcels, for which the equations of motion are solved. A parcel contains a certain number of spherical droplets with equal diameter, velocity, and temperature. The statistical information about the spray droplets can be deduced easily by analysing the existing parcels within a control volume. This results in discrete distribution functions for droplet size, velocity, and temperature. The conservation equations for the continuous phase are solved, and the interfacial interactions with the dispersed phase are modelled as source terms. The volume fraction of the dispersed phase is not considered in the solution of the continuous flow equation, and hence the DDM method is made for multi-phase flow with small dispersed phase volume fraction. Usually the dispersed phase volume fraction should not exceed 5 percent [6], otherwise the error due to the neglected

liquid phase volume fraction in the solution of the continuous phase equations would become too high.

In the Eulerian-Eulerian multi-phase approach, the full set of transport equations for an arbitrary number of interpenetrating phases is solved. Each phase is determined by its volume fraction. The interactions between the phases (e.g. drag force between continuous phase and dispersed phase) are calculated by interfacial exchange terms. These source terms contain important physics of the multi-phase flow. This approach is able to treat the transition from a bulk liquid flow, with a liquid as the continuous phase and a gas as the dispersed phase, to a spray flow with the gas as the continuous and the liquid as the dispersed phase.

For this thesis the Eulerian-Eulerian multi-phase method has been chosen as the numerical modelling approach for simulating the crankcase flow, since this method provides a better description of the multi-phase flow in regions with accumulating liquid phase. The challenge of this study is to provide models for the generation and transport of the oil mist. The liquid oil disintegration due to detachment from moving parts is analysed by the analogy to rotary atomisation. Correlations from there have been adapted to a more complex geometry, like the crankweb. The blow-by flow across the piston rings is simulated by a zero dimensional chamber model and delivers the gas mass flow rate at the boundaries of the CFD simulation. The droplet entrainment due to the blow-by gas flow is also considered. To overcome the loss of the droplet statistics of the Eulerian-Eulerian approach, a methodology for transporting the droplet size distribution function has been applied. Two moments of the droplet size distribution are transported and two moments are approximated by the given shape of the distribution function [13]. This method provides a lot more information about the droplet phase at the expense that a few additional transport equations must be solved. The alternative approach to the transport of the moments of the droplet size distribution function is to split the liquid phase into a number of droplet size classes and to solve the complete set of conservation equations for them. But this approach is computationally more expensive and time-consuming, and a reasonable CPU time of the calculations is one of the core requirements for such simulations.

The influence of the most important phenomena on the crankcase flow is analysed in this thesis. The main purposes of this study are to deliver a better understanding of the oil and air flows in the crankcase and to provide a simulation tool describing the most important effects of the flow. CFD simulations on base geometries are performed to show the gas flow and the propagation of the oil mist and the splash oil. This simulation tool provides the base for further investigations.

The flow phenomena in the crankcase, such as blow-by, the oil mist generation, and the processes in the lubricating oil circuit are described in section 2 of this thesis. Furthermore, the fast and slow processes are discussed in this section. The third section deals with the models from the literature. The Eulerian-Eulerian multi-phase approach, models for blow-by, the liquid disintegration on rotating discs, and the transport of droplet size distribution are described in section 3. Section 4 deals with the numerical solution technique of the developed crankcase flow simulation tool. The results of the CFD simulations for blow-by flow and the oil disintegration on the crankweb are presented in section 5. A summary of this thesis, the conclusions, and the outlook to further works are given in section 6.

2 Flow Phenomena in the Crankcase

This section gives a general overview of the flow phenomena occurring in the crankcase of an IC engine. At first the blow-by and the different types of ventilation systems are discussed. The physical effects causing the formation of the oil mist are described, and an overview of the lubricating oil circuit is given. Finally the time scales of the different processes are quantified and the most important processes are determined.

2.1 Blow-by and Ventilation Systems

2.1.1 Blow-by Formation

Blow-by is the leakage of gas from the combustion chamber into the crankcase, as shown in Figure 1. It arises during the operation of any combustion engine. The leakage from the combustion process mainly occurs during the compression and expansion strokes, when the pressure in the combustion chamber reaches a maximum.
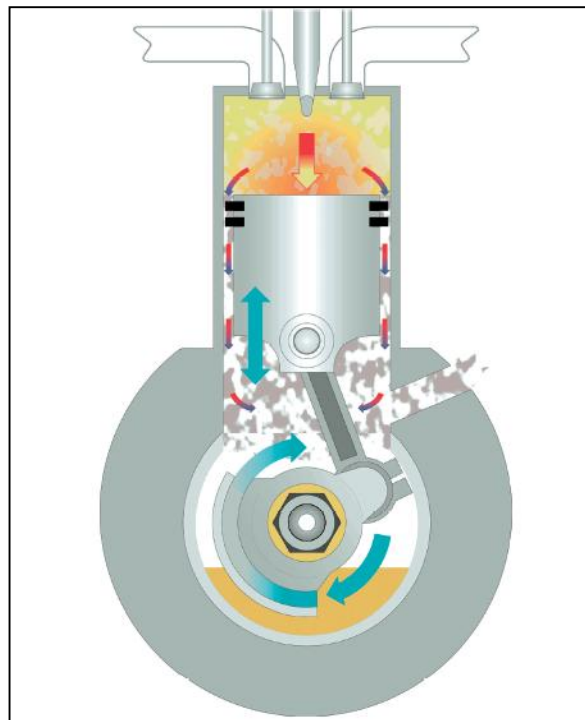

Figure 1: Crankcase ventilation (figure from [43])

The air from the intake manifold enters the cylinder and takes part in the combustion process. From the top land crevice, gas can leak down to the crankcase. Figure 2 shows three different ways for the blow-by gas flow [33]. One part of the gas flows between the piston ring and the cylinder wall. A second part flows behind the piston ring in the region between the ring groove and the rings. Piston ring flutter may increase this amount of the blow-by

significantly. The third significant part leaks down through the piston ring gaps. Other sources for blow-by are valve guides and the bearings of the turbocharger. At heavy duty engines the air compressor can also be a significant source of blow-by gas, which finally enters the crankcase [10].
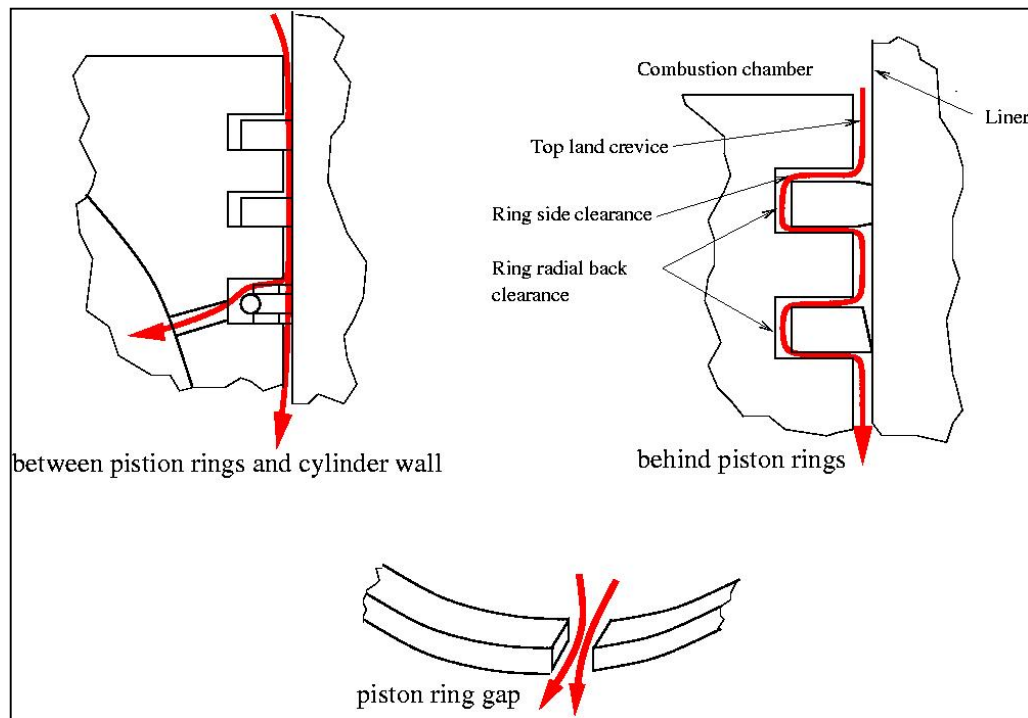

Figure 2: Generation of combustion blow-by (adapted from [33])

The percental blow-by flow rate (= ratio of blow-by volume flow rate and total volume flow rate through the intake manifold or the exhaust pipe) typically varies in the range between 0.3 and 1.5 percent, under certain conditions even more. The amount of blow-by gas strongly depends on load and speed. In [33] investigations about the amount of blow-by gas were performed on gasoline engines for passenger cars. The authors measured a blow-by flow rate percentage of common engines at full load between 0.5 percent and 1.5 percent. At part load or idle state, values from 1 to 3.8 percent were reached. Investigations in [11] on heavy-duty Diesel engines showed that the amount of blow-by gas lies in the range between 0.4 and 0.8 percent, and by a general rule of thumb one can say there is approximately 0.5 l/min of blow-by per rated engine horsepower. The operating temperature has influence on the blow-by gas volume flow rate. A cold engine produces more blow-by gas than a warm engine, because the piston ring gaps and the groove between cylinder wall and piston are bigger at low temperature. Measurements in [10] showed that the blow-by flow rate for cold engines is almost 50 percent higher than for warm engines. Furthermore, the measurements on heavy-duty Diesel engines showed that the highest blow-by flow rates occur in the middle

engine speed range. There is a tendency of increasing blow-by flow rate with increasing engine torque. This seems to be reasonable, because the higher the engine torque, the higher is the peak pressure in the combustion chamber and, hence, the higher is the pressure ratio between combustion chamber and crankcase.

Liner bore distortion, which may occur during engine assembly, can have significant impact on the amount of blow-by gas [33]. Due to piston ring and liner wear, the blow-by increases over an engine's life. Engines of different manufacturers and different models exhibit different blow-by flow rates. As mentioned above, piston ring flutter is a special case, which can lead to high amounts of blow-by. Piston ring flutter occurs when the pressure difference between the combustion chamber and the crankcase is not big enough to push the piston ring tightly onto the piston ring groove. The motion of the piston leads to flutter of the ring in the piston ring groove. That typically happens at special combinations of speed and load of the engine.

Permanent blow-by gas flow would lead to a pressure increase in the crankcase, if the crankcase was not ventilated.

2.1.2 Ventilation Systems

Blow-by gases consist of unburnt hydrocarbons (HC), burnt gases, carbon monoxide (CO), particles, and oxides of nitrogen (NOx). Their contribution to the entire pollution of the engine lies between 20 and 30 percent [33], [27]. Without ventilation, the blow-by gas would cause lubricating oil contamination leading to ageing, oxidation, sludge formation, deposits and excess crankcase pressure. The absence of a crankcase ventilation system or an insufficient system can lead to crankcase explosions, which caused fatal accidents in the past.

The easiest way of crankcase ventilation is to blow the crankcase gases out through the draft tube. Systems with a connection between the crankcase and the atmosphere outside the engine are called open systems. Contrary to the open crankcase ventilation system there is the closed crankcase ventilation system (CCV), which guides the blow-by gas back into the intake manifold. Hence, the blow-by gas takes part in the combustion again, and no pollutants enter into the atmosphere. In the industrialised countries closed crankcase ventilation systems have been demanded by the emission legislation since many years. The legislation in California was the pioneer in the early sixties with an enactment requiring CCV for gasoline engines in passenger cars. Similar regulations followed in all important markets over the world, and the requirement of CCV to reach the given exhaust-gas limits have been extended to Diesel engines for passenger cars, as well as for motor trucks [58].

There are different requirements to the crankcase ventilation system. Some engines work with crankcase pressures smaller than the atmospheric pressure. The small underpressure prevents escape of blow-by gas into the atmosphere via leakages. For open systems this was really important to reach the pollution limits of the crankcase gas. On the other hand it can be useful to have a positive pressure in the crankcase, which avoids that unfiltered air enters the engine via leakages [43]. Unfiltered air would cause contamination of the engine oil and would accelerate the oil ageing.

There are many different crankcase ventilation systems. In [58] seven different ventilation systems are described for gasoline engines, and there exists even more. Beside the distinction between open and closed crankcase ventilation, one can distinguish between systems which only vent out the blow-by gas from the crankcase, and systems in which additional fresh, filtered air is guided through the crankcase to remove the blow-by gases. The latter system is called positive crankcase ventilation system (PCV). A further important distinctive aspect is whether the system works with or without pressure control valve (PCV; attention: double meaning in literature with "positive crankcase ventilation").

The main components in the condensate of blow-by gas from a gasoline engine are unburnt hydrocarbons and water [83]. These components can dilute and contaminate the engine oil, cause corrosion of critical parts and contribute to sludge formation. The purpose of the crankcase ventilation system is to remove these harmful gases from the crankcase before damage occurs. A very simple ventilation system for gasoline engines is shown in Figure 3. This system is uncontrolled, because there is no pressure control valve. The blow-by gases are drawn from the crankcase into the intake manifold in front of the throttle body. The oil mist separator cleans the blow-by gas from the splash oil and the fine oil particles. This system is cheap and simple, but the pressure in the crankcase depends on the flow resistance of the air cleaner, and hence there is no specified ventilation [58]. Because the gas discharge occurs in front of the throttle body, the pressure difference for operating the oil mist separator is quite small.

Figure 4 shows a crankcase ventilation system for gasoline engines, where the gas discharge takes place behind the throttle body. The benefit of this system is a higher pressure difference for operating the oil mist separator. The pressure control valve regulates the pressure level in the crankcase and avoids too big underpressure. At part load the underpressure behind the throttle body can reach values of 600 mbar and more. Such a pressure difference is too big for the crankcase ventilation, since it would lead to entrainment of the lubricating oil into the blow-by gas tube, and consequently to high oil consumption [33]. The pressure control valve enables an almost constant pressure in the crankcase,

independent from the pressure in the intake manifold, the load, and the speed of the engine. In a modern crankcase ventilation system, the oil mist separator and the pressure control valve are included in a single component [55].
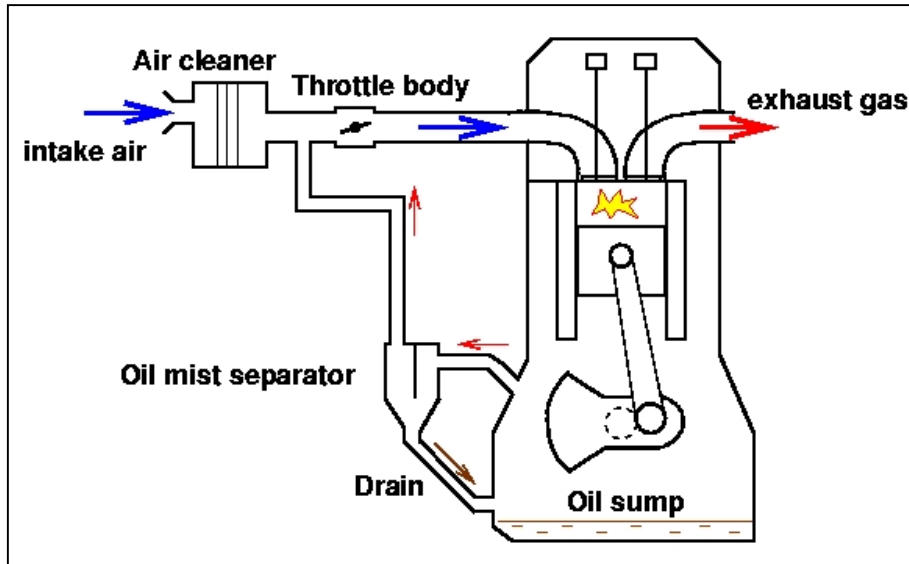

Figure 3: Uncontrolled ventilation with gas discharge in front of the throttle body (reproduced from [58])
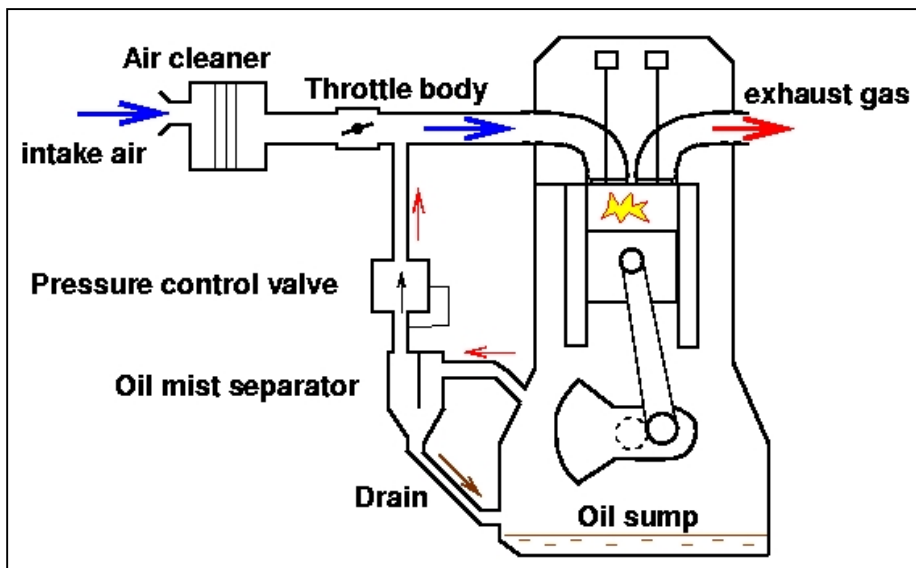

Figure 4: Controlled ventilation with gas discharge behind the throttle body (reproduced from [58])

Figure 5 shows a throttled ventilation system with gas discharge in both directions, in front of and behind the throttle body. Compared to the system in Figure 3, this system has better ventilation at part load and idling, where the underpressure behind the air cleaner is very low [58]. The by-pass tube containing a throttle enters the intake manifold behind the throttle body and provides lower pressure. The check valve prevents fresh air by-pass flow around the throttle body.
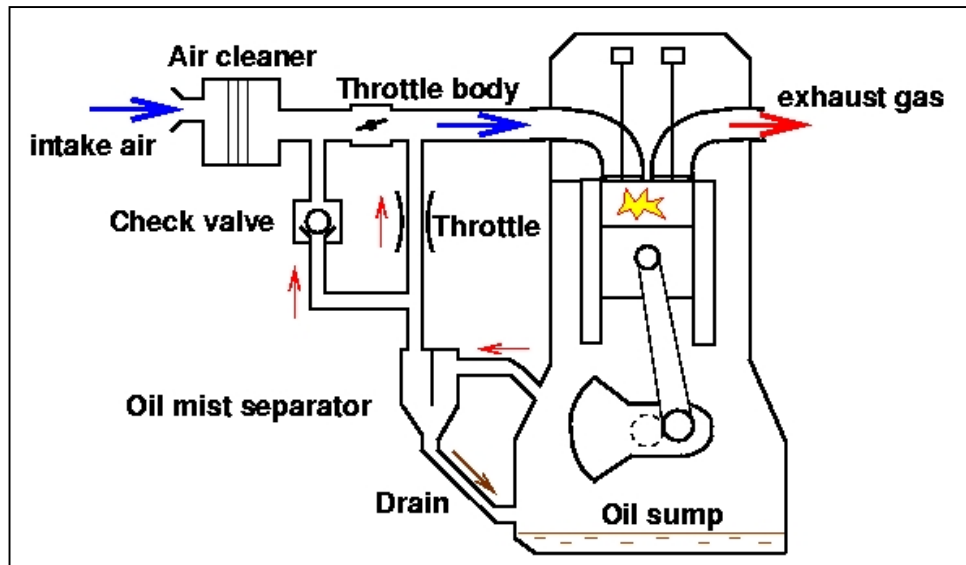
Figure 5: Throttled ventilation with gas discharge both in front of and behind the throttle body

(reproduced from [58])

In Figures 6 and 7 positive crankcase ventilation systems for gasoline engines are shown. These systems help to prevent condensation of water and unburnt fuel in the crankcase. Water is a main product which results from the combustion of hydrocarbons. A gasoline engine of average size for passenger cars produces about 60 g of water vapour per unit volume blow-by gas and hour [54]. This water vapour content corresponds to a dew point of 43 °C. This means that, if the temperature in the crankcase is less than this dew point temperature, the water vapour will condense. If the engine is often driven for short-runs, or it is permanently used under light load, the condensate can accumulate and can cause corrosion and oil dilution. In winter, frozen water can disturb the flow of the lubricating oil in the circuit and can cause engine damages.

In positive crankcase ventilation systems, fresh filtered air from the intake manifold with a lower concentration of water vapour and zero concentration of fuel, is vented into the crankcase and mixes with the crankcase gas. The gas mixture will have a lower dew point, and subsequently the risk of condensation of both water vapour and unburnt fuel is reduced. Figure 6 shows a PCV system for gasoline engines with reverse flow in the ventilation pipe [33], [58]. At part load there is high underpressure in the intake manifold behind the throttle body and hence the blow-by gases are vented out of the crankcase through the oil mist separator and a throttle. The pressure in the crankcase is low, and there is an additional flow of fresh air from the intake manifold behind the air cleaner into the crankcase. At full load there is a higher blow-by gas flow rate, and the underpressure behind the throttle body is much smaller. The pressure in the crankcase exceeds the pressure in the intake manifold

between air cleaner and throttle body, and this is why the flow direction in the ventilation pipe changes. In this case a second oil mist separator prevents that oil droplets enter the intake manifold. This oil mist separator is operated in both flow directions.
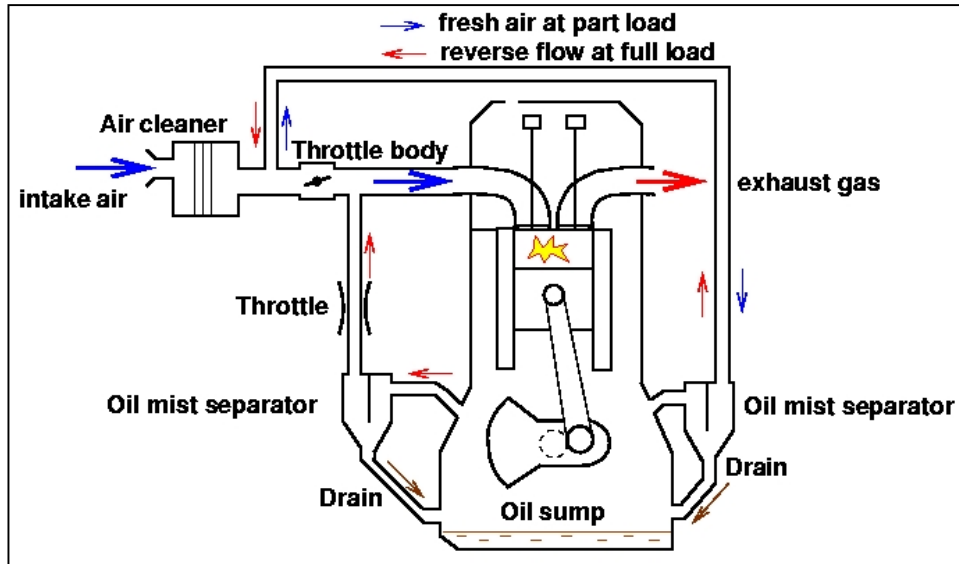

Figure 6: Positive crankcase ventilation system with reverse flow in the ventilation pipe (reproduced from [58])
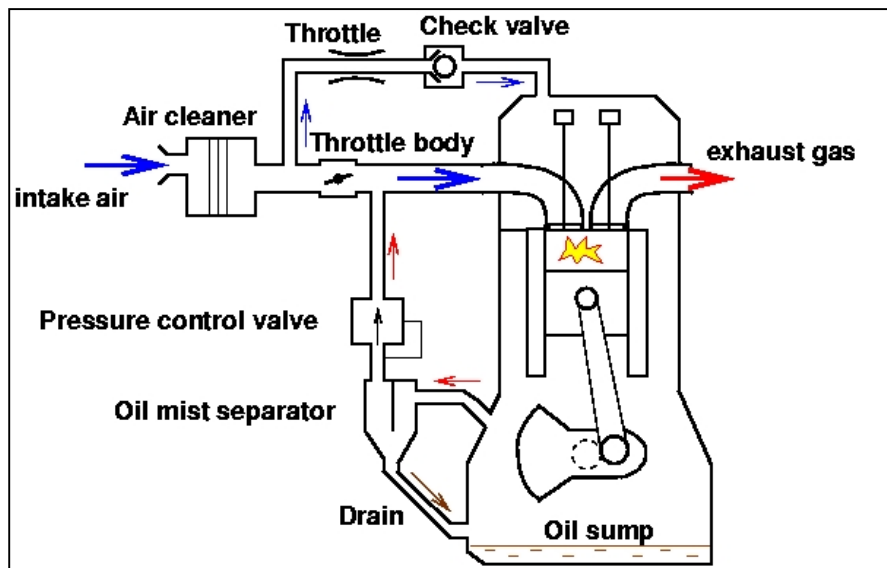

Figure 7: Controlled positive crankcase ventilation system for a gasoline engine (reproduced from [58])

The controlled positive crankcase ventilation system for gasoline engines is shown in Figure 7. The pressure control valve regulates the pressure difference between intake manifold and crankcase. Fresh air is drawn into the crankcase via a throttle. A check valve prevents reverse flow and thus no second oil mist separator is required in this kind of a system.

In the literature, different estimates can be found about the positive or negative effects of the positive crankcase ventilation system on the engine oil quality. Some authors and filter manufacturers are convinced that it is necessary to put as much fresh air as possible into the crankcase for different loads and speeds [54]. Due to the reduced condensation of water and fuel vapour, the PCV system prevents oil contamination and reduces sludge formation [37], [80]. Other authors have doubts about the above benefits from the PCV system. They argue that even the oxygen in the blow-by gas causes oxidation of the engine oil. If there is additional fresh air vented into the crankcase like in the PCV systems, the oxidation and ageing of the oil is further accelerated [58], and there is also an increased sludge formation [12]. The PCV system has advantages when the engine is cold or often operated for short-runs, because there is less danger of water vapour condensation. But the effect of increased oil oxidation and oil ageing cannot be disregarded.

Diesel engines work with a lean air/fuel ratio at part load, and thus the water vapour concentration of the blow-by gas is far from the critical concentration at the dew point. Consequently, the risk of vapour condensation at low crankcase temperatures is not as high as in gasoline engines.

Figure 8 shows an open (left) and a closed (right) crankcase ventilation system for a Diesel engine. The engine is supercharged and has an air cooler. The open system is very simple. The blow-by gas is cleaned from the oil droplets by an oil mist separator and then vented into the atmosphere. Due to the emission legislation in many countries, the open system becomes less important. The closed system has a pressure control valve, which regulates the pressure in the crankcase. The blow-by gas is vented into the intake manifold in front of the turbocharger.

For Diesel engines, a sufficient oil mist separation is very important, since oil particles would cause damage to the fast rotating blades of the turbocharger [77]. Furthermore, the efficiency of the turbocharger would drop due to coke deposits on the turbocharger turbine. Also, the air cooler performance would be reduced due to the accumulation of oil [43]. The oil deposits would cover the surface areas of the air cooler with an insulating layer, causing a substantial decrease of the heat exchange efficiency. Also the inlet valves would suffer from oil deposits, which could lead to loss of engine power, higher fuel consumption, and higher emissions.

This section gave an overview of existing crankcase ventilation systems. One can see that there are many different designs for the different purposes. But all of them have the same aims. Firstly, the blow-by gas has to be guided out of the crankcase to ensure a more or less constant pressure level. Secondly, the gas leaving the crankcase has to be cleaned from the

splash oil and the oil mist to ensure low oil consumption of the engine. One purpose of this thesis is to model the blow-by formation in a CFD simulation. Therefore it is necessary to know the process leading to the formation of the blow-by, and how this gas is guided out from the crankcase. The process of oil mist formation by the blow-by gas is discussed in section 2.3.
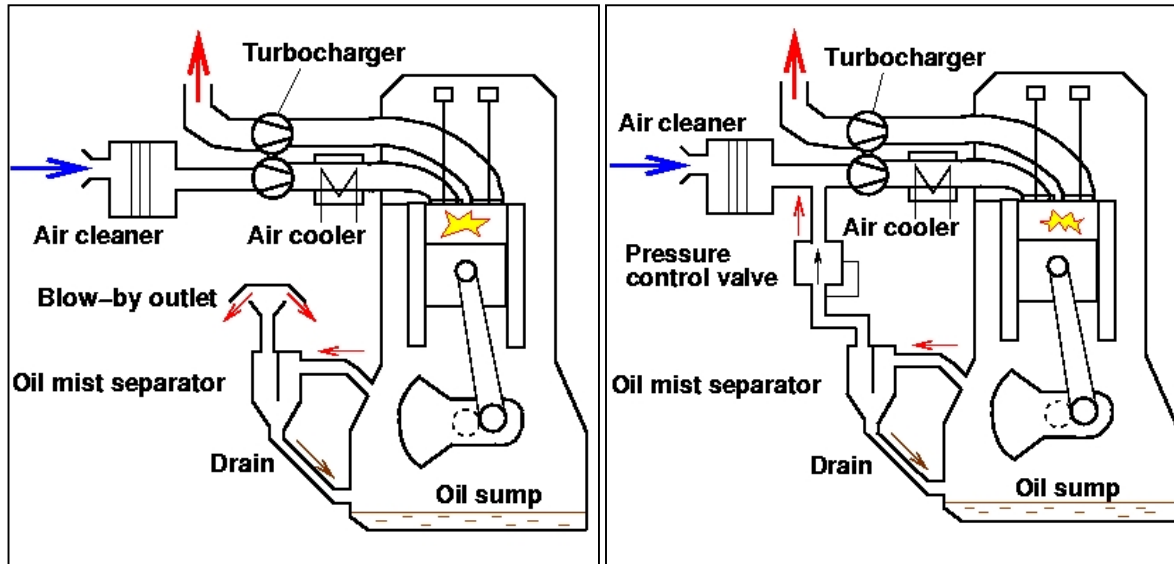

Figure 8: Schematic of an open (left) and a closed (right) crankcase ventilation system (CCV) for a Diesel engine (reproduced from [77])

2.2 Lubricating Oil Circuit

The lubricating oil circuit supplies oil to the oil consumers. Points of lubrication are all bearings of the engine, piston and liner walls, and the camshaft. Further oil consumers are the turbocharger and the piston cooling jets, where the splashing oil is used for heat convection to reduce the temperature of the piston bottom. From the oil reservoir at the bottom of the engine, the oil is sucked by the oil pump through the pick up filter screen. From the pump it is pushed through the oil filter and the oil cooler before it enters the main oil gallery. From there it is distributed to the different oil consumers. After passing the lubrication points, the oil flows back to the oil reservoir. The oil which has lubricated the crankshaft and conrod bearings flows as a film on the moving parts and detaches from there. This splash oil reaches the crankcase wall and flows down to the oil reservoir. The oil from the piston cooling jets contributes to the splash oil in the crankcase.

The way of the oil from the pick up filter screen in the oil reservoir to the different oil consumers is determined by a complex system of bore holes, pressure control valves, and calibrated nozzles. This system guarantees that the oil consumers are provided with the right

amount of engine oil at an appropriate pressure. In a cold engine during warm-up, the oil viscosity and also the flow resistance in the oil circuit are much higher than at higher oil temperature. The oil pump produces a low oil pressure at low engine speed and a high oil pressure at high engine speed. The lubrication system has to ensure sufficient oil supply at all operating points and at different operating temperatures of the engine. Simulation tools help to design the lubrication system.

FLOWMASTER [38] is a commercial program for the analysis of one-dimensional fluid dynamics, e.g., in networks of pipes and passages with losses. The losses of the components are determined either by measurements or by characteristic parameters, e.g. hydraulic diameter, length, and surface roughness of the pipe. Applied to the lubrication system, the results are volume flow rates through the components and the pressure distribution in the lubrication system. Figure 9 shows the oil flow distribution in a 3.0 litres V6-Diesel engine calculated with this software tool. Engine oil with the specification SAE 0W-40 at 120 °C, and an assumed oil pump efficiency of 80 percent were used.

The plots show for different engine speeds the oil flow rate distributed to the different groups of oil consumers, such as the main bearings, the conrod bearings, the camshaft bearings, the piston cooling jets, the turbocharger, the cylinder head, the hydraulic valve lash adjuster (HVLA) system, and the amount of oil escaping via the pressure regulator valve of the oil pump. In general, the dominant oil consumers are the bearings, the piston cooling jets, and the cylinder head. The oil flow rate through the piston cooling nozzles slightly increases with the engine speed. The oil pump delivers too much oil at high engine speed, and thus the amount of oil released through the pressure regulator valve increases significantly. Excessive flow of released oil via the pressure regulator valve causes the danger of oil foaming and must be prevented [41]. The presented engine is a low-noise engine with reduced bearing clearance. This is why the oil flow rate through the bearings is small compared to other common engines of similar construction type.

For the investigation of the crankcase flow, special attention is paid to the oil flow rate through the crankshaft and conrod bearings, because this oil appears as a film on the moving parts of the crank drive, disintegrates into droplets, and causes a fraction of coarse oil droplets in the crankcase. Thus the oil escaping from the bearings determines a boundary condition for the simulation of the crankcase flow. Hence, a reliable determination of the oil volume flow rate through the bearings is necessary.
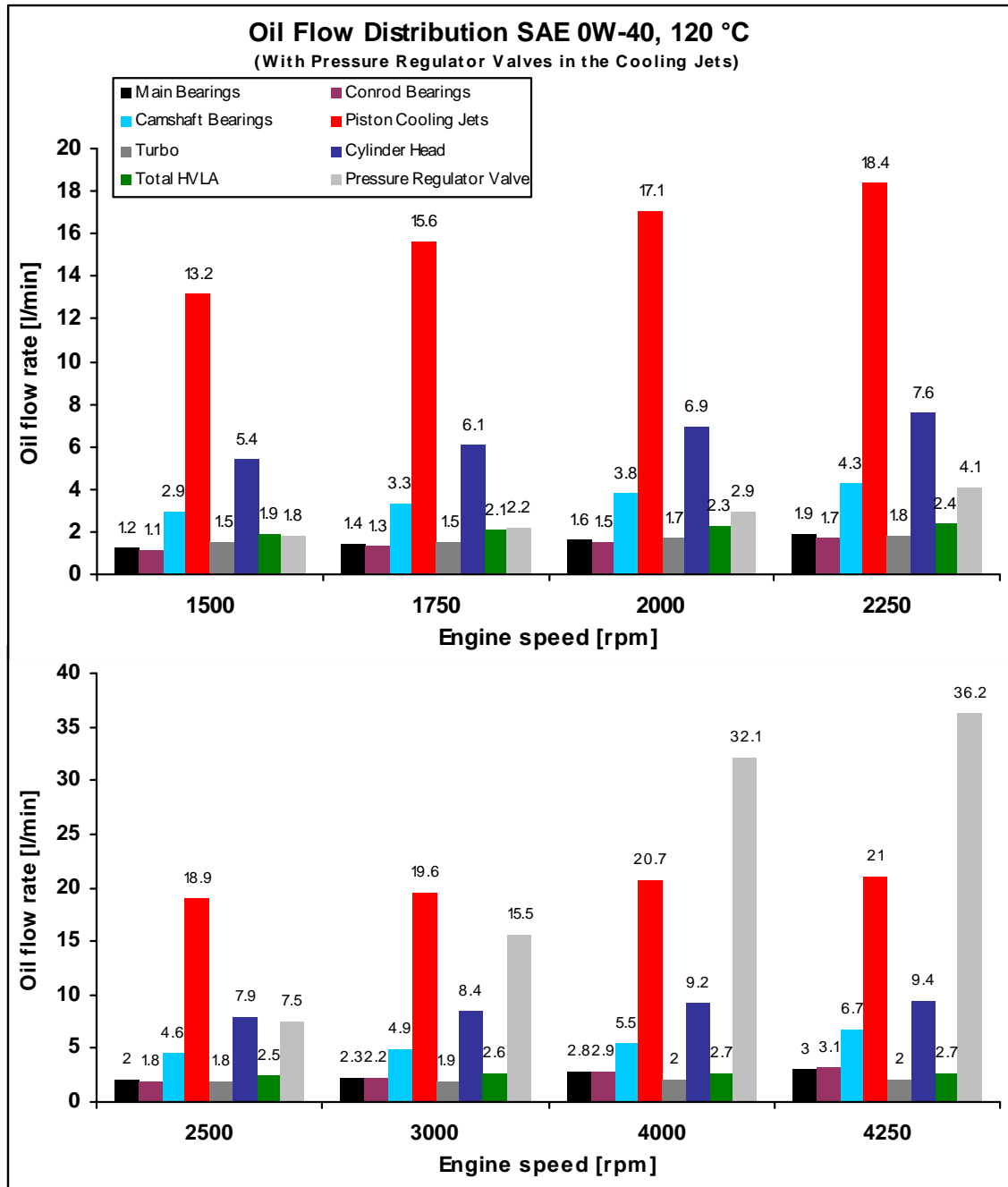
Figure 9: Results from FLOWMASTER calculations on the oil flow distribution for a 3.0 litre Diesel engine (reproduced from [40])

There are different tools and methods for simulation of the oil flow in the bearings. All of them are based on solving the Reynolds equations for the conditions in the bearing. Hydro-Dynamic models (HD) assume rigid bearings. Elasto-Hydro-Dynamic (EHD) models consider the elastic deformation of the bearing parts due to the oil film pressure. Advanced models solve the energy equation together with the Reynolds equations to include the influence of the temperature on the oil viscosity. These models are based on the Thermo-Elasto-Hydro-Dynamic (TEHD) lubrication theory. A comparison of the different models

can be found in [23]. The target of such simulations is to determine the oil flow rate, the peak oil film pressure, the minimum oil film thickness, and the possibility of cavitation, and to check the bearing capacity. FLOWMASTER [38], which was applied to produce the results in Figure 9, uses only a simple HD bearing model to determine the oil flow rate in the bearing. The result strongly depends on the bearing clearance, the supplied oil pressure, and the oil viscosity. The commercial software tool EXCITE [8] can solve the TEHD equations for simulating the conditions in the bearing. The combination of the bearing simulation tool of EXCITE and the oil circuit simulation of FLOWMASTER would further increase the reliability of the results for the oil flow rates, which are used as boundary conditions for the CFD simulations in this thesis.

2.3 Oil Mist Formation

The fine fraction of oil droplets and particles in the crankcase with diameters less than $10\,\mu m$ is called the oil mist. These fine droplets and aerosols consist of engine oil, hydrocarbons, water, soot, and solid metal or non-metal particles [16]. It is assumed that there are two main formation processes for the oil mist. On the one hand, there is atomisation of the engine oil in the small gaps around the piston rings. If the critical pressure ratio between crankcase and combustion chamber is exceeded, the blow-by gas can reach speed of the sound in the gaps. This high-speed gas jet causes oil film atomisation and entrainment of oil droplets. On the other hand there is condensation in the crankcase, which produces very small droplets. The low boiling components of the engine oil and the unburnt fuel evaporate at hot zones in the engine. Due to the fine particulate matter in the gas, which acts as condensation nuclei, the vapour condenses and provides a further fraction of fine droplets in the oil mist.

In [33] the composition of the blow-by gas condensate was analysed for a passenger car gasoline engine. For this purpose, samples of the blow-by gas were taken from the crankcase and condensed at $12\,°C$. The liquid condensate was then analysed [83] and allowed for conclusions on the composition of the oil mist. The content of engine oil components covers the range between 10 and 40 percent. The main part of the condensate consists of fuel components, the remnant is water. It is interesting to see that the high boiling components of the gasoline are enriched in the blow-by condensate. This means that the concentration of these fuel components in the condensate was higher than the concentration in the fuel itself. Otherwise the low boiling components of the gasoline were found only in small concentrations. The hydrocarbon components of the gasoline have boiling temperatures between $0\,°C$ and $200\,°C$. Hence, the gas temperature in the crankcase is too high for condensation of the low boiling fuel components. Diesel has a range of higher boiling

temperatures, which starts at approximately 170 °C and ends at 340 °C. Consequently it can be expected, that notable concentrations of all components of the Diesel fuel can be detected in the condensate of the blow-by gas [29].

The droplets and particles of the oil mist have diameters smaller than 10 μm. Most oil mist separators are designed for an average droplet diameter size between 0.5 and 1.5 μm [76], [77]. Figure 10 shows the Probability Density Function (PDF) of the normalised particle mass (PM, %) for a Diesel engine. The two curves were measured in real time with two different measurement methods at the same operation point of the engine [16]. The values of the blue curve were measured with the Electrical Low-Pressure Impactor (ELPI), the green curve with the gravimetric measurement method. The curves show peaks at a size of about 1 μm. According to [11], 90 percent of the particle mass have diameters smaller than 3 μm, 75 percent have diameters smaller than 2 μm, and 40 percent smaller than 1 μm.
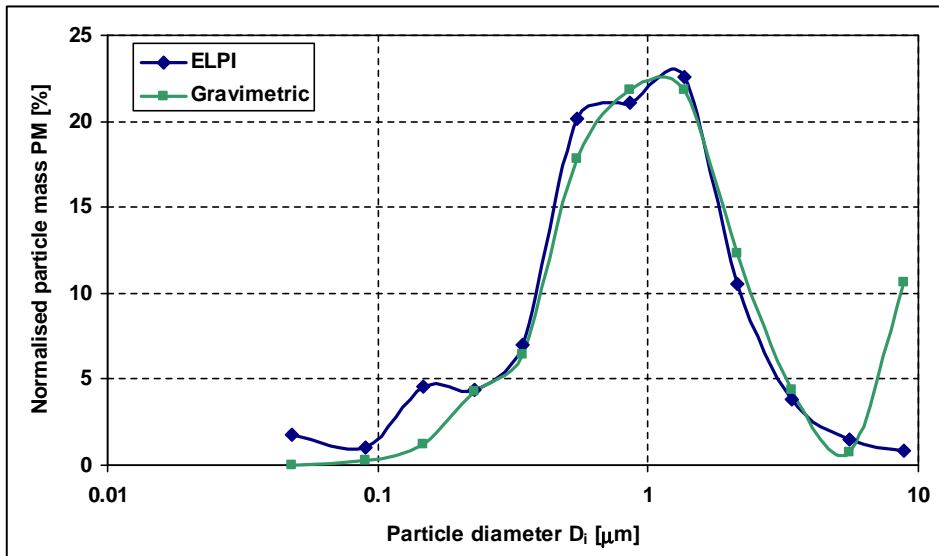

Figure 10: Blow-by particle sizes in a Diesel engine measured in real-time with the Electrical Low-Pressure Impactor and with the gravimetric measurement method (reproduced from [16])

In [75] measurements of the droplet size distribution upstream from the oil mist separator were carried out. The droplet volume distribution functions of six different engines, gasoline and Diesel, operated at different operation points, are shown in Figure 11. All in all eighty curves show that the droplet size distribution functions are quite similar, although the conditions may be considerably different. This is reasonable, because the physical generation processes are closely the same for different engines and at different loads and speeds of the engines. Measurements from [10] showed that higher engine torque produces smaller droplets, because the higher cylinder pressure leads to higher momentum of the blow-by flow in the leakage around the piston rings, and consequently the atomisation of the liquid oil

delivers smaller droplets. Furthermore, a cold engine produces less small droplets and aerosols than a warm engine, since the oil viscosity of a cold engine is higher and there is less evaporation of light fragments of the engine oil and the fuel components. Thus there is a reduced formation of droplets due to condensation.

To sum up, one can say that the oil mist is a complex mixture of different components. Apart from engine oil, there are also other components forming the oil mist. The droplet size varies in the range between 0.1 and 10 µm and is influenced by engine type and operation conditions. The most probable droplet size is approximately 1 µm.
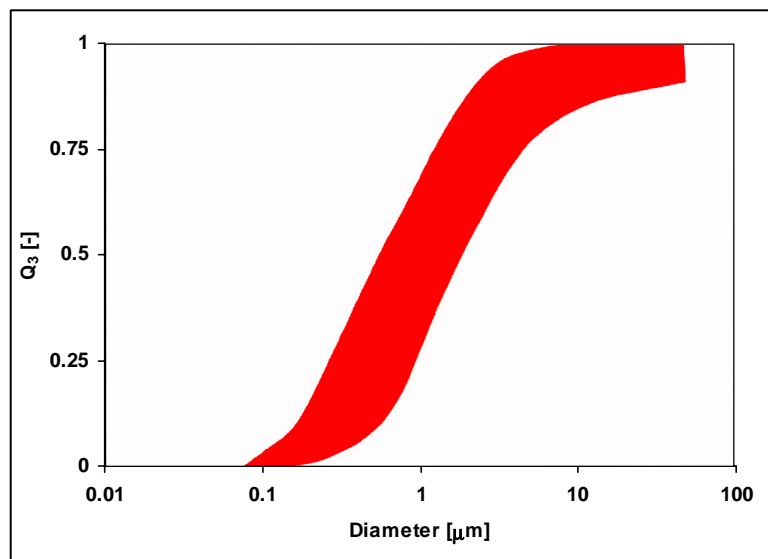

Figure 11: Spectrum of measured cumulative droplet size distributions upstream from the oil mist separator (reproduced from [75])

2.4 Fast and Slow Processes in the Crankcase

The complex multi-phase flow in the crankcase exhibits various flow phenomena. There is droplet detachment from the moving and rotating parts, there is gas and oil mist flow generated by blow-by. Oil flows back to the oil sump as a film down the crankcase wall. At some edges the oil retains and drips off. There is also evaporation of the low boiling components of the engine oil and the unburnt fuel. In colder regions of the crankcase, the vapour condenses and forms very small droplets.

For the CFD simulation, the time scales of these different processes are very important. For the intended flow simulation of a few revolutions of the crankshaft, it is important to distinguish between fast processes, which are relevant for the CFD simulation time interval, and slow processes, which need much more time than the time covered by the simulation.

E.g. if the engine runs at 3000 revolutions per minute (rpm), the time for a single revolution is 0.02 seconds. If a physical process takes several seconds, the CFD simulation would have to contain hundreds of revolutions to describe such a process. Hence, a CFD simulation of the present kind cannot deal with such slow processes. Due to the expected large numbers of cells on the computational grids and the very small time steps of approximately one degree crank angle (CA) at a given engine speed, only simulations of a few revolutions can be afforded with today's work stations.

For comparison of the different processes in the crankcase, a characteristic process time $t_{process}$ is defined for each process separately. The process time is then divided by a reference time t_{ref} to obtain the characteristic dimensionless time scale $\tau_{process}$ of the process described by the relation

$$\tau_{process} = \frac{t_{process}}{t_{ref}} \ .$$
(1)

The reference time is defined as

$$t_{ref} = \frac{1}{n} \ .$$
(2)

It is determined by the inverse of the engine speed, which seems to be the most reasonable quantity for setting the reference time, since it influences most of the flow phenomena in the crankcase directly. This means that, if a process takes place in one revolution of the crankshaft, the dimensionless process time scale is approximately one. Such processes will be called "fast process", because they are relevant for the short time covered by the CFD simulation. If the process takes much more time, the process time scale is much greater than one. Such processes will be called "slow processes". In the next step, the time scales for the various processes will be estimated.

For a spatial classification of the physical processes, a characteristic length is required. There are several possibilities to define the length scale. The length of the crankshaft, the bore of the cylinder or the conrod length would be suitable lengths. When the piston moves up and down, it covers twice the distance of the stroke. Hence, for many processes in the crankcase, the stroke s seems to be a good choice for the reference length scale l_{ref}, as defined by

$$l_{ref} = s \ .$$
(3)

A further definition is required to distinguish between small and large droplets. The oil mist represents the small droplets. As described in section 2.3, the oil mist consists of droplets with diameters less than 10 μm. On the other hand, droplets significantly larger than 10 μm, like the droplets from splashed oil, are called large droplets. The value of 10 μm is an arbitrary threshold, but it helps to separate the processes and is reasonable in the view of the dynamics of the droplet motion in the crankcase.

The first process of consideration is the blow-by. The pressure difference between the combustion chamber and the crankcase leads to the continuous gas flow depending on the pressure ratio and the motion of the piston rings. This process is periodic, for a two-stroke engine at every revolution, for a four-stroke engine at every second revolution. So it is reasonable to take the time for one revolution as the characteristic process time, as shown by

$$t_{blow-by} = t_{ref} \quad . \tag{4}$$

Thus, the dimensionless time scale for blow-by $\tau_{blow-by}$ equals

$$\tau_{blow-by} = \frac{t_{blow-by}}{t_{ref}} = 1 \quad . \tag{5}$$

Oil droplets dripping off represent processes, which are driven by the gravitational force. Neglecting the drag force, the gravitational force leads to constant acceleration of the droplet. If the droplet starts falling from zero velocity, the time required to pass the distance of the characteristic length can be described by

$$s = \frac{1}{2} g t^2 \quad \rightarrow \quad t_{drip-off} = \sqrt{\frac{2s}{g}} \quad , \tag{6}$$

and the dimensionless time scale is then determined by

$$\tau_{drip-off} = \frac{t_{drip-off}}{t_{ref}} = n \sqrt{\frac{2s}{g}} \quad . \tag{7}$$

This equation describes the lower limit of this time scale, because considering the drag force would lead to higher values. Then the droplet is accelerated until there is a balance between the drag force and the gravitational force at the terminal velocity. This maximum falling velocity depends on the droplet diameter, and that is why small droplets would have a much higher drip off time scale.

The oil flow along the wall of the crankcase is driven by the gravitational force. This oil flows back to the oil sump as a film. In a steady film flow the film thickness is constant, because there is a balance between the shear force on the wall and the gravitational force. Assuming steady film flow, vertical wall, and laminar flow at low Reynolds number leads to a parabolic velocity profile as shown in Figure 12. The mean velocity,

$$U_{wallfilm} = \frac{1}{3} \frac{g \delta^2 \rho}{\mu} \quad , \tag{8}$$

is obtained by integrating the velocity profile from the wall to the film surface at $y = \delta$ and dividing it by the film thickness [78], [20]. The time required for the wall film to move the distance of the reference length is given by

$$t_{wallfilm} = \frac{l_{ref}}{U_{wallfilm}} = \frac{3 \mu \, s}{g \, \delta^2 \rho} \quad , \tag{9}$$

leading to the dimensionless time scale for the wall film flow, defined as

$$\tau_{wallfilm} = \frac{t_{wallfilm}}{t_{ref}} = \frac{3 \mu \, s \, n}{g \, \delta^2 \rho} \quad . \tag{10}$$
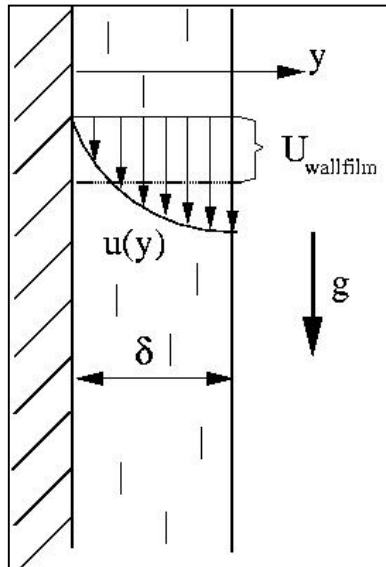

Figure 12: Mean velocity of the steady wall film flow

Liquid disintegration due to detachment from moving parts is a further process of interest in the crankcase. The liquid oil film motion on the moving parts is driven by centrifugal forces. The oil detaches from the crank train. The detachment velocity of the ligaments and droplets is nearly equal to the circumferential velocity of the point from where the liquid

detaches, which has the radial r_0 in the present case. The characteristic process time for rotary detachment $t_{rot-det}$ is defined as

$$t_{rot-det} = \frac{l}{r_0\,\omega} = \frac{s}{2\pi\,\text{n}\,r_0} \quad . \tag{11}$$

$t_{rot-det}$ is simply the time needed for a detached droplet to move the distance of the reference length. The dimensionless time scale results from the process time divided by the reference time, and it equals

$$\tau_{rot-det} = \frac{t_{rot-det}}{t_{ref}} = \frac{s}{2\pi\,r_0} \quad . \tag{12}$$

Condensation of fuel and oil component vapours is the last process considered here. In general condensation takes place if the vapour concentration on the liquid droplet surface is smaller than in the ambient gas. The mass transport is driven by the vapour concentration gradient. The vapour concentration on the liquid surface is a function of the saturation pressure, which depends on the surface temperature. The latent heat of evaporation is released and may lead to a temperature increase of the liquid. The higher the liquid temperature on the interface, the higher the vapour concentration near the surface, and the lower is the difference to the ambient vapour concentration. This process always runs in the direction which leads to equilibrium.

For single component liquids, the saturation pressure is defined by the temperature alone. For multi-component liquids, all species have an influence on the saturation state. There the vapour mass fraction on the droplet surface of each component depends on the composition of the liquid inside the droplet and on the temperature [21]. This case is more complex. Although fuels and engine oils are mixtures of many different hydrocarbons and additives, most simulations for evaporation and condensation use pure liquids. This is why a model pure liquid is required, which has similar properties as the original multi-component fluid. N-dodecane ($C_{12}H_{26}$) is such a fluid, which is often used to describe the thermal properties of Diesel fuel. For engine oil it is more difficult to find a suitable alternative fluid, since there is a huge variety of different oils with different properties.

For determining the characteristic process time of condensation, it is necessary to define a criterion for that process, e.g. the time which is required for the droplet growth from a certain initial diameter to a certain final diameter. The mass transfer rate due to condensation or evaporation for a single droplet according to the well established model of Abramzon and Sirignano [2], [3] can be described by

$$\dot{m}_{drop} = 2\pi\ r_{drop}\ \overline{\rho}_{gas}\ \overline{D}_Y\ Sh^*\ \ln(1+B_M) = -\frac{d(\frac{4\pi}{3}r_{drop}^3\ \rho_{liq})}{dt}\ . \tag{13}$$

Apart from the droplet radius r_{drop}, the gas mixture density $\overline{\rho}_{gas}$ in the vapour film around the droplet, the diffusion coefficient $\overline{D}_Y$, and the modified Sherwood number Sh^*, the mass transfer rate depends on the Spalding mass transfer number B_M, which is defined as

$$B_M = \frac{Y_S - Y_{amb}}{1-Y_S}\ . \tag{14}$$

Y_S is the vapour mass fraction on the droplet surface and Y_{amb} is the vapour mass fraction in the ambient gas. The model works in both directions, for condensation as well as for evaporation, resulting in a negative or a positive mass transfer number, respectively. Equation (13) can be transformed into

$$\dot{d}_{drop} = 2\dot{r}_{drop} = \frac{-2\overline{\rho}_{gas}\ \overline{D}_Y\ Sh^*\ \ln(1+B_M)}{d_{drop}\ \rho_{liq}} = \frac{d(d_{drop})}{dt}\ . \tag{15}$$

Equation (15) describes the change of the droplet size in time. Separation of time and diameter dependent dimensions and the subsequent integration leads to

$$t_{cond} = \int_0^{t_{cond}} dt = \int_{d_{drop,1}}^{d_{drop,2}} \frac{d(d_{drop})}{\dot{d}_{drop}} = \int_{d_{drop,1}}^{d_{drop,2}} \frac{-d_{drop}\ \rho_{liq}}{2\overline{\rho}_{gas}\ \overline{D}_Y\ Sh^*\ \ln(1+B_M)} dd_{drop}\ . \tag{16}$$

t_{cond} determines the representative time for condensation. This is the time required for the growth of the droplet from a certain diameter $d_{drop,1}$ to diameter $d_{drop,2}$ at a given constant ambient vapour mass fraction. Finally, the non-dimensional time scale for condensation can be defined as

$$\tau_{cond} = \frac{t_{cond}}{t_{ref}} = n\ t_{cond}\ . \tag{17}$$

Further details about the model, the calculation, and the applied assumption for the determination of the characteristic condensation time can be found in the appendix section 8.1. Two calculations of the dimensionless condensation time scale, $\tau_{cond-fuel,1}$ and $\tau_{cond-fuel,2}$, have been performed. The time required for an N-dodecane droplet to grow from $10\ \mu m$ to $15\ \mu m$ at a constant ambient temperature and a slight supersaturation of the ambient vapour leads to the dimensionless condensation time scale $\tau_{cond-fuel,1}$. The second time scale $\tau_{cond-fuel,2}$ results from a calculation at similar ambient conditions. There the droplet grows from $1\ \mu m$ to $1.5\ \mu m$. In both cases the droplet diameter increases by a factor

of 1.5. A droplet with a diameter of 10 μm has the same mass as 1000 droplets with diameters of 1 μm. This means that the same amount of vapour is condensated, either if 1000 droplets grow from 1 μm to 1.5 μm, or if one droplet grows from 10 μm to 15 μm. Thus, the relative gains of mass are equal in both cases, and it is reasonable to compare the time scales $\tau_{cond-fuel,1}$ and $\tau_{cond-fuel,2}$. The engine oil time scale $\tau_{cond-oil}$ has been estimated by an analysis of the logarithmic term in Equation (13) in comparison with the fuel condensation calculation for $\tau_{cond-fuel,2}$.

The input values used for the calculations of the process time scales of all considered processes are listed in Table 1. The purpose was to determine representative values, which can occur during ordinary operation of the engine. By reasonable variation of these values, the dimensionless time scales would be different. But they would still remain in the same order of magnitude. Thus, the time scales of the processes can be compared and subsequently separated into fast and slow processes.

Reference Data	Engine speed n	50 (3000)	s^{-1},(rpm)
	Characteristic length: stroke s	0.1	m
Oil properties	Kinematic viscosity at 100 °C ν	$14.9 \cdot 10^{-6}$	m²/s
(OMV Truck LD SAE 15W-40)	Dynamic viscosity at 100 °C μ	0.0124	Ns/m²
	Density at 100 °C ρ	831.75	kg/m³
Wall film data	Height of steady film flow δ	0.001	m
Detachment data	Radius of liquid detachment r_0	0.05	m
Condensation data	Saturation ratio S	1.01	-
(N-dodecane $C_{12}H_{26}$)	Droplet start temperature $T_{drop,1}$	373	K
	Initial droplet diameter $d_{drop,1}$	10/1	μm
	Final droplet diameter $d_{drop,2}$	15/1.5	μm
	Temperature of ambient gas T	373	K
	Pressure p	100 000	Pa

Table 1: Set up of calculation for fast and slow processes

Inserting the input values from Table 1 into Equations (5), (7), (10) and (12) of the dimensionless time scales of the processes and performing the condensation calculations presented shown in appendix 8.1, leads to the results for the dimensionless process time scales presented in Table 2.

In Figure 13 all non-dimensional times are compared on a logarithmic scale. One can see that blow-by and rotary detachment of the droplets are the fastest processes. Wall film flow,

condensation of the 10 μm fuel droplet, and condensation of the engine oil droplet with 1 μm diameter are the slowest processes. The dripping process of oil droplets is more or less slow, because it has to be considered that the drag force was neglected in the calculation of the time scale. By taking into account the drag force, the drip-off time scale would be larger. The condensation of fuel vapour is more difficult to assign to the fast or slow processes, because it can be both, fast or slow, depending on the ambient conditions and it depends on the droplet diameter. As shown in section 8.1, the time for condensation is approximately proportional to the square of the droplet diameter. This means that, if the droplets are very small, the process can become very fast.

$\tau_{blow-by}$	$\tau_{drip-off}$	$\tau_{wallfilm}$	$\tau_{rot-det}$	$\tau_{cond-fuel,1}$	$\tau_{cond-fuel,2}$	$\tau_{cond-oil}$
1.0	7.14	22.78	0.32	90.96	0.89	>16.05

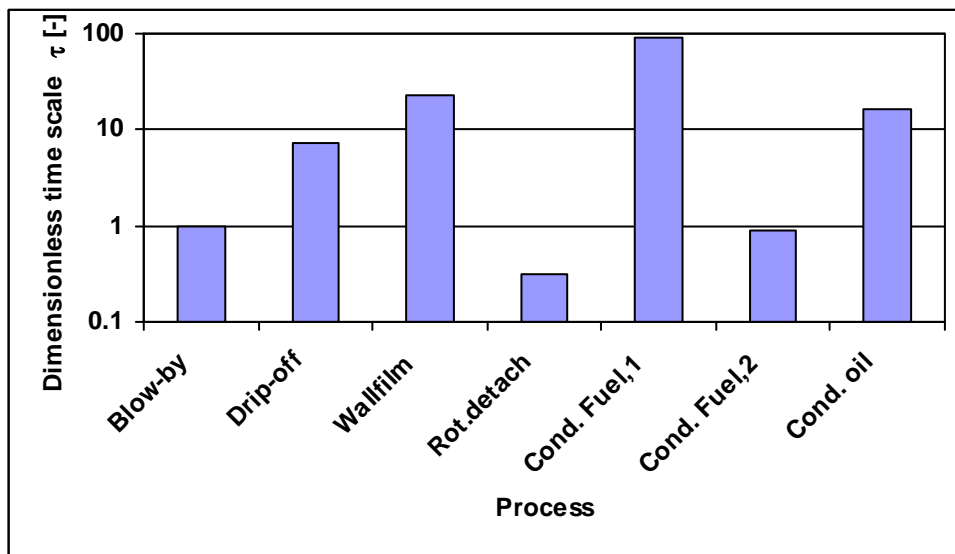Table 2: Calculation of time scales for the processes in the crankcase

Figure 13: Comparison of the time scales of physical processes in the crankcase

As a conclusion one can say that blow-by and rotary detachment of liquid are the most important fast processes, which have to be considered in the simulation of the crankcase flow. They will be a part of further investigations in the following sections. Separate models for blow-by, as well as for the droplet detachment from the rotating crank train, will be applied in the CFD simulation. The processes driven by the gravitational force, such as wall film flow and drip-off, are too slow for account in the simulation. There will be no focus on these processes in the further investigations. The condensation and evaporation of the engine oil is also too slow and will be neglected. Although the condensation of fuel droplets can be

a fast process, and fuel vapour can be an important component of the blow-by gas, it will not be considered in the further investigations. If the combustion works well, the amount of unburnt fuel is small. Thus, unburnt fuel and the condensation of fuel droplets will be neglected in the following investigations.

3 Models for the Crankcase Flow

The relevant models from the literature for the multi-phase flow in the crankcase are discussed in this section. At first, the Eulerian multi-phase approach is described briefly. Since blow-by has been indicated as an important (fast) process in the crankcase flow simulations, the model for determination of the gas mass flow rate into the crankcase is presented in detail in the second subchapter of this section. Then model correlations from different authors describing drop formation by rotating discs are discussed, since this process has also been found to be fast. At last, a method for transporting the moments of a droplet size distribution function is discussed. With this approach, the segregation of the liquid phase into several liquid droplet size classes can be avoided.

3.1 Multi-phase Flow Modelling

In flows with more than one component it is necessary to model the phenomena with an approach taking into account the different phases. The term "phase" does not necessarily indicate different fluids. Also the same fluid can change its state, e.g. by evaporation of liquid or condensation of vapour. There are different methods for simulating multi-phase flows.

The Discrete Droplet Method (DDM) [32] is an Eulerian-Lagrangian approach, which is often used for multi-phase flows with dilute dispersed liquid phases. The Lagrangian approach is to follow the track of fluid particles of the dispersed phase and integrate the equations of motion over time. The flow field of the continuous phase delivers the ambient conditions for the particles. Particles with similar properties (e.g. diameter or velocity class) are merged to droplet parcels. The equations of motion are solved for these parcels. The interactions between the dispersed and the continuous phases are modelled as source terms in the conservation equations.

The method applied for the simulations in this thesis, however, is the Eulerian-Eulerian multi-phase approach, which can be applied in different ways. If the discretisation is fine enough, the interface between the different phases can be tracked, and one can solve the flow equations within each phase in the same way as for single flows. Such methods are called Volume of Fluid (VOF) approaches. But in most cases the interface tracking would exceed the reasonable or even feasible resolutions in space and time. The resulting computational effort would be much too high. E.g. for droplet flow at high velocity, the resolution in space of the computational meshes of all small-scaled surfaces would require enormous computational effort.

Hence it is necessary to compute average values instead of tracking the complete interface between the phases. So the computational effort can be reduced. The phases are determined by their volume fractions. The volume fraction is the ensemble averaged value of the phase indicator function, which determines the presence of a phase at any point in space at any time. Figure 14 shows a two phase flow field consisting of air and liquid. In each computational cell the phases are characterised by the average values of the flow quantities volume fraction, density, velocity, enthalpy, and turbulence. The interface is not tracked, and hence there is no information about the exact position of the surface. However, for large-scaled surfaces, the gradient of the phase volume fraction indicates the position of the interface. For small-scaled surfaces, e.g. droplets smaller than the cell size, this information is lost.

The multi-phase conservation equations based on the framework of [31] are presented here in short form without detailed derivations. These equations are solved by the multi-phase CFD code AVL FIRE [6], which is used for the flow simulations of this thesis. An elaborated summary of the derivations in [31] can be found in [85].
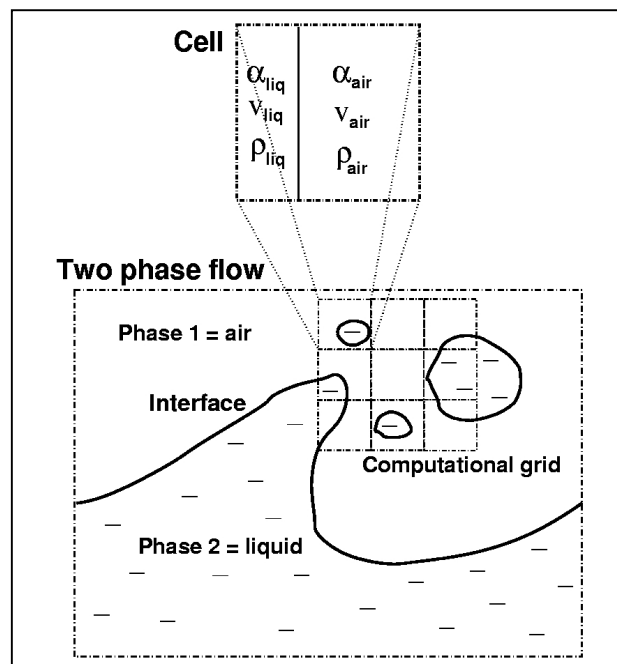

Figure 14: Sketch of a two-phase flow field

3.1.1 Transport Equations

The general form of the differential conservation equation for single-phase flow of a property ϕ according to [5] can be described by the equation

$$\frac{\partial \rho \phi}{\partial t} + \frac{\partial}{\partial x_j}\left(\rho U_j \phi\right) = \frac{\partial \mathring{J}_A}{\partial x_j} + \rho \mathring{J}_m \ . \tag{18}$$

Here and in all other transport equations, the Einstein convention that, whenever one subscript appears twice in a term, summation over the range of that subscript is implied. ϕ is the corresponding property per unit mass, ρ is the fluid density, $\mathring{J}_A$ is the local diffusion (surface) flux of ϕ at the control boundary per unit time, and $\mathring{J}_m$ is the source or sink of ϕ per unit mass and unit time. Applying to mass conservation, i.e. $\phi = 1$ and setting $\mathring{J}_m$ and $\mathring{J}_A$ on the right-hand side to zero, leads to the continuity equation of single-phase flow in differential form. The momentum equation can be obtained by setting $\phi = U_i$, introducing the pressure forces and viscous stresses for $\mathring{J}_A$ and introducing the body forces for $\mathring{J}_m$. Similar operations can be performed to obtain the conservation equation for energy (total enthalpy: $\phi = h$).

The single-phase flow conservation equations for phase k are consistent within the region bounded by the phase interface, e.g. the liquid region beneath the interface in Figure 14. Above the interface the conservation equations for air describe the flow there.

A helpful tool to isolate each component theoretically is the phase indicator function, also called the component indicator function $\chi_k(\mathbf{x}, t; \varphi)$ of Equation (19). This function "picks out" component k at a certain realisation φ of an ensemble and ignores all other components and interfaces. χ_k is a function of space and time at any realisation φ, and it is defined as

$$\chi_k(\mathbf{x}, t; \varphi) = \begin{cases} 1 & \mathbf{x} \in k \ \ at \ any \ \varphi \\ 0 & \mathbf{x} \notin k \ \ at \ any \ \varphi \ . \end{cases} \tag{19}$$

For the following ensemble averaging procedure, it is necessary to consider the flow events in many realisations. The aim of the statistical ensemble averaging is to track the most probable flow field properties. E.g. in the case of droplet flow, the trajectory of the droplet motion will be different for each experiment. The trajectory obtained after the ensemble averaging of many realisations φ will be the most probable one. However, there will still be some parcels, from time to time, moving on unprobable paths. Ω is the set of all realisations representing the ensemble, where φ is one certain realisation of Ω ($\varphi \in \Omega$). Each realisation has its own probability of occurrence, say $dm(\varphi)$. In [31] the ensemble average of the quantity f, which is denoted by a bar placed above the symbol, is defined as

$$\overline{f}(\mathbf{x}, t) = \int_\Omega f(\mathbf{x}, t; \varphi) \, dm(\varphi) \ . \tag{20}$$

The phase volume fraction α_k results as an ensemble average of the phase indicator function χ_k, as shown in the equation

$$\alpha_k = \overline{\chi_k} \ .$$
(21)

All the other variables, such as density, velocity, enthalpy, turbulence kinetic energy, turbulent dissipation rate, shear stresses, heat flux, and so on, are defined in terms of weighted averages. The variables are either component-weighted variables, that is, weighted with the component function χ_k as the fluid density

$$\overline{\rho}_k = \frac{\overline{\chi_k \rho}}{\alpha_k} \ ,$$
(22)

or mass-weighted (Favré averaged), that is weighted by $\rho \chi_k$, such as the phase velocity

$$\overline{\mathbf{U}}_k = \frac{\overline{\chi_k \rho \mathbf{U}}}{\alpha_k \overline{\rho}_k} \ .$$
(23)

It can be shown that the spatial derivative of the phase indicator function, $\partial \chi_k / \partial x_j$, acts as an interface indicator of phase k. The general multi-phase flow conservation equation is obtained after multiplication of the general conservation equation for single-phase flow, Equation (18), with the phase indicator function χ_k and a subsequent transformation. Contrary to the single-phase flow equation, the multi-phase flow equation contains the phase indicator function in each term and the interfacial terms on the right-hand side. Applying the general multi-phase conservation equation for mass, momentum, enthalpy and turbulence separately, performing the ensemble averaging procedure with all equations, subsequent simplification, and modelling of the interfacial terms lead to the resulting equations presented here.

In the following equations, bars on the flow properties determining the averaged values are omitted for convenience.

3.1.1.1 Mass Conservation Equation

The mass conservation equation for phase k is represented by the equation

$$\frac{\partial \alpha_k \rho_k}{\partial t} + \frac{\partial}{\partial x_j} \left(\alpha_k \rho_k U_{k,j} \right) = \sum_{l=1, l \neq k}^{n_{ph}} \Gamma_{kl} \qquad k = 1, ..., n_{ph} \ .$$
(24)

The right-hand side is not zero. The term Γ_{kl} represents the mass exchange between the phases k and l.

The total number of phases is denoted by n_{ph}. The compatibility condition

$$\sum_{k=1}^{n_{ph}} \alpha_k = 1 \tag{25}$$

must be satisfied.

3.1.1.2 Momentum Conservation Equation

In the multi-phase momentum conservation equation

$$\frac{\partial \alpha_k \rho_k U_{k,i}}{\partial t} + \frac{\partial}{\partial x_j} \left(\alpha_k \rho_k U_{k,j} U_{k,i} \right) = -\alpha_k \frac{\partial p}{\partial x_i} + \frac{\partial}{\partial x_j} \left[\alpha_k (\tau_{k,ij} + \tau_{k,ij}^t) \right] + \alpha_k \rho_k g_i$$
$$+ \sum_{l=1,l\neq k}^{n_{ph}} M_{kl,i} + U_{k,i} \sum_{l=1,l\neq k}^{n_{ph}} \Gamma_{kl} \qquad k = 1,...,n_{ph} \quad , \tag{26}$$

g_i is a component of the body force vector and represents the gravitational acceleration, $M_{kl,i}$ represents the momentum transfer between phases k and l, and p is the pressure. The term $U_k \Gamma_{kl}$ represents the interfacial momentum transfer due to mass transfer. Pressure is assumed uniform for all phases, as described by the equation

$$p_k = p \qquad k = 1,...,n_{ph} \quad . \tag{27}$$

The phase k shear stress tensor τ_k is given as

$$\tau_{k,ij} = \mu_k \left[\left(\frac{\partial U_{k,j}}{\partial x_i} + \frac{\partial U_{k,i}}{\partial x_j} \right) - \frac{2}{3} \delta_{ij} \frac{\partial U_{k,m}}{\partial x_m} \right] , \tag{28}$$

where μ_k is the molecular dynamic viscosity, and Newtonian fluid is assumed. The Reynolds stress τ_k^t is

$$\tau_{k,ij}^t = -\rho_k \overline{U'_{k,i} U'_{k,j}} = \mu_k^t \left[\left(\frac{\partial U_{k,j}}{\partial x_i} + \frac{\partial U_{k,i}}{\partial x_j} \right) - \frac{2}{3} \delta_{ij} \frac{\partial U_{k,m}}{\partial x_m} \right] - \frac{2}{3} \delta_{ij} \rho_k k_k \quad . \tag{29}$$

The model is closed by giving the turbulent viscosity μ_k^t as

$$\mu_k^t = \rho_k C_\mu \frac{k_k^2}{\varepsilon_k} \quad . \tag{30}$$

3.1.1.3 Energy Equation

The energy equation,

$$\frac{\partial \alpha_k \rho_k h_k}{\partial t} + \frac{\partial}{\partial x_j}\left(\alpha_k \rho_k U_{k,j} h_k\right) = \frac{\partial}{\partial x_j}\left[\alpha_k \left(q_{k,j} + q_{k,j}^t\right)\right] + \alpha_k \rho_k \theta_k + \alpha_k \rho_k g_j U_{k,j}$$

$$+ \frac{\partial}{\partial x_j}\left[\alpha_k U_{k,i}\left(\tau_{k,ij} + \tau_{k,ij}^t\right)\right] + \alpha_k \frac{\partial p}{\partial t} + \sum_{l=1,l\neq k}^{n_{ph}} H_{kl} + h_k \sum_{l=1,l\neq k}^{n_{ph}} \Gamma_{kl} \qquad k = 1,...,n_{ph} \ , \tag{31}$$

is represented as a conservation equation of the total enthalpy h_k, which includes the thermal and the kinetic energies, described by the equation

$$h_k = c_{P,k} T_k + \frac{\mathbf{U}_k^2}{2} \ . \tag{32}$$

Here θ_k is a specific enthalpy source, H_{kl} represents the energy transfer between phases k and l. The conductive heat flux vector $\mathbf{q}_k$ is defined as

$$q_{k,j} = \frac{\kappa_k}{c_{p,k}} \frac{\partial h_k}{\partial x_j} \ , \tag{33}$$

where κ_k is the phase k thermal conductivity. The turbulent heat flux vector $\mathbf{q}_k^t$ equals

$$q_{k,j}^t = -\rho_k \overline{U_{k,j}' h_k'} = \frac{\mu_k^t}{\sigma_T} \frac{\partial h_k}{\partial x_j} \ . \tag{34}$$

U_k' represents the turbulent velocity fluctuations and h_k' the turbulent enthalpy fluctuation. σ_T is the turbulent Prandtl number.

3.1.1.4 Turbulence Model

The k-ε model solves two additional transport equations for the turbulent kinetic energy, as described in the equation

$$\frac{\partial \alpha_k \rho_k k_k}{\partial t} + \frac{\partial}{\partial x_j}\left(\alpha_k \rho_k U_{k,j} k_k\right) = \frac{\partial}{\partial x_j}\left[\alpha_k\left(\mu_k + \frac{\mu_k^t}{\sigma_k}\right)\frac{\partial k_k}{\partial x_j}\right] + \alpha_k P_k - \alpha_k \rho_k \varepsilon_k$$

$$+ \sum_{l=1,l\neq k}^{n_{ph}} K_{kl} + k_k \sum_{l=1,l\neq k}^{n_{ph}} \Gamma_{kl} \qquad k = 1,...,n_{ph} \ , \tag{35}$$

and the turbulent dissipation rate, as described in the equation

$$\frac{\partial \alpha_k \rho_k \varepsilon_k}{\partial t} + \frac{\partial}{\partial x_j}\left(\alpha_k \rho_k U_{k,j} \varepsilon_k\right) = \frac{\partial}{\partial x_j}\left[\alpha_k\left(\mu_k + \frac{\mu_k^t}{\sigma_\varepsilon}\right)\frac{\partial \varepsilon_k}{\partial x_j}\right] + \sum_{l=1,l\neq k}^{n_{ph}} D_{kl} + \varepsilon_k \sum_{l=1,l\neq k}^{n_{ph}} \Gamma_{kl}$$

$$+ \alpha_k C_1 P_k \frac{\varepsilon_k}{k_k} - \alpha_k C_2 \rho_k \frac{\varepsilon_k^2}{k_k} - \alpha_k C_4 \rho_k \varepsilon_k \frac{\partial U_{k,j}}{\partial x_j} \qquad k = 1,...,n_{ph} \ . \tag{36}$$

In these equations, K_{kl} and D_{kl} represent the exchange terms for turbulence. The production term P_k due to shear for phase k is given as

$$P_k = \tau_{k,ij}^t \frac{\partial U_{k,i}}{\partial x_j} \ . \tag{37}$$

The used assumptions in the modelling of the closure terms in the turbulent kinetic energy equation are [51]:

- Turbulence level of the dispersed phase is assumed to equal the continuous phase turbulence level.
- The interaction between the two phases is neglected.

The assumptions used lead to the closure of k and ε equations in single-phase flows. The used closure coefficients from turbulent kinetic energy and dissipation equation are provided in Table 3.

σ_k	σ_ε	σ_T	C_1	C_2	C_4	C_μ
1.0	1.3	0.9	1.44	1.92	-0.33	0.09

Table 3: Closure Coefficients of the k-ε model

3.1.2 Interactions between the Liquid and Gaseous Phases

3.1.2.1 Drag Force

The interaction between the two phases is represented in the momentum equation by a drag force. The drag force on a single droplet or bubble moving in an ambient gas or liquid is described in the equation

$$\mathbf{F}_D = \frac{1}{2} c_D \rho_c \frac{d_d^2 \pi}{4} |\mathbf{U}_c - \mathbf{U}_d| (\mathbf{U}_c - \mathbf{U}_d) \ , \tag{38}$$

where the subscript c denotes the continuous phase and subscript d the dispersed phase. The drag force depends on the relative velocity between the phases, the projected area of the droplet or bubble, and on the drag coefficient c_D. The drag force $\mathbf{M}_{D,dc}$ per unit volume between continuous and dispersed phase is described by

$$\mathbf{M}_{D,dc} = N''' \mathbf{F}_D = \frac{6\alpha_d}{d_d^3 \pi} \mathbf{F}_D = \frac{3}{4} c_D \frac{\alpha_d \rho_c}{d_d} |\mathbf{U}_c - \mathbf{U}_d| (\mathbf{U}_c - \mathbf{U}_d) = -\mathbf{M}_{D,cd} \ . \tag{39}$$

$\mathbf{M}_{D,dc}$ is given by the number of droplets or particles per unit volume, $N''' = 6\alpha_d / \pi d_d^3$, multiplied by the single particle drag force. To obtain the drag force of all particles contained in a certain control volume, $\mathbf{M}_{D,dc}$ has to be multiplied by the volume of the control volume, e.g. the computational cell volume. Uniform velocity of all particles in the control volume and an average uniform droplet diameter d_d are assumed. Hence the smaller the size of the control volume the more accurate the drag force term due to different relative velocities.

Special attention has to be paid to the drag coefficient c_D, which takes into account the particle shape and the flow conditions. The drag coefficient is investigated very well for rigid, spherical particles. There are a lot of correlations describing the drag coefficient for a certain range of the particle Reynolds number Re defined as

$$Re = \frac{|\mathbf{U}_c - \mathbf{U}_d| d_d}{\nu_c} \; . \tag{40}$$

For Stokes flow, i.e. at low particle Reynolds number, there is an analytical solution for the drag coefficient given as

$$c_D = \frac{24}{Re} \; . \tag{41}$$

Schiller and Naumann [79] delivered the correlation in Equation (42) valid up to a particle Reynolds number of 1000.

$$c_D = \frac{24}{Re}\left(1 + 0.15 Re^{0.687}\right) \tag{42}$$

Putnam [71] developed a similar correlation for the drag coefficient, which is given by

$$c_D = \frac{24}{Re}\left(1 + \frac{1}{6} Re^{0.667}\right). \tag{43}$$

This correlation is also valid for particle Reynolds numbers smaller than 1000. For higher Reynolds numbers $10^3 \le Re \le 10^5$, a constant drag coefficient of approximately 0.43 is applied.

A more accurate description of the drag coefficient for a sphere is given by the standard drag curve from [25] represented by the Equations (44). The standard drag curve consists of empirical and semi-empirical equations to cover a large range of the particle Reynolds number [59]. Remarkable is the drop in the drag coefficient at a very high Reynolds number

of about $4 \cdot 10^5$. This is caused by the laminar-turbulent transition of the boundary layer, which causes the flow to follow the sphere contour farther and therefore reduces the drag.

$$c_D = \begin{cases} \dfrac{3}{16} + \dfrac{24}{Re} & \text{for } Re \leq 0.01 \\[2mm] \dfrac{24}{Re}\left(1 + 0.1315 Re^{(0.82 - 0.05 \log_{10} Re)}\right) & \text{for } 0.01 \leq Re < 20 \\[2mm] \dfrac{24}{Re}\left(1 + 0.1935 Re^{0.6305}\right) & \text{for } 20 \leq Re < 260 \\[2mm] 44.0048\, Re^{(-1.1242 + 0.1558 \cdot \log_{10} Re)} & \text{for } 260 \leq Re < 1500 \\[2mm] 0.0034906\, Re^{\left(2.5558 - 0.9295 \cdot \log_{10} Re + 0.1049(\log_{10} Re)^2\right)} & \text{for } 1500 \leq Re < 1.2 \cdot 10^4 \\[2mm] 0.012075\, Re^{(0.637 - 0.0636 \cdot \log_{10} Re)} & \text{for } 1.2 \cdot 10^4 \leq Re < 4.4 \cdot 10^4 \\[2mm] 4.5814 \cdot 10^{-5}\, Re^{(1.5809 - 0.1546 \cdot \log_{10} Re)} & \text{for } 4.4 \cdot 10^4 \leq Re < 3.38 \cdot 10^5 \\[2mm] 29.78 - 5.3 \log_{10} Re & \text{for } 3.38 \cdot 10^5 \leq Re < 4.0 \cdot 10^5 \\[2mm] 0.1 \log_{10} Re - 0.49 & \text{for } 4.0 \cdot 10^5 \leq Re < 10^6 \\[2mm] 0.19 - \dfrac{80000}{Re} & \text{for } Re \geq 10^6 \end{cases} \tag{44}$$

The correlations in Equations (41) to (44) are compared in Figure 15. The Stokes flow exhibits very low Reynolds numbers. The standard drag curve is a sophisticated description. The correlations from Schiller and Naumann as well as from Putnam are similar and deliver an easy and sufficient description of the drag coefficient. Therefore these correlations will be used in the further calculations.
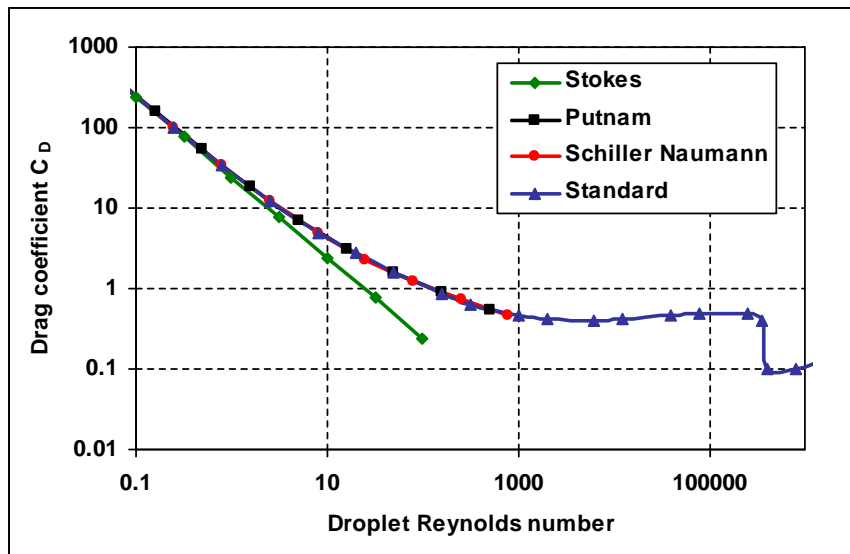

Figure 15: Drag coefficient as a function of the droplet Reynolds number

There is a difference in the drag coefficient between a single particle and the particles in a swarm. The higher the particle concentration of the swarm, the higher is the drag coefficient. The flow around each particle is influenced by the flow around the neighbouring particles, and this causes an increase of the drag force. The swarm density is represented by the volume fraction α_d of the dispersed phase.

A correlation from [28], where the particle drag coefficient in a swarm $c_{D,\alpha}$ is modelled as a function of the drag coefficient of a single particle, the Reynolds number, and the dispersed phase volume fraction α_d is represented by

$$
\begin{aligned}
c_{D,\alpha} &= c_D \left(1 - \alpha_d\right)^{-\beta} \\
\beta &= 3.7 - 0.65\, e^{-0.5\left(1.5 - \log_{10}(Re)\right)^2} \quad for\ 0.01 \le Re < 10000 \ .
\end{aligned}
\tag{45}
$$

Another correlation from [65] based on Equation (43) is given as

$$
c_{D,\alpha} = \frac{24}{Re}\left[\left(1 - \alpha_d\right)^{-2.65} + \frac{1}{6} Re^{0.667}\left(1 - \alpha_d\right)^{-1.78}\right] \ .
\tag{46}
$$

Figure 16 shows the influence of α_d on the drag coefficient according to Equation (46). As an example, for a Reynolds number of 100 the drag force at $\alpha_d = 0.2$ is approximately 55 percent higher than the value at $\alpha_d = 0$, which is the value for a single droplet.
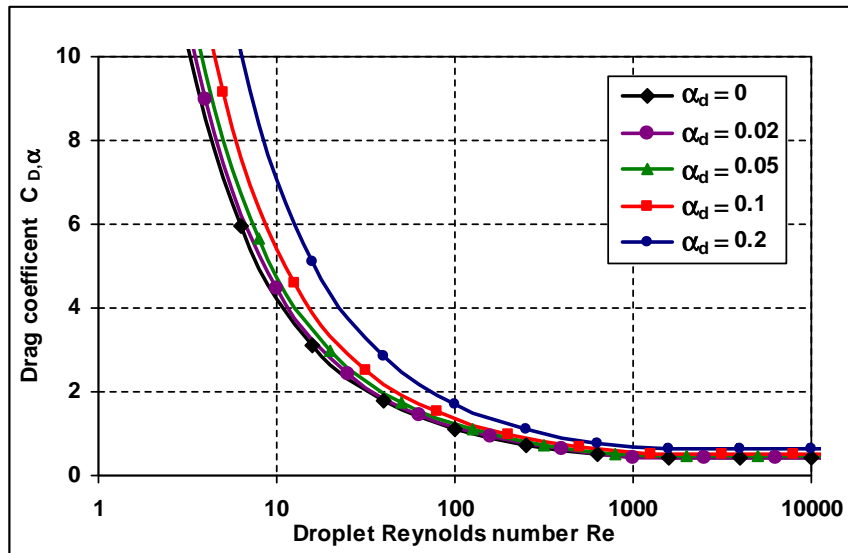

Figure 16: Drag coefficient depending on volume fraction and Re according to Equation (46)

The drag coefficient correlations above assume rigid spheres. For fluid particles this assumption is only valid at low Reynolds or Weber numbers. For higher values of Re, droplets or bubbles are deformed. They can oscillate, and if the aerodynamic force on the

fluid particle is high enough, they may break-up. For deformed particles of ellipsoidal shape correlations can be found in the literature. The aspect ratio E is defined as the ratio of the half-axes of the ellipsoid in flow direction and perpendicular to it, represented by the equation

$$E = \frac{b}{a} \ . \tag{47}$$

An aspect ratio of one represents a sphere; an aspect ratio of zero represents a disc.

A simple correlation from [49] and [50] for the drag coefficient of deformed liquid droplets is given by the equation

$$c_{D,E} = c_D \left(1 + 2.632\,y \right) \ . \tag{48}$$

This correlation is often used for oscillating droplets calculated with the TAB model of [66]. It expresses the fact that the drag coefficient of a distorted droplet $c_{D,E}$ should lie between that of a rigid sphere and that of a disc. The parameter y is the dimensionless value of the droplet distortion and can be calculated either with the equation

$$y = \frac{2x}{a} = 2\left(1 - \frac{r}{a}\right) = 2\left(1 - E^{\frac{1}{3}}\right) \tag{49}$$

according to [49], or with the equation

$$y = \min\left(1, \frac{x}{r}\right) = \min\left(1, \frac{a}{r} - 1\right) = \min\left(1, E^{-\frac{1}{3}} - 1\right) \tag{50}$$

according to [50]. The quantity x determines the displacement of the equator of the droplet from its equilibrium position. The maximum value of y is unity, since a further deformation of the droplet would lead to break-up.

Another correlation from [63] is represented by the equation

$$c_{D,E} = 2(E-1)(E-0.5)c_{D,E=0} - 4E\left(E-1\right)c_{D,E=0.5} + 2E\left(E-0.5\right)c_{D,E=1} \ . \tag{51}$$

There $c_{D,E}$ results from a quadratic interpolation between the drag coefficients of a sphere $c_{D,E=1}$, of a disc $c_{D,E=0}$, and of an ellipsoid $c_{D,E=0.5}$. To obtain the drag coefficients for $c_{D,E=0}$ and $c_{D,E=0.5}$ in a certain range of the Reynolds number, many numerical simulations have been performed in [63]. $c_{D,E=0}$ is determined by the equation

$$c_{D,E=0} = \begin{cases} \dfrac{64}{\pi \, Re} \left(1 + 0.1241 Re^{0.8369}\right) & for \; Re \le 20 \\[3mm] \dfrac{64}{\pi \, Re} \left(1 + 10^{x}\right) & for \; 20 \le Re < 200 \end{cases} \tag{52}$$

$$with \quad x = -1.1656 + 1.1885 \log_{10} Re - 0.1223 \left(\log_{10} Re\right)^2 \;,$$

and yields an extended formulation to the disc drag coefficient correlations from [25]. $c_{D,E=0.5}$ is represented by the equation

$$\frac{c_{D,E=0.5}}{c_{D,E=1}} = \begin{cases} 0.9053 \left(1 + 10^{-2.9570 + 1.2006 \log_{10} Re - 0.0708 \left(\log_{10} Re\right)^2}\right) & for \le 20 \\[3mm] 0.9053 \left(1 + 10^{-4.2784 + 2.9449 \log_{10} Re - 0.6160 \left(\log_{10} Re\right)^2}\right) & for \; 20 \le Re < 200 \;. \end{cases} \tag{53}$$

For larger Reynolds numbers a linear interpolation between $c_{D,E=0}$ and $c_{D,E=1}$ can be performed, because the above correlations are valid for Reynolds < 200 only. Therefore, following [25], it is a sufficient approximation to use a constant value of 1.17 for $c_{D,E=0}$.

Figure 17 shows the drag coefficient $c_{D,E}$ for different values of the aspect ratio E. It is remarkable that at low droplet Reynolds numbers the drag coefficient is smaller for a disc than for a sphere. However, over the whole range of the droplet Reynolds number the difference is rather small. E.g. at $Re = 100$ and at $E = 0.35$, the disc drag coefficient is about 6 percent higher than that of a spherical particle. Thus the dependency of the drag coefficient on droplet deformation will be disregarded in the performed simulations of this thesis.
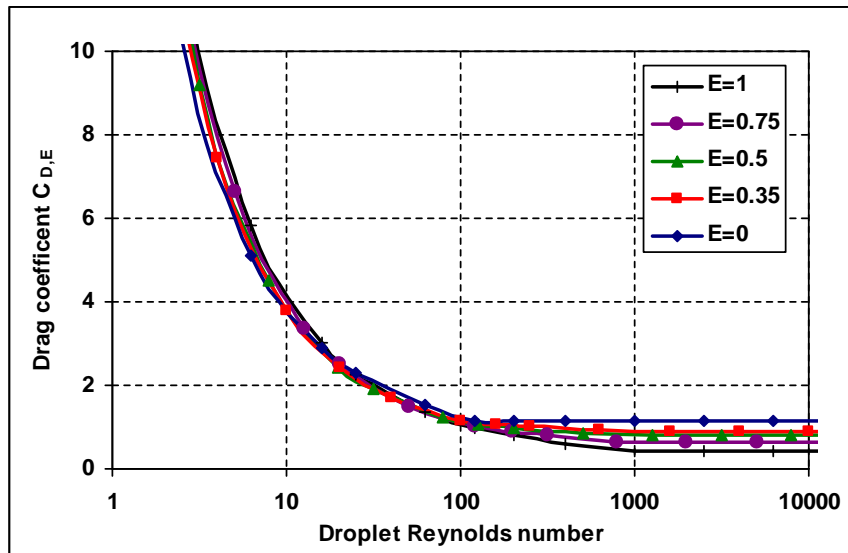

Figure 17: Drag coefficient depending on droplet deformation and Re according to Equation (51)

3.1.2.2 Turbulent Dispersion Force

An important mechanism of dispersed multi-phase flows is the turbulent transport of the dispersed phase by turbulent eddies. Physically, turbulent diffusion is the result of the fluctuating component of the forces acting on the particles. A rigorous analysis in [72] shows that the effect of turbulent transport of particles appears as a force in the momentum equation. This results from ensemble averaging over the drag force fluctuations on all particles at a certain location in space.

Based on the work performed in [52], the turbulent dispersion force, also called turbulent diffusion force, can be described by the equation

$$\mathbf{M}_{T,dc} = -c_{T,dc} k_c \nabla \alpha_d = -\mathbf{M}_{T,cd} \ . \tag{54}$$

This yields to an expression of $\mathbf{M}_{T,dc}$ depending on the turbulent kinetic energy of the continuous phase and oriented along the negative gradient of the dispersed phase volume fraction. Subscripts *cd* and *dc* denote the interactions between the continuous and the dispersed phases in both ways. The coefficient $c_{T,dc}$ is a function of particle concentration, the defined time constant of the particles and the time constant representing fluctuation time of the turbulent eddies. In the simplest approach, $c_{T,dc}$ is modelled as a constant parameter leading to diffusion of the dispersed phase.

3.1.2.3 Condensation and Evaporation

Condensation and Evaporation leads to mass transfer represented by the term Γ_{kl} in Equation (24), and to a heat transfer term H_{kl} in Equation (31). Due to the considerations in section 2.4, the condensation will not be considered in the CFD simulations of this thesis. Therefore the models for evaporation and condensation are not presented in this section. A well established model, however, which was used for estimating the condensation time scale, is represented in appendix 8.1.

3.2 Blow-by

This section describes the blow-by model in the crankcase flow simulations. Blow-by is the leakage of combustion gas into the crankcase. The simulation with the chamber model determines the gas mass flow rate into the crankcase, and it provides the boundary conditions for the gaseous phase in the CFD simulation. The gas velocities in the gaps between the piston rings are very high and can reach the speed of sound. These gas jets cause atomisation of the lubrication oil film on the cylinder wall and the formation of an oil mist. A model

estimating the mass flow rate of the atomised oil and a correlation determining the average droplet diameter of the oil mist are presented here.

3.2.1 Chamber Model

The leakage of combustion gas into the crankcase is driven by the pressure difference between cylinder and crankcase. The chamber model [60], also called the labyrinth model, is a simple approach to describing the blow-by gas flow rate into the crankcase. The following assumptions are quoted in [24].

- The piston ring gap is the only way for leaking. Hence, the system is constituted by a series of gas chambers, which are joined by rectangular channels determined by the width of the piston ring gap and the thickness of the piston rings (cf. Figure 2 in section 2.1.1).

- The gas flow between the chambers is adiabatic, and the mass flow rate through the channels is calculated by a one-dimensional approach.

- The gas in the chambers is ideal.

- The blow-by gas flow does not affect the pressure in the combustion chamber.

- The gas temperature in each chamber is set constant.

Figure 18 illustrates the chamber model for calculating the blow-by gas flow rate. Every gas chamber has two openings with defined areas A. The volume of the chamber is determined by the volume captured between one and its subsequent piston ring. The first and the last chambers are the combustion chamber and the crankcase, respectively. In these chambers, the gas conditions are constant and act as boundary conditions for the model.

The change of pressure with time is determined by the derivative of the state equation with respect to time, as shown in the equation

$$p_i = \frac{m_i R T_i}{V_i} \rightarrow \frac{dp_i}{dt} = \left(\dot{m}_{i-1,i} - \dot{m}_{i,i+1}\right)\frac{R T_i}{V_i} + \frac{m_i R}{V_i}\frac{\partial T_i}{\partial t} \ . \tag{55}$$

$\dot{m}_{i-1,i}$ is the gas mass flow rate from chamber $i-1$ into chamber i, and $\dot{m}_{i,i+1}$ is the gas flow rate from chamber i into chamber $i+1$. Chamber zero is the combustion chamber and chamber $n_{cham}+1$ is the crankcase. V_i is the volume of the chamber, which is constant, and R is the gas constant. The number of chambers n_{cham} is equal to the number of piston rings n_{ring} minus one.

The assumption of constant temperature in the gas chamber,

$$T_i \approx const. \rightarrow \frac{\partial T_i}{\partial t} = 0 \ , \tag{56}$$

leads to a simplification of Equation (55). However, this assumption is no matter of course. By applying the first law of thermodynamics for open processes to the control volume of the gas chamber, one can see that the temperature in the gas is only constant if the difference between incoming and outgoing gas enthalpy, as well as the change of internal energy in the gas is exactly equal to the heat transfer across the chamber wall. Nevertheless, the isothermal assumption leads to an enormous simplification, because it would be really difficult to find a reliable description of the heat transfer across the chamber wall. Furthermore, the chambers have long-drawn-out shapes around the piston. Their surface areas for heat transfer are big, and so it can be expected that the gas temperature in the chambers are almost equal to the temperature of the ring groove wall, which is more or less constant.
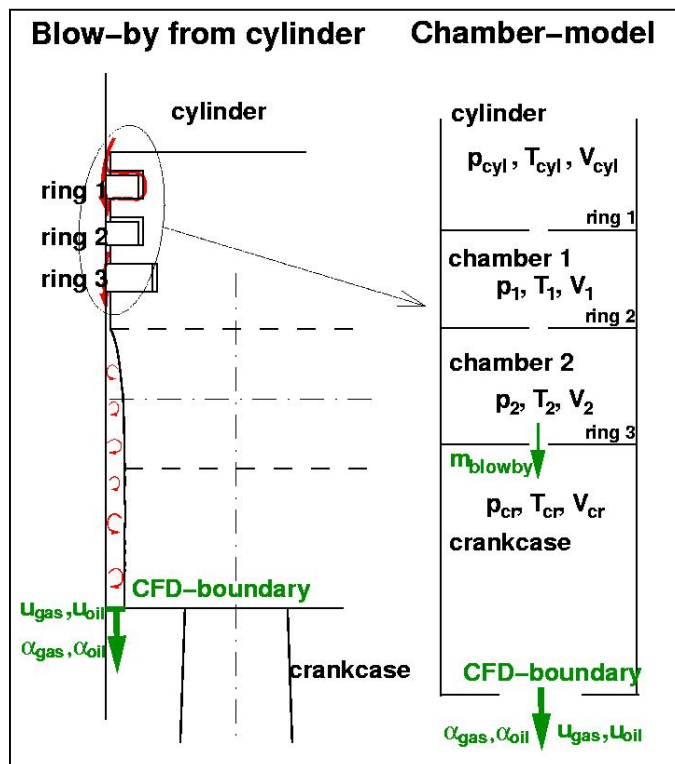

Figure 18: Chamber model for calculation of the blow-by gas flow

Due to the different pressure levels, the gas flows from the combustion chamber into the crankcase via the chambers. This flow is assumed to be adiabatic. Hence, the gas mass flow rate from chamber $i-1$ into chamber i depending on the pressure ratio p_i / p_{i-1} can be described by

$$\&_{i-1,i} = \begin{cases} K_C \, A_i \sqrt{\kappa \, R \, T_{i-1}} \; \rho_{i-1} \left(\dfrac{p_i}{p_{i-1}}\right)^{\frac{1}{\kappa}} \sqrt{\dfrac{2}{\kappa-1}\left[1-\left(\dfrac{p_i}{p_{i-1}}\right)^{\frac{\kappa-1}{\kappa}}\right]} & \text{subcritical} \\[4ex] K_C \, A_i \sqrt{\kappa \, R \, T_{i-1}} \; \rho_{i-1} \left(\dfrac{2}{\kappa+1}\right)^{\frac{\kappa+1}{2(\kappa-1)}} & \text{supercritical} \; , \end{cases} \quad (57)$$

which is the flow equation for isentropic flow [68]. K_C is the flow coefficient, which lies in the range between 0.8 and 0.9, and κ is the isentropic exponent of the gas, which is about 1.4 for air.

Depending on the pressure ratio between the chambers, there are two different flow regimes, subcritical and supercritical. If the pressure ratio is above the critical pressure ratio of Equation (58), there is choked flow or also called critical flow. This means that the velocity in the smallest flow area cannot exceed the speed of sound. To reach higher velocities, a Laval nozzle would be required.

$$\text{supercrital:} \quad \frac{p_{i-1}}{p_i} \geq \left(\frac{\kappa+1}{2}\right)^{\frac{\kappa}{\kappa-1}} \quad (58)$$

An equation similar to Equation (57) can be written for the gas mass flow rate from chamber i into chamber $i+1$, $\&_{i,i+1}$, replacing subscripts $i-1$ by i and i by $i+1$. By inserting Equation (57) for $\&_{i-1,i}$ and the corresponding equation for $\&_{i,i+1}$ into Equation (55), one can obtain a function for the pressure change of chamber i, as described by

$$\&_i(t) = f\big[p_{i-1}(t), p_i(t), p_{i+1}(t)\big] \qquad for \; i=1,...,n_{cham} \; . \quad (59)$$

The derivative of the pressure with respect to time depends on the current pressures in the actual, the previous, and the subsequent chamber and it is denoted by function f. Applying Equation (59) to the chambers i from $i=1$ to $i=n_{cham}$ leads to a system of ordinary differential equations (ODE) of first order. This system has to be solved numerically to obtain the gas mass flow rate due to blow-by.

The chamber model is quite simple, because it assumes constant flow area between the chambers. A more sophisticated approach, as it is implemented in the software tool AVL-GLIDE [9], additionally considers the dynamics of the piston rings. The motion of the rings leads to a varying flow area between the chambers. Therefore, a multi-body simulation of piston and piston rings combined with gas flow simulation is performed. Such simulations

show peaks in the blow-by mass flow rate curve, if piston ring flutter occur. The blow-by model implemented into the CFD code for this thesis can deal with both approaches. Either the gas mass flow rate is determined by the chamber model or a result data file from an AVL-GLIDE simulation is used. The model implementation and the numerical solution procedure for the ODE system of Equation (59) is described in section 4.3.1.

3.2.2 Oil Mist due to Atomisation

The oil film between the cylinder wall and the piston and piston rings ensures low friction and little wear between the gliding surfaces. The oil control ring is positioned underneath the piston rings and strips the accumulated oil from the cylinder wall to ensure a uniform oil film thickness for lubrication. Through crevices in the oil control ring and bores or small gaps in the piston, the stripped oil is guided back into the crankcase. The blow-by gas jet causes atomisation of the oil film, which is illustrated in Figure 19. The velocity of the blow-by gas jet can be very high, and in case of supercritical pressure ratio, it can reach the speed of sound. These high gas velocities produce an oil mist of very small droplets.
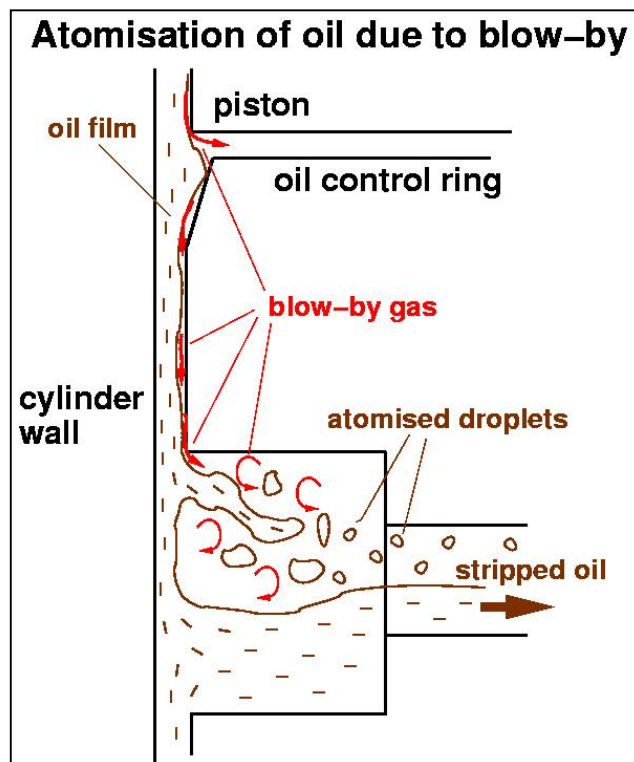

Figure 19: Oil mist generation due to blow-by

A simple correlation is proposed to determine the amount of oil atomised through the blow-by gas jets. This oil is then guided as an oil mist into the crankcase. The oil mass flow rate is determined by the equation

$$\dot{m}_d = \dot{m}_{oil} = \frac{1}{2} d_{cyl} \, \pi \, c_m \, \rho_d \, \delta_{strip} \quad with \qquad c_m = \frac{s \, n}{30} \; . \tag{60}$$

It constitutes the average amount of oil, which is stripped from the cylinder wall per unit time.

The strip-thickness δ_{strip} is a model parameter and determines the average oil film thickness, which is stripped from the cylinder wall and then atomised due to the blow-by gas jets. The factor one half considers that the major amount of the oil is stripped from the cylinder wall during the downward movement of the piston. The average piston velocity c_m depends on the stroke s and the engine speed n. Although the oil mass flow rate of Equation (60) mainly depends on the user given parameter δ_{strip}, it takes into account two important facts. First: The higher the engine speed, the higher the mass flow rate of stripped oil. Second: A big engine, defined by the cylinder diameter d_{cyl}, produces more oil mist than a small engine. The evaluation of reasonable values for δ_{strip} is difficult, because it is not possible to perform direct measurements of the oil mass atomised due to blow-by. In [48] the volume flow rate of lubricating oil through the piston ring packs was measured. If one assumes that this amount of oil is completely atomised by the blow-by gas jets, the order of magnitude for δ_{strip} lies in the range between 10 nm and 100 nm. The oil mass flow rate $\dot{m}_d$ is a mean value and set constant over the entire engine cycle, contrary to $\dot{m}_c$, which is a function of time.

For the calculation of the mean diameter of the atomised droplets, the analogy to a co-axial liquid gas flow is applied. In [86] the atomisation of a liquid jet surrounded by a co-axial gas jet has been investigated, and a correlation for the Sauter mean diameter of the droplets is cited. The authors distinguish between primary instability, which occurs at the interface of parallel flowing gas and liquid streams, and a secondary instability, which occurs on the tongues of liquid drawn out of the jet surface by the primary shear instability. The secondary destabilisation mechanism is the well-known Rayleigh Taylor instability, which develops when a liquid surface is accelerated in a direction perpendicular to its plane. The presented break-up model results in the correlation,

$$d_{32,d} = \frac{0.68 \, \gamma_C^{\frac{1}{2}} \left(\rho_d \, v_{gas}\right)^{\frac{1}{4}} \sigma^{\frac{1}{2}}}{\rho_{gas}^{\frac{3}{4}} \left\{ U_{gas} \left[1 + \left(\frac{\rho_{gas}}{\rho_d}\right)^{\frac{1}{2}} \right] - U_d \right\} U_{gas}^{\frac{1}{4}}} \approx C_{model} \frac{\rho_d^{\frac{1}{4}} v_{gas}^{\frac{1}{4}}}{\rho_{gas}^{\frac{3}{4}}} \sigma^{\frac{1}{2}} U_{gas}^{-\frac{5}{4}} \; , \tag{61}$$

for the Sauter mean droplet diameter, which is assumed to be approximately one fifth of the most unstable Rayleigh-Taylor wavelength on the liquid tongues: $d_{32,d} \approx \lambda_{RT} / 5$.

The Sauter mean diameter of the droplets is a function of the fluid properties, the surface tension, and the gas jet velocity U_{gas}. The proportionality constant γ_C influences λ_{RT} and is set to $0.055\ m^{1/2}$ in [86]. The liquid velocity U_d of Equation (61) is neglected for the current blow-by model, because it is much smaller than the gas velocity U_{gas}, which is determined by the maximum gas velocity in the flow area between the chambers. The gas jet velocity U_{gas} depends on the pressure ratio between the chambers of the chamber model. According to [68] the flow velocity for adiabatic and isentropic gas flow can be calculated with Equation (62) depending on sub-critical or supercritical pressure ratios.

$$U_{gas} = U_{max} = \begin{cases} \sqrt{RT_{i-1}\dfrac{2\kappa}{\kappa-1}\left(1-\left(\dfrac{p_i(t)}{p_{i-1}(t)}\right)^{\frac{\kappa-1}{\kappa}}\right)} & \dfrac{p_i(t)}{p_{i-1}(t)} > \left(\dfrac{2}{\kappa+1}\right)^{\frac{\kappa}{\kappa-1}} \\[4mm] \sqrt{RT_{i-1}\dfrac{2\kappa}{\kappa+1}} & \dfrac{p_i(t)}{p_{i-1}(t)} \le \left(\dfrac{2}{\kappa+1}\right)^{\frac{\kappa}{\kappa-1}} \end{cases} \tag{62}$$

Figure 20 shows the curve of the ratio of the pressures in the crankcase and in the last (here the second) chamber over the complete engine cycle of the chamber model simulation from section 4.3.1 below. One can see that the pressure ratio is always less than the critical value of 0.528 for air with an isentropic exponent $\kappa = 1.4$. This means that there is choked flow over the complete engine cycle with the speed of sound as the maximum velocity in the smallest area between the chambers. Similar simulations performed at different loads and speeds, illustrated in Figure 51 in section 4.3.3 below, have shown that only for the lower engine speeds the subcritical pressure ratio with values greater than the critical value is reached. Hence it is reasonable to declare the speed of sound as the dominating gas velocity for the oil atomisation due to blow-by.

The temperature in the critical flow area at choked flow is determined by

$$T_{crit} = T_{n_{cham}}\frac{2}{\kappa+1}\ . \tag{63}$$

The equation

$$U_{gas} = \sqrt{\kappa R T_{crit}} = \sqrt{RT_{n_{cham}}\frac{2\kappa}{\kappa+1}}\ , \tag{64}$$

determines the gas jet velocity for the atomisation model as a function of the gas temperature in the last chamber $T_{n_{cham}}$. Due to the assumption of constant chamber temperatures the atomisation velocity does not vary over the engine cycle. The piston velocity is not considered for U_{gas}, since it is much smaller than the velocity expressed by Equation (64).

The gas density in Equation (61) is determined by the critical density which is calculated by

$$\rho_{gas} = \rho_{crit} = \frac{p_{crit}}{RT_{crit}} = \frac{p_{n_{cham}}}{RT_{n_{cham}}} \left(\frac{2}{\kappa + 1} \right)^{\frac{1}{\kappa - 1}}. \tag{65}$$
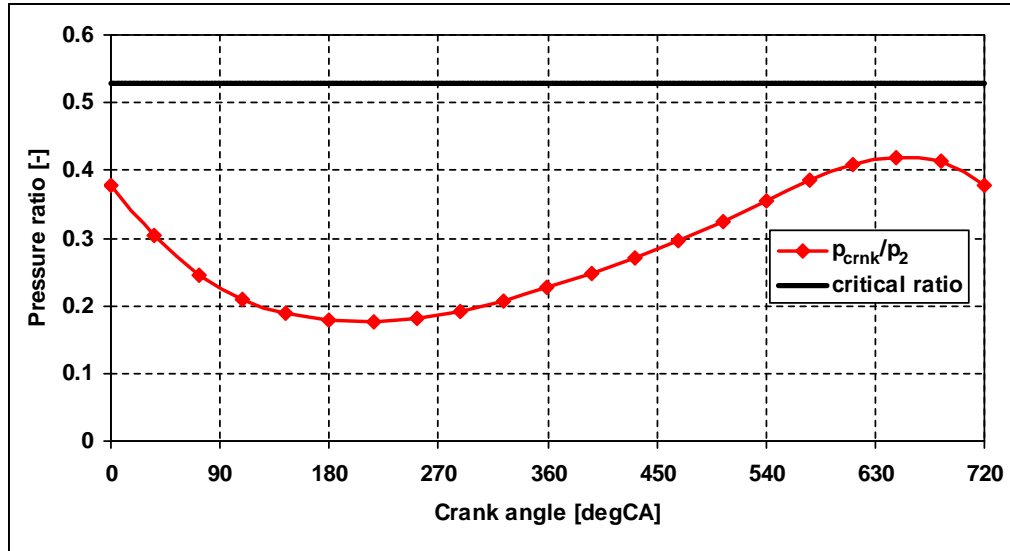

Figure 20: Ratio of the crankcase pressure p_{crnk} and the pressure in last but one chamber p_2

The retention time of the oil and gas is much longer than the time for flowing from one chamber to the other. Thus it is reasonable to assume equal temperature for gas and liquid oil in the chambers. If gas and oil flow from one chamber to the next, the gas temperature changes very fast, while the oil temperature changes much slower, since the time for the heat transfer is not long enough to reach equilibrium. Hence the liquid density ρ_d and the surface tension σ in Equation (61) are determined at the temperature of the last chamber $T_{n_{cham}}$.

3.3 Liquid Break-up at Rotating Discs

3.3.1 Analogy to Rotary Atomisers

The moving crank drive produces splash oil due to disintegration of the lubrication oil from the main and the conrod bearings. The oil flows as a film down the surfaces of the crankshaft and the conrod, driven by centrifugal forces. At certain positions, i.e. at the edges of the rotating parts, the oil retains and disintegrates into ligaments and droplets. Figure 21 shows the crankshaft of a V-12 engine. There are massive crankwebs to minimise the unbalance of the dynamic crank drive forces. One can imagine that the oil from the bearings may flow down the crankweb surfaces, which are more or less sectors of a disc, and disintegrate at the crankweb edges. This is a similar process as exploited with rotary atomisers, which are often

used in chemical engineering processes to generate certain droplet spectra. Therefore, it is reasonable to use the analogy to the rotary atomiser for describing the phenomena of liquid disintegration at the rotating crank drive.

Figure 21: Crankshaft of a V-12 engine

Due to their wide use in chemical industry, rotary atomisers are well investigated. The principle is simple. A liquid flow enters the centre of the rotating disc and is redirected. The liquid flows as a film on the surface towards the edge of the disc, where film thickness and velocity profile are determined by the balance between shear and centrifugal forces. Disturbances create surface waves, which lead to varying conditions in the film and at the disc edge. Hence the film thickness on the disc is a function of position and time. The liquid forms a rim at the disc edge, from where the disintegration starts. Many authors in the literature distinguish between three different disintegration regimes at rotary atomisers. There are dropwise disintegration, ligament disintegration, and sheet disintegration. The dropwise disintegration is shown in Figure 22 left. There the liquid forms a rim along the disc edge, from where individual droplets detach. The ligament disintegration is shown in Figure 22 centre. It has an impressive form due to the uniform distance between the ligaments. This regime leads to droplets of almost uniform size, and this is why rotary atomisers are often operated in this regime. The sheet disintegration is shown in Figure 22 right. There the liquid rim itself detaches from the disc edge, and the liquid sheet disintegrates into droplets of very different sizes.
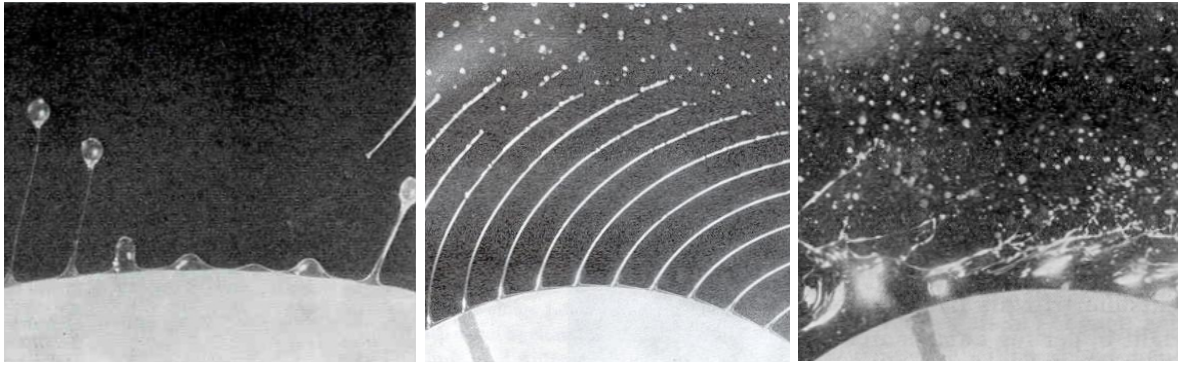
Figure 22: Different disintegration regimes in rotary atomisation from left to right: dropwise, ligament, and sheet (from [17])

The film thickness δ at the disc edge depends on the liquid kinematic viscosity ν_d, the volume flow rate $\dot{V}$, and the angular speed ω, and can be calculated with the equation

$$\delta = \sqrt[3]{\frac{6\nu_d \dot{V}}{\pi\omega^2 d_{disc}^2}} \ , \tag{66}$$

as described in [17]. To correspond to the notation of the previous sections, the subscript d is used to represent the dispersed phase, which is the liquid phase here.

The liquid rim thickness a at the disc edge simply results from a balance between surface and centrifugal forces, as described by the equation

$$a = \sqrt{\frac{4\sigma}{d_{disc}\omega^2\rho_d}} = 2We^{-\frac{1}{2}}d_{disc} \ . \tag{67}$$

Hege [44] shows a derivation, where he uses the Froude number $Fr = d_{disc}\omega^2/(2g)$ in the equation for a. This rim thickness can also be represented as a function of the Weber number of rotary atomisers, which defined by Equation (72) below.

Figure 23 represents the film and rim thicknesses according to Equations (66) and (67) for three different disc diameters d_1, d_2, and d_3 of 50, 100, and 200 mm. The liquid used is the engine oil OMV TRUCK LD SAE 15W-40 at an operation temperature of 100 °C. The values for the oil volume flow rate and the rotational speed of the disc result from the volume flow rate curve of Figure 24. This curve results from the lubricating oil circuit calculation described in section 2.2, and is used to deal with representative conditions occurring in the crankcase. Therefore it is assumed that approximately one half of the oil passing the main bearing enters the crankweb and takes part in the disintegration process.

It is easy to comprehend that, at constant oil flow rate and rotational speed, larger disc diameters lead to smaller film and rim thicknesses. Furthermore, high rotational speeds lead

to small rim thicknesses. At the given oil volume flow rate curve, which is almost linear, an increase of the rotational speed also leads to a decrease of the film thickness.
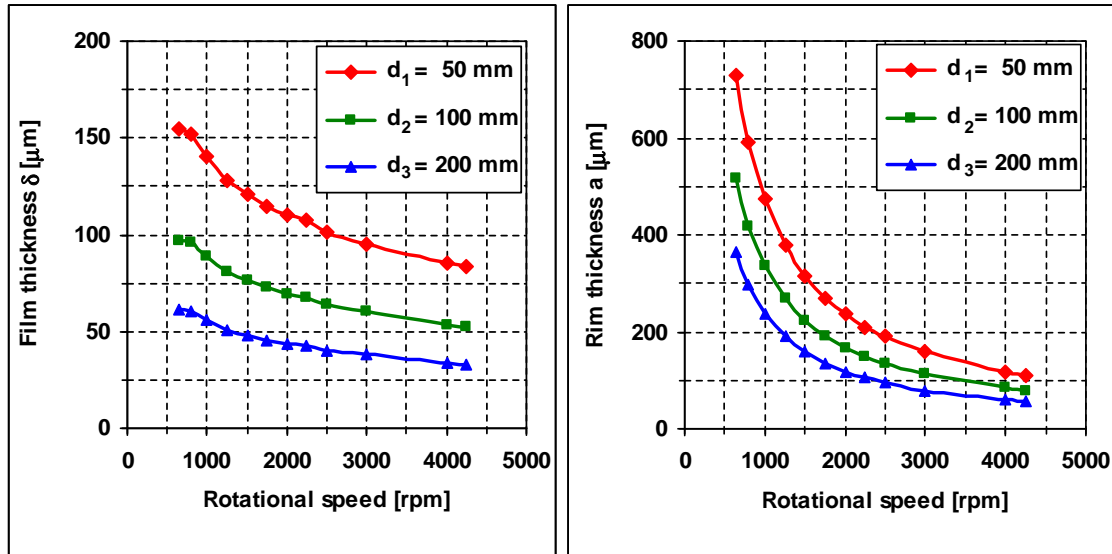

Figure 23: Film (left) and rim thicknesses (right) for disc diameters of 50, 100 and 200 mm for a given oil volume flow rate curve (from Figure 24)
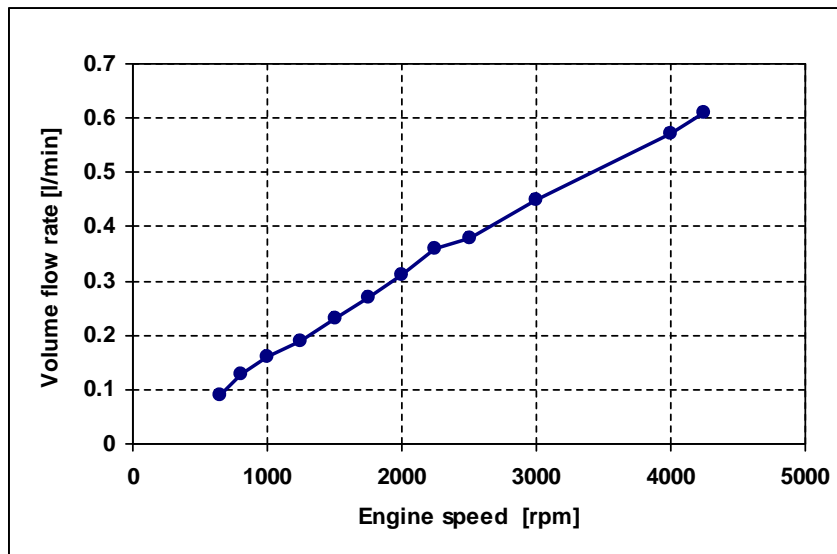

Figure 24: Estimated volume flow rate of the engine oil over crankweb

3.3.2 Disintegration Regimes

There are several authors who have worked on the determination of the different disintegration regimes of rotary atomisers. As mentioned above, one can distinguish between dropwise disintegration, ligament disintegration, and sheet disintegration. Some correlations of different authors are represented here. Most of them use dimensionless variables to

determine the regimes. In the following notations with respect to further use in software routines, the abscissa variable in the disintegration regime nomograms is called x_1, and the ordinate variable is called x_2. All presented correlations are transformed into this notation.

Hege [44], [45] specifies a correlation for the so-called optimal volume flow rate of rotary atomisers, which ensures the ligament disintegration regime. Therefore he uses the dimensionless variables of Equation (68) with the Froude number for x_2.

$$x_1 = \frac{d_{disc}\omega\sigma}{2\rho_d g \dot{V}} \qquad x_2 = Fr = \frac{d_{disc}\omega^2}{2g} \tag{68}$$

The correlation of the optimal volume flow rate for ligament disintegration is determined by the equation

$$\dot{V}_{lig} = \frac{d_{disc}\omega\sigma}{2\rho_d g}\left(\frac{2\pi}{Fr}\right)^{\frac{3}{4}} \rightarrow x_{2,lig} = 6.2832\,x_1^{\frac{4}{3}} \quad . \tag{69}$$

Hege found out that the double of the optimal volume flow rate leads to sheet disintegration, as described by

$$\dot{V}_{sheet} \approx 2\dot{V}_{lig} \rightarrow x_{2,sheet} = 15.8326\,x_1^{\frac{4}{3}} \quad . \tag{70}$$

The indices *drop*, *lig* and *sheet* are equivalent with dropwise, ligament and sheet disintegration. The distance between ligaments according to [44] is given by the equation

$$l_{lig} = a\pi\sqrt{2\left(1 + \frac{3\nu_d\,\rho_d}{\sqrt{\sigma\,\rho_d\,a}}\right)} \quad , \tag{71}$$

which results from a linear stability analysis applied to a liquid ring with thickness a.

In Figure 25 , the purple-coloured curve represents ligament disintegration, and the black curve represents sheet disintegration. Here and in the following diagrams of this section, the "representative" crankcase conditions, illustrated by the coloured curves in the diagrams, are determined by the oil volume flow rate curve of Figure 24, the engine oil OMV TRUCK LD SAE 15W-40, and the three disc diameters d_1, d_2, and d_3 of 50 mm, 100 mm, and 200 mm.

One can see that both disintegration regimes, ligament and sheet, are passed by the volume flow rate curves. Hege did not provide a correlation for dropwise disintegration, and this regime is therefore not considered in the diagram. The experimental data base for the correlations of Hege is given in Table 12 of section 8.2.1 in the appendix.
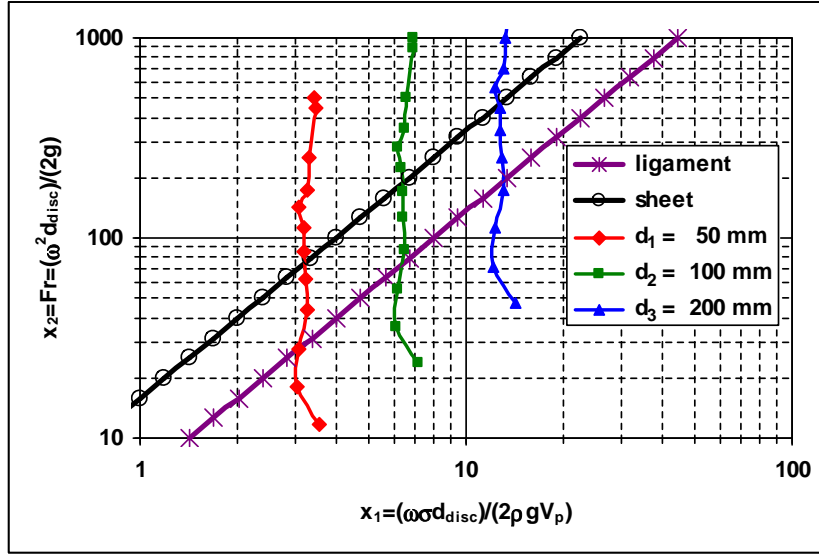
Figure 25: Optimal volume flow rate for ligament disintegration due to Hege [44], [45]

Some authors use the following dimensionless quantities in their correlations for the different disintegration regimes. The Weber number for rotary atomisers is defined as

$$We = \frac{\omega^2 d_{disc}^3 \rho_d}{\sigma} \quad , \tag{72}$$

and the equation

$$Z = \frac{\mu_d^2}{d_{disc} \rho_d \sigma} = Oh^2 \tag{73}$$

determines the square of the Ohnesorge number Oh. Z represents the ratio of viscous forces and surface forces.

The volume flow rate number $\dot{V}^*$ is determined by the equation

$$\dot{V}^* = \frac{\dot{V}^2 \rho_d}{d_{disc}^3 \sigma} \quad , \tag{74}$$

and represents the dimensionless volume flow rate. The fluid number K_F contains only liquid properties and the gravitational acceleration and is determined by

$$K_F = \frac{\rho_d \sigma^3}{g \mu_d^4} \quad . \tag{75}$$

K_F is similar to the reciprocal value of the Morton number for flows with a continuous liquid phase ($Mo = g \mu_l^4 (\rho_l - \rho_g) / \rho_l^2 \sigma^3$), if the liquid density ρ_l is much bigger than the gas density ρ_g.

Grave [42], who is cited in [17], uses functions of We, Z, $\dot{V}^*$, and K_F for the definition of the coordinates x_1 and x_2, as given by the equations

$$x_1 = \frac{\dot{V}^{*0.5}}{Z^{0.47} K_F^{0.295}} \quad \text{and} \quad x_2 = We^{0.5} Z^{0.922} K_F^{0.491} \quad . \tag{76}$$

With a closer look the volume flow rate $\dot{V}$ can be detected as the dominating quantity of x_1, while the angular speed ω is the dominating quantity of x_2. Grave delivers correlations for the transition between the different disintegration regimes. This is contrary to the equations of Hege, who determined the regime itself and not the transition between the regimes.

The transition between dropwise disintegration and ligament disintegration $drop/lig$ is determined by the equation

$$x_{2,drop/lig} = 0.0453 \left(\log K_F \right)^{1.77} Z^{0.14} x_1^{-\frac{5}{3}} \quad . \tag{77}$$

However, this formulation can create problems for fluid numbers less than unity. Then the logarithmic value of K_F is less than zero and raising this value to the power of 1.77 is an undefined operation. For oils with a high viscosity fluid numbers below unity may occur.

Following [46], the transition between ligament and sheet disintegration $lig/sheet$ is determined by the equation

$$\dot{V}^* We^{\frac{3}{5}} Z^{\frac{1}{6}} = 1.77 \quad . \tag{78}$$

Transforming this equation into the coordinates of Equation (76) yields as result the equation

$$\rightarrow x_{2,lig/sheet} = 1.61 \, x_1^{-\frac{5}{3}} \quad . \tag{79}$$

Furthermore, there is a fourth disintegration regime called atomisation. To obtain this regime, the rotational speed of the disc has to be very high. Then the liquid film at the disc edge disintegrates directly into droplets without forming a liquid rim along the disc edge. The transition into this regime is described by the equation

$$x_{2,atom} = 230 \, x_1^{\frac{1}{6}} \quad . \tag{80}$$

Figure 26 shows the volume flow rate curve of Figure 24 at the different disc diameters drawn in the nomogram determined by the coordinates of Grave. At low rotational speed and low oil volume flow rate, there is dropwise disintegration. With increasing rotational speed

and volume flow rate, ligament and sheet disintegration are also passed. The atomisation disintegration regime is never entered by the three curves. The experimental data base for the correlations of Grave is given in Table 13 of section 8.2.1 in the appendix.
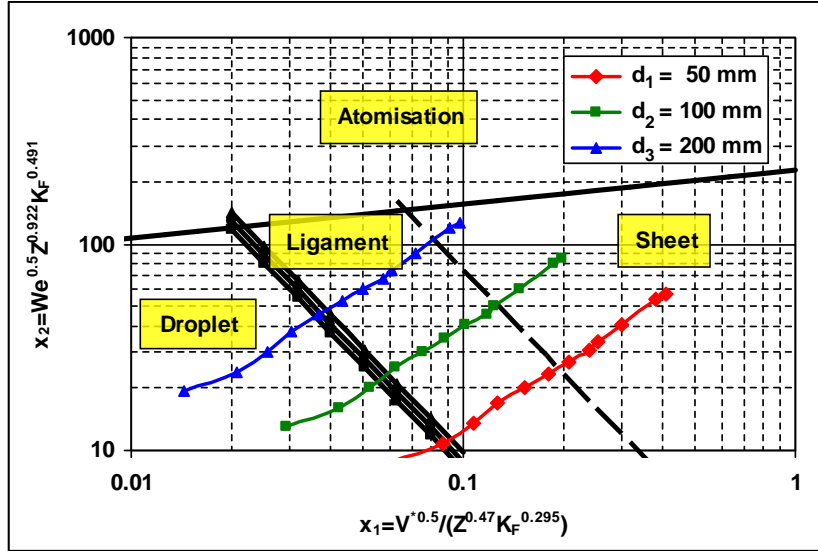

Figure 26: Disintegration regimes due to Grave [42]

Mehrhardt [57] is another author, who performed measurements on rotary atomisers and developed correlations for the disintegration regimes and for the droplet size distribution functions. Also he uses functions of We, Z, and $\dot{V}^{*}$ for the definition of the coordinates x_1 and x_2, as shown in the equations

$$x_1 = Z^{0.5} = Oh \quad \text{and} \quad x_2 = \dot{V}^{* \frac{5}{6}} We^{\frac{1}{2}} Z^{\frac{5}{36}} \; . \tag{81}$$

The transition between dropwise disintegration and ligament disintegration is determined by the equation

$$\dot{V}^{*} We^{\frac{3}{5}} Z^{\frac{1}{6}} = f_1(Z)\left[1+\left(\frac{f_1(Z)}{1.77}\right)^2\right]^{-0.5} \quad \text{with} \quad f_1(Z) = 5.45 \cdot 10^{-3} \, Z^{-0.233} \; . \tag{82}$$

Transforming this equation into the coordinates x_1 and x_2 of Equation (81) yields as result the equation

$$\rightarrow x_{2,drop/lig} = \frac{1.29916 \cdot 10^{-2}}{x_1^{\frac{7}{18}}}\left(1+\frac{9.48083 \cdot 10^{-6}}{x_1^{\frac{14}{15}}}\right)^{-\frac{5}{12}} \; . \tag{83}$$

The transition between ligament and sheet disintegration is described by Equations (84) and (85). Those equations are based on Equation (78) from [46]. The term f_2 is introduced to improve agreement with measurements at higher values of the Ohnesorge number Oh.

$$\dot{V}^* We^{\frac{3}{5}} Z^{\frac{1}{6}} = f_2(Z) \left[1 + \left(\frac{f_2(Z)}{1.77} \right)^2 \right]^{-0.5} \quad with \ \ f_2(Z) = 0.44 \, Z^{-0.36} \tag{84}$$

$$\rightarrow x_{2,lig/sheet} = \frac{0.5045}{x_1^{\frac{3}{5}}} \left(1 + \frac{0.06180}{x_1^{\frac{36}{25}}} \right)^{-\frac{5}{12}} \tag{85}$$

Mehrhardt quoted the correlation

$$\dot{V}^* We^{\frac{2}{5}} Z^{-\frac{1}{5}} = 0.814 (1 - \cos\gamma)^{\frac{6}{5}} \tag{86}$$

for the transition between wetted and not wetted regions on the rotary atomiser. If the volume flow rate on the disc is small, and consequently inertia forces of the film flow are small compared to the surface tension forces, no film flow is possible. γ is the wetting angle between the liquid and the disc surfaces and strongly depends on the material of the wall, the fluid properties, and also on the degree of pollution of the disc surface.

Figure 27 shows the volume flow rate curves drawn into the disintegration regime nomogram of Mehrhardt. Here also all three disintegration regimes are passed. It is not possible to transform Equation (86) into a function of x_1 and x_2. Hence the non-wetted region cannot be drawn as a curve in the map of Figure 27. It has to be checked for each operation point separately. The experimental data base for the correlations of Mehrhardt is given in Table 14 of section 8.2.1 in the appendix.

In this section correlations from different authors for the disintegration regimes on rotary atomiser have been compared for a representative oil volume flow rate curve. There is a general agreement of the correlations, since all volume flow rate curves pass the disintegration regimes in a similar manner. The equations of Grave, as well as the equations of Mehrhardt, can be recommended for further use in the simulation of the oil disintegration on the rotating crank drive.
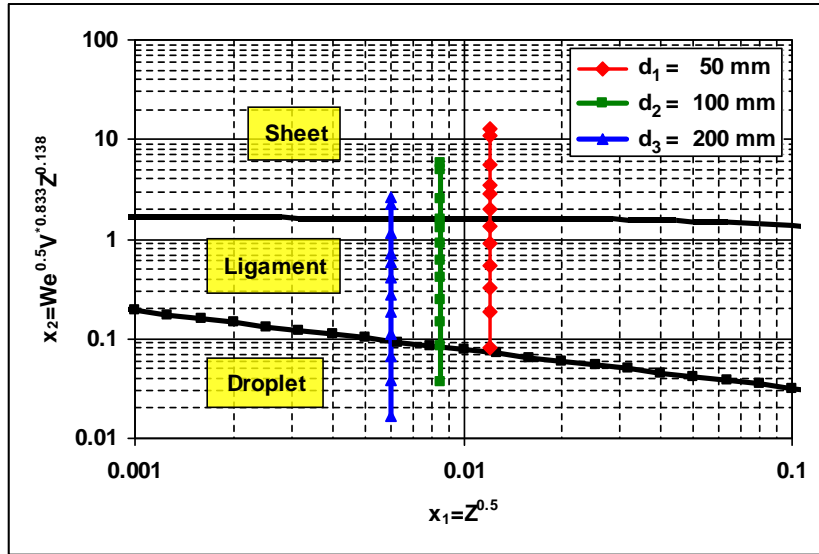
Figure 27: Disintegration regimes due to Mehrhardt [57]

3.3.3 Diameter of the Detached Droplets

The diameter of the droplets, which result from the liquid disintegration on the rotating crank drive, is important for the CFD simulations. Due to the different processes forming the droplets, most authors provide separate droplet diameter correlations for the different disintegration regimes.

Fraser & Eisenklam [39] do not distinguish between different disintegration regimes and propose the correlation

$$d_d = 0.4252 \left[\frac{2\sigma}{(2\pi\omega)^2 d_{disc}\, \rho_d} \right]^{\frac{1}{2}} , \tag{87}$$

for the so-called main droplet diameter. Equation (87) is transformed into SI-units according to [17]. The experiments showed that the main droplet was formed together with two satellite droplets, whose diameters had a constant ratio to the main droplet diameter d_d of 0.5 and 0.36. Hence the Sauter mean diameter (SMD), which is the diameter of interest for the CFD model, can be deduced easily as shown in the equation

$$d_{32,d} = \frac{d_d^3 + (0.5 d_d)^3 + (0.36 d_d)^3}{d_d^2 + (0.5 d_d)^2 + (0.36 d_d)^2} = 0.849\, d_d . \tag{88}$$

Hege [44], [45] distinguishes between primary droplets detached directly from the rim along the disc edge, and secondary droplets which result from disintegration of the ligament at a certain distance from the edge. According to this distinction, primary droplets are droplets from dropwise disintegration and secondary droplets are droplets from ligament

disintegration. Hege assumes droplets of more or less uniform size, and hence there is no information about any kind of mean diameter. He proposes a correlation for dropwise disintegration, described by the equation

$$d_d = 1.9a = 1.9\sqrt{\frac{4\sigma}{d_{disc}\omega^2\rho_d}} \quad , \tag{89}$$

where the droplet diameter is proportional to the rim thickness. For ligament disintegration he suggests the correlation described by the equation

$$d_d \approx \sqrt{\frac{2\sigma}{\omega^2\rho_d d_{disc}}}\nu_d^{-\frac{1}{12}} \quad . \tag{90}$$

Sheet disintegration is a more complex process, which produces droplets of varying size. Therefore it is more difficult to find reasonable droplet diameter correlations. Walzel [87] provided a correlation for the Sauter mean diameter from sheet disintegration on a non-rotating disc. Adapting this correlation for rotary atomisers results in the equation

$$d_{32,d} = 1.1748\cdot C_3\frac{1}{d_{disc}\omega}\left(\frac{\rho_d}{\rho_c}\right)^{\frac{1}{6}}\left(\frac{\sigma\dot{V}}{\rho_d}\right)^{\frac{1}{3}} \quad . \tag{91}$$

This transformation is shown in detail in section 8.2.2 of the appendix. The recommended value for the model parameter C_3 is 1.13 for non-rotating discs. Variation of this parameter can compensate the error due to using this correlation for sheet disintegration on rotating discs.

Figure 28 shows the comparison of the above droplet diameter correlations. The conditions are the same as in the previous section, where the liquid is the engine oil OMV TRUCK LD SAE 15W-40, and the three disc diameters d_1, d_2, and d_3 are 50 mm, 100 mm, and 200 mm. The left figure shows the correlations of Equations (89) and (90) from Hege [44], [45], and Equation (91) from Walzel [87]. The disintegration regimes are determined by the Equations (77), (79), and (80) from Grave. The model parameter C_3 was set to 2.55 to get a smooth transition from the ligament to the sheet disintegration regimes. The figure on the right side shows the correlation of Equation (87) from Fraser and Eisenklam [39], which is valid for all disintegration regimes. Although the sources of the correlations are quite different, the two diagrams show good agreement. The larger the disc diameter and the higher the rotational speed, the smaller the droplet diameters.
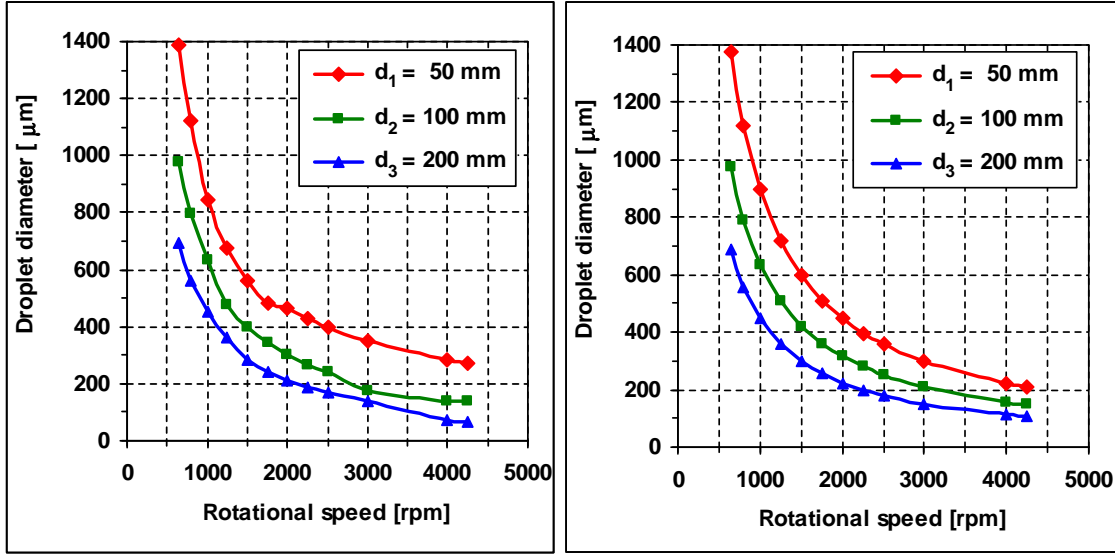
Figure 28: Droplet diameter correlations of Hege [44] and Walzel [87] (left)

and Fraser & Eisenklam [39] (right)

Mehrhardt [57] performed many photographic measurements to determine the droplet size in sprays from rotary atomisers. He developed correlations for different mean droplet diameters, as well as parameters for different droplet size distribution functions to match the experimental data. Therefore he uses a dimensionless diameter d^*, which is defined by the equation

$$d_{drop}^* = \frac{d_{drop}}{\left(\dfrac{\mu_d}{\rho_d \omega}\right)^{0,5}} \quad . \tag{92}$$

By distinction between the different disintegration regimes, and by applying the least squares fit method to match the experimental data, Mehrhardt got the following correlations for the Sauter mean diameter. The droplet diameter for dropwise disintegration is given by the equation

$$d_{32,d}^* = 1.075 \, We^{-0,315} \, \dot{V}^{*-0,094} \, Z^{-0,319} \quad . \tag{93}$$

The correlations for ligament and sheet disintegration are described by the equations

$$d_{32,d}^* = 1.176 \, We^{-0,124} \, \dot{V}^{*0,157} \, Z^{-0.253} \quad , \tag{94}$$

and

$$d_{32,d}^{*} = 1.757\,We^{-0,237}\,\mathring{V}^{*0,018}\,Z^{-0.273}\ .\tag{95}$$

By evaluation of all measurement data, independent from their disintegration regime, Mehrhardt developed the equation

$$d_{32,d}^{*} = 1.267\,We^{-0.199}\,\mathring{V}^{*0,052}\,Z^{-0.276}\ ,\tag{96}$$

for the non-dimensional Sauter mean diameter. Mehrhardt also noted that the average error of these correlations, which is defined as the root mean square of the difference between the measured and calculated droplet sizes, was quite high with values up to 40 percent.

  Figure 29 compares the different correlations for the Sauter mean diameter of Mehrhardt. On the left-hand side, the droplet diameters are calculated with the Equations (93), (94) and (95), where the disintegration regimes have been determined by the Equations (83) and (85). Although the general tendency of decreasing diameter with increasing disc diameter and increasing rotational speed is visible, these curves show an curious behaviour at the transitions between the different regimes (which are shown in Figure 27 for the same data points). The diagram on the right-hand side shows the Sauter mean diameters calculated with Equation (96).
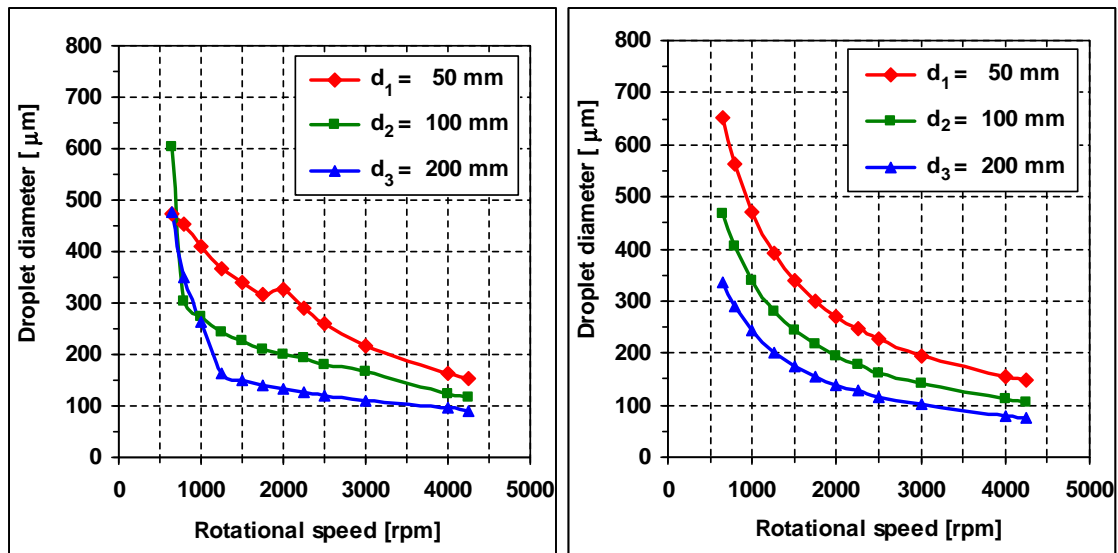

Figure 29: Droplet diameter correlations from Mehrhardt [57] with (left) and without (right) consideration of the disintegration regime

  In this section, several correlations for the diameters of droplets from liquid disintegration in rotary atomisers were compared for representative crankcase conditions. There are

remarkable differences between the correlations shown in Figure 28 and in Figure 29. Hence it is difficult to choose suitable correlations for further use in CFD simulations. The correlations of Mehrhardt yield droplet diameters much smaller than those from the correlations in Figure 28, which result from different authors and show good agreement. Hence, the correlations from Mehrhardt cannot be recommended for the application in the CFD simulations. The droplet diameter correlations of Hege and Walzel, and of Fraser & Eisenklam are the recommended ones.

3.4 Transport of the Droplet Size Spectrum

The Eulerian multi-phase conservation equations of section 3.1 are derived for an arbitrary number of interpenetrating phases, which are determined by the phase volume fractions. The special physics of the multi-phase flow is represented by the transfer terms modelling the phase interactions. Most of the phase interaction models assume uniform conditions for the interaction between two phases. E.g., for the drag formulation of the droplet flow, all particles of the dispersed phase are approximately spherical and have the same diameter. This leads to uniform drag forces. Uniform droplet diameters are rare in real spray clouds, and hence this assumption neglects the effect that the ratio of drag and inertia forces on small droplets is much stronger than on large droplets.

To overcome this problem, one can distribute the dispersed phase into several phases assigned to certain droplet diameter classes. The complete set of conservation equations is then solved for each phase representing a certain droplet diameter class. This method is applied in Diesel spray simulations as an alternative approach to the DDM method as performed in [15], where the phase interactions due to drag, evaporation, break-up and so on are calculated for every droplet size class separately. This method yields a good description of sprays, especially in the dense spray region, but the drawback is the high computational effort due to solving the complete set of conservation equations for all phases.

An Eulerian method of modelling poly-disperse sprays without segregation into droplet size classes is suggested in [13] and [14]. Parts of these works are represented here. There the moments of the droplet size distribution are transported in an Eulerian framework. This method avoids the use of statistical particles for the determination of the distribution function, as it is often applied in PDF methods, e.g. for the turbulent reactive flows in [69]. CFD simulations with statistical particles cause a very high memory consumption determining the main drawback of the PDF methods. The transport of the moments of the droplet size distribution is described here. Of course the same methodology can be applied for bubbly flow, where the dispersed phase is gaseous and the continuous phase is liquid. For convenience, the following method is described for droplet flows only.

3.4.1 Moments of the Droplet Size Spectrum

We assume a large number of droplets N_{tot} to be contained within the control volume V_{tot} and observed over the time t_{tot}. The droplets have different radii r, velocities $\mathbf{U}$, temperatures T, and locations $\mathbf{x}$. Hence, one can define the droplet number probability density function $\tilde{f}$ (PDF) as a derivative of the droplet number distribution function $\tilde{N}$, as described by the equation

$$\tilde{f}(r,\mathbf{U},T,\mathbf{x},t) = \frac{1}{N_{tot}} \frac{d^9 \tilde{N}(r,\mathbf{U},T,\mathbf{x},t)}{dr\, d\mathbf{U}\, dT\, d\mathbf{x}\, dt} \quad . \tag{97}$$

An important simplification of the following considerations is due to the assumption that the droplet velocity and temperature can be represented as functions of the droplet radius in space and time. Hence, the droplet number probability density function is no more a function of $\mathbf{U}$ and T, and it yields

$$\mathbf{U} \approx \mathbf{U}(r,\mathbf{x},t) \; and \; T \approx T(r,\mathbf{x},t) \;\rightarrow\; \tilde{f}(r,\mathbf{U},T,\mathbf{x},t) = \tilde{f}(r,\mathbf{x},t) = \frac{1}{N_{tot}} \frac{d^5 \tilde{N}(r,\mathbf{x},t)}{dr\, d\mathbf{x}\, dt} \quad . \tag{98}$$

The integral of $\tilde{f}$ over the space of the independent variables equals unity to ensure an important property of the PDF.

$$\int_{r=0}^{\infty} \int_{V_{tot}} \int_{t_{tot}} \tilde{f}(r,\mathbf{x},t)\, dr\, d\mathbf{x}\, dt = 1 \tag{99}$$

The transport of the droplet size distribution function requires the determination of local distribution functions, which describe the droplet cloud within a small volume ΔV_{tot} over a short time Δt_{tot}. The number of droplets observed there can be described by the equation

$$N_{\Delta tot} = N_{tot} \int_{r=0}^{\infty} \int_{\Delta V_{tot}} \int_{\Delta t_{tot}} \tilde{f}(r,\mathbf{x},t)\, dr\, d\mathbf{x}\, dt \quad . \tag{100}$$

Now one can define the local droplet size distribution function $n(r,\Delta V,\Delta t)$ for the volume ΔV and the time step Δt by the equation

$$n(r,\Delta V,\Delta t) = \frac{N_{tot}}{N_{\Delta tot}} \int_{\Delta V_{tot}} \int_{\Delta t_{tot}} \tilde{f}(r,\mathbf{x},t)\, d\mathbf{x}\, dt \quad . \tag{101}$$

In the following equations, the expression of the dependency of n on ΔV and Δt is omitted for convenience.

The function n is more correctly called a local droplet number probability density function, as according to the equation

$$\int_0^\infty n(r)\,dr = 1 \; , \tag{102}$$

the integral over all droplet radii equals unity. The definition of the function $N(r)$ by the equation

$$N(r) = \frac{1}{\Delta V_{tot}} N_{tot} \int_{\Delta V_{tot}} \int_{\Delta t_{tot}} \tilde{f}(r,\mathbf{x},t)\,d\mathbf{x}\,dt = \frac{N_{\Delta tot}}{\Delta V_{tot}} n(r) = N''' n(r) \tag{103}$$

enables the calculation of the local moments of the droplet size distribution function. Equation (103) shows that $N(r)$ is a multiple of $n(r)$, where N''' denotes the total number of droplets per unit volume.

At this point the derivation in [13] starts. The probability P of droplets having radii between limits r_- and r_+ in the equation

$$P(r_- \leq r < r_+) = \int_{r_-}^{r_+} n(r)\,dr \tag{104}$$

is given by the integral of the droplet size distribution function $n(r)$ between the limits. Integrating the above defined function $N(r)$ between the limits r_- and r_+ determines the number of droplets per unit volume having radii between the limits. Hence, the moments of the droplet number probability distribution can be defined as

$$Q_m = \int_0^\infty N(r)r^m dr \; , \tag{105}$$

where m is the moment index.

In the described model of [13], the first four moments are used. The zeroth moment Q_0 represents the total number of droplets per unit volume, and one can see that Q_0 is equal to N'''. The first moment Q_1 is the total sum of the droplet radii per unit volume. The second and third moments, Q_2 and Q_3, are such that the total surface area of the droplets per unit volume is $4\pi Q_2$, and the droplet volume per unit volume is $4\pi Q_3 / 3$, if spherical droplets are assumed.

Mean droplet diameters are often used to characterise the droplet sizes in droplet clouds and sprays. By using the above four moments, all mean droplet diameters from d_{10} to d_{32} can be defined by the equation

$$d_{pq}^{p-q} = 2^{p-q} \frac{Q_p}{Q_q} \; . \tag{106}$$

The four moments contain information about the droplet size distribution. The most important moment is the third moment, because the transport of Q_3 is equivalent to the continuity equation of the dispersed phase. The second moment Q_2 is important for all models depending on the interfacial area between the droplet and the gas phases, such as drag, heat transfer, and mass transfer. The speed at which the four moments are convected in the Eulerian transport equations is defined by the moment-average velocities in the equation

$$U_{d,mj} = \frac{\int\limits_{0}^{\infty} N(r) r^m U_{d,j} dr}{Q_m} \; . \tag{107}$$

Subscript d indicates the dispersed phase, which is here the droplet phase. Subscript m is the moment index, and j denotes the velocity component. $U_{d,j}$ is the individual velocity of the droplets with radius r. This moment averaging can be applied also to other quantities, e.g. the moment-average temperature or a general quantity ϕ, by replacing $U_{d,j}$ by ϕ.

One should note the different convection velocities of the moments. In general, the droplets are travelling at different velocities, and it is not a trivial problem to select the "right" convection velocity. The convection velocity has to be a suitable average value of the droplet velocities, and one could suggest to transport all moments with the mass-average velocity $\mathbf{U}_{d,3}$. In fact, the third moment Q_3 has to be transported with this velocity in order to fulfil the continuity equation. But what happens to the other moments? Small droplets, which contribute to high values of Q_2, are more influenced by drag forces than large droplets, which contribute to small values of Q_2. Hence, a small droplet has in general a smaller relative velocity against the gaseous phase than a large droplet. Transporting both moments, Q_2 and Q_3, with the mass-average velocity would neglect this effect, and so there is no physical reason for doing this. This is why it seems to be a good approach that the net convection of mass occurs at the mass-average velocity, and the net convection velocity of the surface area is the surface area-average velocity $\mathbf{U}_{d,2}$. The same assumption is valid for the two other moments, Q_0 and Q_1, which should be transported with $\mathbf{U}_{d,0}$ and $\mathbf{U}_{d,1}$.

The equation

$$\alpha_d = \frac{4\pi}{3} Q_3 \tag{108}$$

emphasises once more that the third moment Q_3 multiplied by $4\pi / 3$, assuming spherical droplets, is the total droplet volume per unit volume of space, which is equal to the volume fraction of the droplet phase.

3.4.2 Transport of the Moments of the Droplet Size Distribution

The transport equations of the moments and the moment-average velocities as derived in [13] are presented here. The transport equation of the third moment is described by the equation

$$\frac{4\pi}{3}\frac{\partial}{\partial t}\left(\rho_d Q_3\right) + \frac{4\pi}{3}\frac{\partial}{\partial x_j}\left(\rho_d Q_3 U_{d,3j}\right) = -S_{Q_3} \ , \tag{109}$$

which is effectively the continuity equation of the dispersed droplet phase. The convection velocity required is the expected moment-average value, which is in fact the mass-average velocity. Hence, comparing Equation (109) with the mass conservation Equation (24), one can see that these equations are identical. The volume fraction α_k corresponds to $4\pi Q_3 / 3$, and the mass transfer term Γ_{kl} corresponds to $-S_{Q_3}$, which represents condensation and evaporation.

The second moment Q_2 is transported with the surface area-average velocity as described by the equation

$$\frac{\partial}{\partial t}\left(Q_2\right) + \frac{\partial}{\partial x_j}\left(Q_2 U_{d,2j}\right) = -S_{Q_2} \ . \tag{110}$$

The source term S_{Q_2} is influenced by all phenomena changing the droplet size and consequently the droplet surface area, such as condensation and evaporation $S_{Q_2,evap}$, collisions $S_{Q_2,coll}$, break-up processes $S_{Q_2,br}$, and thermal expansion $S_{Q_2,exp}$, as described by the equation

$$S_{Q_2} = S_{Q_2,evap} + S_{Q_2,coll} + S_{Q_2,br} + S_{Q_2,exp} \ . \tag{111}$$

The transport equation for the mass-average velocity is described by the equation

$$\frac{4\pi}{3}\frac{\partial Q_3 \rho_d U_{d,3i}}{\partial t} + \frac{4\pi}{3}\frac{\partial}{\partial x_j}\left(Q_3 \rho_d U_{d,3j} U_{d,3i}\right) = \frac{4\pi}{3}\frac{\partial}{\partial x_j}\left(Q_3 \mu_d^t \sigma_v \frac{\partial U_{d,3i}}{\partial x_j}\right) - U_{d,3i}S_{Q_3} - S_{U_{d,3i}} \tag{112}$$

Equation (112) is a momentum conservation equation and shows some differences from the momentum conservation equation for general multi-phase flow, Equation (26). The left-hand sides of the two equations match exactly. On the right-hand side, however, there is no

pressure term in Equation (112), and the diffusion formulation is different. In the derivation resulting in Equation (112), the droplet phase is dispersed from the beginning. This is in contrast to the derivations resulting in Equation (26), where a coherent liquid phase, determined by the phase indicator function, is assumed. The derivation in [13] for the momentum equation starts from the Lagrangian momentum formulation for a single droplet. There the pressure acts indirectly on the droplets via the drag force. The pressure gradient leads to acceleration or deceleration of the gas, causing a relative velocity between gas and droplet. Subsequently the droplet phases are also accelerated or decelerated due to drag, and hence the pressure term is absent. Furthermore, the turbulence effects in the dispersed droplet phase are incorporated by the use of a coefficient σ_v being a function of the dispersed phase properties and the gas phase turbulence [13]. This turbulent diffusion formulation contains no strain tensor as used in Equation (26). The body forces, as well as the interfacial forces, are contained in the source term $S_{U_{d,3i}}$, and the momentum transfer due to mass exchange $U_{d,3i}S_{Q_3}$ equals the term $U_{k,i}\Gamma_{kl}$ in (26). Nevertheless, the differences between Equations (112) and (26) due to different assumptions in the derivations are not crucial for the crankcase flow simulations, and both equations reveal a good representation of the droplet phase velocity.

The components of the surface area-average velocity are described by the equation

$$
\frac{\partial}{\partial t}\left(Q_2 U_{d,2i}\right) + \frac{\partial}{\partial x_j}\left(Q_2 U_{d,2j} U_{d,2i}\right) + \frac{\partial}{\partial x_j}\left[Q_2\left(U_{d,3i}-U_{d,2i}\right)\left(U_{d,3j}-U_{d,2j}\right)\right] =
$$
$$
\frac{\partial}{\partial x_j}\left(Q_2 \nu_d \sigma_v \frac{\partial U_{d,2i}}{\partial x_j}\right) - U_{d,2i}S_{Q_2} - S_{U_{d,2i}} \ .
$$

(113)

Equation (113) is obtained from momentum equations following the same pattern as performed the mass-average velocity equation. But there are some important differences. There is a third term on the left-hand side, which causes a convective momentum flux depending on the relative velocity between surface area-average velocity $\mathbf{U}_{d,2}$ and mass-average velocity $\mathbf{U}_{d,3}$. This term reduces the difference between the two moment-average velocities. The source term $S_{U_{d,2i}}$ gets its contribution due to drag.

3.4.3 Influences of Phase Interactions on the Droplet Size Distribution

The droplet size distribution changes due to the processes as evaporation, droplet collisions, droplet break-up, drag forces, and thermal expansion. Condensation and evaporation are not considered in this thesis, since they are slow process. Consequently, thermal expansion is also not considered, since the temperature change of the oil droplets is a slow process similar to condensation and evaporation. Break-up is not considered for the

droplet flow in the crankcase, since the expected relative velocities between gas and droplets are small. Droplet break-up plays an important role in the atomisation process of high-speed fuel jets as they occur in Diesel injection. The results of the derivations in [13] for the drag force and the collision model are represented here.

3.4.3.1 Drag Force

The source term due to drag for the dispersed phase momentum Equation (112) is described by the equation

$$S_{U_{d,3i}} = 6\pi\mu_c\left(U_{d,3i} - U_{c,i}\right)Q_1 + 1.8\pi\left(\rho_c\left|\mathbf{U}_{d,3} - \mathbf{U}_c\right|Q_2\right)^{0.687}\left(\frac{\mu_c Q_1}{2}\right)^{0.313}\left(U_{d,3i} - U_{c,i}\right). \qquad (114)$$

This equation is based on the drag coefficient formulation of Equation (42) in section 3.1.2, where c_D depends on the droplet Reynolds number, which is a function of the droplet radius. Inserting Equations (40) and (42) into the drag force Equation (38), integrating it over all droplet radii in the domain and performing moment-averaging, we get the desired drag force source term per unit volume.

Following the same pattern for the source term of the surface area-average velocity in Equation (113) yields the equation

$$S_{U_{d,2i}} = \frac{9Q_0}{2\rho_d}\mu_c\left(U_{d,2i} - U_{c,i}\right) + \frac{1.35}{\rho_d}\left(U_{d,2i} - U_{c,i}\right)\left(\frac{\mu_c Q_0}{2}\right)^{0.313}\left(\rho_c\left|\mathbf{U}_{d,3} - \mathbf{U}_c\right|Q_1\right)^{0.687}. \qquad (115)$$

The formulation for the drag coefficient of Equation (42) is valid for droplet Reynolds numbers less than 1000, and hence these source term formulations are valid only if all droplets of the ensemble do not exceed this limit. The Reynolds number of a droplet in a practical crankcase flow hardly can exceed 1000, because the relative velocities and the droplet sizes are normally too small. The effects of droplet volume fraction and deformation on the drag coefficient are not considered in the above formulations.

3.4.3.2 Droplet Collisions

Droplet collisions do not have any influence on the total droplet mass, but influence the size spectrum and therefore have an effect on the total droplet surface area. Therefore there is no influence on the moment Q_3, but there is an influence on Q_2 and the transport Equation (110) has a source term $S_{Q_{2,coll}}$ due to collisions, as shown in Equation (111).

It is a widely accepted fact that, when two droplets interact during flight, several processes may occur. An extensive experimental investigation of the stochastic collisions of drops of

two intersecting streams with visualisation of the processes occurring at collisions is given in [18]. A further experimental and theoretical investigation of unstable binary droplet collisions is given in [19]. Depending on the Weber number *We* and the impact parameter *B* , the droplets may experience bounce, stable coalescence, temporary coalescence followed by disruption, or temporary coalescence followed by fragmentation (separation), as illustrated in Figure 30.
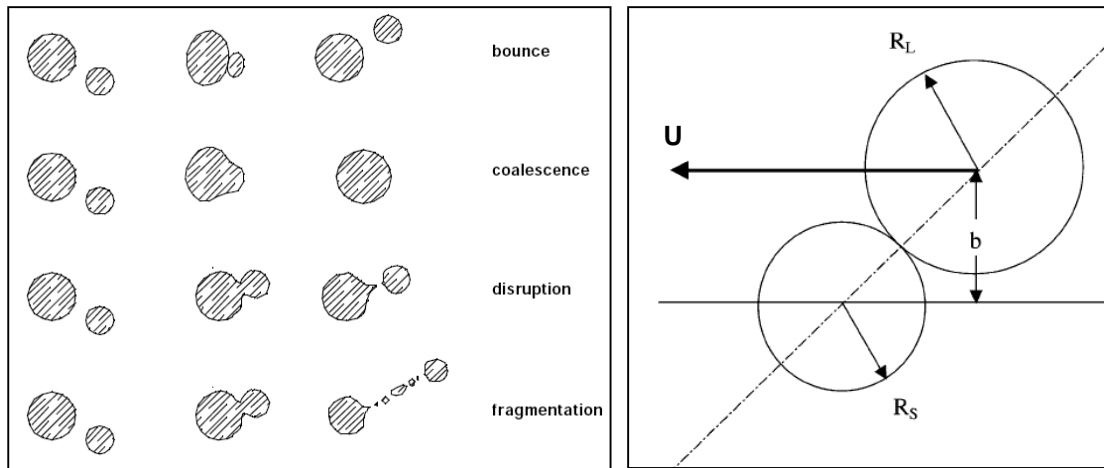

Figure 30: Left: Sketch of possible collision outcomes (figure from [1]); right: Definition of the impact parameter *B* (figure from [70])

The Weber number *We* is the ratio of the inertial force to the surface force and is defined in the equation

$$We = \frac{2r_s\rho_d\overline{U}_{rel}^2}{\sigma} \ , \tag{116}$$

where σ is the surface tension of the droplet fluid against the ambient medium, r_s is the radius of the smaller droplet, and U_{rel} is the relative velocity between the two droplets. The droplet impact parameter *B* is defined by the equation

$$B = \frac{b}{r_s + r_L} \ , \tag{117}$$

were b , r_s and r_L (here uncapitalised) are defined in Figure 30 right.

The different collision regimes can be drawn in nomograms against *We* and *B* , as presented in [74] for hydrocarbon droplets in air at ambient pressure. Such a stability nomogram is shown in Figure 31 left. Region (I) represents coalescence with minor deformation, (II) is bouncing, (III) coalescence after substantial deformation, (IV) is reflexive separation for near head-on collisions, and (V) is stretching separation for

off-centre collisions. An extended version of stability nomograms, which involves the numbers of satellite droplets formed by reflexive and stretching separation after head-on, near-head-on, and off-center collisions can be found in [19]. Furthermore, correlations describing the formation process of satellite droplets by stretching separation in unstable binary collisions have been developed in [22].
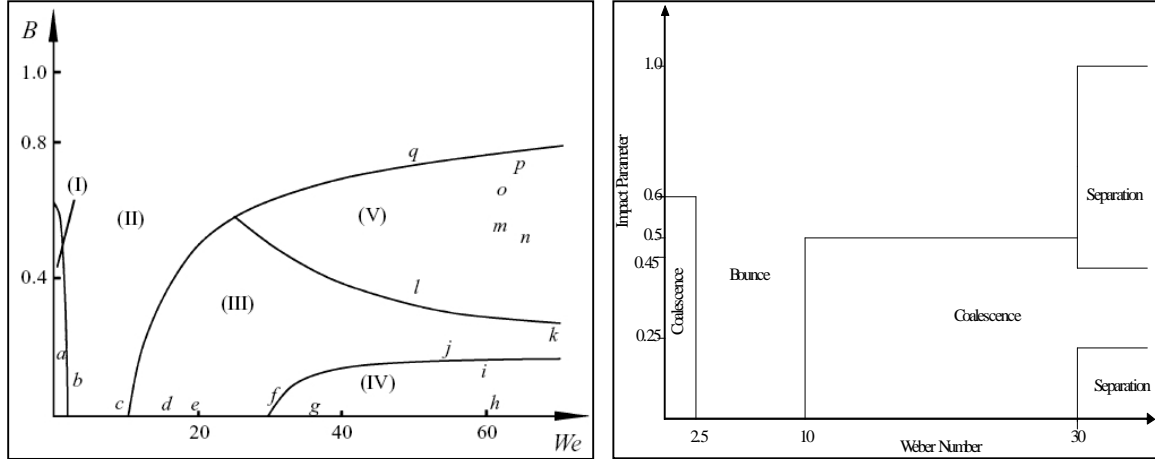

Figure 31: Left: Scheme of various collision regimes of HC droplets in air at ambient pressure (figure from [74]); right: Simplified scheme of collision regimes (figure from [13])

Figure 31 right shows the simplified map of the collisions regimes used for the calculation of the source $S_{Q_2,coll}$ in [13]. Bouncing has no influence on the droplet surface area. Coalescence reduces the total surface area Q_2, and separation leads to an increase of the moment Q_2, because the surface area of the droplets after the collision is larger than the surface of the two large droplets before the collision. The formation process of satellite droplets formed by reflexive and stretching separation is not considered. For the determination of the collision surface source term for hydrocarbon droplets it is relevant to determine the probabilities $P_{coal,a}$ of collisions leading to coalescence with We less than 2.5, $P_{coal,b}$ for We between 10 and 30, and $P_{coal,c}$ for We greater than 30, and for P_{sep} for collisions leading to separation at We greater than 30. By definition of an average value of all relative velocities for collision $\overline{U}_{rel}$, the probability of having We in a certain range can be modelled as the probability that the smaller of the two colliding droplets is contained in a certain radius range. This information is gained from integrals over the droplet number distribution function $n(r)$, which is per definition a probability density function. The entire probabilities $P_{coal,a}$, $P_{coal,b}$, $P_{coal,c}$, and P_{sep} are then determined by the impact parameter, which is assumed to be a uniform random variable between 0 and 1, and by the probability of being in a certain range of We.

The source term $S_{Q_2,coll}$ in Equation (111) is calculated by the equation

$$S_{Q_2,coll} = N_{coll} \left(P_{coal,a} \delta Q_{2,a} + P_{coal,b} \delta Q_{2,b} + P_{coal,c} \delta Q_{2,c} + P_{sep} \delta Q_{2,sep} \right) . \tag{118}$$

The terms $\delta Q_{2,a}$, $\delta Q_{2,b}$, $\delta Q_{2,c}$ are the modelled changes of the surface area for the three coalescence regions, which are set to $-0.41 r_a^2$, $-0.41[(r_b + r_c)/2]^2$, and $-0.41 r_c^2$ respectively. Here r_a, r_b and r_c are the corresponding droplet radii at the transition Weber numbers 2.5, 10, and 30 in Figure 31. $\delta Q_{2,sep}$ is the change of the surface area due to separation, which is modelled as $+0.71 r_c^2$.

The probability of occurrence of a collision of two droplets in the same control volume per unit volume and unit time, N_{coll}, is modelled by the equation

$$N_{coll} = C_{coll} \pi \overline{U}_{rel} \left(Q_0 Q_2 + Q_1^2 \right) . \tag{119}$$

The average relative velocity at the collisions assumed to be half the difference of the gas phase and the mass-average velocities $\overline{U}_{rel} \approx 0.5 |\mathbf{U}_{d,3} - \mathbf{U}_c|$. C_{coll} is a model constant usually set to 0.15 [13].

3.4.4 Droplet Size Distribution Function

The formulations for the transport of the moments and the source terms of the transport equations are valid for arbitrary droplet size distribution functions. The approach in [13] and [14] proposes the transport of the second and third moments Q_2 and Q_3, while the zeroth and first moments, Q_0 and Q_1, are approximated by given droplet size distribution function, which is determined by the equation

$$n(r) = \frac{16\, r}{r_{32,ref}^2} e^{-\frac{4r}{r_{32,ref}}} . \tag{120}$$

$n(r)$ is a droplet number probability density function, where $r_{32,ref}$ is the reference Sauter mean radius (SMR) of the distribution. The corresponding dimensionless droplet number PDF as function of the dimensionless radius $\acute{r}$ is described by the equation

$$\acute{h}(\acute{r}) = 16\, \acute{r}\, e^{-4\acute{r}} \quad with \quad \acute{r} = \frac{r}{r_{32,ref}} . \tag{121}$$

This normalised form conserves the property, that integrating over a certain corresponding radius range of $\acute{h}(\acute{r})$ yields the same quantities as integrating over $n(r)$. The dimensionless droplet volume probability density function is determined by the equation

$$\mathring{v}(\mathring{r}) = \frac{128}{3}\mathring{r}^4 e^{-4\mathring{r}} \ .$$

(122)

The aim of the chosen droplet number distribution was to have an analytically integrable function, such that the volume distribution it produces is a reasonable approximation to a Rosin-Rammler (RR) distribution v_{RR} with an exponent κ_{RR} of two. The original RR volume distribution function is described by the equation

$$v_{RR}(r) = \frac{\kappa_{RR}}{r_{RR}^{\kappa_{RR}}} r^{\kappa_{RR}-1} \exp\left[-\left(\frac{r}{r_{RR}}\right)^{\kappa_{RR}}\right] \ .$$

(123)

r_{RR} is known as the Rosin-Rammler mean radius, which is not equivalent to the reference SMR $r_{32,ref}$. The RR distribution is often used for characterising fuel sprays. The drawback of the RR distribution is that it predicts an infinite number of droplets of size zero if κ_{RR} is less than four. Thus Q_0 would also tend to infinity and cause numerical problems. The distribution function in Equation (120), in contrast, does not suffer from this problem. Figure 32 shows the dimensionless droplet number and droplet volume PDFs in Equations (121) and (122). The droplet volume PDF has its maximum at the reference SMR, the droplet number PDF has its maximum at $r_{32,ref}/4$.
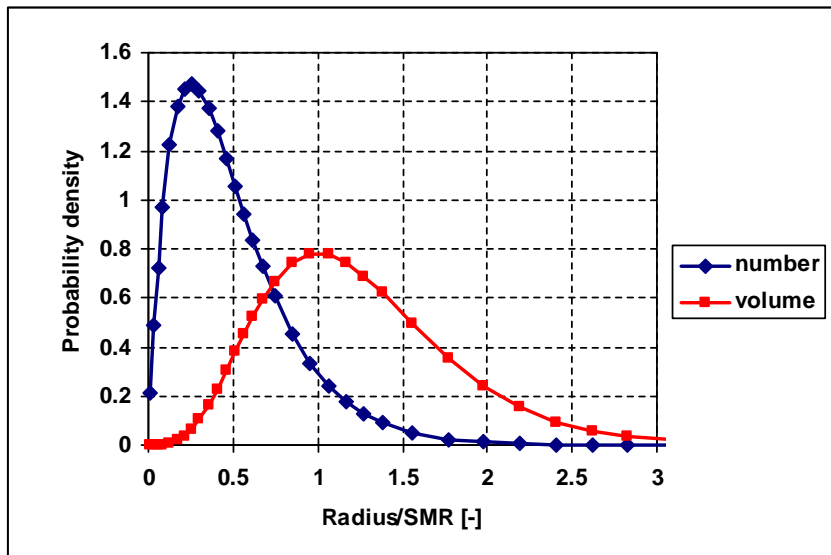
Figure 32: PDFs of the droplet number and droplet volume in Equations (121) and (122)

The local SMR r_{32} is given by the equation

$$r_{32} = \frac{Q_3}{Q_2} \ ,$$

(124)

and it is determined as the ratio of Q_3 and Q_2, which are transported in separate equations.
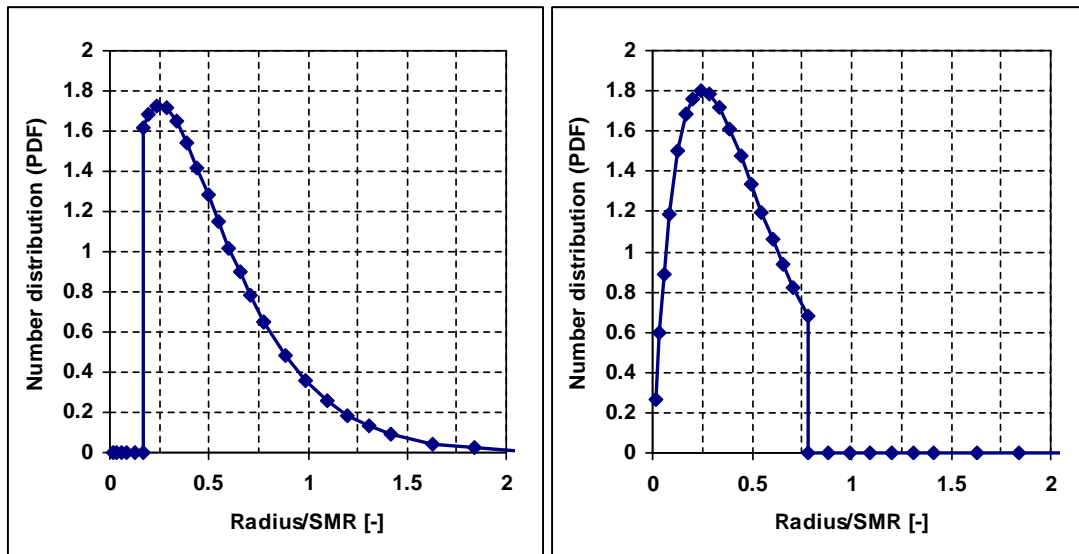

Figure 33: Truncation of the droplet number distribution function to remove small droplets (left) and to remove large droplets (right)

The idea in [13] was to keep $r_{32,ref}$ constant and to match the distribution determined by the transported values of Q_3 and Q_2 by truncating the size distribution either at the large or at the small droplets out. This means that, if the local SMR is greater than the reference SMR, the droplet number distribution is obtained by removing the small droplets from the distribution as shown in Figure 33 left. If the local SMR is smaller than the reference SMR, the large droplets are removed from the distribution, as shown in Figure 33 right. Of course the truncated distribution is re-normalised so that the integral over the whole radius range equals unity.

4 Model Features and Numerical Solution Technique

In the previous section models from the literature relevant for the present simulations have been discussed. This section deals with the numerical solution technique of the developed crankcase flow simulation tool. Existing models from the literature have been adapted and extended for the special application of the crankcase flow simulation. Blow-by and oil disintegration on the rotating crankshaft have been indicated as the most relevant processes for the CFD simulations. Thus they are treated in separate models, which provide the boundary conditions of velocity, liquid mass, and droplet diameter for the CFD simulation of the propagation of the oil mist and the oil droplets in the crankcase. Additional transport equations for the moments of a droplet size distribution function considering the effects of different droplet diameters in the oil mist and the splash oil are solved. The first two parts of this section treat numerical aspects for solving conservation equations with the CFD solver FIRE. The discretisation of the multi-phase transport equations and some consideration for solving the transport of the moments of a droplet size distribution function are discussed. Then the models for blow-by and oil disintegration on the crankweb are presented in detail in the third and fourth parts of this section. Sensitivity analyses of the model parameters including different operation conditions give an overview of the model outcome.

4.1 CFD with FIRE

The CFD code FIRE [5] solves the multi-phase conservation equations represented in section 3.1. The method is fully implicit and allows the use of unstructured moving grids composed of arbitrary polyhedral cells. This section describes briefly the approximation of the conservation equations, which are partial differential equations (PDE), by the finite volume discretisation. The numerical solution procedure, including discretisation principles, grid features, data structure, and solution algorithm are provided in detail in [5] and [6].

When considering the numerical solution procedure of sets of transport equations, it is useful to express them by a general differential equation. The multi-phase conservation equations for mass, momentum, energy and turbulence can be expressed in the form of the equation

$$\underbrace{\frac{\partial \alpha_k \rho_k \phi_k}{\partial t}}_{\text{Rate of change: } R} + \underbrace{\frac{\partial}{\partial x_j}\left[\alpha_k \rho_k \left(U_{k,j} - U_{gr,j}\right)\phi_k\right]}_{\text{Convection: } C} = \underbrace{\frac{\partial}{\partial x_j}\left(\alpha_k \Gamma_{\phi k}\frac{\partial \phi_k}{\partial x_j}\right)}_{\text{Diffusion: } D} + \underbrace{\frac{\partial}{\partial x_j}\left(\alpha_k s^A_{\phi k,j}\right) + s^V_{\phi k}}_{\text{Sources: } S} \; , \qquad (125)$$

by inserting the variables from Table 4. Note that the index summation rule for subscript j is applied. The mean flow variable $\phi_k(x,t)$ of phase k is a function of space and time and

represents either a scalar, such as total enthalpy h_k, TKE k_k, or TED ε_k, or vector components, such as the fluid velocity $U_{k,i}$. The first term R on the left-hand side denotes the rate of the change of the transported quantity. The term C stands for the convective transport rate, where $\mathbf{U}_{gr}$ is the velocity vector of a moving control volume (CV). The first term on the right-hand side, D, represents the diffusive transport, where $\Gamma_{\phi k}$ stands for the diffusion coefficient. The term S denotes the specific source or sink of ϕ_k. This source consists of the volumetric term $S_{\phi k}^V$ and the surface term $\partial \alpha_k S_{\phi k}^A / \partial x_j$ considering the diffusion flux, which is not described by the nominal diffusion flux in D. Equation (125) is similar to Equation (18) in section 3.1 representing the general form of the differential conservation equation for single-phase flow. Differences result from the formulation of the equation with the phase volume fraction α_k and the additional consideration of the velocity $\mathbf{U}_{gr}$ of the moving control volume, which is required for moving computational grids.

Variable	ϕ_k	$\Gamma_{\phi k}$	$s_{\phi k,\, j}^{A}$	$s_{\phi k}^{V}$
Mass	1	0	0	$\displaystyle\sum_{l=1,l\neq k}^{n_{Ph}}\Gamma_{kl}$
Momentum	$U_{k,i}$	$\mu_{eff} = \mu_k + \mu_k^t$	$\mu_{eff}\left(\dfrac{\partial U_{k,j}}{\partial x_i} - \dfrac{2}{3}\delta_{ij}\dfrac{\partial U_{k,m}}{\partial x_m}\right) - \dfrac{2}{3}\delta_{ij}\rho_k k_k$	$\alpha_k\left(-\dfrac{\partial p}{\partial x_i} + \rho_k g_i\right) + \displaystyle\sum_{l=1,l\neq k}^{n_{Ph}}\mathrm{M}_{kl,i} + U_{k,i}\sum_{l=1,l\neq k}^{n_{Ph}}\Gamma_{kl}$
Enthalpy	h_k	$\dfrac{\kappa_k}{c_{p,k}} + \dfrac{\mu_k^t}{\sigma_T}$	$\left(\tau_{k,ij} + \tau_{k,ij}^t\right)U_{k,i}$	$\alpha_k\rho_k\theta_k + \alpha_k\rho_k g_j U_{k,j} + \alpha_k\dfrac{\partial p}{\partial t} + \displaystyle\sum_{l=1,l\neq k}^{n_{Ph}}\mathrm{H}_{kl} + h_k\sum_{l=1,l\neq k}^{n_{Ph}}\Gamma_{kl}$
Turbulent kinetic energy (TKE)	k_k	$\mu_k + \dfrac{\mu_k^t}{\sigma_k}$	0	$\alpha_k\mathrm{P}_k - \alpha_k\rho_k\varepsilon_k + \displaystyle\sum_{l=1,l\neq k}^{n_{Ph}}\mathrm{K}_{kl} + k_k\sum_{l=1,l\neq k}^{n_{Ph}}\Gamma_{kl}$
Turbulent dissipation rate (TED)	ε_k	$\mu_k + \dfrac{\mu_k^t}{\sigma_\varepsilon}$	0	$\alpha_k C_1 \mathrm{P}_k \dfrac{\varepsilon_k}{k_k} - \alpha_k C_2 \rho_k \dfrac{\varepsilon_k^2}{k_k} - \alpha_k C_4 \rho_k \varepsilon_k \dfrac{\partial U_{k,j}}{\partial x_j} + \displaystyle\sum_{l=1,l\neq k}^{n_{Ph}}\mathrm{D}_{kl} + \varepsilon_k\sum_{l=1,l\neq k}^{n_{Ph}}\Gamma_{kl}$

Table 4: Variables in the general conservation Equation (125)

Equation (125) can be transformed into an integral form, which is obtained by integrating over the control volume V, and applying the generalised Gauss theorem, given in the equation

$$\int_V \nabla \cdot \mathbf{F}\, dV = \int_A \mathbf{F} \cdot \mathbf{n}_A\, dA = \int_A \mathbf{F} \cdot d\mathbf{A} \quad \text{or} \quad \int_V \frac{\partial F_j}{\partial x_j}\, dV = \int_A F_j dA_j \ , \tag{126}$$

in vector as well as in the index notation for any flux vector $\mathbf{F}$. This leads to the general conservation equation in integral form, as shown in the equation

$$\int_V \frac{\partial \alpha_k \rho_k \phi_k}{\partial t} dV + \int_A \left[\alpha_k \rho_k \left(U_{k,j} - U_{gr,j}\right)\phi_k\right] dA_j = \int_A \left(\alpha_k \Gamma_{\phi k} \frac{\partial \phi_k}{\partial x_j}\right) dA_j + \\ + \int_A \left(\alpha_k s^A_{\phi k, j}\right) dA_j + \int_V s^V_{\phi k} dV \ . \tag{127}$$

For the numerical solution procedure, a discretisation has to be performed on Equation (127). Therefore, it is assumed that the control volume V, i.e. the volume of a cell in the computational grid, is bounded by a number of piecewise smooth surfaces $i_f = 1,..,n_f$. Figure 34 shows the control volume (CV) around the point P and the adjacent CV around the neighbouring point P_f. The face i_f connects the two adjacent computational cells, where the face vector $\mathbf{A}_f = \mathbf{n}_A \cdot A_f$ points outward in normal on the face surface. The face i_b is a boundary face with the surface vector $\mathbf{A}_b$. All dependent variables of the considered CV are stored at point P, which is in fact the geometric centre of the computational cell. $\mathbf{x}_P$ is the position vector of P in a Cartesian coordinate system. All boundary conditions are stored at the geometrical centre of the boundary face i_b.
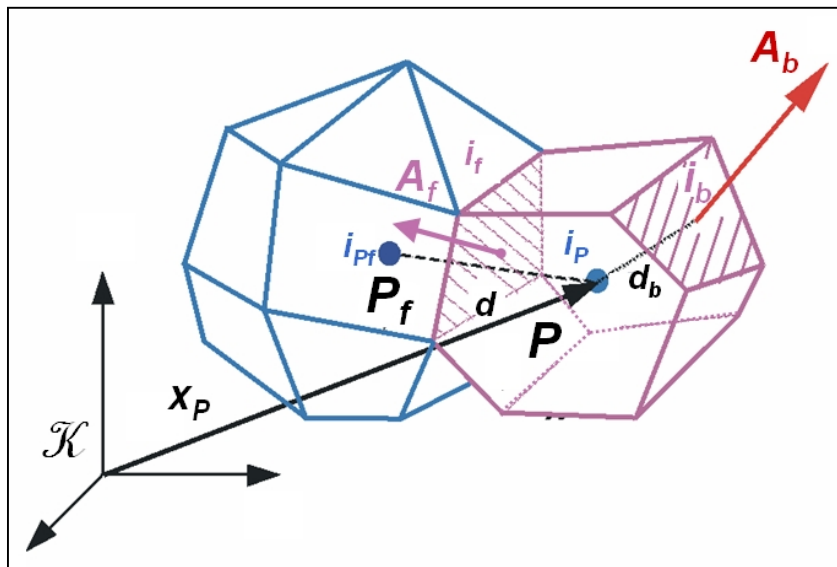

Figure 34: General polyhedral control volume of an unstructured computational mesh according to [6]

The volume integrals in Equation (127) are approximated by the equation

$$\int_V (...) \, dV \approx (...)_P V_P \ ,$$
(128)

assuming uniform distribution of the flow variable $\phi_k(x,t)$ within the computational cell. Similar assumptions are applied for the surface integrals in Equation (127), which are approximated by the equation

$$\int_A F_j \, dA_j = \sum_{f=1}^{n_f} \int_{A_f} F_j \, dA_j \approx \sum_{f=1}^{n_f} (F_j A_j)_f \ .$$
(129)

Note that subscript P indicates a cell value, and subscript f indicates a face value.

Consequently, the general transport equation can be rewritten in the approximated form as shown in the equation

$$\frac{\partial}{\partial t} \underbrace{(\alpha_k \rho_k \phi_k V)_P}_{R} + \sum_{f=1}^{n_f} \underbrace{\left[\alpha_k \rho_k \left(U_{k,j} - U_{gr,j}\right) A_j\right]_f (\phi_k)_f}_{C_f} - \sum_{f=1}^{n_f} \underbrace{(\alpha_k \Gamma_{\phi k})_f \left(\frac{\partial \phi_k}{\partial x_j} A_j\right)_f}_{D_f} =$$

$$\sum_{f=1}^{n_f} \underbrace{\left(\alpha_k s_{\phi k,j}^A A_j\right)_f}_{S_\phi^A} + \underbrace{\left(s_{\phi k}^V\right) V_P}_{S_\phi^V} \ .$$
(130)

On the left-hand side there are the rate of change of the transported quantity, the convective, and the diffusive fluxes across the cell faces. The sources are put on the right-hand side. By introducing the scalar $\psi = \alpha_k \rho_k \phi_k$ and denoting the convection flux via the cell faces as $C_f = \dot{m}_f \phi_f$, with the mass flux term $\dot{m}_f$, Equation (130) can be transformed into the equation

$$\frac{\partial}{\partial t} (\psi V)_P + \sum_{f=1}^{n_f} \dot{m}_f \phi_f - \sum_{f=1}^{n_f} D_f = \sum_{f=1}^{n_f} \left(S_\phi^A\right)_f + S_\phi^V \ .$$
(131)

Equation (131) denotes the general transport equation in approximated form for any flow variable ϕ. The further discretisation procedure, which is provided in detail in [5], includes the transformation of (131) into the algebraic equation

$$a_P \phi_P = \sum_{f=1}^{n_f} a_{P_f} \phi_{P_f} + S_\phi \ .$$
(132)

The time integration is performed, the convection and diffusion terms are determined, the source terms are reorganised, and the boundary conditions are applied. The discretisation scheme has to provide a good representation of the flow variable at the cell face ϕ_f. A

sophisticated gradient approximation algorithm delivers the gradient of the flow variable at the cell face $(\partial\phi/\partial x_j)_f$. ϕ_P in Equation (132) denotes the value of the flow variable in cell P, and a_P is its central coefficient containing contributions from the convection and diffusion terms, the time integration and the linearised part of the source term. The coefficients a_{P_f} associated with the values of ϕ at the neighbouring cells P_f and the term S_ϕ determine the right-hand side of the algebraic transport equation.

For a computational domain with n_{cell} control volumes, a system of $n_{cell} \times n_{Ph} \times n_\phi$ coupled algebraic equations of the form (132) need to be solved by the CFD solver. The number of phases is denoted by n_{Ph}, and n_ϕ is the number of dependent flow variables ϕ, as quoted in Table 4. The results are the values of the dependent flow variables at the cell centre ϕ_P.

Special attention is paid to the momentum equation, because a principal difficulty lies in the determination of the pressure field [67], [36]. The CFD solver of AVL FIRE uses a SIMPLE-like (Semi-Implicit-Method for Pressure-Linked Equations) algorithm, which is explained in detail in [5]. The pressure is assumed to be uniform for all phases. The discrete continuity equations of the phases are combined to an overall continuity equation, and then converted into an equation for the pressure correction. The pressure corrections are then used to update the pressure and velocity fields, so that the velocity components obtained from the solution of the momentum equations satisfy the continuity equation.

For the solution of the algebraic equation systems, the multi-phase CFD solver uses the iterative, preconditioned conjugate gradient method. The algebraic equations for every flow variable are solved in a sequence. This means that each equation system for the considered flow variable is decoupled by treating the other variable as known. This is done in an iterative process, called outer iteration process, for every time step of the calculation, until convergence is achieved. The (simplified) solution algorithm of the FIRE multi-phase solver based on the segregated SIMPLE-like approach, is summarised below:

1. Provide numerical grid, calculate geometrical quantities for all CV, as shown in Figure 34, and initialise the values of the flow variables for all phases at the initial time t_0.

2. Begin the time stepping loop. Save the current variable values as the old ones. In case of moving grids, determine the position of the cell vertices, update the geometrical data, and determine the grid velocities $\mathbf{U}_{gr}$ for all cell faces. Set the boundary conditions for the current time step.

3. Begin the outer iteration loop. If the enthalpy equation is solved, calculate the temperature from the total enthalpy, Equation (32) in section 3.1.1.3. For compressible flow calculate the densities of the gaseous phases from the equations

of state. Update the turbulent viscosity and other fluid properties, which depend on the temperature.

4. Assemble and solve the algebraic equations for the volume fractions α_k of all phases, as shown in Equation (132).

5. Assemble and solve the algebraic equations for the velocity components $U_{k,i}$ of all phases.

6. Solve the pressure correction equation according to the SIMPLE-like approach and use the outcome to correct the pressure and the velocity components of all phases.

7. Solve the equations for turbulent kinetic energy k_k and its dissipation rate ε_k.

8. Assemble and solve Equation (132) for the total enthalpy h_k.

9. Solve additional transport equations, if necessary; e.g. the moments of the droplet size distribution function.

10. Return to Step 3 and repeat the procedure until the convergence criterion is satisfied.

11. Return to Step 2 and repeat up to the prescribed number of time steps.

4.2 Transport of the Droplet Size Distribution

This section discusses the numerical implementation of the additional transport equations for the moments of the droplet size distribution function. There are two ways for the simulation of the oil mist and droplet propagation within an Eulerian-Eulerian framework. In the first (standard) approach, a constant Sauter mean diameter is assigned to the liquid droplet phase, for which the transport equations are solved. This method is easy to handle, because the droplet diameter is constant, and hence there are no additional transport equations for the droplet size. Applied in crankcase flow simulations with two phases on simplified crankcase geometries, this method shows good results [34], [35]. But the constant droplet diameter, which does not change in space and time, is also the drawback of this method. The effects of locally varying droplet diameters, generated due to different conditions at the formation process, are not considered by the global diameter. Splitting the liquid phase into several phases and assigning each of them a constant droplet class diameter, could overcome this problem. But this would lead to high computational effort, since for each of these droplet phases the complete set of conservation equations would have to be solved.

For this reason the second approach uses one liquid phase and solves additional transport equations for the moments of the droplet size distribution. Hence, the averaged droplet diameter is determined by the local moments and changes in space and time. The idea and the model equations of this second approach, based on the work of [13], have been discussed in section 3.4. The implementation of the transport equations into the CFD code FIRE and some numerical considerations are treated here.

By following the approach of [13], additional transport equations for the moment Q_3 of the droplet volume, the moment Q_2 of the droplet surface area, and the moment-average velocity components of both moments, $U_{d,3i}$ and $U_{d,2i}$, are solved for the liquid droplet phase. Although Q_3 is equivalent to the dispersed phase volume fraction α_d, as shown in Equation (108), the transport equation of Q_3 is solved separately. As pointed out in section 3.4.2, there are slight differences in the momentum conservation equations for the moment-average velocity vector $\mathbf{U}_{d,3}$, Equation (112) in section 3.4.2, and for the phase velocity vector $\mathbf{U}_k$ originally applied in the FIRE multi-phase solver, Equation (26) in section 3.1.1.2. Hence, $\mathbf{U}_{d,3}$ and $\mathbf{U}_k$ cannot match exactly. Subsequently it was decided to solve the momentum equation for the components of $\mathbf{U}_{d,3}$ and the transport equation for the moment Q_3, which is transported with the velocity $\mathbf{U}_{d,3}$, separately.

The discretisation of the transport equation of the third droplet moment Q_3 is shown in the equation

$$
\frac{4\pi}{3} \frac{\partial}{\partial t}(\rho_d Q_3) + \frac{4\pi}{3} \frac{\partial}{\partial x_j}(\rho_d Q_3 U_{d,3j}) = -S_{Q_3}
$$

$$
\Rightarrow \frac{d}{dt}(\rho_d Q_3 V)_P + \sum_{f=1}^{n_f}\left[\rho_d\left(U_{d,3j} - U_{gr,j}\right)A_j\right]_f (Q_3)_f = \frac{3}{4\pi}\left(-S_{Q_3}\right)_P V_P \ .
$$

(133)

The discretisation procedure is performed according to the rules discussed in the previous section. The convective transport of Q_3 occurs with the mass-average velocity $\mathbf{U}_{d,3}$. The convection term is enhanced by the grid velocity $\mathbf{U}_{gr}$.

The solution procedure in FIRE requires the set-up of the convection, diffusion, and source terms according to the general transport equation in approximated form, Equation (131). This is shown in the equations

$$\phi = Q_3 \quad \text{and} \quad \psi_P = (\rho_d Q_3)_P$$
$$\dot{m}_f = \left[\rho_d (U_{d,3j} - U_{gr,j}) A_j\right]_f$$
$$D_f = 0$$
$$S_\phi^A = 0$$
$$S_\phi^V = -\frac{3}{4\pi} S_{Q_3} V_P \quad,$$

(134)

where the transported scalar ψ_P, the mass flux term $\dot{m}_f$, the diffusive flux term D_f and the source terms, S_ϕ^V and S_ϕ^A, are defined. For $\dot{m}_f$, D_f and S_ϕ^A the cell face values are required, while ψ_P and S_ϕ^V are determined by the cell centre values.

Since there is no diffusion term in Equation (133), the diffusion flux is zero. The surface term of the source S_ϕ^A is also zero. The volumetric source term S_ϕ^V gets its contribution due to mass exchange between the droplet and the gas phases. Condensation and evaporation effects are not considered in the presented crankcase flow simulations, and hence the term S_ϕ^V will also be zero in the applied simulations.

The discretisation of the transport equation of the surface moment Q_2 is shown in the equation

$$\frac{\partial}{\partial t}(Q_2) + \frac{\partial}{\partial x_j}(Q_2 U_{d,2j}) = -S_{Q_2}$$

$$\Rightarrow \frac{d}{dt}(Q_2 V)_P + \sum_{f=1}^{n_f}\left[(U_{d,2j} - U_{gr,j}) A_j\right]_f (Q_2)_f = \left(-S_{Q_2}\right)_P V_P \quad.$$

(135)

There the convective transport of Q_2 occurs with the average velocity $\mathbf{U}_{d,2}$ of the surface area. By comparing Equation (135) with the general transport Equation (131), the terms in the equations

$$\phi = Q_2 \quad \text{and} \quad \psi_P = (Q_2)_P$$
$$\dot{m}_f = \left[(U_{d,2j} - U_{gr,j}) A_j\right]_f$$
$$D_f = 0$$
$$S_\phi^A = 0$$
$$S_\phi^V = -S_{Q_2} V_P \quad,$$

(136)

are obtained. Here the flux term $\dot{m}_f$ does not concern the transport of mass, but it is part of the convective transport of Q_2 with velocity $\mathbf{U}_{d,2}$. D_f and S_ϕ^A are zero. The volumetric source term gets its contribution from physical processes influencing the droplet size or droplet surface area, as there are condensation, evaporation, collisions and break-up effects. Since condensation and break-up processes are not considered in the current crankcase flow

simulation, S_{Q_2} and subsequently S_ϕ^V, are determined by the collision model, which has been discussed in section 3.4.3.2.

The discretisation of the momentum equation for computing the components of the mass-average velocity $U_{d,3i}$, which is shown in the equation

$$\frac{4\pi}{3}\frac{\partial \, Q_3 \rho_d U_{d,3i}}{\partial \, t} + \frac{4\pi}{3}\frac{\partial}{\partial x_j}\left(Q_3 \rho_d U_{d,3j} U_{d,3i}\right) =$$

$$= \frac{4\pi}{3}\frac{\partial}{\partial x_j}\left(Q_3 \mu_d^t \sigma_t \frac{\partial U_{d,3i}}{\partial x_j}\right) - U_{d,3i} S_{Q_3} - S_{U_{d,3i}} \qquad (137)$$

$$\Rightarrow \frac{d}{dt}\left(Q_3 \rho_d U_{d,3i} V\right)_P + \sum_{f=1}^{n_f}\left[Q_3 \rho_d \left(U_{d,3j} - U_{gr,j}\right)A_j\right]_f \left(U_{d,3i}\right)_f - \sum_{f=1}^{n_f}\left(Q_3 \mu_d^t \sigma_t\right)_f \left(\frac{\partial U_{d,3i}}{\partial x_j}A_j\right)_f$$

$$= \frac{3}{4\pi}\left(-U_{d,3i} S_{Q_3} - S_{U_{d,3i}}\right)_P V_P \ ,$$

is very similar to the momentum equation for the phase velocity $U_{k,i}$ of Table 4 in section 4.1. By taking into account that $\alpha_d = 4\pi/3 \cdot Q_3$, one can see that there are only small differences in the formulation of the diffusion term, and the pressure term is absent. All other terms remain unchanged. Comparing again the current transport equation with the general transport Equation (131), the mass flux term, the diffusive term, and the source terms can be written, as listed in the equations

$$\phi = U_{d,3i} \quad \text{and} \quad \psi_P = \left(Q_3 \rho_d U_{d,3i}\right)_P$$
$$\dot{m}_f = \left[Q_3 \rho_d \left(U_{d,3j} - U_{gr,j}\right)A_j\right]_f$$
$$D_f = \left(Q_3 \mu_d^t \sigma_t\right)_f \left(\frac{\partial U_{d,3i}}{\partial x_j}A_j\right)_f \qquad (138)$$
$$S_\phi^A = 0$$
$$S_\phi^V = \frac{3}{4\pi}\left(-U_{d,3i} S_{Q_3} - S_{U_{d,3i}}\right)_P V_P \ .$$

There is no mass exchange between the liquid and the vapour phases, and hence S_{Q_3} is zero. Thus the volumetric source term S_ϕ^V gets its only contribution from $S_{U_{d,3i}}$, which is determined by the drag force described by Equation (114) in section 3.4.3.1.

In order to complete the set of relations, the equations for the components of the average velocity of the surface area have to be solved. The momentum equation for $U_{d,2i}$ is described by the equation

$$\frac{\partial}{\partial t}\left(Q_2 U_{d,2i}\right)+\frac{\partial}{\partial x_j}\left(Q_2 U_{d,2j} U_{d,2i}\right)+\frac{\partial}{\partial x_j}\left[Q_2\left(U_{d,3i}-U_{d,2i}\right)\left(U_{d,3j}-U_{d,2j}\right)\right]=$$

$$\underbrace{\hspace{1.5cm}}_{I}\qquad\underbrace{\hspace{2cm}}_{II}\qquad\underbrace{\hspace{3.5cm}}_{III}\tag{139}$$

$$\frac{\partial}{\partial x_j}\left(Q_2 \nu_d \sigma_t \frac{\partial U_{d,2i}}{\partial x_j}\right)-U_{d,2i} S_{Q_2}-S_{U_{d,2i}}\;.$$

The main difference to the momentum equation for the mass-average velocity is the third term on the left-hand side, which provides a convective momentum flux depending on the difference between $\mathbf{U}_{d,3}$ and $\mathbf{U}_{d,2}$. This third term is not considered in the original structure of the general transport Equation (131), and hence it has to be treated separately.

This third term can be either treated as a source contributing to the right-hand side of Equation (139), or it is treated as a part of the convection term. Following the second method, the convection term describing the convective transport of the velocity component $U_{d,2i}$ has to be rearranged. The third term in Equation (139) contains the mass-average velocity component $U_{d,3i}$, and hence the second and the third terms, II and III, have to be transformed as shown by the relations

$$\frac{\partial}{\partial x_j}\left(Q_2 U_{d,2j} U_{d,2i}\right)+\frac{\partial}{\partial x_j}\left[Q_2\left(U_{d,3j}-U_{d,2j}\right)\left(U_{d,3i}-U_{d,2i}\right)\right]=$$

$$=\frac{\partial}{\partial x_j}\left(Q_2 U_{d,2j} U_{d,2i}\right)+\frac{\partial}{\partial x_j}\left[Q_2\left(U_{d,3j}-U_{d,2j}\right)\left(U_{d,2i}\frac{U_{d,3i}}{U_{d,2i}}-U_{d,2i}\right)\right]=$$

$$=\frac{\partial}{\partial x_j}\left(Q_2 U_{d,2j} U_{d,2i}\right)+\frac{\partial}{\partial x_j}\left[Q_2\left(U_{d,3j}-U_{d,2j}\right)\left(\kappa_{U_i}-1\right)U_{d,2i}\right]=\tag{140}$$

$$=\frac{\partial}{\partial x_j}\left\{Q_2\left[2U_{d,2j}-U_{d,3j}+\left(U_{d,3j}-U_{d,2j}\right)\kappa_{U_i}\right]U_{d,2i}\right\}.$$

The velocity ratio κ_{U_i}, defined by the equation

$$\kappa_{U_i}=\frac{U_{d,3i}}{U_{d,2i}}\;,\tag{141}$$

is introduced to eliminate $U_{d,3i}$ from the convective flux. Since all transport equations are solved in an iterative process, κ_{U_i} is determined by the velocity components from the previous iteration.

Performing the discretisation procedure and considering the grid velocity leads to the relation

$$\frac{d}{dt}\left(Q_2 U_{d,2i} V\right)_P + \sum_{f=1}^{n_f}\left\{Q_2\left[2U_{d,2j} - U_{d,3j} + \left(U_{d,3j} - U_{d,2j}\right)\kappa_{U_i} - U_{gr,j}\right]A_j\right\}_f \left(U_{d,2i}\right)_f$$

$$- \sum_{f=1}^{n_f}\left(Q_2 \nu_d \sigma_t\right)_f \left(\frac{\partial U_{d,2i}}{\partial x_j}A_j\right)_f = -\left(U_{d,2i}S_{Q_2} + S_{U_{d,2i}}\right)_P V_P \quad . \tag{142}$$

Also here the mass flux term, the diffusive term, and the source terms for the general transport Equation (131) can be written, as listed in the equations

$$\phi = U_{d,2i} \quad \text{and} \quad \psi_P = \left(Q_2 U_{d,2i}\right)_P$$

$$\dot{m}_f = \left\{Q_2\left[2U_{d,2j} - U_{d,3j} + \left(U_{d,3j} - U_{d,2j}\right)\kappa_{U_i} - U_{gr,j}\right]A_j\right\}_f$$

$$D_f = \left(Q_2 \nu_d \sigma_t\right)_f \left(\frac{\partial U_{d,2i}}{\partial x_j}A_j\right)_f \tag{143}$$

$$S_\phi^A = 0$$

$$S_\phi^V = -\left(U_{d,2i}S_{Q_2} + S_{U_{d,2i}}\right)_P V_P \quad .$$

The volumetric source term gets its contribution from S_{Q_2} due to collisions and from $S_{U_{d,2i}}$ due to the drag force, as defined in Equation (115) in section 3.4.3.1.

In an alternative approach, the third term of Equation (139) is fully integrated into the source term on the right-hand side. This leads to the transport equation for $U_{d,2i}$ in an approximated form, as shown in equations

$$\frac{d}{dt}\left(Q_2 U_{d,2i} V\right)_P + \sum_{f=1}^{n_f}\left[Q_2\left(U_{d,2j} - U_{gr,j}\right)A_j\right]_f \left(U_{d,2i}\right)_f - \sum_{f=1}^{n_f}\left(Q_2 \nu_d \sigma_t\right)_f \left(\frac{\partial U_{d,2i}}{\partial x_j}A_j\right)_f =$$

$$- \sum_{f=1}^{n_f}\left[Q_2\left(U_{d,3j} - U_{d,2j}\right)A_j\right]_f \left(U_{d,3i} - U_{d,2i}\right)_f - \left(U_{d,2i}S_{Q_2} + S_{U_{d,2i}}\right)_P V_P \quad , \tag{144}$$

and

$$\phi = U_{d,2i} \quad \text{and} \quad \psi_P = \left(Q_2 U_{d,2i}\right)_P$$

$$\dot{m}_f = \left[Q_2\left(U_{d,2j} - U_{gr,j}\right)A_j\right]_f$$

$$D_f = \left(Q_2 \nu_d \sigma_t\right)_f \left(\frac{\partial U_{d,2i}}{\partial x_j}A_j\right)_f \tag{145}$$

$$S_\phi^A = -\left[Q_2\left(U_{d,3j} - U_{d,2j}\right)A_j\right]_f \left(U_{d,3i} - U_{d,2i}\right)_f$$

$$S_\phi^V = -\left(U_{d,2i}S_{Q_2} + S_{U_{d,2i}}\right)_P V_P \quad .$$

Both approaches for the third term have been implemented and tested for simple cases. Simulations with and without the third term have been compared. However, this term can

increase the numerical diffusion, and sometimes it leads to instability of the numerical scheme. There were no problems in droplet flows with a preferred flow direction, since there the gradient of the relative velocity points more or less in the direction of the flow. In an arbitrary droplet flow field with reverse flow and vortices, the tests showed sometimes very high contributions of this term locally, which led to unreasonably high velocities $\mathbf{U}_{d,2}$, especially in regions where the surface moment Q_2 is rather small. Moving computational meshes enforce this problem. This is why the third term of Equation (139) has been neglected in the simulations presented in sections 5.2 and 5.3.

Now all additional transport equations for the moments of the droplet size distribution function are defined. They are solved together with the other conservation equations as listed in Table 4. The source terms S_{Q_2}, $S_{U_{d,2i}}$, and $S_{U_{d,3i}}$, represent the drag force and the collision effects, which have been discussed in section 3.4.3.

4.3 Blow-by

The idea of the chamber model [60] has been discussed in section 3.2. The numerical solution procedure, results for a test example, and the set-up of the boundary conditions for the CFD simulation are presented here.

4.3.1 Chamber Model

The simulation with the chamber model is separated from the CFD simulation. It is performed at the beginning of the CFD simulation to obtain the gas mass flow rate into the crankcase and it provides the boundary conditions for the complete engine cycle.

The derivative of the pressure with respect to time, as shown by Equation (59) in section 3.2.1 above, depends on the current pressures in the actual, the previous, and the subsequent chamber. Determining Equation (59) for all chambers i from $i=1$ to $i=n_{cham}$ in the model leads to a coupled system of ordinary differential equations of first order (ODE), which is solved by the classical Runge-Kutta method of 4th order. This method is often applied for physical simulations, because it is a good compromise between computational effort and accuracy [81].

In each time step the derivative of the pressure of each chamber is evaluated four times: once at the initial point, $k_{1,i}$, twice at trial midpoints, $k_{2,i}$ and $k_{3,i}$, and once at a trial endpoint, $k_{4,i}$. From these derivatives the final function value is calculated with a weighted mean derivative, as described by

$$p_i(t + \Delta t) = p_i(t) + \frac{\Delta t}{6}(k_{1,i} + 2k_{2,i} + 2k_{3,i} + k_{4,i}) \ . \tag{146}$$

The four derivatives of the pressure are calculated according to

$$
\begin{aligned}
k_{1,i} &= f\left[p_{i-1}(t), p_i(t), p_{i+1}(t)\right] \\
k_{2,i} &= f\left[p_{i-1}(t) + \frac{\Delta t}{2}k_{1,i-1}, p_i(t) + \frac{\Delta t}{2}k_{1,i}, p_{i+1}(t) + \frac{\Delta t}{2}k_{1,i+1}\right] \\
k_{3,i} &= f\left[p_{i-1}(t) + \frac{\Delta t}{2}k_{2,i-1}, p_i(t) + \frac{\Delta t}{2}k_{2,i}, p_{i+1}(t) + \frac{\Delta t}{2}k_{2,i+1}\right] \\
k_{4,i} &= f\left[p_{i-1}(t) + \Delta t\, k_{3,i-1}, p_i(t) + \Delta t\, k_{3,i}, p_{i+1}(t) + \Delta t\, k_{3,i+1}\right] \ .
\end{aligned}
\tag{147}
$$

The pressure and the temperature curves of the cylinder are boundary conditions needed for the chamber model. These curves can be obtained from measurements or from one-dimensional engine flow simulations.

Contrary to the pressure and temperature curves in the cylinder, the pressure and temperature in the crankcase are more or less constant. While the cylinder pressure changes from approximately atmospheric pressure to a peak value of 100 bar and more during combustion, the pressure in the crankcase depends on the ventilation system and varies with a few millibars around the atmospheric pressure. Hence it is reasonable to set the crankcase pressure and temperature constant. The error caused by this simplification is considered to be small.

The gas temperature in the chambers is assumed to be constant. Due to this simplification, which has already been discussed in section 3.2, the solution of additional differential equations for the temperature change in the chambers is avoided. The applied boundary conditions of the chamber model are summarised as

$$
\begin{aligned}
p_{i=0}(t) &= p_{cyl}(t) \\
T_{i=0}(t) &= T_{cyl}(t) \\
p_{i=n_{cham}+1}(t) &= p_{crnk} \approx const. \\
T_{i=n_{cham}+1}(t) &= T_{crnk} \approx const. \\
T_i &= const. \quad for \ i = 1, ..., n_{cham}.
\end{aligned}
\tag{148}
$$

Figure 35 shows the cylinder pressure and temperature curves of a passenger car Diesel engine at 3000 rpm and full load. The engine has four cylinders and is supercharged. The curves are obtained from a one-dimensional, thermodynamic engine cycle and gas dynamic simulation performed with AVL-BOOST [4]. The cylinder pressure curve shows a peak of

about 141 bar at 9 degrees crank angle after the ignition top dead centre (ITDC). The maximum mean gas temperature in the cylinder of 1794 K occurs at 27 deg CA after ITDC. These curves represent the condition in the cylinder for blow-by gas simulation.
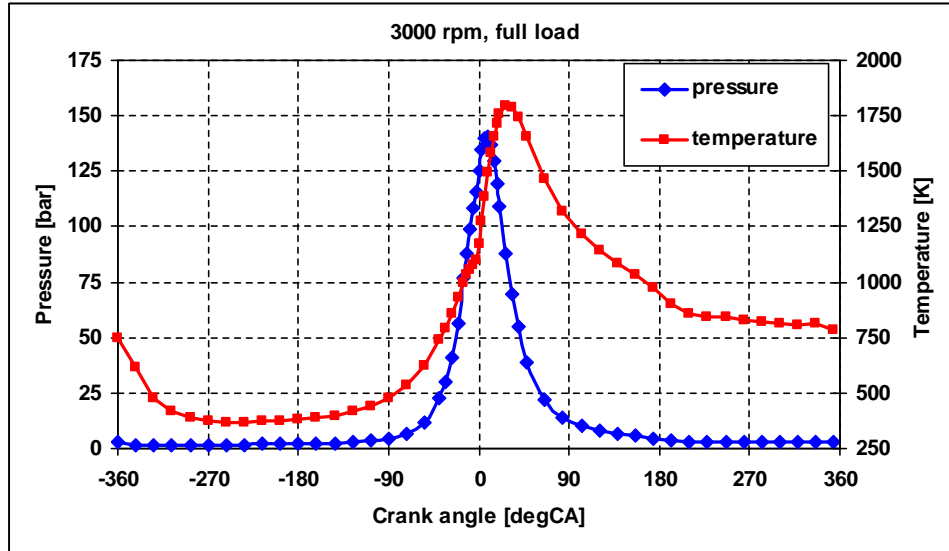
Figure 35: Mean cylinder pressure and temperature as boundary conditions of blow-by calculation

The described blow-by model constitutes a typical initial value problem. This means that, beside of the boundary conditions, the initial pressure in the chambers at starting time t_0 has to be known. From this initial condition, the chamber model simulation starts. It is performed over the complete engine cycle delivering the pressure in the chambers and the gas mass flow rate into the crankcase. In general the pressures in the chambers at t_0 are not known. So which initial conditions can be applied?

The answer is simple. The engine cycle is a periodic process. This means that, in a four-stroke engine, running in steady mode, the cylinder pressure and temperature are reproduced every 720 deg CA. Thus, the pressure curves in the chambers also return every engine cycle. So it is appropriate to start the blow-by simulation with arbitrary pressure values in the chambers and to perform it for a certain number of engine cycles until the difference in the pressure curves from one cycle to the other is negligible. Then the simulation is converged and the blow-by gas mass flow rate can be obtained from the last cycle of the simulation. In the simulations presented in this thesis, the convergence has been controlled by the integral value of the gas mass flow rate into the crankcase. Between five and ten engine cycles are necessary to achieve a converged cycle. The chamber pressure in those simulations was initialised with the crankcase pressure, as described by

$$p_i(t=0) = p_{crnk} \qquad for \quad i = 1,...,n_{cham}.$$ (149)

With the converged cycle of the blow-by simulation, the averaged gas mass flow rate into the crankcase is determined by

$$\dot{m}_c = \dot{m}_{blow-by} = \frac{\sum_0^{n_{dat}} \dot{m}_{i-1,i}\Delta t}{t_{cycl}} \qquad with \quad t_{cycl} = \frac{4\pi}{\omega} = \frac{120}{n}.$$ (150)

$\dot{m}_{blow-by}$ results from the integration of the mass flow rate through any piston ring, $\dot{m}_{i-1,i}$, over one complete engine cycle and the division by the time needed for an engine cycle t_{cycl}, which is written here for a four-stroke engine. n_{dat} is the number of time steps per engine cycle, n denotes the rotational speed of the engine in revolutions per minute [rpm] and the index c stands for the continuous phase. The volume flow rate of the blow-by gas into the crankcase is then simply obtained by the equation

$$\dot{V}_{blow-by} = \frac{\dot{m}_{blow-by}}{\rho_c}.$$ (151)

ρ_c is the density of the crankcase gas. Engineers often use litres per minute as the dimension for the amount of blow-by gas leaking into the crankcase. To obtain $\dot{V}_{blow-by}$ in [l/min] for one cylinder, the result of Equation (151) in [kg/s] has to be multiplied by 60 000. The blow-by volume flow rate of the entire engine into the crankcase is obtained after further multiplication of $\dot{V}_{blow-by}$ with the number of cylinders.

For comparison of different operation points and different engine types, it is useful to define the percental blow-by flow rate as

$$R_{blow-by} = \frac{\dot{m}_{blow-by}}{\dot{m}_{discharge}} = \frac{\dot{m}_{blow-by}}{\frac{V_{cyl}\rho_c}{t_{cycl}}\lambda_l} = \frac{4\,\dot{m}_{blow-by}\,t_{cycl}}{d_{cyl}^2\,\pi\,s\rho_c\lambda_l}.$$ (152)

$R_{blow-by}$ is the ratio between the blow-by mass flow rate and the discharge mass flow rate $\dot{m}_{discharge}$ of the cylinder. The latter is defined by the volumetric efficiency λ_l of the engine and the theoretical swept-volume mass flow rate, which is determined by the cubic capacity V_{cyl} of the cylinder, the gas density ρ_c, and the time t_{cycl}.

The chamber model is evaluated in a test example, presented here. The operation conditions and the set-up are listed in Table 5.

General calculation data	Engine speed n	3000	rpm
	Load	100 (full)	%
	Number of piston rings (including oil control ring	3	-
	Number of chambers	2	-
	Bore d_{cyl}	0,09	m
	Stroke s	0,08	m
	Averaged crankcase pressure p	100 000	Pa
	Averaged crankcase temperature T	373	K
	Gas constant (crankcase gas) R	287	J/(kgK)
	Adiabatic exponent κ	1.4	-
Chamber data	Volume chamber 1 V_1	$1.12 \cdot 10^{-6}$	m³
	Volume chamber 2 V_2	$1.01 \cdot 10^{-6}$	m³
	Temperature chamber 1 T_1	473.15	K
	Temperature chamber 2 T_2	453.15	K
Ring data	Effective flow area Ring 1 $K_c A_1$	$1.922 \cdot 10^{-7}$	m²
	Effective flow area Ring 2 $K_c A_2$	$1.922 \cdot 10^{-7}$	m²
	Effective flow area Ring 3 $K_c A_3$	$1.922 \cdot 10^{-7}$	m²

Table 5: Set-up of blow-by test example for a supercharged passenger car Diesel engine

The engine evaluated in these studies is a supercharged passenger car Diesel engine and runs at 3000 rpm. Three rings, i.e. two piston rings and an oil control ring constitute two chambers for the blow-by simulation. The applied cylinder pressure and cylinder temperature curves have been illustrated in Figure 35.

The simulation of several engine cycles is necessary to achieve a converged solution. In the presented test example, ten engine cycles have been performed. Figure 36 shows the evolution of the chamber pressure (top) and the gas mass flow rate via the rings (bottom) of the first four cycles from 0 to 2880 deg CA. Cylinder and crankcase pressures are given, the chamber pressures p_1 and p_2 are calculated. According to Equation (149) the chamber pressures are initialised with the crankcase pressure. One can see the evolution of the chamber pressures from the initial pressure of one bar.
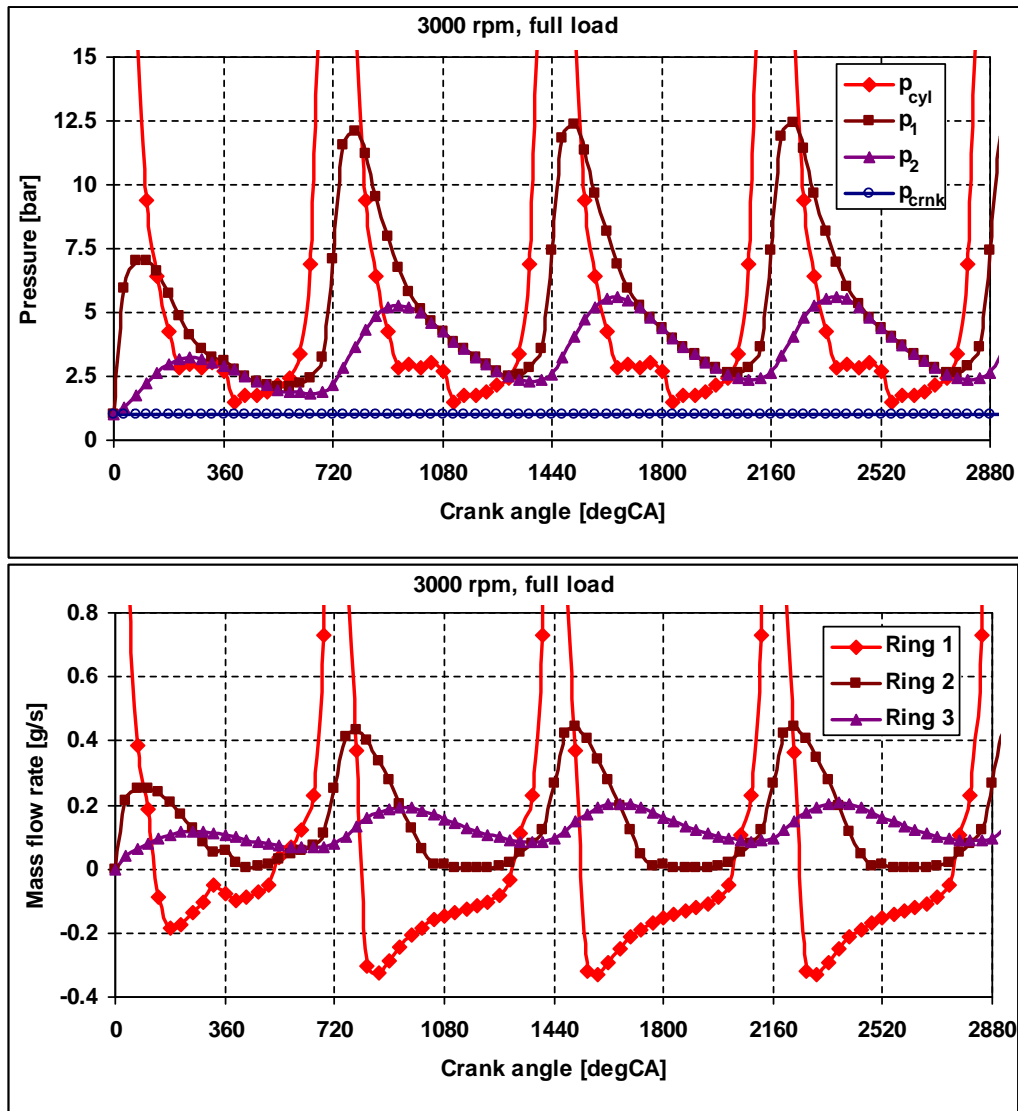
Figure 36: Evolution of chamber pressures (top) and evolution of the mass flow rate via piston rings (bottom)

In the first and second chambers maximum pressures of about 12.5 bar and 6 bar, respectively are reached. After three cycles, the observed change of the pressure curves seems small. The integral blow-by mass flow rate was used as the convergence criterion. Between the ninth and tenth cycles the relative change of the integral blow-by mass flow rate was less than 0.1 percent. The evolution of the mass flow rate curves goes similar to the pressure curves. Due to the initialisation of the chamber pressure with atmospheric pressure, the gas mass flow rate through the second and third rings is zero at t_0. In Figure 36 bottom, the peaks of the mass flow rate curve through ring 1 were cut to have a better illustration. The peak reaches a positive mass flow rate of about 3 g/s. It is also remarkable that the gas mass flow rate curve via ring 1 is alternating between positive and negative values. Its amplitude is much higher than the amplitude of the curve of ring 2, which exhibits only positive values. Furthermore, the amplitude of the mass flow rate curve via ring 2 is higher

than the amplitude of the corresponding curve via ring 3. Hence it is obvious that the peaks in the pressure and mass flow rate curves are damped by the chambers.

The converged solutions of the blow-by simulation, which have been achieved after ten engine cycles, are shown in Figure 37 for the chamber pressures and in Figure 38 for the gas mass flow rates via the piston rings. It is interesting that, at about 90 deg CA, the cylinder pressure is lower than the pressure in the first chamber. From that point on, the gas mass flow rate via ring 1 is negative, which means that gas flows from chamber one back into the cylinder. In [60] this phenomenon is confirmed by measurements. Between approximately 300 and 570 deg CA, the pressures in the first and second chambers are almost equal. Hence, the mass flow rate via ring 2 is close to zero in this time interval. At about 590 deg CA, the cylinder pressure is again higher than the pressure in the first chamber. From that point on, gas again flows from the cylinder into the first chamber via ring 1.
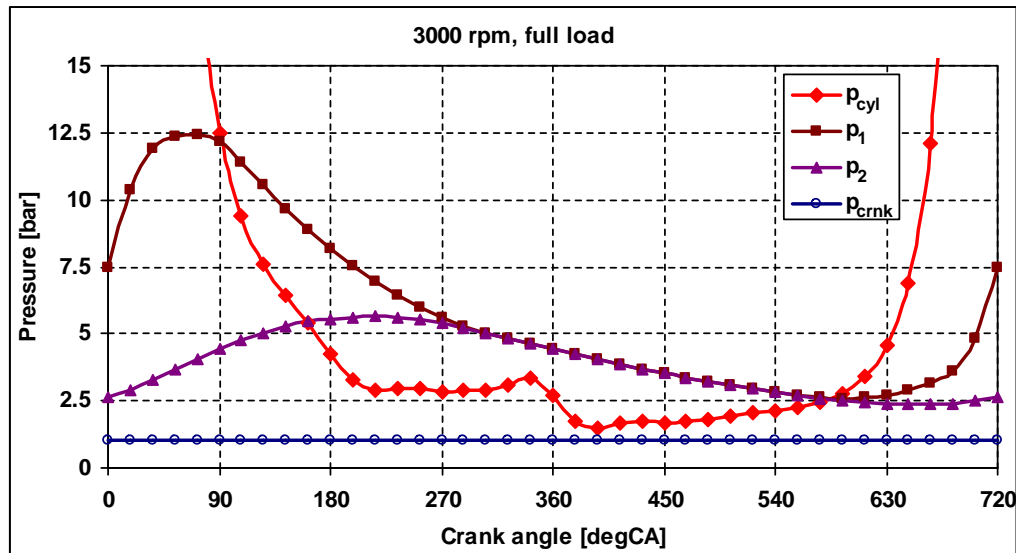
Figure 37: Pressure in chambers of converged cycle at 3000 rpm and full load

The peaks in the curve of the mass flow rate via ring 1 and in the cylinder pressure curve occur at about 8 deg CA after ITDC. The maximum mass flow rate via ring 2 occurs at 66 deg CA at a later time. The gas mass flow rate curve via ring 3 exhibits its maximum much later at 212 deg CA. This curve is the most important one, because it determines the gas mass flow rate into the crankcase, which is then used as a boundary condition for the CFD simulations. In Figure 38 this curve seems to be very smooth. Therefore, it is plotted a second time at a different scale in Figure 39. One can see that the gas mass flow rate varies between $8.683 \cdot 10^{-2}$ and 0.2063 g/s.
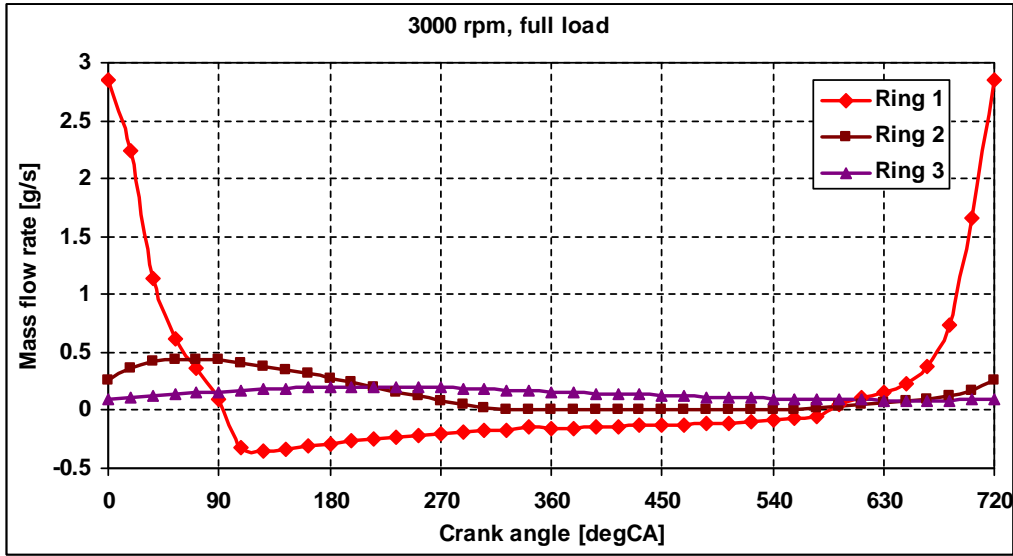
Figure 38: Gas mass flow rate via rings of converged cycle at 3000 rpm and full load
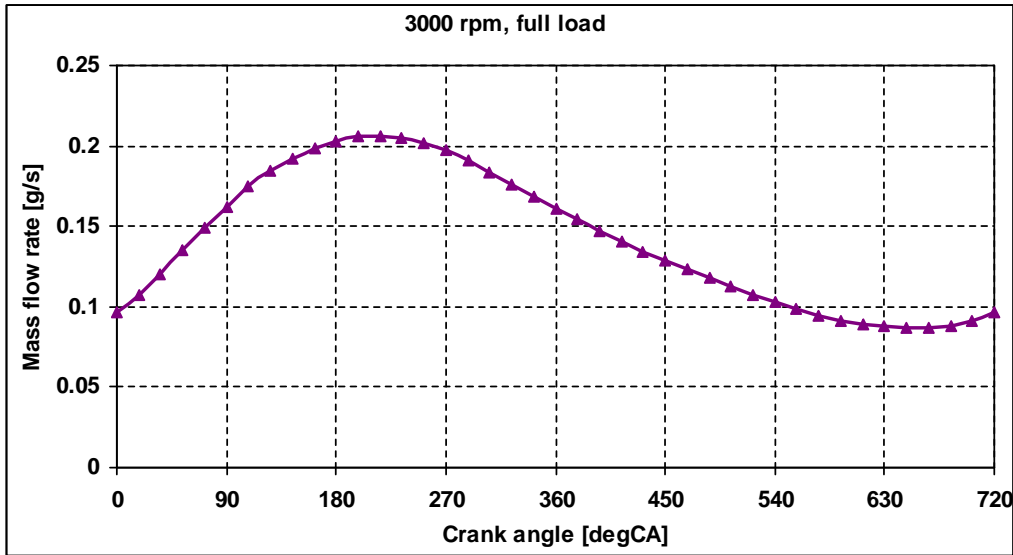
Figure 39: Gas mass flow rate via last ring into the crankcase at 3000 rpm and full load

Figure 40 shows the calculated Sauter mean diameter of the atomised droplets depending on the pressure and the temperature in the last (second) chamber. Again the engine oil OMV Truck LD SAE 15W-40 with the fluid properties shown in Figure 60 below is used for the calculation. The expected result is that the droplet diameter decreases with increasing chamber pressure, since the bigger the pressure, the bigger the gas density in the denominator of Equation (61) in section 3.2.2 above. It is interesting to observe that a bigger temperature in the chamber leads to a slightly bigger droplet Sauter mean diameter. On the one hand, an increased temperature in the chamber leads to larger gas velocities and smaller values for the liquid density and the surface tension, which would decrease the droplet diameter. On the other hand, the gas viscosity in the critical area increases and the gas

density in the denominator of Equation (61) in the critical area decreases at increasing gas temperature. The latter effects, which cause an increase of the droplet diameter, dominate in the current case.

Figure 41 shows the Sauter mean diameter of the atomised droplets over the complete engine cycle. The diameter varies between 2.3 and 4.6 μm. Considered together with Figure 37 one can observe that, the bigger the pressure in the second chamber, the smaller the droplet diameter. The minimum occurs at 212 deg CA, where the chamber pressure curve has its maximum. According to Equation (65) in section 3.2.2 above, the critical gas density is proportional to the pressure in the chamber before, because the gas temperature is assumed to be constant. Since the gas density acts in the denominator of the droplet diameter correlation in Equation (61), a higher density leads to smaller droplet diameters.

Oil mist is in general defined as the fraction of oil droplets in the crankcase with droplet diameters less than 10 μm. It is a notable result that the presented estimation of the droplet diameter delivers droplets of the "right" size. This indicates blow-by once more as a source for the small oil droplets in the crankcase. The measurements of the oil mist discussed in section 2.3 shows that the droplet diameters can be even smaller than the droplet diameter illustrated in Figure 40. This leads to the assumption that condensation effects, which are not treated in the CFD simulations of this thesis, deliver a further important fraction of small droplets in the oil mist. However, condensation has been assigned to the slow processes in the crankcase. Hence, it contributes to the oil mist over a longer time. In the simulated time covered by the CFD simulation, however, this effect can be neglected.
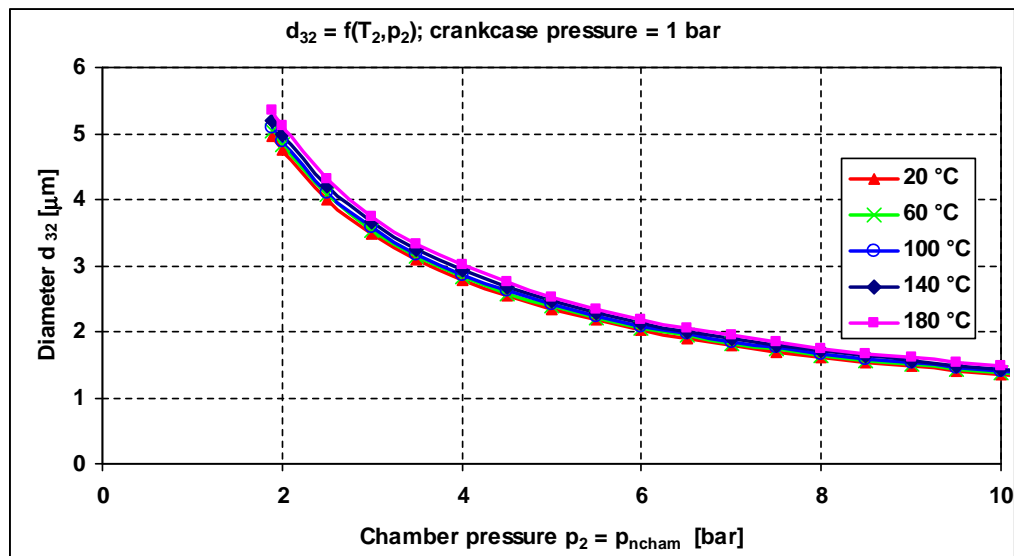
Figure 40: Droplet diameter depending on pressure p_{ncham} and the temperature T_{ncham} in the last chamber
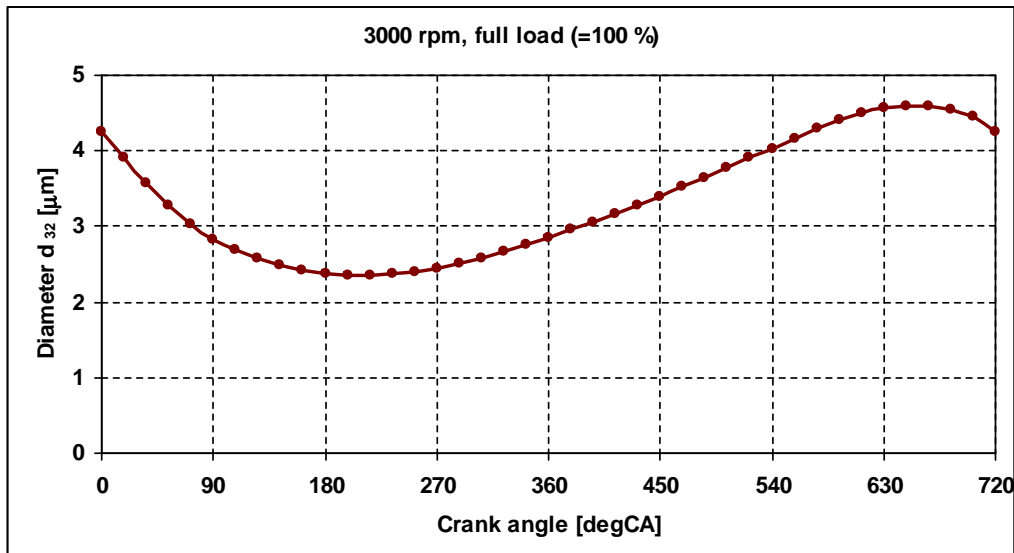
Figure 41: Droplet Sauter mean diameter of atomised droplets over the engine cycle

4.3.2 Blow-by as a CFD Boundary Condition

This section deals with the boundary conditions for the CFD simulations resulting from the blow-by model. The previous sections have delivered correlations for the gas and oil mass flow rates due to blow-by. After calculation of the required mass flow rates and the droplet diameter, this information has to be converted into CFD boundary conditions, since there are inlet velocities and volume fractions for both, the continuous gas phase and the dispersed liquid oil phase.

The piston design determines the CFD boundary regions on the computational mesh. Such a region is called selection [7], and it consists of a set of nodes or faces on the mesh. Figure 42 shows two different designs of pistons for Diesel engines. There are different ways to guide the blow-by gas into the crankcase. The piston in Figure 42 top has two piston rings and one oil control ring. From the groove of the oil control ring there are recesses at the right and the left side of the piston pin hole. The diameter of the piston is slightly reduced at the side of the piston pin to provide space for the blow-by gas, which is guided into the crankcase around the piston skirt (see Figure 42 top right). Figure 42 bottom shows an alternative piston design with three piston rings and one oil control ring. This piston has several holes connecting the groove of the oil control ring and the crankcase to guide the blow-by gas and the stripped oil into the crankcase.

A computational mesh resolving the exact geometry of the piston ring grooves, the crevice between piston and cylinder wall, as well as the recesses or bore holes for guiding the blow-by gas would require a very fine mesh resolution with an enormous number of cells. To keep the computational effort moderate, this region is not resolved by the grid, and in case of

a piston design according to Figure 42 top, the blow-by boundary conditions are applied at the end of the piston skirt. If the piston is designed similar to Figure 42 bottom, the boundary conditions would be applied at the orifices of the bore holes.

Figure 42: Blow-by gas is guided into the crankcase: around the piston skirt (top)
or through bore holes (bottom)

Figure 43 shows the blow-by inlet selection for the CFD simulation on a simplified crankcase geometry. The grid shows two quarter geometries of the cylinders. The zoomed view shows the blow-by inlet positioned at the top edge, where the piston skirt ends. This mesh illustrates the simplified piston geometry (flat piston) with the blow-by guidance corresponding to Figure 42 top. The length and width of the blow-by inlet depend on the real piston dimensions. In the current case, the width is about 0.5 mm, and the length covers a circumferential range of about 40 mm.
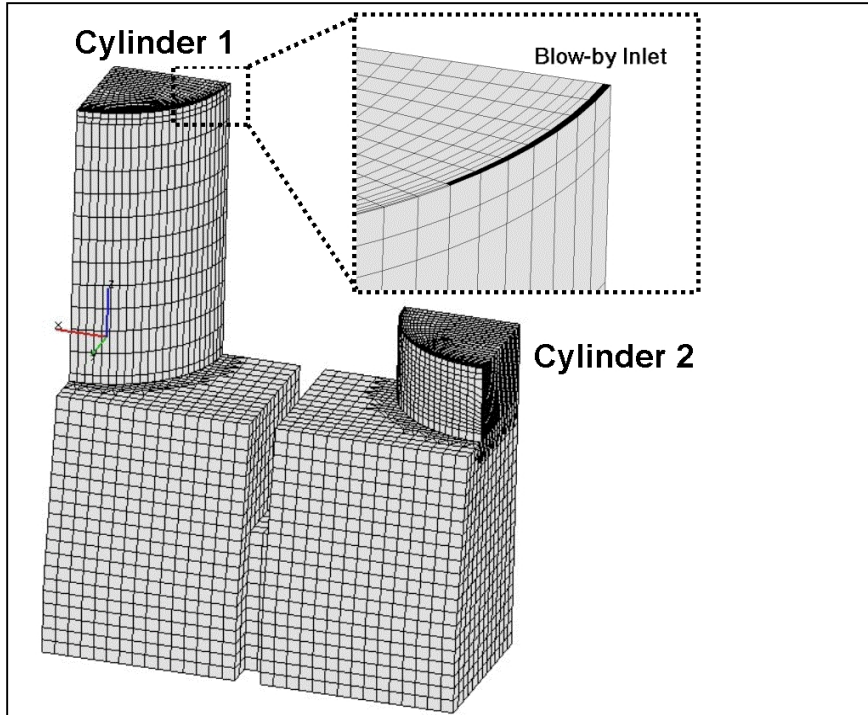
Figure 43: Boundary selection on CFD grid for blow-by inlet

The CFD boundary conditions require the set-up of the flow velocity and the phase volume fraction. The equations

$$\dot{m}_d = \rho_d A_{b,blw} \alpha_{d,b} U_{d,b} \ , \tag{153}$$

and

$$\dot{m}_c = \rho_c A_{b,blw} \alpha_{c,b} U_{c,b} \ , \tag{154}$$

determine the liquid and gaseous phase mass flow rates resulting from the blow-by model. $U_{d,b}$ and $U_{c,b}$ are the liquid and gaseous phase velocities at the boundary inlet, $\alpha_{d,b}$ and $\alpha_{c,b}$ are the liquid and gaseous volume fraction values at the boundary inlet. The compatibility condition, described by the relation

$$\alpha_{d,b} + \alpha_{c,b} = 1 \ , \tag{155}$$

has to be ensured. So there are three equations for four unknown variables $U_{d,b}$, $U_{c,b}$, $\alpha_{d,b}$ and $\alpha_{c,b}$. $A_{b,blw}$ is the entire surface area of the blow-by inlet selection, which is defined by the sum of all boundary faces of the selection, as described by the equation

$$A_{b,blw} = \sum_{b=1}^{n_b} A_b \ .$$

(156)

The diameter of the atomised oil droplets is small. Thus the ratio between drag and inertia forces is high. It can be expected that the gas and the liquid phase velocities are almost equal, $U_{d,b} \approx U_{c,b}$. With this assumption, the above system of equations from (153) to (155) can be solved easily, resulting in the boundary conditions of the relations

$$\alpha_{d,b} = \frac{1}{\dfrac{\dot{m}_c}{\dot{m}_d} \dfrac{\rho_d}{\rho_c} + 1} \quad and \quad \alpha_{c,b} = 1 - \alpha_{d,b} \ ,$$

(157)

for the volume fraction of the liquid and the gaseous phases. The boundary velocity of both phases is determined by the equation

$$U_{c,b} = U_{d,b} = \frac{\dot{m}_c}{\rho_c A_{b,blw} \alpha_{c,b}} \ .$$

(158)

If the simulation is performed with transport of the moments of the droplet size distribution, the average droplet diameter is not required, because the interfacial momentum exchange is calculated in each cell locally, as shown in Equations (114) and (115). In that case, the boundary values of the droplet volume and the droplet surface moments, $Q_{3,b}$ and $Q_{2,b}$, are determined by the equations

$$Q_{3,b} = \frac{3}{4\pi} \alpha_{d,b} \ ,$$

(159)

and

$$Q_{2,b} = \frac{Q_{3,b}}{r_{32}} = \frac{3}{2\pi} \frac{\alpha_{d,b}}{d_{32,d,b}} \ .$$

(160)

The moment $Q_{3,b}$ can be obtained directly from the liquid volume fraction at the boundary face. The surface moment $Q_{2,b}$ is determined by the droplet volume moment and the local Sauter mean radius, which is here the local droplet radius $r_{32,d,b} = d_{32,d,b}/2$.

4.3.3 Blow-by Model at Different Operation Points of the Engine

This section is about the outcome of the chamber model for the blow-by simulation at different operation points. The blow-by gas mass flow rate across the piston rings and the pressures in the chambers are evaluated at different engine speeds and loads. The set-up of the test examples is similar to the example presented in section 4.3.1 in Table 5. Only the

cylinder pressure and temperature curves, obtained from several thermodynamic engine cycle simulations with AVL-BOOST, have been exchanged for the different simulations. For the four different engine speeds of 1000, 2000, 3000 and 4000 rpm, the cylinder pressure and temperature curves at full load (100 %) and part load (25 %) are applied to the blow-by simulation. Figure 44 shows the cylinder pressure and Figure 45 shows the cylinder temperature curves of all eight operation points over a complete engine cycle from 0 to 720 deg CA.
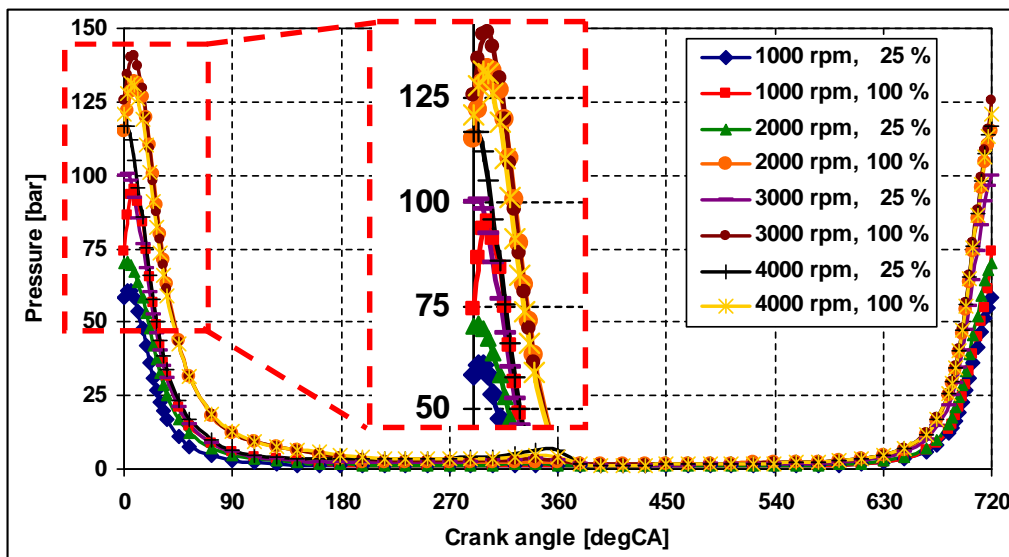
Figure 44: Cylinder pressure curves at different operation points of the engine

One can see that, at full load, the peak pressure and the maximum temperature in the cylinder are higher than at part load. The maximum pressure occurs at 3000 rpm and full load. The lowest peak pressure and also the lowest temperatures in the cylinder take place at 1000 rpm and 25 percent load. There is a doubtable peak at about 360 deg CA in the cylinder pressure curve at 4000 rpm and part load. This may result from an insufficient set-up of the turbocharger in the BOOST simulation. However, the cylinder pressure and temperature curves are not gained from measurements, they are obtained from the separate BOOST simulation and act as boundary conditions for the chamber model. Defects in the boundary conditions will surely affect the output from the blow-by model. The pressure and temperature curves during the compression and combustion stroke seem to be reliable, and they have a bigger influence on the blow-by mass flow rate into the crankcase. The variation of the engine speed and load at different operation points of a Diesel engine gives a good overview of the outcome of the applied chamber model.
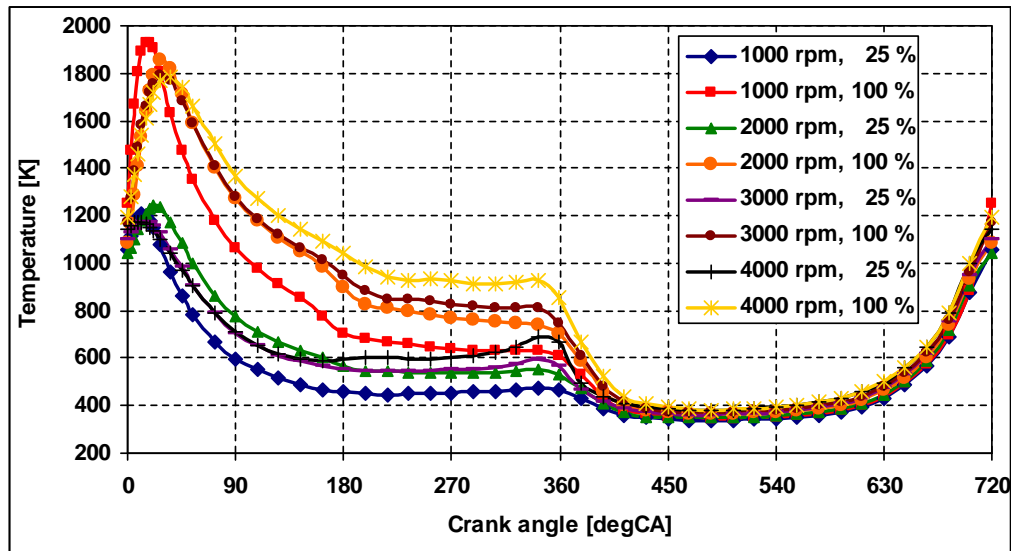
Figure 45: Cylinder temperature curves at different operation points of the engine

Figure 46 shows the pressure in the first chamber for all engine conditions considered here. It is obvious that, for the same engine speed, the peak pressures at full load are always higher than at part load. The highest peak pressure is about 15.7 bar at 57 deg CA and occurs at 2000 rpm and full load. This may be surprising, since the highest cylinder peak pressure of all eight operation points occurs at 3000 rpm and full load. At that point, the peak pressure in chamber 1 reaches only 12.4 bar at 66 deg CA. This results from the fact that, at 3000 rpm, the time needed for the pressure increase in the chamber is shorter than at 2000 rpm. The chamber pressure is a function of the time, and it depends on the incoming and outgoing mass flow rate, which consequently depends on the upstream and downstream chamber pressures. One has to take into account that, due to the different engine speeds, the pressure changes occur at different time scales. The longer there is a high pressure level in the upstream chamber, the longer is the time available for the pressure increase in the downstream chamber. Hence, at low engine speed, the time for the pressure increase in the chamber to follow the pressure in the upstream chamber is longer than at high engine speed. However, at 1000 rpm and full load, the peak pressure in the cylinder is much lower than at 2000 rpm and 3000 rpm and full load. Thus, the peak pressure in chamber 1 at 1000 rpm is even lower than the corresponding peak pressure at 2000 rpm and full load.

Figure 47 shows the pressure curves of the second chamber over the engine cycle. The higher the engine speed, the smoother the pressure curve, since the time for pressure increase and decrease is lower at high engine speed. The maximum peak pressures in chamber 2 of about 7 bar occur at 1000 and 2000 rpm and full load.
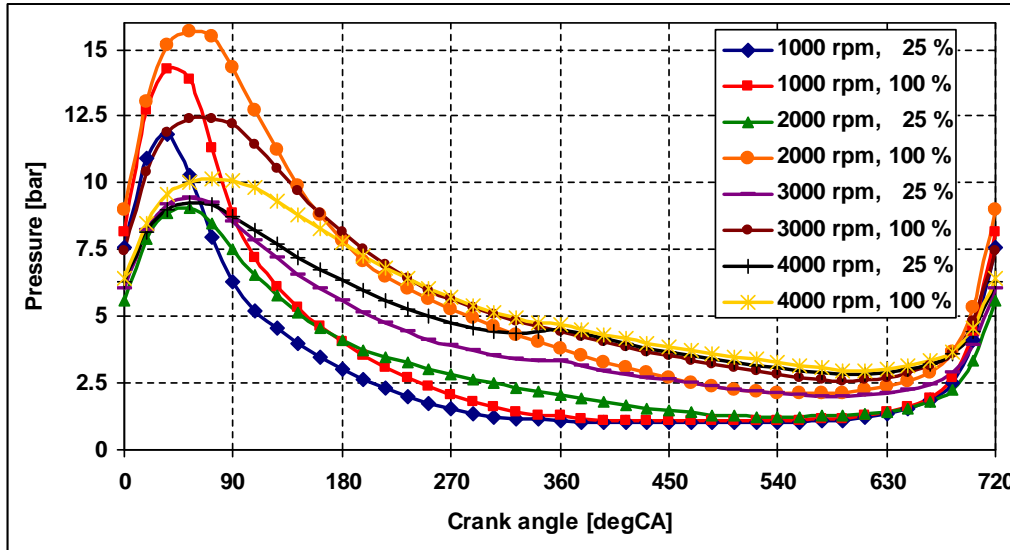
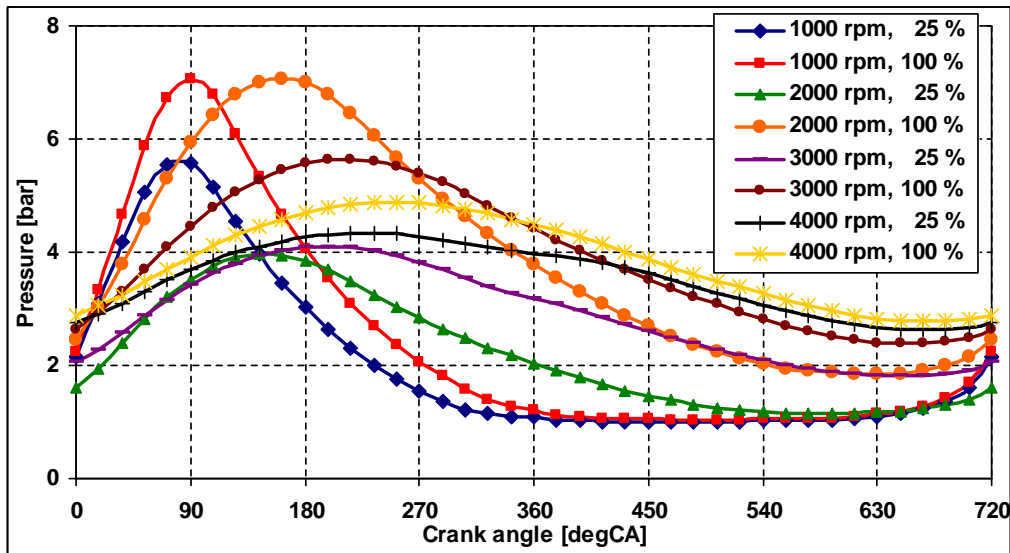Figure 46: Pressure in first chamber at different operation points of the engine

Figure 47: Pressure in second chamber at different operation points of the engine

Figures 48 and 49 show the curves of the gas mass flow rates via the first and the second piston rings. The mass flow rate via ring 1 goes in both directions and assumes positive or negative values. If the gas mass flow rate is negative, the gas flows from chamber one back to the cylinder. The maximum mass flow rates via ring 1 reach values between 2.5 and 3 g/s. They occur at the full load operation points with the engine speeds of 2000, 3000 and 4000 rpm. The highest negative mass flow rate is about -0.4 kg/s.

The mass flow rate via ring 2 in Figure 49 is always positive and exhibits maximum values up to 0.55 g/s. The cylinder pressure peak at 360 deg CA of the curve at 4000 rpm and part load causes also peaks in the mass flow rate curves. One can detect that, after a certain time,

the mass flow rates via ring 2 decrease to very small values for all operation points. This indicates that then the pressures in chambers 1 and 2 are almost equal.
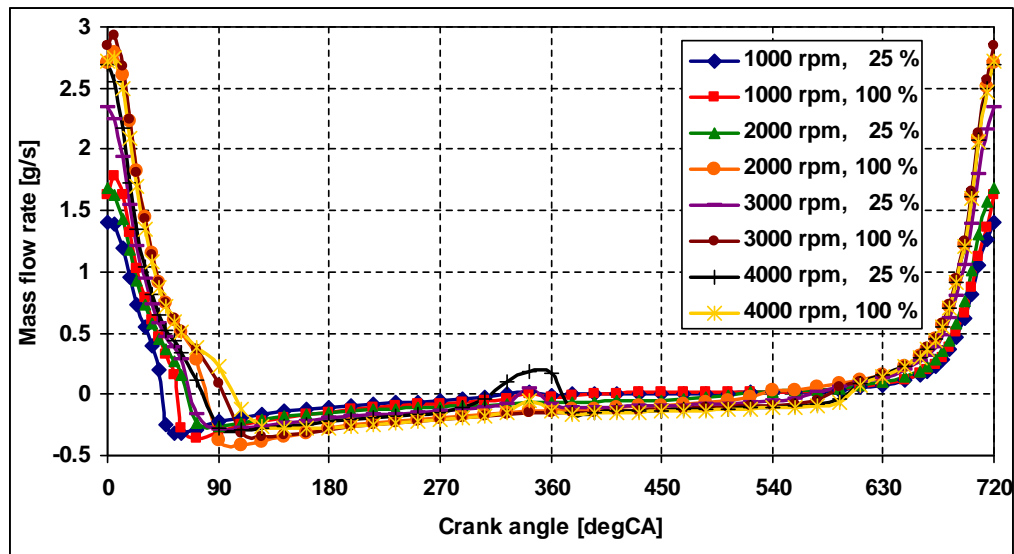
Figure 48: Gas mass flow rate via first ring at different operation points of the engine
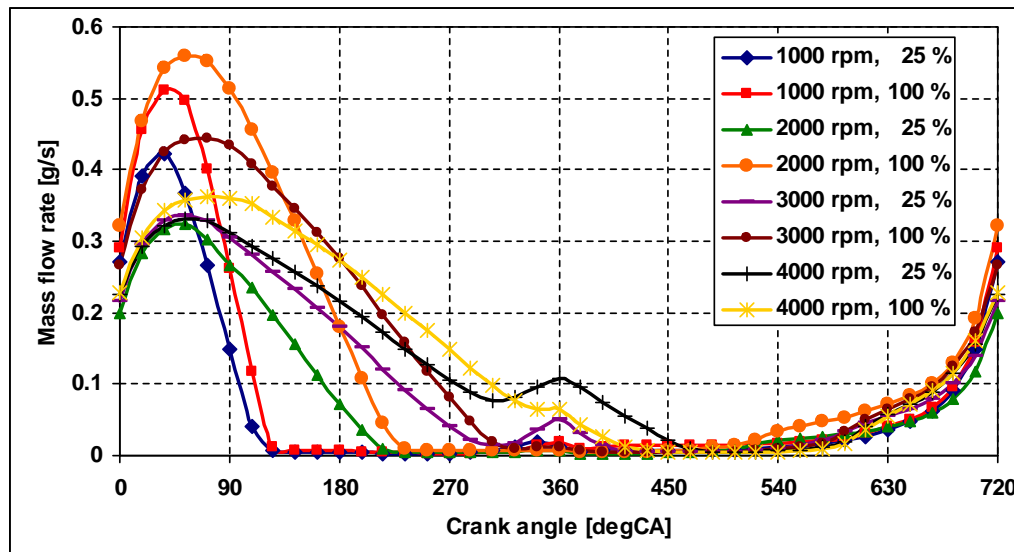
Figure 49: Gas mass flow rate via second ring at different operation points of the engine

The curves of the gas mass flow rates into the crankcase are shown in Figure 50. All eight operation points show curves with a more or less smooth shape, with one maximum and one minimum. Since the pressure in the crankcase is assumed to be the constant ambient pressure, the curves are similar to the pressure curves of chamber 2 illustrated in Figure 47. The operation point at 2000 rpm and part load yields the lowest peaks in the blow-by flow rate curves. The operation points at 1000 and 2000 rpm and full load show the highest peaks in the blow-by mass flow rate curves, followed by the points at 3000 rpm full load and

1000 rpm part load. The operation points at 4000 rpm show the smoothest mass flow rate curves, since there are the shortest times for the pressure increase and decrease in the chambers.
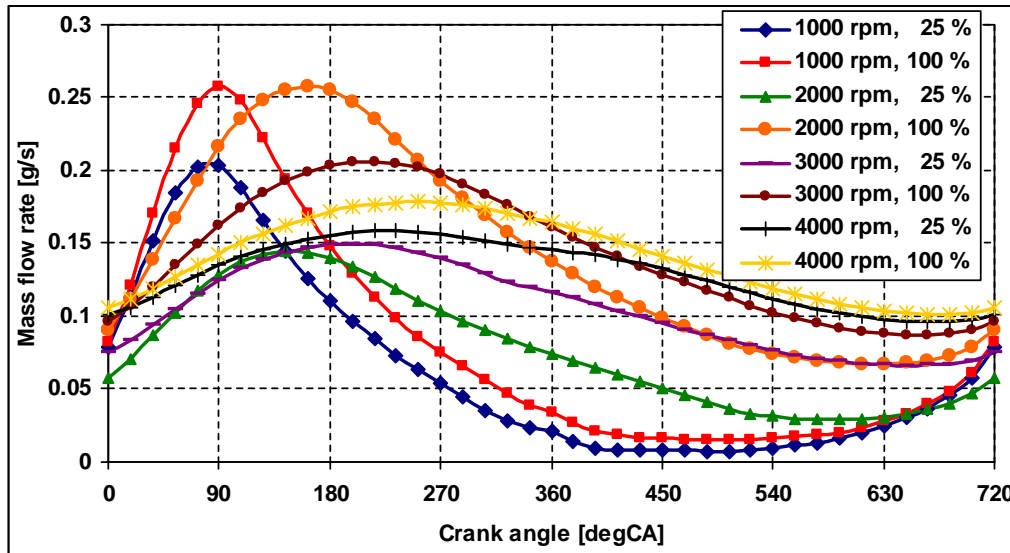
Figure 50: Gas mass flow rate via third ring into the crankcase at different operation points of the engine

Figure 51 shows the pressure ratio curves between the crankcase pressure and the pressure in the last chamber. This graph illustrates that, over the major part of the engine cycle, the pressure ratio is smaller than the critical value of 0.528. Only for the two operation points at 1000 rpm, the time with sub-critical pressure ratio is longer than the time with supercritical pressure ratio. At 2000 rpm part load, the pressure ratio is supercritical over approximately half the engine cycle. At 2000 rpm full load and 3000 rpm part load the pressure ratio is supercritical over almost the complete engine cycle, and at 3000 rpm full load, and the two operation points at 4000 rpm, the pressure ratio is supercritical over the complete engine cycle. This analysis shows once more that, except for very low engine speeds, the application of speed of sound as the dominant atomisation velocity in Equation (61) is reasonable.

Figure 52 shows the curves of the Sauter mean diameter of the atomised droplets over the complete engine cycle for the different operation points. Considered together with Figure 47, one can say that, the higher the pressure in the second chamber, the smaller the droplet diameter. The smallest droplet diameters of approximately 2.0 µm are obtained at 1000 and 2000 rpm and full load. The curve at 1000 rpm and part load shows the biggest droplet diameter with 8.9 µm. If one considers the Sauter mean diameter averaged over the complete engine cycle, it is obvious that, the higher the engine speed, the lower the mean value of the Sauter mean diameter. From this point of view, the operation point at 1000 rpm and part load produces the biggest atomised droplets during one engine cycle. On the other hand, the

operation point at 4000 rpm and full load produces the smallest atomised droplets. To sum up, Figure 52 shows clearly that the oil atomisation due to the blow-by gas jets produces oil mist, since the Sauter mean diameter of all atomised droplets at all considered operation points of the engine is always less than 10 μm.
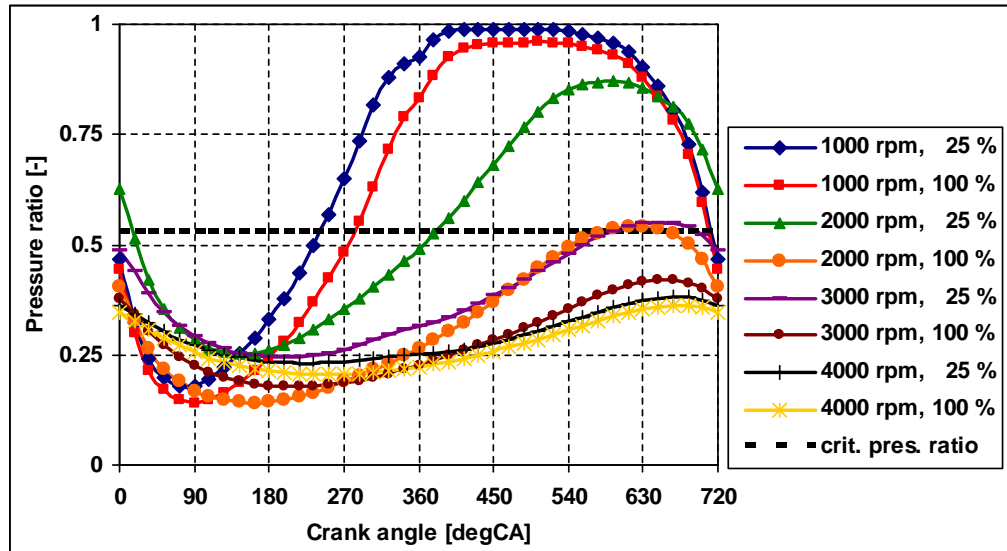

Figure 51: Ratio between crankcase pressure and pressure in the last but one chamber p_{crnk}/p_2 at different operation points
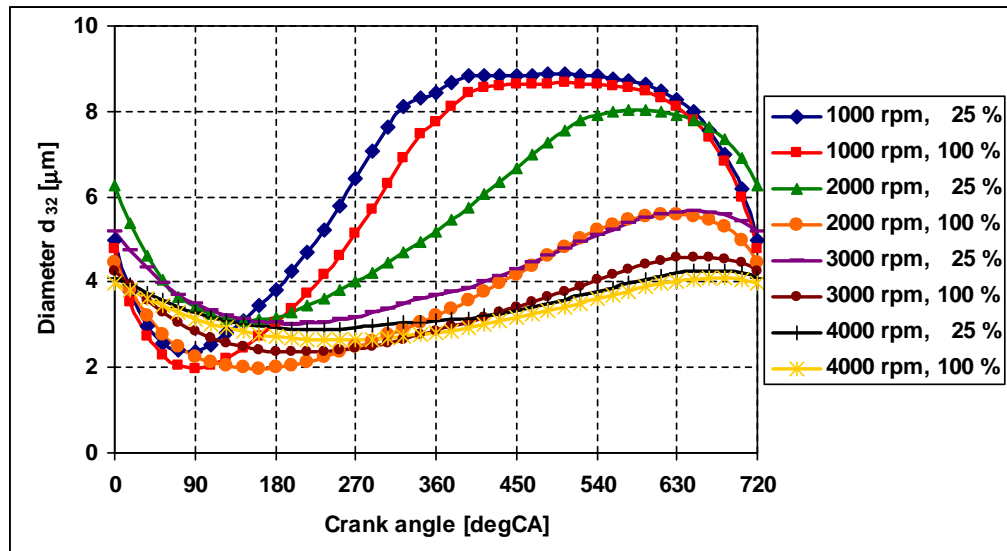

Figure 52: Droplet Sauter mean diameter of atomised droplets over the engine cycle at different operation points

Figure 53 shows the mean blow-by volume flow rate of one cylinder for all operation points. While at full load the blow-by is almost constant at 2000, 3000 and 4000 rpm, there is an increase with the engine speed of the blow-by volume flow rate at part load. The

maximum blow-by volume flow rate is 9.16 l/min and occurs at 3000 rpm and full load. This means that the entire Diesel engine with four cylinders has a blow-by volume flow rate of 36.64 l/min, which is a high, but reasonable value.
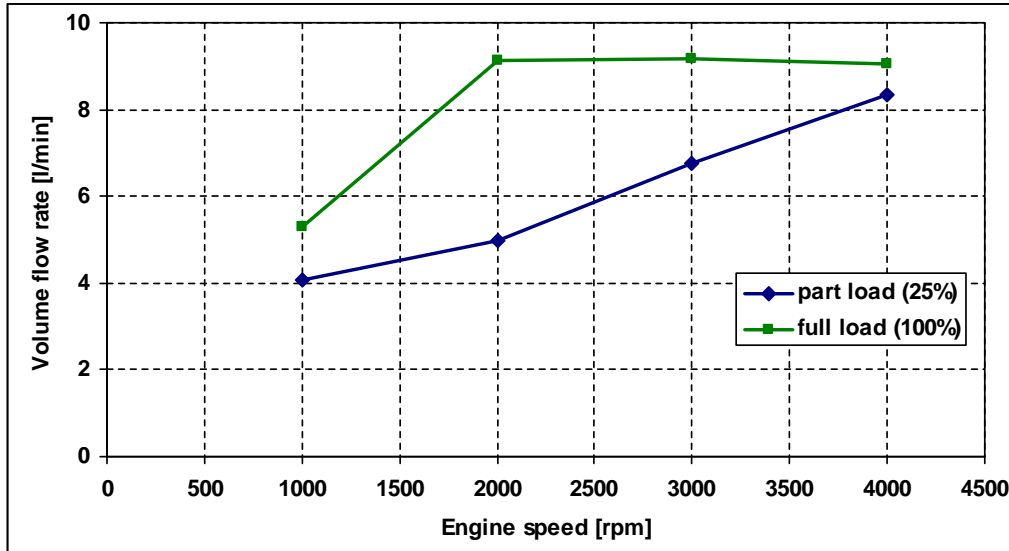
Figure 53: Blow-by volume flow rate at different operation points of the engine

Figure 54 shows the percental blow-by volume flow rate according to Equation (152) of section 4.3.1 for all eight operation points. There was no information available about the volumetric efficiency of the engine, and hence λ_l was simply set to one. This means that there is equal gas exchange in the cylinder for all engine speeds, even at full load and at part load. This is not realistic, because at low engine speed the turbocharger provides less volumetric efficiency than at high engine speed. But for comparing the outcome of the chamber model at the different engine data points, this simplification is acceptable.

As it is expected the blow-by volume flow rate percentage (= ratio of blow-by volume flow rate and total volume flow rate through the intake manifold or the exhaust pipe) is high at low engine speed and low at high engine speed. At high engine speed, the gas mass, which passes the engine, is higher than at low engine speed. Thus the blow-by flow rate percentage is lower there. Full load produces more blow-by gas than part load, since the pressure level in the cylinder is higher at full load.

The analysis of the chamber model simulations at the different operation points of the engine has shown that this model is able to deliver reasonable results for the blow-by mass flow rates. The integral blow-by volume flow rate is often measured on engine test beds. This integral value can be used for validation of the chamber model in real engine applications. The chamber volumes and the flow area between the chambers have to be

adjusted to obtain agreement with the measured mean value of the blow-by volume flow rate. Furthermore, this analysis has shown that both the engine load and the engine speed have significant influence on the amount of blow-by gas entering the crankcase. The CFD simulation of section 5.2 below will show the propagation of the blow-by gas and the oil mist in a simplified crankcase geometry. The blow-by model, including the simulation of the gas mass flow rate entering the crankcase, the estimation of the oil mass flow rate, and the droplet diameter of the oil mist yields the important boundary conditions for such CFD simulations.
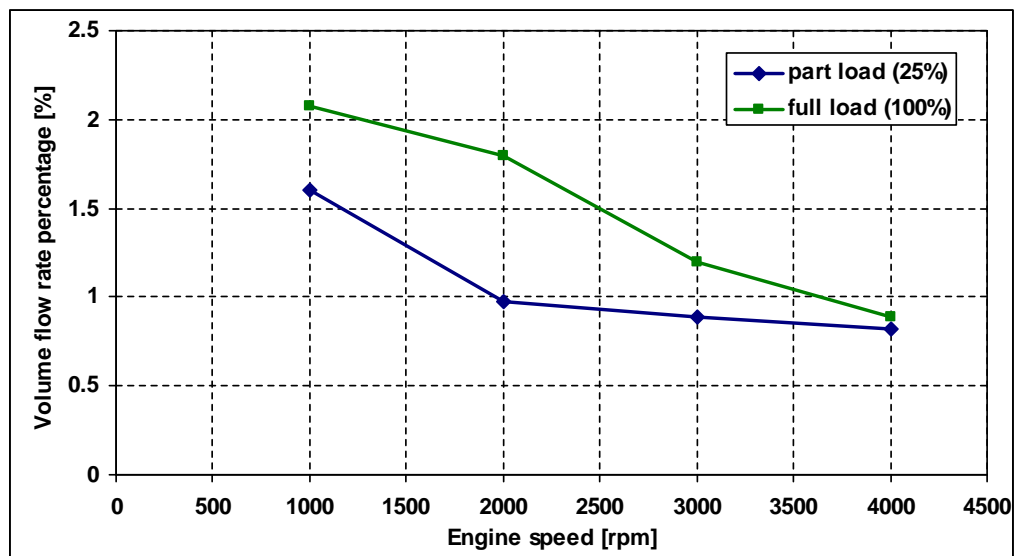
Figure 54: Volume flow rate percentage at different operation points of the engine

4.4 Oil Disintegration at the Rotating Crankweb

The liquid oil, which has passed the crankshaft and conrod bearings, flows over the surfaces of the moving crank drive, detaches from there and disintegrates into oil droplets. This process is the cause for the large oil droplets and splash oil in the crankcase. Section 3.3 describes this process by using the analogy to rotary atomisers. The present section proposes a model based on correlations from the literature for the liquid disintegration, and the droplet formation from the crankweb with respect to the application in a CFD simulation.

Figure 55 shows the crank drive of a 1-cylinder research engine on the test bed. On the left side one can see an observation window in the crankcase wall. The piston is near the top dead centre (TDC), and hence the conrod is almost in its top position. The figure on the right-hand side shows a zoomed view of the crank drive near the bottom dead centre (BDC). One can see the more or less sharp edges along the crankweb, from where the oil detaches. However, there is also oil detaching from the conrod, the housing of the conrod bearing

shell, and other points of the crank drive. This study only treats the liquid oil disintegration from the crankweb edge, where the analogy to rotary atomisers is applied. The base of this analogy is the assumption that the major fraction of oil, which has passed the bearings, disintegrates at these sharp edges of the crankweb.
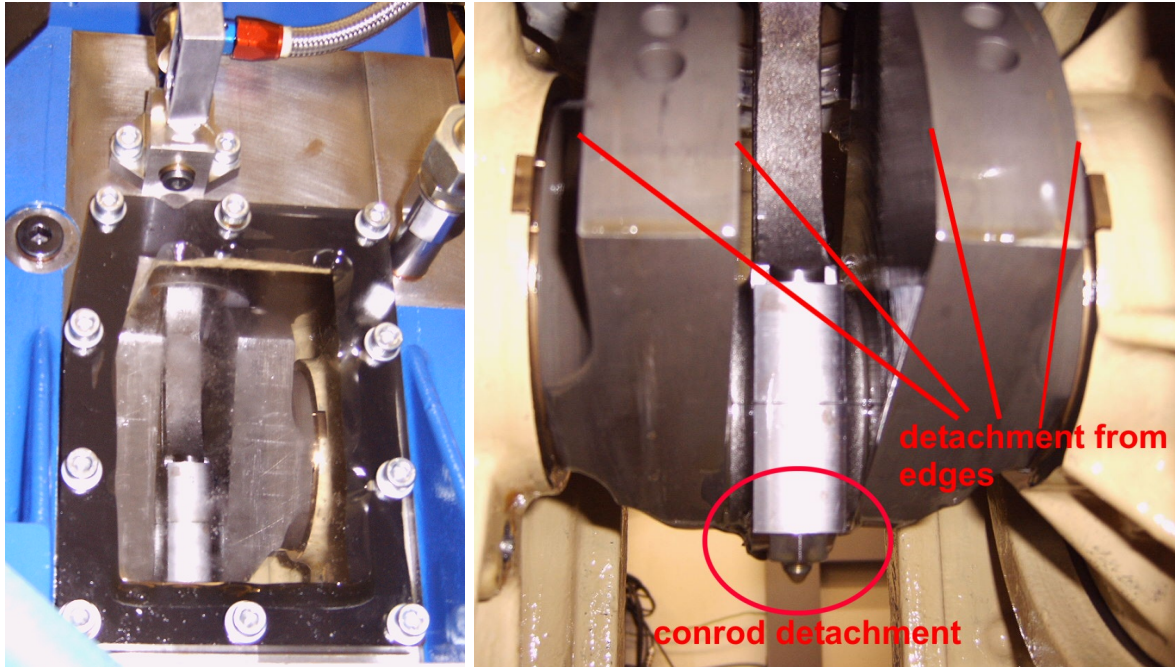

Figure 55: Crank drive of 1-cylinder engine on test bed

Figure 56 confirms the above assumption. Figure 56 left shows the engine running at 1000 rpm, while Figure 56 right shows the engine at 2000 rpm. The oil splashes onto the window. The higher the engine speed, the more splash oil is visible. In particular view one can detect a higher splash oil concentration on the windows along the fictitious prolongation of the crankweb surface. Along two vertical lines there is more splash oil visible than elsewhere. This effect can be observed more clearly at lower engine speed. At higher engine speed the droplet detachment from other sources is superposed to the disintegration at the crankweb edges resulting in a more diffuse image of the splash oil on the crankcase window.
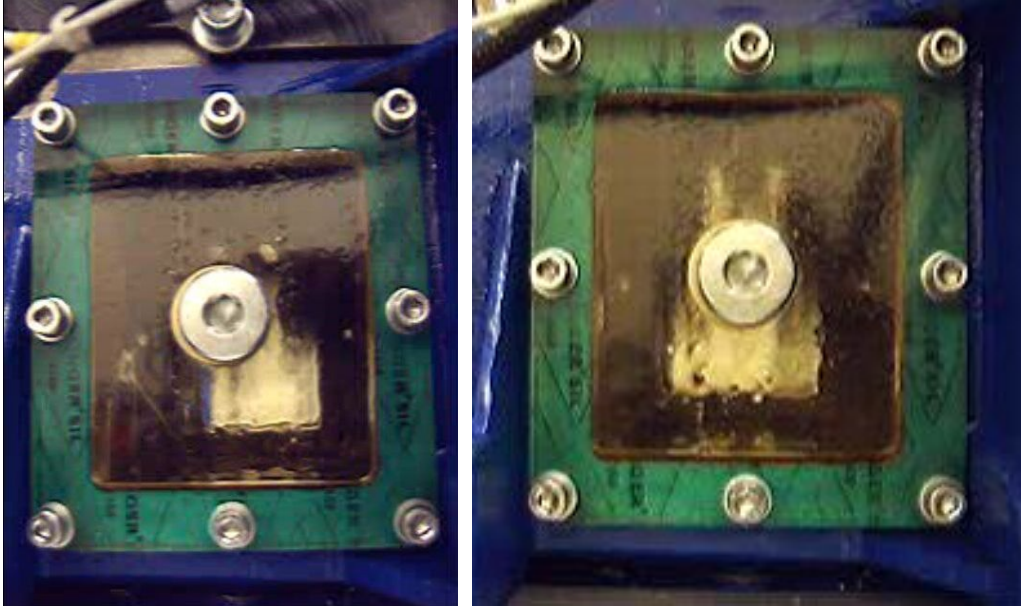
Figure 56: View into crankcase of running engine at 1000 and 2000 rpm

4.4.1 Oil Disintegration at the Crankweb as a CFD Boundary Condition

This section describes the model for the CFD simulation of the oil disintegration at the crankweb. The film flow on the crankweb surface is not simulated, because this would require a very fine resolution of the computational mesh leading to unreasonably high simulation times. Hence, the CFD simulation starts at the edge of the crankweb by determination of the boundary conditions for an inlet selection from the rotary atomiser model. The liquid phase velocity of the detached oil, the volume fraction, the moments of the distribution in case of transport of the droplet size distribution, and the mean droplet diameter for determination of the interfacial momentum exchange are the boundary conditions of interest. In a first step, the oil disintegration from the circular discs is dealt with. Then the model deals with the oil disintegration from a real crankweb geometry with constant volume flow rate over the disc. In the last step, the volume flow rate for the oil disintegration is a function of the angular position.

4.4.1.1 Oil Disintegration at the Circular Disc

The oil disintegration on a fully circular disc is the elementary case for simulation. The disintegration regime and the mean droplet diameter have to be determined with the correlations discussed in sections 3.3.2 and 3.3.3. The determination of the velocity and the volume fraction of the liquid phase at the CFD boundary are discussed here.

The detachment velocity of the liquid phase $\mathbf{U}_{d,b}$, as described by the equation

$$\mathbf{U}_{d,b} = U_r \mathbf{e}_r + U_t \mathbf{e}_t \ , \tag{161}$$

is a combination of the radial velocity component U_r and the tangential component U_t. Subscript d represents the dispersed liquid phase, and subscript b stands for the value at the CFD boundary. The tangential velocity component is simply determined by the circumferential velocity at the disc edge, as described by the equation

$$U_t = \frac{1}{2} d_{disc} \omega = d_{disc} \frac{\mathrm{n}\pi}{60} \ . \tag{162}$$

The determination of the radial velocity component is more complex. The oil forms a liquid rim along the disc edge. The diameter of this rim depends on the balance between centrifugal forces and surface tension forces. From this rim, the liquid detaches in form of droplets or ligaments, depending on the disintegration regime. At ligament disintegration, there are regular ligaments distributed with constant distance along the disc edge. Figure 57 illustrates the liquid disintegration with uniform distance l_{lig} between the ligaments. According to the assumption in [44], where the formation of the ligament has been analysed, the ligament diameter d_0 is equal to the rim thickness a. The number of ligaments n_{lig} is determined by the distance between the ligaments and the disc diameter.
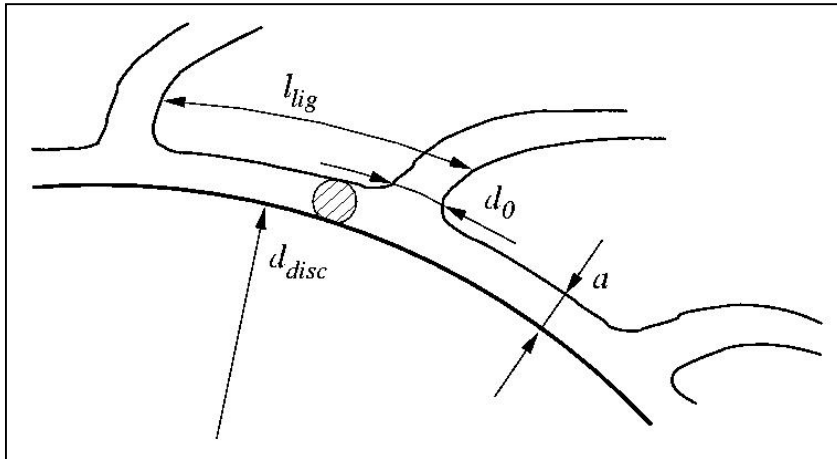

Figure 57: Ligament disintegration at a counter clock-wise rotating disc

Applying $n_{lig} = d_{disc} \pi / l_{lig}$ and $d_0 \approx a$ for the equation of the volume flow rate leads to the equation

$$\overset{\scriptstyle\text{o}}{V} = n_{lig} \frac{d_0^2 \pi}{4} U_r = n_{lig} \frac{a^2 \pi}{4} U_r \ . \tag{163}$$

Equation (163) can be transformed into an expression for the radial velocity component according to [44], which reads

$$U_r = \frac{4\,\dot{V}\,l_{lig}}{a^2 \pi^2 d_{disc}} \quad.$$ (164)

The ligament distance and the rim thickness are quoted in the equations

$$l_{lig} = a\pi \left(2 + \frac{6\,\mu_d}{\sqrt{\sigma\,\rho_d\,a}} \right)^{\frac{1}{2}} \quad and \quad a = \left(\frac{2\,\sigma}{r_{bn}\,\rho_d\,\omega^2} \right)^{\frac{1}{2}} ,$$ (165)

similar to the Equations (71) and (67) in section 3.3. r_{bn} is the radial location of the point of detachment, which is here the disc radius $d_{disc}/2$.

In the strict sense, Equation (164) is only valid for the ligament disintegration regime. However, due to the following reasons, Equation (164) is also applied for dropwise and sheet disintegration. Figure 22 in section 3.3 shows the processes for the three disintegration regimes. One can see that the distances between the points from where the droplets detach at dropwise disintegration, and the distances between the ligaments for ligament disintegration regime, are similar. This is reasonable because the formation process is the same. In [44] it is assumed that disturbances on the surface of the liquid rim grow, and furthermore they lead to the detachment of the ligaments or droplets. The distance between the ligaments results from a linear stability analysis and determines the wavelength of the fastest growing disturbance on the rim, which is simplified as a liquid ring with thickness a. Hence, there is a good reason to apply the correlation for the radial detachment velocity component U_r also for the dropwise disintegration regime. At sheet disintegration, the liquid rim itself detaches from the edge and disintegrates into the droplets, as shown in Figure 22 right. It is difficult to say if the growing disturbances on the detached liquid rim become important for the radial velocity component U_r. Perhaps in that case the radial component of the wall film velocity at the edge, directly before detachment, is the dominant velocity component. For simplicity, Equation (164) is also applied for sheet disintegration. One should keep in mind that this equation is a good representation of U_r for dropwise and ligament disintegration, but it may not be the best choice for sheet disintegration.

The calculation of the liquid volume fraction can be performed with the equations of the following section, because the disintegration on the fully circular disc is a special case of the disintegration on the real crankweb discussed there.

4.4.1.2   Oil Disintegration at the Crankweb with Constant Volume Flow Rate

A real crankweb is not a circular disc, but it contains at least parts of a disc. Thus the radial dimension of the crankweb edge is a function of the angular position $r_{bn} = r_{bn}(\varphi)$. Along with the analogy to the rotary atomiser, it is assumed that the oil flows uniformly over the crankwebs surface. This means that the volume flow rate is constant in circumferential direction, $d\dot{V}/d\varphi = 0$.

Figure 58 shows half of a single cylinder crankshaft consisting of the massive crankweb, the main bearing pin, and the conrod bearing pin. The computational mesh of the CFD simulation covers this crankshaft. At one side of the crankweb there is a boundary inlet selection with constant width b, drawn in white colour. The size of b it should have the same order of magnitude as the rim thickness. The smaller the width b, the higher the required number of computational cells, because there has to be a local grid refinement in the mesh along this inlet selection. To keep the number of cells for the model tests as small as possible, the inlet selection with its fine boundary faces is only applied on one side of the crankweb. For more advanced simulations this boundary inlet has to be applied on both sides.
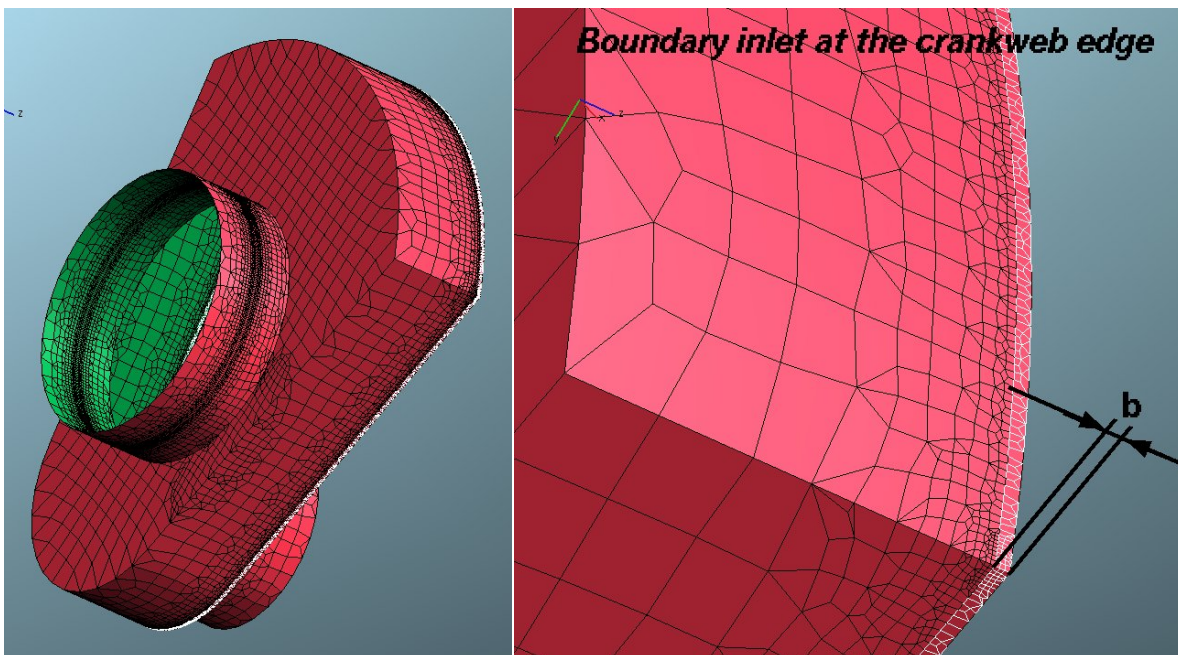

Figure 58: Boundary inlet for oil disintegration on a rotating crankweb

The base of the model is to handle every point on the crankweb edge, represented by the boundary face, as a separate part of a rotary atomiser with a disc diameter d_{disc} of two times the local radius of the edge $r_{bn}(\varphi)$. This means that the disintegration regime and the droplet

diameter $d_{d,b}$ of the detached droplets are calculated for every boundary face separately, according to a "reference rotary atomiser" with disc radius r_{bn}. This method can be applied if, for an observer moving with the crankshaft, the mean wall film flow velocity on the crankweb points into the radial direction. Investigations, which are referenced in [17], confirm this assumption, since they have shown for a circular disc that the difference between the velocity component of the wall film in circumferential direction and the circumferential velocity $r\omega$ is small.

The picture on the left in Figure 59 shows the schematic of the boundary faces of the inlet selection for the simulation of the oil detachment. Every boundary face is defined by its position vector $\mathbf{x}_b$ pointing to the centre of the face, and its area vector $\mathbf{A}_b$. Where $\mathbf{A}_b$ is defined by the face direction vector $\mathbf{n}_A$, $\boldsymbol{\omega}$ is the vector of the angular velocity, and $\mathbf{x}_{0ax}$ is the position vector of one point on the crankshaft axis.
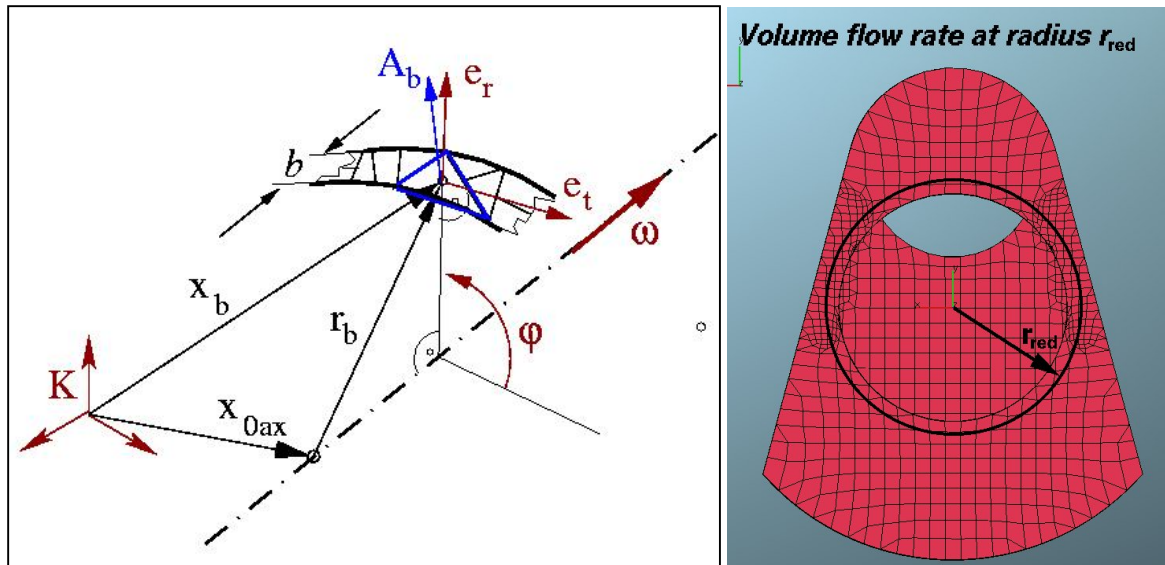

Figure 59: Schematic of inlet face for CFD simulation and reference radius r_{red} at the crankweb

The radius of the face is determined by the equation

$$r_{bn} = \mathbf{e}_r \cdot \mathbf{r}_b = \mathbf{e}_r \cdot \left(\mathbf{x}_b - \mathbf{x}_{0ax} \right) ,$$ (166)

as an inner product of the radial vector $\mathbf{e}_r$ of the face and the radius vector $\mathbf{r}_b$. The tangential and the radial vectors of the face, $\mathbf{e}_t$ and $\mathbf{e}_r$, are determined by the equations

$$\mathbf{e}_t = \frac{\boldsymbol{\omega} \times \mathbf{r}_b}{\left| \boldsymbol{\omega} \times \mathbf{r}_b \right|} ,$$ (167)

and

$$\mathbf{e}_r = \frac{\mathbf{e}_t \times \boldsymbol{\omega}}{\left| \mathbf{e}_t \times \boldsymbol{\omega} \right|} \quad , \tag{168}$$

where $\mathbf{e}_r$ is the normalised cross product between the angular speed vector and the radius vector, and $\mathbf{e}_t$ results from the cross product between the tangential and the angular speed vectors.

The boundary face vector $\mathbf{A}_b$ of the grid may have another direction than the radial vector $\mathbf{e}_r$. For the calculation of the volume flux through the face area, A_{bn} in radial (normal) direction is required, which is given by the equation

$$A_{bn} = \mathbf{A}_b \cdot \mathbf{e}_r = \left(\mathbf{n}_A A_b \right) \cdot \mathbf{e}_r \quad . \tag{169}$$

It is helpful to introduce the reduced face area $A_{bn,red}$, as described by the equation

$$A_{bn,red} = A_{bn} \frac{r_{red}}{r_{bn}} \quad , \tag{170}$$

which is the boundary face area in normal direction A_{bn} reduced onto an arbitrary reference radius r_{red}, as shown in Figure 59 right.

The sum over all reduced boundary faces in normal direction, $A_{n,red}$, is given by the following equation

$$A_{n,red} = 2 \, b \, r_{red} \, \pi = \sum_{b=1}^{n_b} A_{bn,red} \quad . \tag{171}$$

The quantities $A_{bn,red}$ and $A_{n,red}$ are used to determine the fraction of the volume flow rate, which flows through the boundary face at the crankweb edge, as done in the equation

$$\overset{\circ}{V}_b = \overset{\circ}{V} \frac{A_{bn,red}}{A_{n,red}} = \overset{\circ}{V} \frac{A_{bn,red}}{\sum\limits_{b=1}^{n_b} A_{bn,red}} = \overset{\circ}{V} \frac{\dfrac{A_{bn}}{r_{bn}}}{\sum\limits_{b=1}^{n_b} \dfrac{A_{bn}}{r_{bn}}} \quad . \tag{172}$$

One can see that the reference radius r_{red} cancels. This is a required condition, because the volume flow rate of the boundary face $\overset{\circ}{V}_b$ must not depend on the artificially introduced dimension r_{red}.

The radial velocity component in the equation

$$U_{r,b} = \frac{2 \, \dot{V}_b \, l_{lig,b}}{a_b^2 \, \pi^2 \, r_{bn}} \quad , \tag{173}$$

is obtained from Equation (164), by replacing d_{disc} by $2 \cdot r_{bn}$. The local ligament distance $l_{lig,b}$ and the local rim thickness a_b are defined similar to Equation (165) by the relations

$$l_{lig,b} = a_b \pi \left(2 + \frac{6 \, \mu_d}{\sqrt{\sigma \, \rho_d \, a_b}} \right)^{\frac{1}{2}} \quad \text{and} \quad a_b = \left(\frac{2 \, \sigma}{r_{bn} \, \rho_d \, \omega^2} \right)^{\frac{1}{2}} \quad . \tag{174}$$

The circumferential velocity component is given by the equation

$$U_t = r_{bn} \cdot \omega \quad , \tag{175}$$

and therewith both components of the liquid phase velocity $\mathbf{U}_{d,b}$ of Equation (161) are determined. The velocity vector of the continuous phase at the boundary face $\mathbf{U}_{c,b}$, which is air here, consists of the tangential velocity component only.

The liquid volume fraction of the dispersed liquid phase can now be obtained by equation

$$\alpha_{d,b} = \frac{\dot{V}_b}{A_{bn} U_r} \quad . \tag{176}$$

The volume fraction of the continuous phase is obtained from the equation

$$\alpha_{c,b} = 1 - \alpha_{d,b} \quad , \tag{177}$$

to ensure the compatibility condition.

If the simulation is performed without transport of the moments of a droplet size distribution, a mean droplet diameter is required to calculate the interfacial momentum exchange due to drag according to Equation (39) in section 3.1.2.1. Therefore, the Sauter diameter is calculated with the droplet diameters of all boundary faces, as shown in the equation

$$d_{32,d} = \frac{\sum_{b=1}^{n_b} \dot{n}_{d,b} d_{d,b}^3}{\sum_{b=1}^{n_b} \dot{n}_{d,b} d_{d,b}^2} = \frac{\sum_{b=1}^{n_b} \frac{3 \, \dot{V}_b}{4\pi \, d_{d,b}^3} d_{d,b}^3}{\sum_{b=1}^{n_b} \frac{3 \, \dot{V}_b}{4\pi \, d_{d,b}^3} d_{d,b}^2} = \frac{\sum_{b=1}^{n_b} \dot{V}_b}{\sum_{b=1}^{n_b} \frac{\dot{V}_b}{d_{d,b}}} = \frac{\dot{V}}{\sum_{b=1}^{n_b} \frac{\dot{V}_b}{d_{d,b}}} \quad . \tag{178}$$

This value $d_{32,d}$ represents the average momentum exchange between the liquid and the gas phase in the entire computational domain.

If the simulation is performed with transport of the moments of the droplet size distribution, the boundary values of the droplet volume and the droplet surface moments, $Q_{3,b}$ and $Q_{2,b}$, are determined by the equations

$$Q_{3,b} = \frac{3}{4\pi} \alpha_{d,b} \ , \tag{179}$$

and

$$Q_{2,b} = \frac{Q_{3,b}}{r_{32}} = \frac{3}{2\pi} \frac{\alpha_{d,b}}{d_{32,d,b}} \ . \tag{180}$$

Similar to the set-up of the boundary conditions for the blow-by simulation in section 4.3.2, the moment $Q_{3,b}$ can be obtained directly from the liquid volume fraction at the boundary face. The surface moment $Q_{2,b}$ is determined by the droplet volume moment and the Sauter mean diameter of the oil mist droplets, $d_{32,d,b}$.

4.4.1.3 Oil Disintegration at the Crankweb with Volume Flow Rate Function

The present section treats the case that the oil flow on the crankweb surface depends on the angular position. Hence, the oil volume flow rate at the crankweb edge which takes part in the liquid disintegration is not uniformly distributed. This means that $d\mathring{V}/d\varphi \neq 0$, and $r_{bn} = r_{bn}(\varphi)$. E.g., an advanced bearing simulation, as applied in [23], could yield the volume flow rate curve as a function of the angular position φ. Such a function would indicate the amount of oil leaving the bearing at a certain position. In the equations

$$\mathring{V}_{\varphi} = \frac{d\mathring{V}}{d\varphi} = f(\varphi) \quad \text{and} \quad \int_0^{2\pi} \mathring{V}_{\varphi} d\varphi = \mathring{V} \ , \tag{181}$$

$\mathring{V}_{\varphi}$ is defined as the derivative of the total volume flow rate on the disc with respect to the angle φ.

The reference volume flow rate $\mathring{V}_{ref}$, as described by the equation

$$\mathring{V}_{ref} = 2\pi \mathring{V}_{\varphi} \ , \tag{182}$$

represents the volume flow rate of the "reference rotary atomiser", which is determined by $\mathring{V}_{ref}$ for the liquid volume flow rate on the disc $\mathring{V}$ and $2 r_{bn}(\varphi)$ for the disc diameter d_{disc} to calculate the conditions for each boundary face separately. Therefore a simple and fast algorithm is used for the calculation of the volume flow rate at the boundary face. This algorithm avoids the exact determination of the range of the angle φ covered by the

boundary face. A required condition is that the extension of the boundary face in circumferential direction is small, i.e., $A_{bn}/b << 2\pi\, r_{bn}$. Then the volume flow rate at the boundary face $\dot{V}_b$ can be obtained from the equation

$$\dot{V}_b = \dot{V}_{ref}\, \frac{A_{bn,red}}{A_{n,red}}\, C_{cont} = \dot{V}_{ref}\, \frac{A_{bn,red}}{\displaystyle\sum_{b=1}^{n_b} A_{bn,red}}\, C_{cont} = \dot{V}_{ref}\, \frac{\dfrac{A_{bn}}{r_{bn}}}{\displaystyle\sum_{b=1}^{n_b} \dfrac{A_{bn}}{r_{bn}}}\, C_{cont} \quad . \tag{183}$$

The parameter C_{cont}, as described by the equation

$$C_{cont} = \frac{\dot{V}}{\displaystyle\sum_{b=1}^{n_b} \dot{V}_b} \quad , \tag{184}$$

ensures mass conservation, because the sum of the volume fraction rates on all boundary faces has to be equal to the total volume flow rate of the crankweb.

Three steps are required for the calculation of $\dot{V}_b$ and C_{cont}:

1. Calculation of $\dot{V}_b^{(0)}$ with $C_{cont} = 1$ for all boundary faces.
2. Determination of C_{cont} with the values of $\dot{V}_b^{(0)}$ to ensure mass conservation.
3. Calculation of $\dot{V}_b = \dot{V}_b^{(0)}\, C_{const}$.

The radial velocity component in the equation

$$U_{r,b} = \frac{2\, \dot{V}_{ref}\, l_{lig,b}}{a_b^2\, \pi^2\, r_{bn}} \quad , \tag{185}$$

results from Equation (173) replacing $\dot{V}$ by $\dot{V}_{ref}$. All other boundary face values, $\mathbf{U}_{d,b}$, $\alpha_{d,b}$, $d_{32,d,b}$, $Q_{3,b}$ and $Q_{2,b}$, are calculated with the correlation of the previous section.

4.4.2 Sensitivity Analysis of Model Parameters

To check the sensitivity of the rotary atomisation model this section presents the effects of a variation of the operation conditions and the fluid properties on the model. The results show the influence of these parameters on the model outcome, such as the oil film thickness at the disc edge and the rim thickness, the radial velocity component, and the droplet diameter. The disintegration regime and the droplet diameters of rotary atomisation depend on the disc diameter, the rotational speed, the volume flow rate, and on the fluid properties oil density, viscosity, and surface tension against air. An independent variation of these six parameters would lead to a big matrix, which is difficult to manage. Hence, the number of parameters is reduced in order to treat the relevant parameters for the crankcase flow.

Rotational speed and volume flow rate are applied together, according to the volume flow rate curve of Figure 24. Hence in all following illustrations, the dependency on the rotational speed is also a dependency on the volume flow rate, and vice versa. Oil viscosity, density, and surface tension show a strong temperature dependency. Therefore the variation of these parameters is covered by the temperature variation of the engine oil. Figure 60 left shows the dynamic viscosity and the density of the engine oil OMV truck LD SAE 15W-40 depending on the temperature. The surface tension curve, which was measured in [30], is shown in Figure 60 right. All curves show the same tendency: the higher the temperature, the lower density, viscosity and surface tension against air.
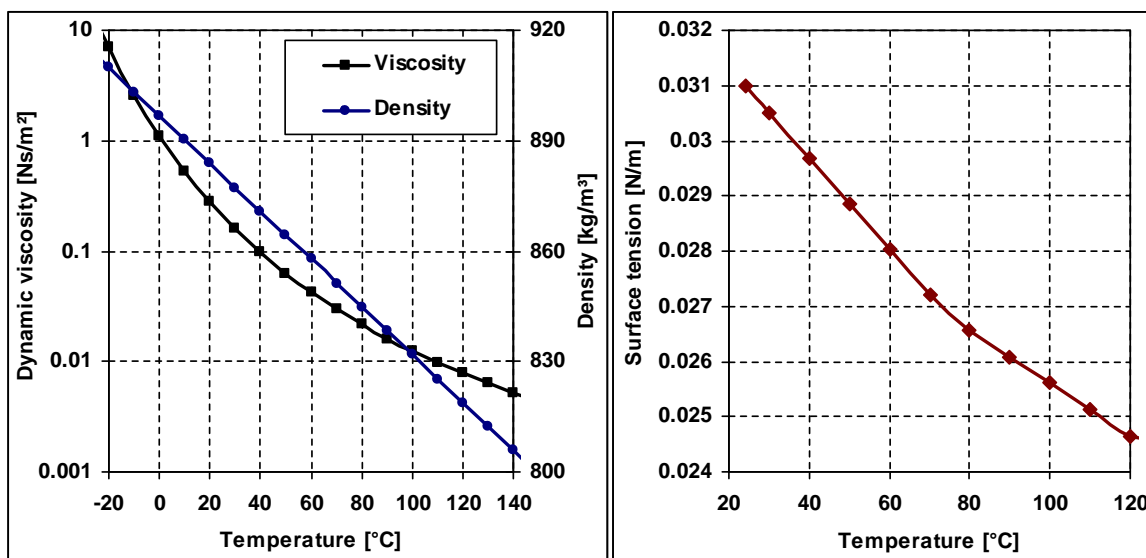
Figure 60: Dynamic viscosity and density (left), and surface tension against air (right) of engine oil

OMW truck LD SAE 15W-40

Although the results for rim and film thickness are not directly used in the CFD model, they yield interesting information about the flow condition on the disc surface. The diameter of the liquid rim at the disc edge is an important dimension influencing the droplet diameter of the disintegrated liquid oil and the radial component of the detachment velocity. In Figure 61 the rim thickness a of Equation (165) for a disc with constant diameter of 100 mm is plotted in two different ways. The figure on the left-hand side shows the rim thickness as a function of the rotational speed, or more correct as a function of the coherence between volume flow rate and rotational speed, at different oil temperatures. One can see that the rim thickness decreases strongly with increasing engine speed. The temperature influence is of minor importance. A higher oil temperature leads to a slightly reduced value of a, as shown in Figure 61 right, where the abscissa shows the temperature and the curves are drawn for different values of the rotational speed. This is reasonable, since a is a function of surface

tension and density, and both of these fluid properties show only a small dependency on the temperature.

The dependency of the parameters on the oil film thickness δ at the disc edge of Equation (66) is shown in Figure 62. Also there the curves are drawn in two different ways. The abscissa of Figure 62 left shows the rotational speed, and the abscissa of Figure 62 right shows the oil temperature. Increasing rotational speed leads to decreasing film thickness. Contrary to the rim thickness curves, there is a strong influence of the temperature on δ. In the observed oil temperature range, the oil viscosity decreases by several orders of magnitude. Hence, the film thickness, which results from the balance of centrifugal and viscous forces, also decreases with increasing oil temperature.
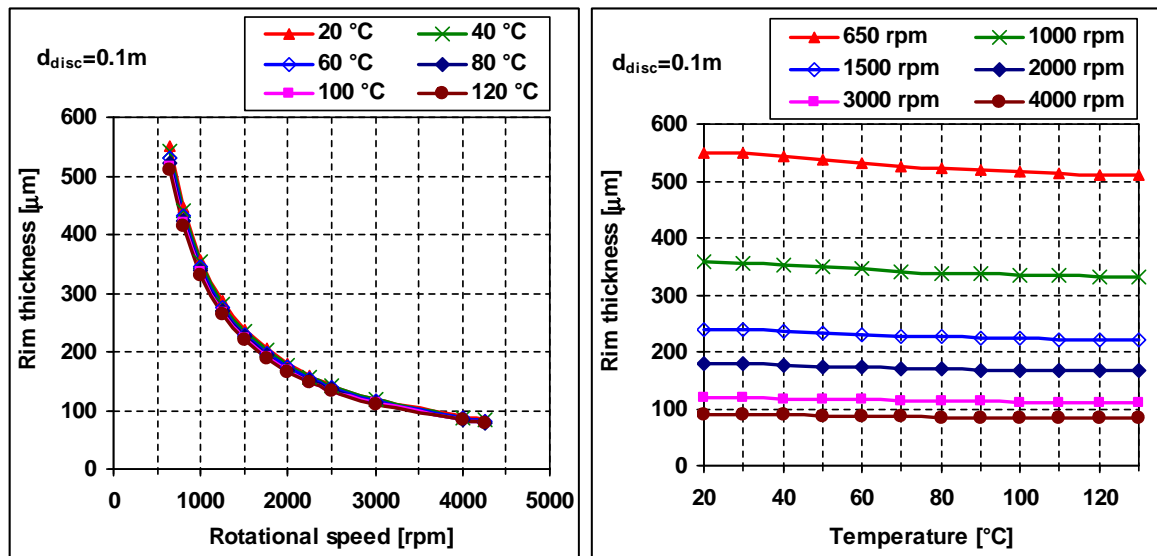
Figure 61: Rim thickness for a disc of 0.1 m diameter depending on oil temperature and the rotational speed
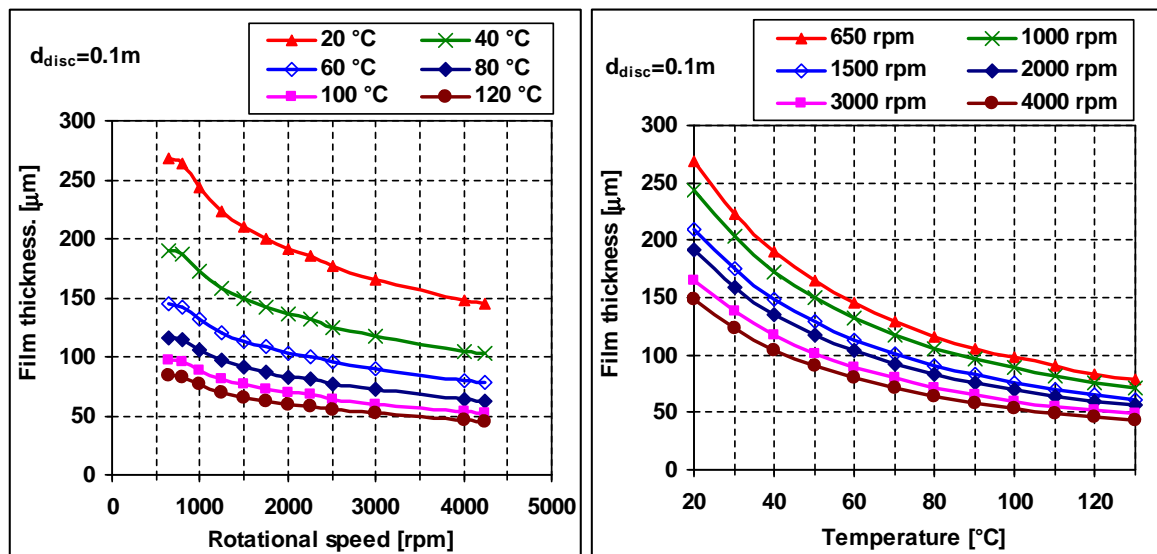
Figure 62: Film thickness on a disc of 0.1 m diameter depending on oil temperature and the rotational speed

The droplet diameters of the illustration in Figure 63 are calculated with Equations (89), (90), and (91), where the disintegration regimes have been determined according to the Equations (77), (79), and (80) of section 3.3. The disc diameter in this figure is kept constant at 100 mm. The higher the rotational speed, the smaller the diameter of the detached droplets. The influence of the temperature on the oil droplet diameter is small. The abrupt increases of the droplet diameter in Figure 63 right at 650 rpm and 1000 rpm result from the switch of the regime from ligament to dropwise disintegration. The disintegration regime is not indicated in those figures. At 650 rpm, there is ligament disintegration from 20 °C to 40 °C, and there is dropwise disintegration at temperatures higher than 40 °C. At 1000 rpm, there is ligament disintegration between 20 °C and 80 °C, and there is dropwise disintegration at temperatures greater than 80 °C. For 1500 rpm and at 2000 rpm, there is ligament disintegration, and for 3000 rpm and 4000 rpm, there is sheet disintegration in the full temperature range. One can observe that, only in the region of ligament disintegration, a noticeable change of the droplet diameter with varying oil temperature is visible. The reason for this can be found in the Equation (90) for the droplet diameter at ligament disintegration, which is a function of the oil viscosity varying strongly with the oil temperature. The droplet diameter correlations for dropwise and sheet disintegration, Equations (89) and (91), do not contain the oil viscosity. Hence, the temperature influence is weak.
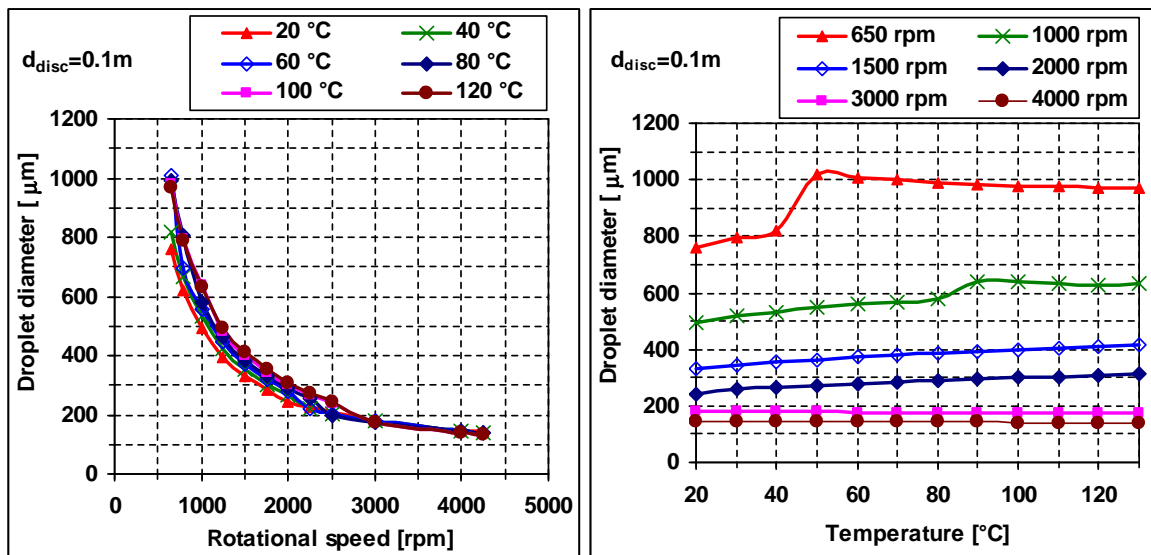

Figure 63: Droplet diameter of detached liquid according to Hege [44] and Walzel [87] for a disc of 0.1 m diameter depending on oil temperature and the rotational speed; disintegration regime according to Grave [42]

Figure 64 shows the model parameter variation in the calculation of the radial component of the detachment velocity, according to Equation (164). The higher the rotational speed and the volume flow rate, the higher the radial velocity component U_r. Although a logarithmic

scale is used for the ordinate, a strong increase of U_r with rising rotational speed is visible. There are very high values for U_r at rotational speeds greater than 3000 rpm, where sheet disintegration is the dominant disintegration regime. As discussed in section 4.4.1.1, the application of Equation (164) in that regime may produce doubtable results. It seems that, at low temperatures and high volume flow rates, the radial velocity component can reach too high values.
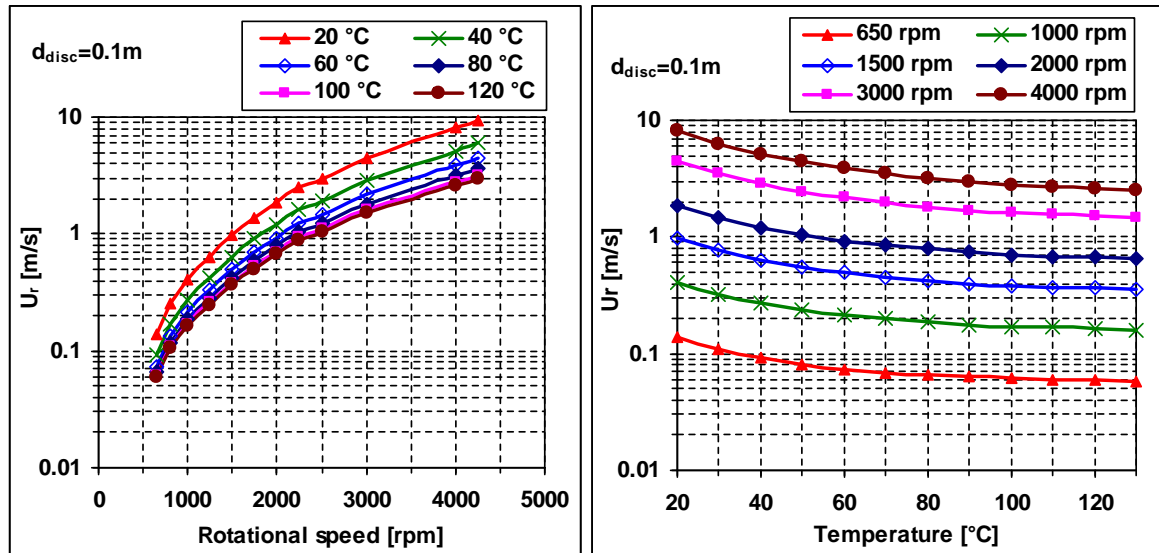

Figure 64: Radial detachment velocity for a disc of 0.1 m diameter depending on oil temperature and rotational speed

The previous figures have shown the parameter variation for a constant disc (or crankweb) diameter of 100 mm. The following illustrations show the results for rim and film thicknesses, droplet diameter, and radial detachment velocity for varying disc diameter, curve of rotational speed, and oil volume flow rate. The fluid properties are kept constant at two oil temperatures of 20 °C, representing a cold engine, and 100 °C, representing a warm engine.

Figure 65 shows that the rim thickness a decreases with increasing disc diameter due to higher centrifugal forces. The difference between the curves at 20 °C and 100 °C is almost negligible.

The film thickness δ at the crankweb edge also decreases with increasing disc diameter. Due to the lower oil viscosity at higher temperature, the film thickness in Figure 66 at 100 °C is much smaller than at 20 °C.
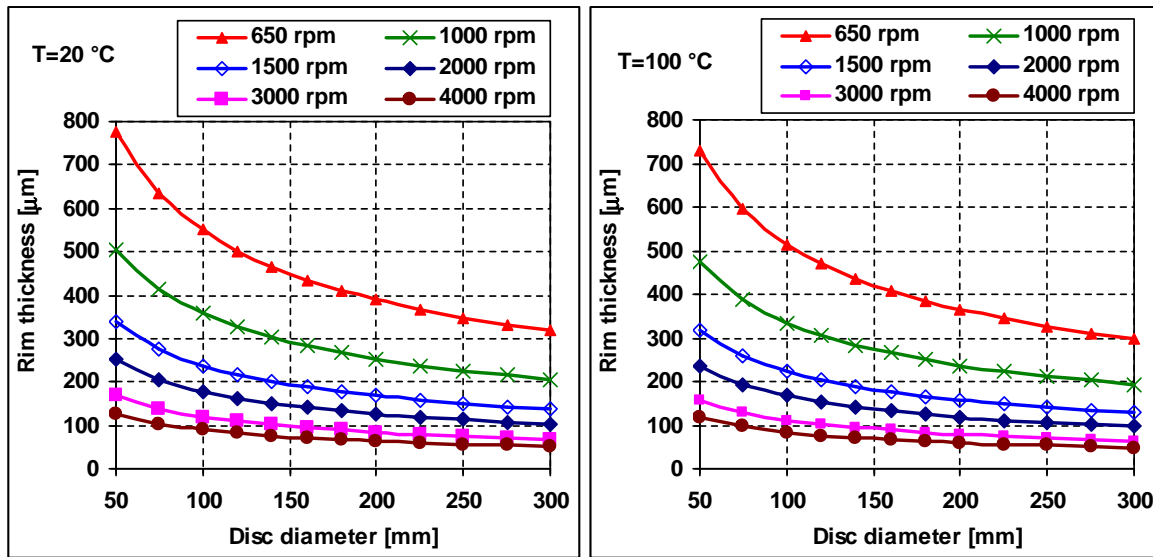
Figure 65: Rim thickness as a function of the disc diameter and rotational speed)
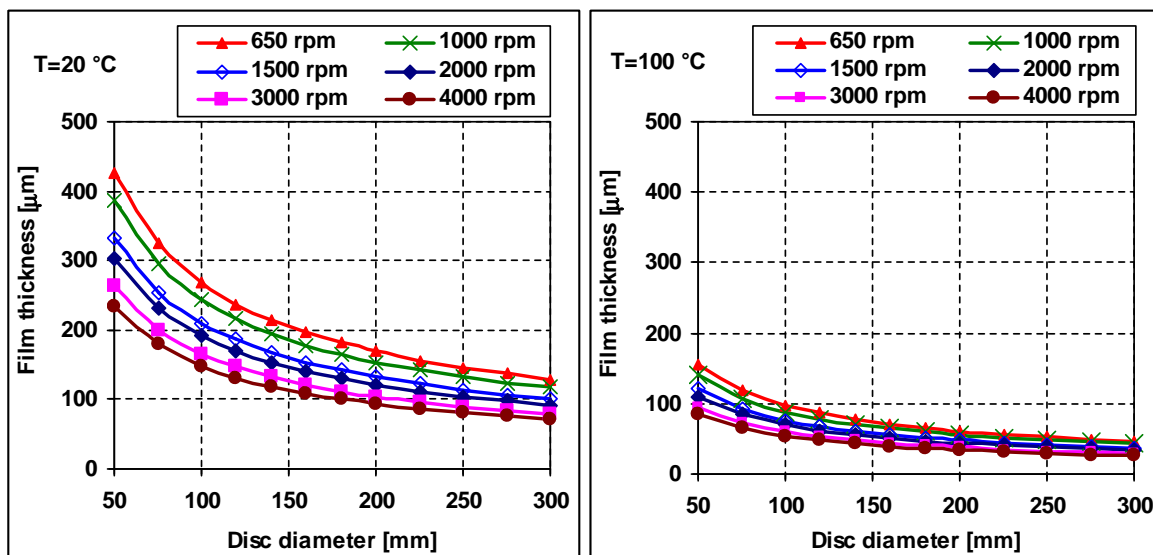
at 20 °C (left) and 100 °C (right)

Figure 66: Film thickness as a function of the disc diameter and rotational speed

at 20 °C (left) and 100 °C (right)

It is an expected result that increasing disc diameter and increasing oil volume flow rate lead to smaller oil droplets, as shown in Figure 67.

Figure 68 shows the influence of the disc diameter on the radial component of the detachment velocity U_r. In Equation (164), the disc diameter is contained in the denominator, and hence the increase of the disc diameter leads decreasing radial velocity. At low disc diameters and high volume flow rates, U_r can reach too high values of 10 m/s and more. As discussed above, these problems result from the application of Equation (164) for

an operation point in the sheet disintegration regime, far away from the ligament disintegration regime, for which this correlation has been derived.
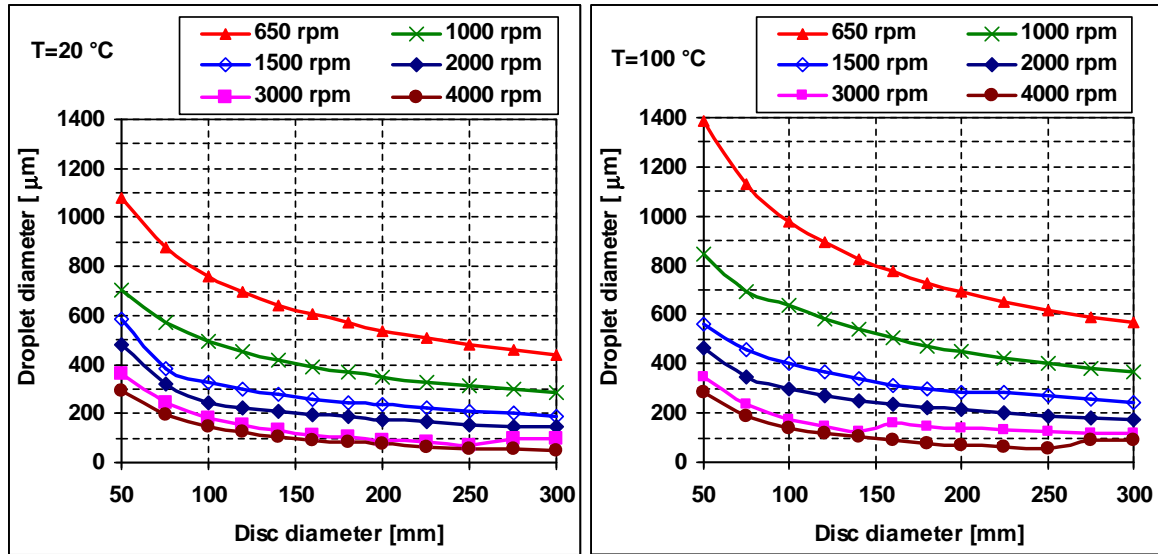

Figure 67: Droplet diameter according to Hege [44] and Walzel [87] as a function of the disc diameter and rotational speed at 20 °C (left) and 100 °C (right); disintegration regime according to Grave [42]
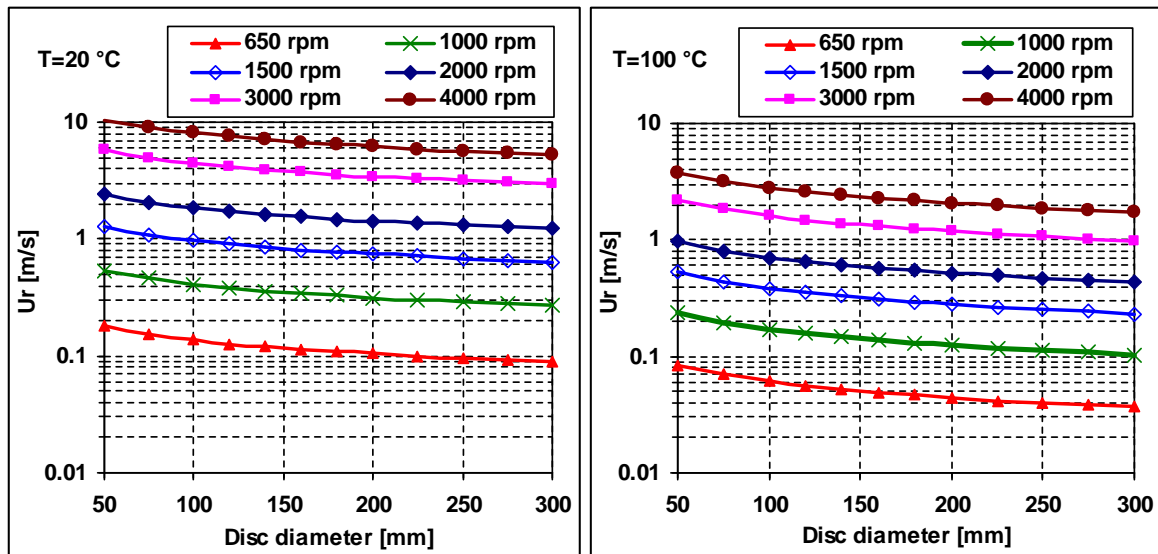

Figure 68: Radial detachment velocity as a function of disc diameter and rotational speed at 20 °C (left) and 100 °C (right)

5 CFD Simulations and Results

The models for liquid disintegration at the crankweb and blow-by presented in section 4 have been implemented into the multi-phase CFD code AVL FIRE. These models include the formation process of the oil droplets and the oil mist flow. They provide the boundary conditions for the liquid and the gaseous phases. The aims of the CFD simulations are to determine the gas flow field in the crankcase, and to describe the propagation of the oil phase there. Additional transport equations for the moments of the droplet size distribution function have been implemented. They allow for a local determination of the Sauter mean diameter of the oil droplets in the flow field.

The present section discusses the results of the CFD simulations on simplified crankcase geometries. Separate simulations for the blow-by flow and the oil disintegration on the rotating crankweb have been performed to show the outcome of these processes independent from other effects. The blow-by simulation was performed on the very simple crankcase geometry with two moving cylinders and without the crank drive. The simulation of oil detachment from the rotating crankweb is performed on a computational mesh, which resolves half of a real crankshaft of a single-cylinder engine. The conrod is not yet modelled, and there is a simplified moving piston. Although the geometry of the crank drive is quite simple, the meshing procedure was a challenge. Conform meshing with nonlinear motion on unstructured grids is not trivial. The used computational meshes are presented in the first chapter of the present section.

It would have been highly desirable to have data from experimental results in order to enable comparison with the simulations. This could not been performed during the work of this thesis, as measurement data on the flow field and the droplet size distribution directly in the crankcase were not available. There are various reasons for this, since it is very difficult to get access to the regions in the crankcase where the droplets are formed. There is a fast moving crank drive and only little space. Furthermore, access from outside through a window to the crankcase is also difficult. The splash oil covers the surface of the window, and hence it is useless for optical measurements. Figure 56 in section 4.4 shows the view into the crankcase of a running engine. Due to the oil film on the window, only a sparse qualitative comparison between simulation and reality is possible.

However, the implemented models use analogies to well validated processes. The chamber model may predict the gas mass flow rate into the crankcase well [60]. The liquid disintegration on rotating discs is investigated very well on rotary atomisers [42], [44], [45], and [57]. Those models provide the boundary conditions for the CFD simulation, which calculates the propagation of the oil droplets and the oil mist. In the previous section,

sensitivity analyses of the model parameters have been shown. The models have been tested at different operation points of the engine. Although there is no direct comparison between CFD simulation and experimental measurements available, the variation of the model parameters has shown that the applied models yield reasonable results. The implementation of the models into the CFD code FIRE provides a sophisticated simulation tool. The following results show the outcome of the developed simulation tool on simplified geometries.

5.1 Moving Meshes in the CFD Simulations

The CFD solver of FIRE can deal with unstructured moving meshes. Especially the generation of the computational grid around the rotating crankshaft was a challenge. At this point, special thanks to Heinrich Kratochwill [47], who made the computational mesh for simulation of the oil disintegration on the crankweb, as shown in the Figures 71 and 73.

Moving meshes have been used for the simulations. The moving bodies cause deformation of the computational cells in the entire domain. The mesh deformation may occur as long as the grid quality is good. This means that the computational cells are deformed as long as there are no twisted faces, negative volumes, or negative normal vectors, and the aspect ratio and the skewness of the cells are below upper limit values. Before the grid quality worsens, the mesh is frozen. Then a completely new mesh is generated, and the deformation of the computational cells due to the moving bodies can be continued. The step from the old mesh to the new one is called rezone. If the CFD simulation passes the time when rezone occurs, the complete flow field is mapped from the old mesh to the new mesh. The spatial mapping algorithm ensures mass conservation and is done automatically by the CFD solver of FIRE. The more complex the motion of the bodies, the stronger the deformation, and the more rezones are required. Although the flow variables are correctly mapped and the mass is conserved, each rezone causes numerical diffusion. Hence, the number of rezones should be as small as possible.

The computational grid for the blow-by flow simulations is shown in Figures 69 and 70. The calculations are performed on a strongly simplified multi-cylinder grid. The number of cells is kept low, and hence it is possible to perform simulations of more than one engine cycle. Two cylinders are represented by two quarter geometries. Symmetry boundary conditions are applied in the cuts through the cylinder axes. The crankshaft and the conrod are not modelled. The piston bottom is assumed to be flat. The inlet boundary selections for the blow-by are placed at the position of the piston skirt, where the piston diameter is slightly reduced according to the piston design illustrated in Figure 42 top in section 4.3.2. From there the blow-by gas and the oil mist are guided into the crankcase.

The computational grid consists of three different blocks, the two cylinder blocks and the crankcase block. They are connected by so called "arbitrary connects" [7]. They enable the connection of blocks with different mesh resolution. The local grid refinement in the region of the arbitrary connects enables a smoother transition between the different blocks. This mesh is simpler than the mesh for the oil detachment simulations, as there is only motion of the pistons. Figure 69 shows the start position at 0 deg CA, where piston 1 stands at the top dead centre (TDC), and piston 2 at the bottom dead centre (BDC). The mesh quality at the dead centre positions, as well as during the whole motion, is good so that no rezones are required. The total number of computational cells is about 28 000.
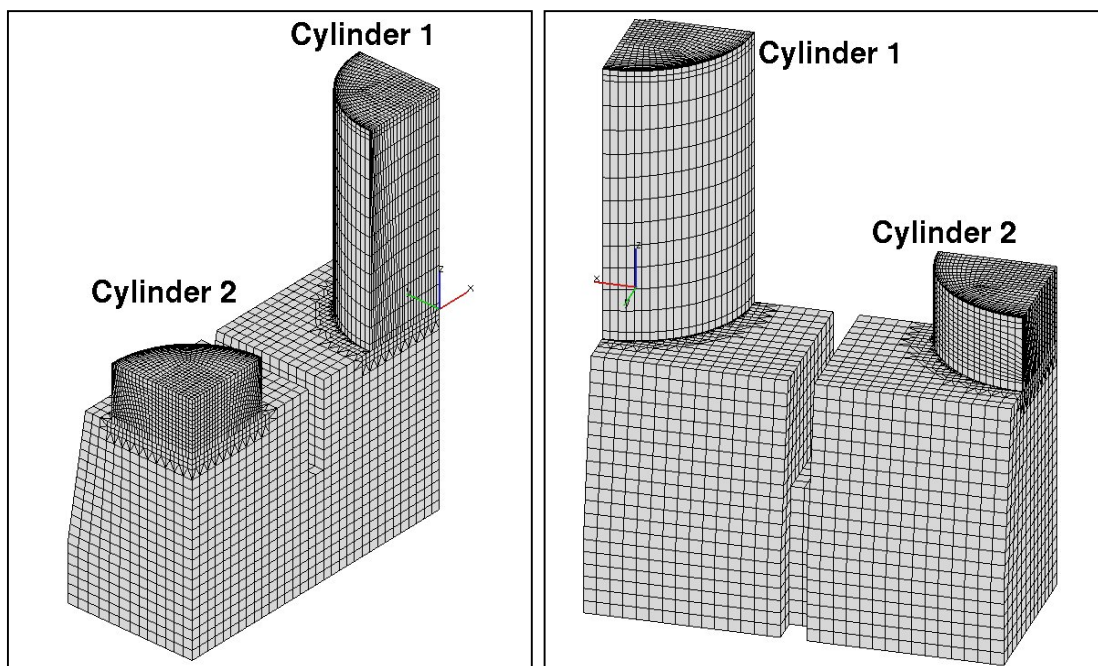

Figure 69: Moving mesh for blow-by flow simulation at 0 deg CA

Figure 70 shows the computational grid at various instants of time, every sixty degrees CA during one revolution. The piston of cylinder 1 starts from TDC position and moves downward to its BDC at 180 deg CA. Then it moves upward again, reaching the starting position at 360 deg CA. The piston of cylinder 2 starts from BDC, moving at a phase shift of 180 deg CA against cylinder 1. The mesh is generated for one revolution of the engine. In all further rotations, the crank drive motion is recurring, and hence the same mesh can be used several times. Therefore the crank angle position of the simulation is determined by adding the corresponding multiple of 360 deg CA to a current mesh crank angle position. Thus only the moving set of the mesh from 0 to 360 deg CA has to be stored.
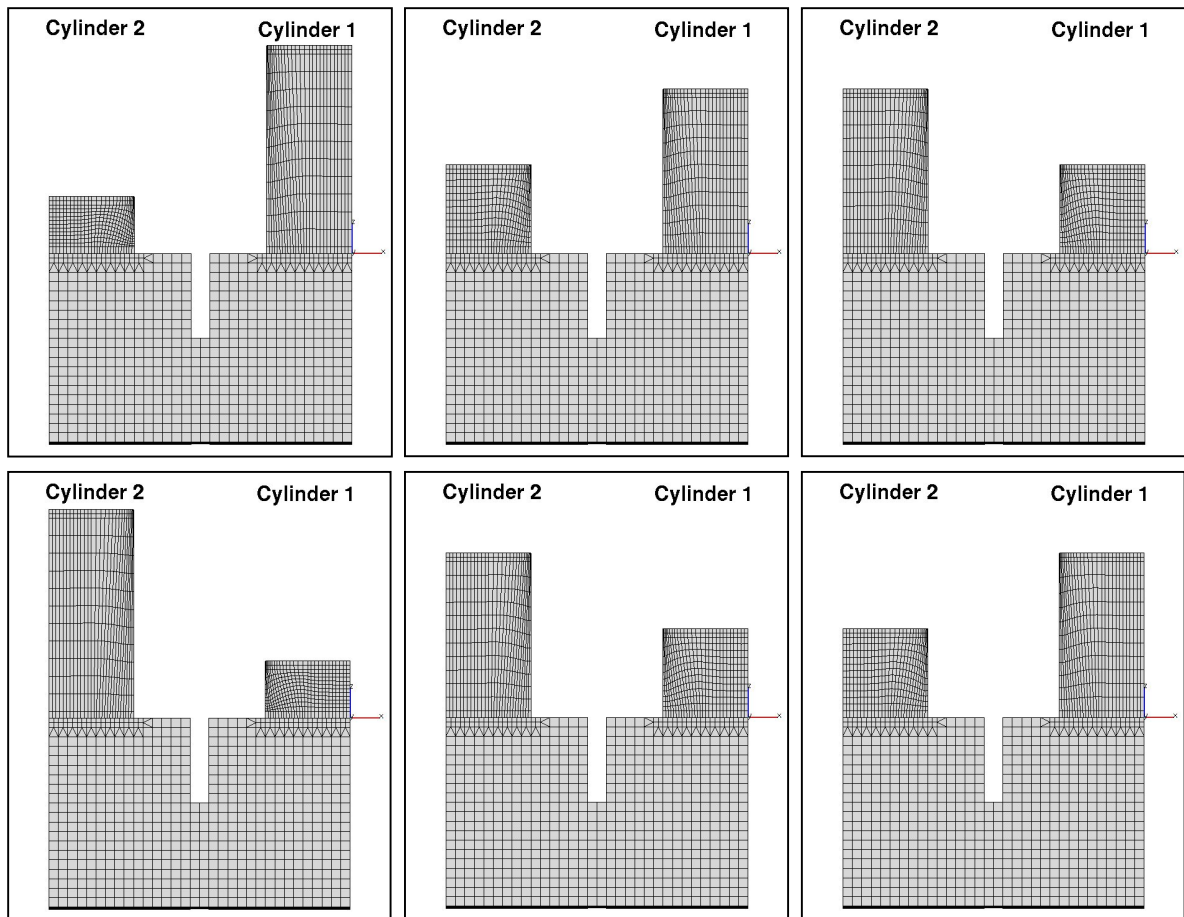
Figure 70: Moving mesh for the blow-by simulation at 0, 60, 120, 180, 240, and 300 deg CA

Figure 71 shows the computational grid for the simulation of the oil detachment. The geometry of the mesh is simplified and represents the crankcase of the single-cylinder engine, which is shown in Figure 72 (and also in Figure 55 of section 4.4). The generation of such a conform computational grid is not trivial, since the complexity of the mesh increases step by step. In first simulations in [34] and [35], the crankshaft was represented by circular discs. In the mesh used in this thesis [47], half of the crankcase is modelled. There is a moving piston, which is modelled as a rectangular prism. The conrod has been neglected. The rotating crankshaft with its massive counter weights is illustrated separately in more detail on the right to the mesh in Figure 71. The computational mesh is refined along the crankweb edge, since there the boundary condition for the oil disintegration is applied.

The crankshaft in the current mesh performs a rotary motion. In general it would be possible to use sliding meshes for rotating bodies. Such a mesh consists of two separate non-deformed meshes: a non-moving part and a rotating part. They are connected via the sliding interface. Sliding meshes require no rezones, since the mesh motion only influences the flux across the sliding interface. However, this methodology is restricted to bodies in rotary motion only. The piston, however, performs a translatory motion, and with respect to

the intended modelling of the conrod motion, the applied meshing procedure with rezones is the only one which enables the generation of such meshes.
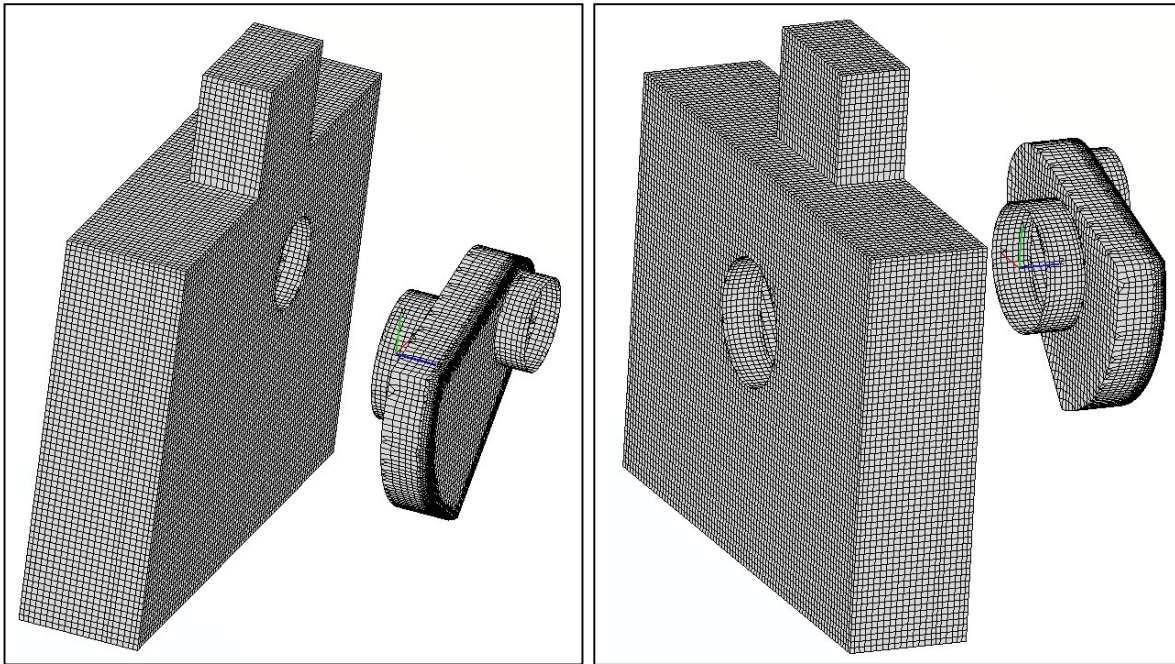

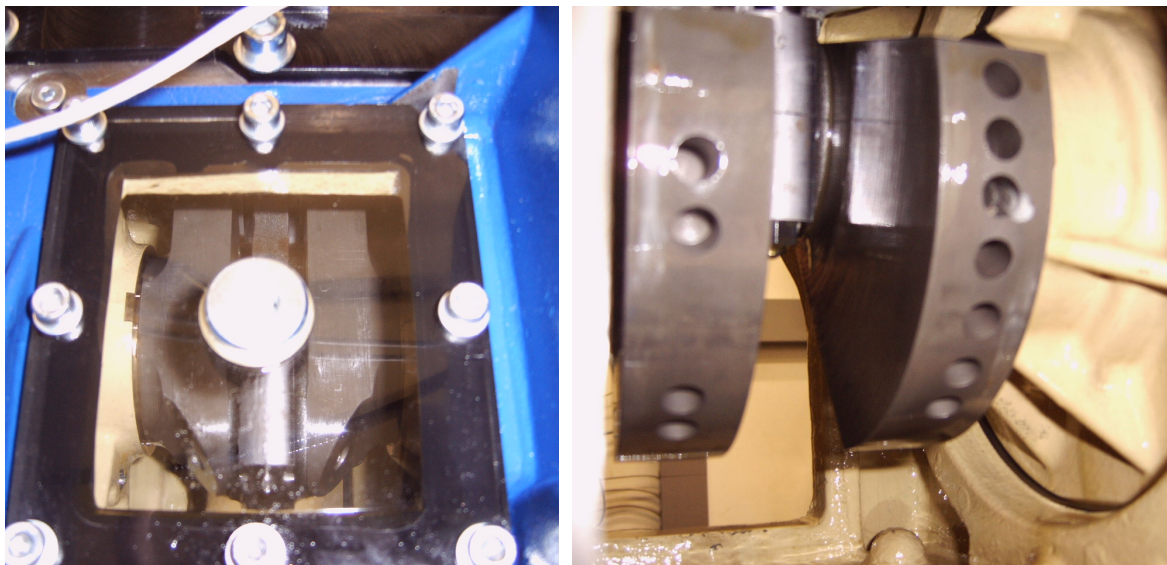Figure 71: Computational grid for the oil detachment simulation

Figure 72: Crank drive of a single-cylinder engine on a testbed for oil detachment simulation

Figure 73 shows cuts through the crankweb perpendicular to the axis of rotation at six different crank angle positions, illustrating one revolution of the crankshaft. In that time, the piston goes down and up. At 0 deg CA, the piston is in the TDC position, and the crank pin is in its upper position. The crankshaft performs a clockwise rotation. One can see the local mesh refinement along the crankweb edge. There are rezones every ten degrees crank angle

at 5, 15, 25, 35…345 and 355 deg CA. This means that the entire computational mesh includes thirty-seven different meshes, connected by rezones. Separate meshes were generated at 0, 10, 20, 30…350 and 360 deg CA, determining the basic positions for the movement procedure. Each computational mesh is different and also the number of cells varies from mesh to mesh. On average, the total number of cells is about 160 000. The mesh generation process is performed automatically with FAME Engine Plus [7]. From a certain position, e.g. at 10 deg CA, the surface of the crankshaft rotates five deg CA backwards to the first rezone position at 5 deg CA, and it moves five degree CA forward until the second position for rezone at 15 deg CA is reached. At the same time, the piston surface moves downward according to the crank drive motion. That way, a section of the moving mesh between 5 and 15 deg CA has been created. The other sections are created in the same manner until the mesh for the complete revolution is finished.

Figure 73: Cuts through the crankweb at 0, 60, 120, 180, 240 and 300 deg CA

Due to the rotation of the crankshaft and the motion of the piston surface, the computational cells and the cell faces also move. This motion creates fluxes of the flow variables in the CFD solver. The convection term takes these fluxes into account by subtracting the velocity $U_{gr,j}$ of the cell face, as shown in the general transport Equation (130) in section 4.1.

The region between piston and topside of the crankweb, marked by the red circle in Figure 73 top left, is shown in more detail in Figures 74 and 75. The figures show the meshes at 5 and 15 deg CA, each before and after rezone. One can observe the very fine grid at the crankweb edge, where the inlet boundary condition for the oil detachment is applied. Via several transition layers, the grid becomes coarser. The mean cell size in the free flow domain is about 3.8 mm. Due to the clockwise rotation of the mesh during the generation process from the basic position at 0 deg CA, the vertical gridlines of the mesh at 5 deg CA before rezone show a slight orientation to the right. After the rezone, the gridlines are orientated to the left, since this position results from the counter-clockwise rotation from the basic mesh at 10 deg CA. Then the crankshaft rotates from 5 to 15 deg CA without rezone. In that section, the gridlines change again their orientation from the left to the right-hand side, resulting in the mesh illustrated in Figure 75 left. Then the second rezone occurs, and the crankshaft rotates from 15 to 25 deg CA. This process is repeated until the full revolution of 360 deg CA is performed.
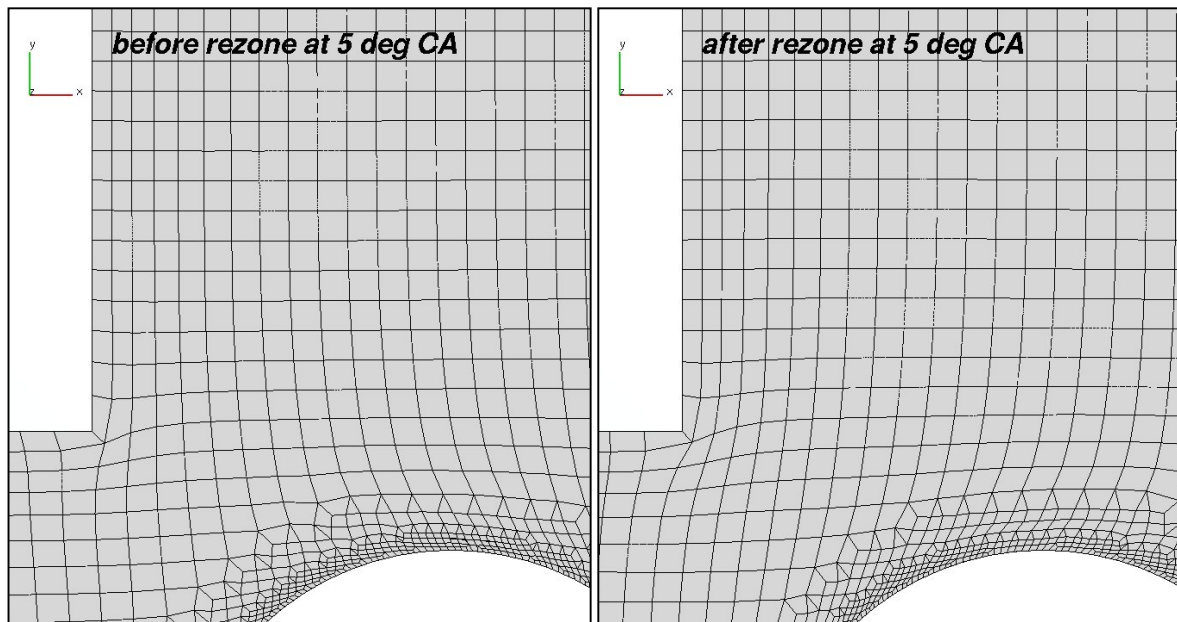

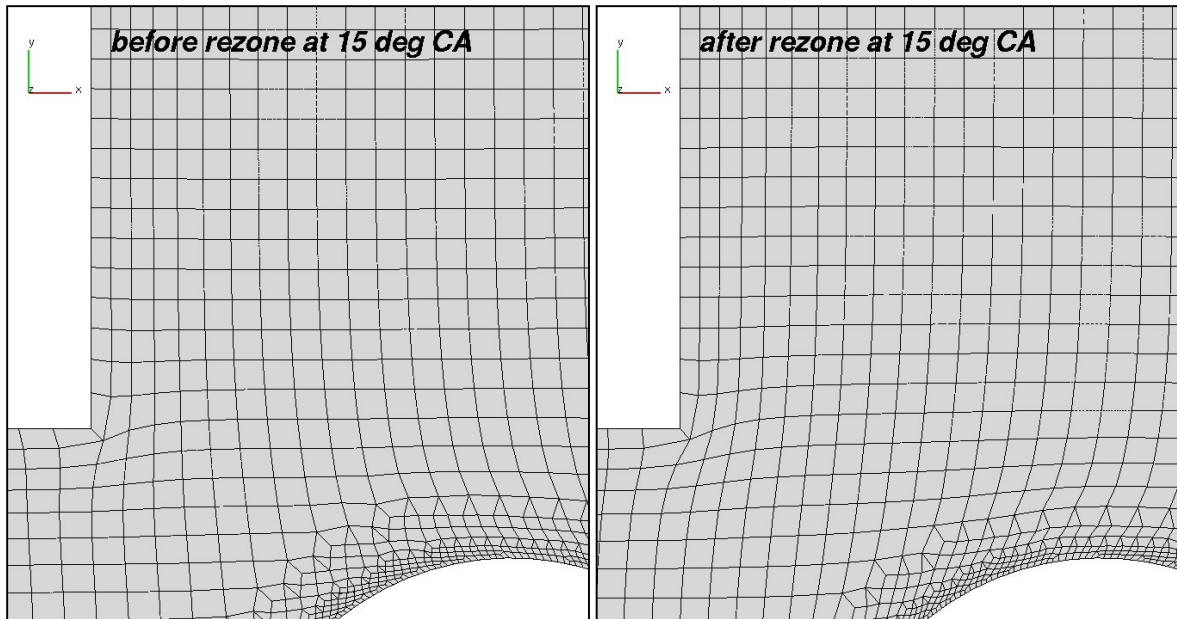Figure 74: Zoomed view of gridlines at 5 deg CA before and after rezone

Figure 75: Zoomed view of gridlines at 15 deg CA before and after rezone

5.2 Simulation of Blow-by Flow

This section presents the results of the blow-by flow simulations, which have been performed on the computational mesh with the two simplified cylinders presented in the previous section in Figure 69. To keep the number of cells as small as possible, the crank drive, including conrod and crankshaft, is not modelled in that simple mesh. Hence, the oil detachment from the crankshaft is not simulated, and the focus of the simulations is on the blow-by flow. Due to the rather small number of cells of about 28 000, the simulation of several engine cycles has been carried out. The calculation set-up and the results of the simulation are discussed in the following sections.

5.2.1 Set-up of the CFD Simulation

The set-up of the blow-by flow simulation is listed in Table 6. The simulation is performed with two phases, air and the engine oil OMV Truck LD SAE 15W-40, for which the fluid properties are listed at 100 °C. The engine speed is 3000 rpm at full load, and the simulation of five engine cycles, that are 3600 deg CA, has been performed. The chamber model, which provides the boundary conditions at the blow-by inlet selections as shown in Figure 43, uses three piston rings. The outcome of the chamber model for the current CFD simulation can be seen in section 4.3. The curves for the gas mass flow rate and for the Sauter mean diameter of the atomised droplets are shown in Figures 39 and 41. The value of 0.1 μm for the strip thickness δ_{strip} has been chosen to determine the mean mass flow rate of the atomised oil droplets into the crankcase.

General calculation set-up	Rotational speed n	3000	rpm	
	Number of phases	2	-	Gas and liquid
	Load	100 (full)	%	
	Bore d_{cyl}	0.09	m	
	Stroke s	0.08	m	
	Time step	$2.78\cdot10^{-5}$	s	= 0.5 deg CA
	Simulated time	3600	deg	10 revolutions
Blow-by model set-up Chamber data	Number of piston rings	3	-	includes oil control ring
	Number of chambers	2	-	
	Volume chamber 1 V_1	$1.12\cdot10^{-6}$	m³	
	Volume chamber 2 V_2	$1.01\cdot10^{-6}$	m³	
	Temperature chamber 1 T_1	473.15	K	
	Temperature chamber 2 T_2	453.15	K	
	Effective flow area Ring 1 $K_c A_1$	$1.922\cdot10^{-7}$	m²	
	Effective flow area Ring 2 $K_c A_2$	$1.922\cdot10^{-7}$	m²	
	Effective flow area Ring 3 $K_c A_3$	$1.922\cdot10^{-7}$	m²	
Atomisation model	Strip thickness δ_{strip}	$1.0\cdot10^{-7}$	m	For Equation (60)
	Model constant γ_C	0.055	m$^{1/2}$	For Equation (61)
Droplet size distribution model set-up	Reference Sauter mean diameter	3.3	μm	Equation (120)
	Minimum Sauter mean diameter	1.1	μm	
	Maximum Sauter mean diameter	10	μm	
	Drag model	On	-	
	Collision model	On	-	
Engine oil properties (OMV Truck LD SAE 15W-40)	Kinematic viscosity v_d	$14.9\cdot10^{-5}$	m²/s	At 100 °C
	Dynamic viscosity μ_d	0.0123931	Ns/m²	
	Density ρ_d	831.75	kg/m³	
	Surface tension σ	0.02561	N/m	
Ambient gas: air at 373 K	Pressure p	100 000	Pa	
	Density ρ_c	0.93413	kg/m³	
	Gas constant R	287	J/kg/K	
	Adiabatic exponent κ	1.4	-	

Table 6: Set-up of the CFD simulation for blow-by flow

The chosen value for the strip thickness is below the value used in previous blow-by flow simulations of [34] and [35], since the measurements of the oil mass flow rate through the piston ring pack in [48] have led to a much better estimation of δ_{strip}.

The simulation is performed with transport of the moments of the droplet size distribution function. The reference Sauter mean diameter was set to 3.3 μm, representing an appropriate average value of the droplet diameter curve in Figure 41. Since only two moments, Q_2 and Q_3, are transported, the reference distribution function is truncated, removing either small or large droplets to obtain the local Sauter mean diameter. Those truncation values (Figure 33 in section 3.4.4) are limited such that the minimum and maximum local Sauter mean diameters cannot exceed values three times smaller and three times larger than the reference Sauter mean diameter. According to [13], the distribution is assumed to be monodisperse whenever that limiter values are exceeded. The collision and the drag force models are active.

The crankcase temperature is assumed to be 100 °C, and the pressure is initialised with 1 bar. It is assumed that the pressure control valve of the ventilation system, e.g. the closed system of Figure 8 in section 2.1.2, ensures almost ambient pressure in the crankcase for the simulated time. The simulation starts at rest with cylinder 1 at the right-hand side in the TDC, and cylinder 2 on the left-hand side in the BDC. The CPU time on a Linux workstation, 3.2 GHz in single processor mode, was about 11 hours for the first engine cycle and about 48 hours for all five engine cycles.

5.2.2 CFD Simulation Results

Figures 76, 77, and 78 show the oil volume fraction, the local droplet Sauter mean diameter, and the gas velocity vectors, respectively, in the symmetry plane through the cylinder axis during the first engine cycle from 90 to 720 deg CA. The oil volume fraction is drawn with isolines, where the minimum volume fraction is $5 \cdot 10^{-6}$. The higher the isoline density in a region, the higher the volume fraction gradient, and one can expect a high oil droplet concentration there. The Sauter mean diameter of the atomised droplets is only plotted in regions with an oil volume fraction greater than $5 \cdot 10^{-6}$. The gas velocity plots are interpolated onto a coarser grid to get a smooth vector distribution for showing the overall flow field. Hence, the blow-by gas jet is not fully resolved in that coarser illustration. The original mesh resolution in the region of the blow-by inlet is much finer there.

The blow-by gas mass flow rate and the droplet diameter curves of Figures 39 and 41 are drawn for an engine cycle with the ignition top dead centre at 0 deg CA. For cylinder 1 on the right-hand side, the crank angle values of the curves and the crank angle of the CFD

simulation are identical, since piston 1 starts from TDC. For cylinder 2 on the left-hand side, a time shift of 180 deg CA has to be considered, since piston 2 starts to move from the BDC reaching the ignition top dead centre after 180 deg CA. Thus, for cylinder 2, the simulation starting position at 0 deg CA corresponds to 540 deg CA in the curves of Figures 39 and 41.

At 90 deg CA, the oil volume fraction distributions are different in the two cylinders, since the pistons start from different positions. Piston 1 starts at the TDC, producing a gas and oil jet pushed forward by the piston motion. Piston 2 on the left-hand side starts at the BDC, depositing some oil along the liner, since the blow-by inlet velocity is of the order of the mean piston velocity of about 8 m/s. The piston velocity is the dominating velocity at 90 deg CA, and the gas is pumped from the right cylinder 1 to the left cylinder 2. The orange coloured cloud in the droplet diameter distribution indicates that piston 2 reaches the maximum of the droplet diameter curve of about 4.6 µm. Meanwhile, piston 1 on the right-hand side approaches the maximum of the gas mass flow rate curve, which occurs slightly after 180 deg CA, as shown in Figure 39. The blow-by gas jet along the liner wall carries the oil droplets into the crankcase. During the downward motion, the deposited oil is accumulated and transferred in a radial direction towards the cylinder axis.

From 180 deg CA to 360 deg CA, piston 1 moves upwards, and the oil cloud is partially sucked back, following the upward motion of the piston. The three-dimensional flow transports some oil radially inwards under the flat piston, forming a cumulative cloud close to the blow-by inlet. In the meantime, piston 2 moves downwards, and the first oil droplets leave the cylinder region and enter the space of the crankcase underneath the cylinders. From 360 to 540 deg CA, this process goes in the opposite direction, since piston 1 moves downwards, pushing the gas to the left-hand side, where piston 2 moves upwards. Hence, the oil droplets are sucked back again, and, at 450 and 540 deg CA, a concentrated droplet cloud underneath the piston bottom of cylinder 2 can be observed.

In the following time steps at 630 and 720 deg CA, a growing oil droplet cloud is visible. It is interesting that, at 630 deg CA, the average Sauter mean diameter of the oil droplets underneath piston 2 on the left-hand side is bigger than the average droplet size underneath piston 1 on the right-hand side. This results from the time shift in the droplet diameter curves. Piston 2 has already passed the crank angle with the biggest droplet diameter, while piston 1 did not yet pass that region. After the first cycle at 720 deg CA, the oil mist is only purely distributed in the crankcase. The oil cloud is visible in the region underneath the pistons, but only a small fraction of the oil has entered the crankcase housing. The very small droplet diameters cause high drag forces, so that the droplets can clearly follow the gas flow

induced by the up and down moving pistons. Hence, for observing the propagation of the oil mist in the whole crankcase, the simulation of further engine cycles is necessary.
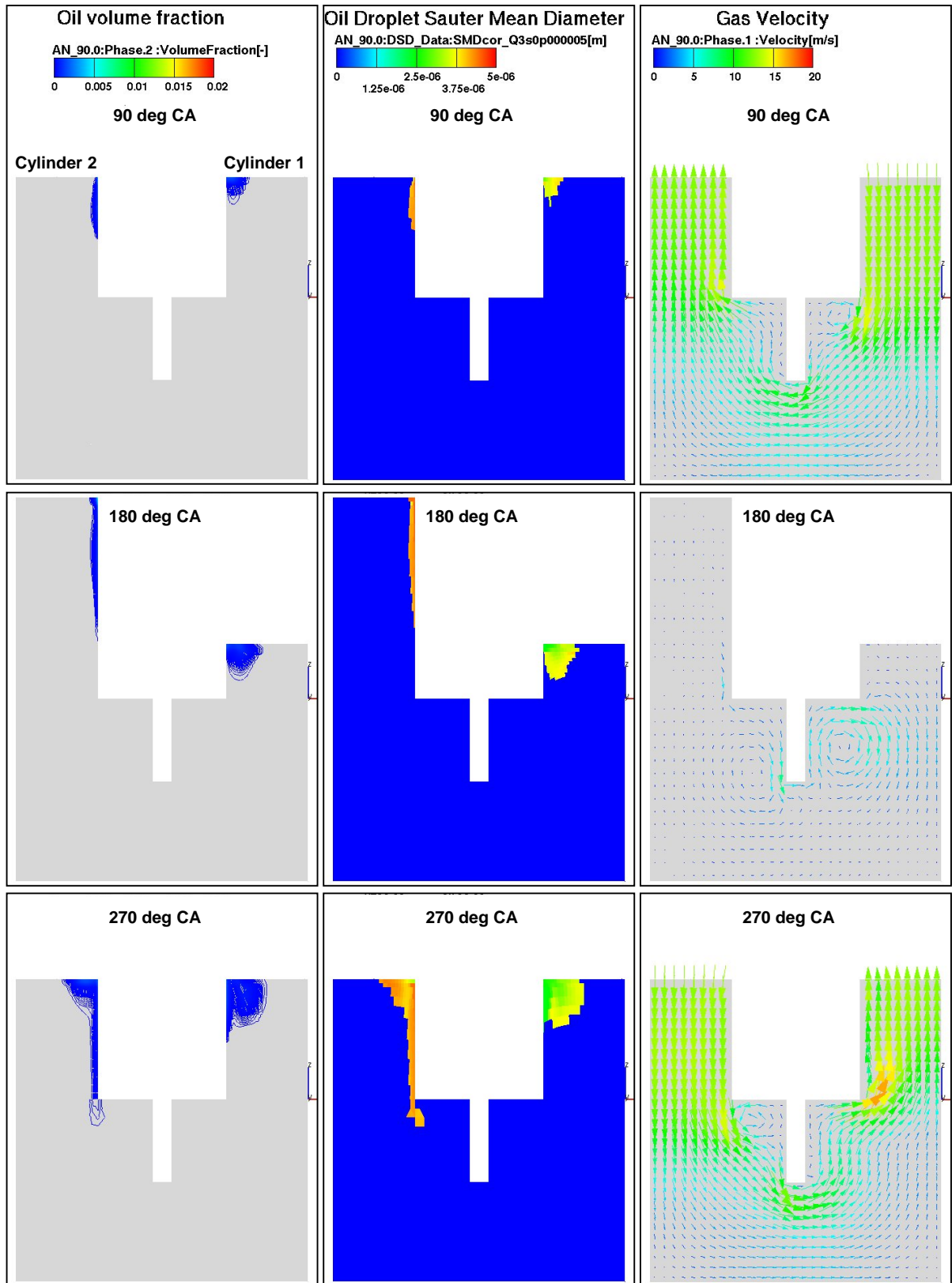

Figure 76: Oil volume fraction, local droplet Sauter mean diameter, and gas velocity at 90, 180 and 270 deg CA
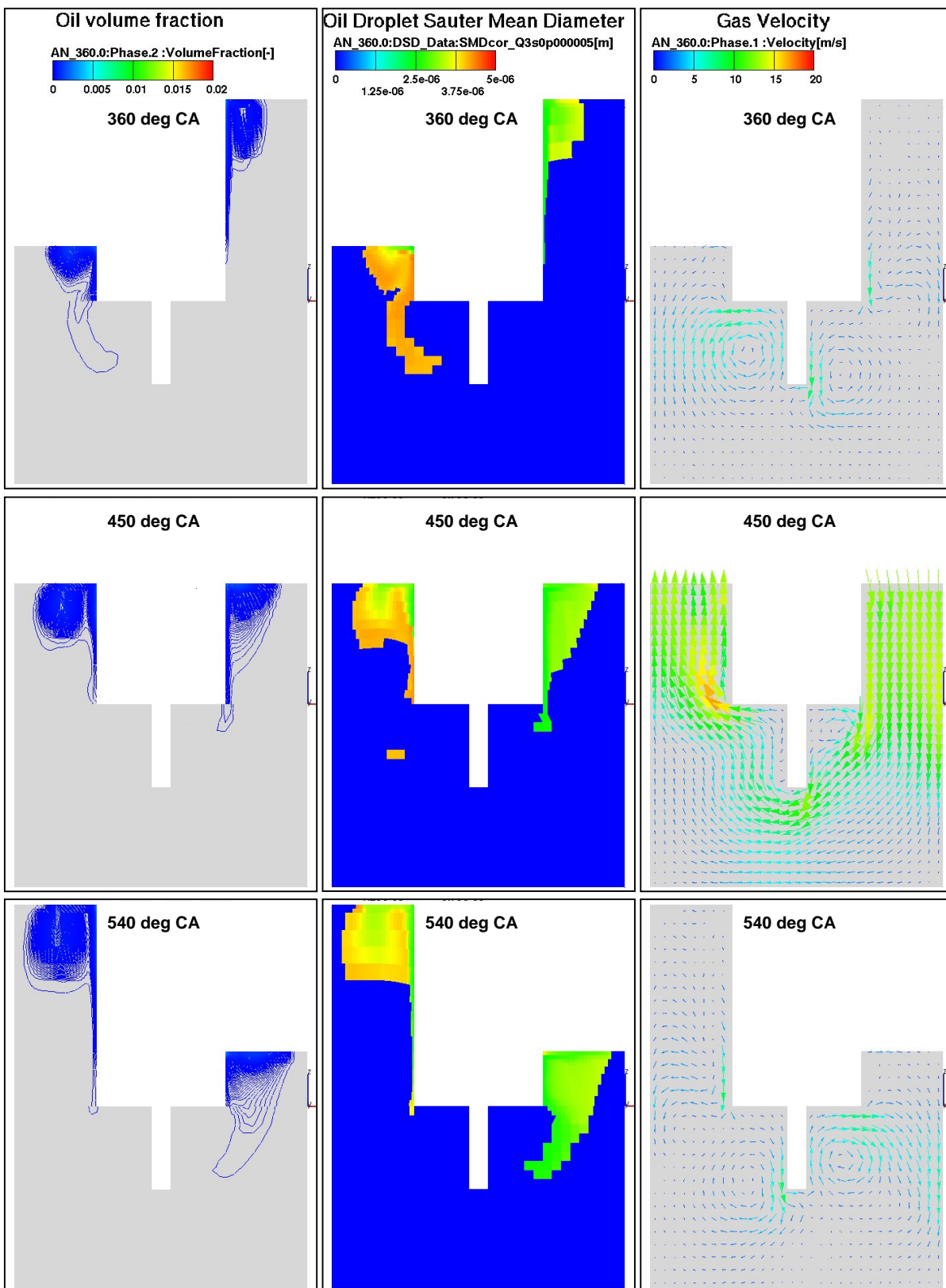
Figure 77: Oil volume fraction, local droplet Sauter mean diameter, and gas velocity during the first simulated engine cycle at 360, 450 and 540 deg CA
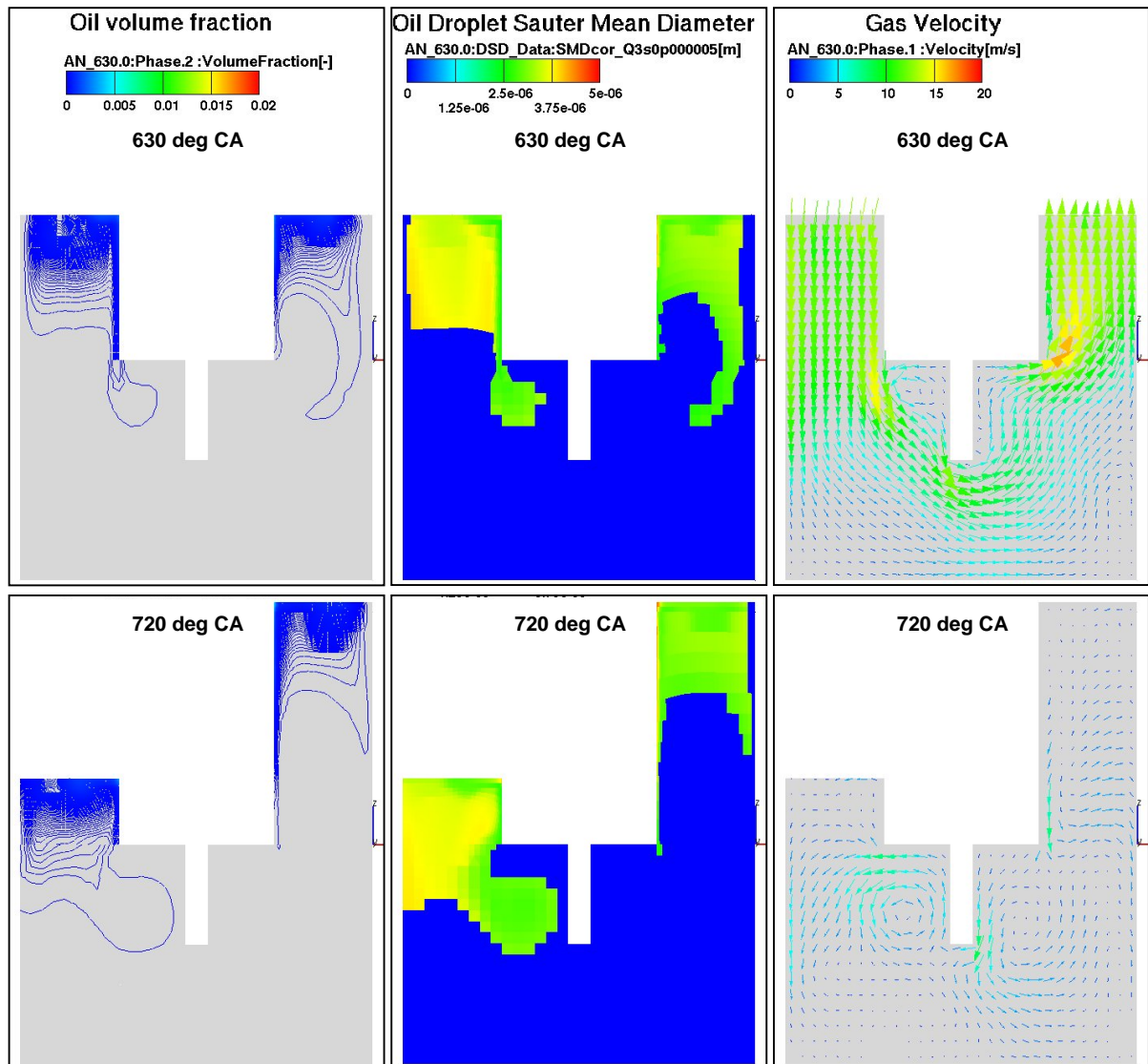
Figure 78: Oil volume fraction, local droplet Sauter mean diameter, and gas velocity during the first simulated engine cycle at 630 and 720 deg CA

Figure 79 shows a three-dimensional view of the distribution of the liquid oil volume fraction and the local droplet Sauter mean diameter during the first cycle from 0 to 720 deg CA. The figures show surface cuts, where the cell values in the boundary layer of the computational mesh are extrapolated onto the surface which covers the entire computational domain. In that view, cylinder 2 is positioned in the front, and cylinder 1 at the back. One can observe clearly the oil propagation from the blow-by inlet along the piston skirt at the liner. During the downward motion of the piston, the oil cloud is pushed downwards by the gas flow. When the piston moves upwards, the oil cloud is partially sucked back. The red coloured zone around the blow-by inlet in the droplet diameter cut indicates that large droplets are injected at that time.
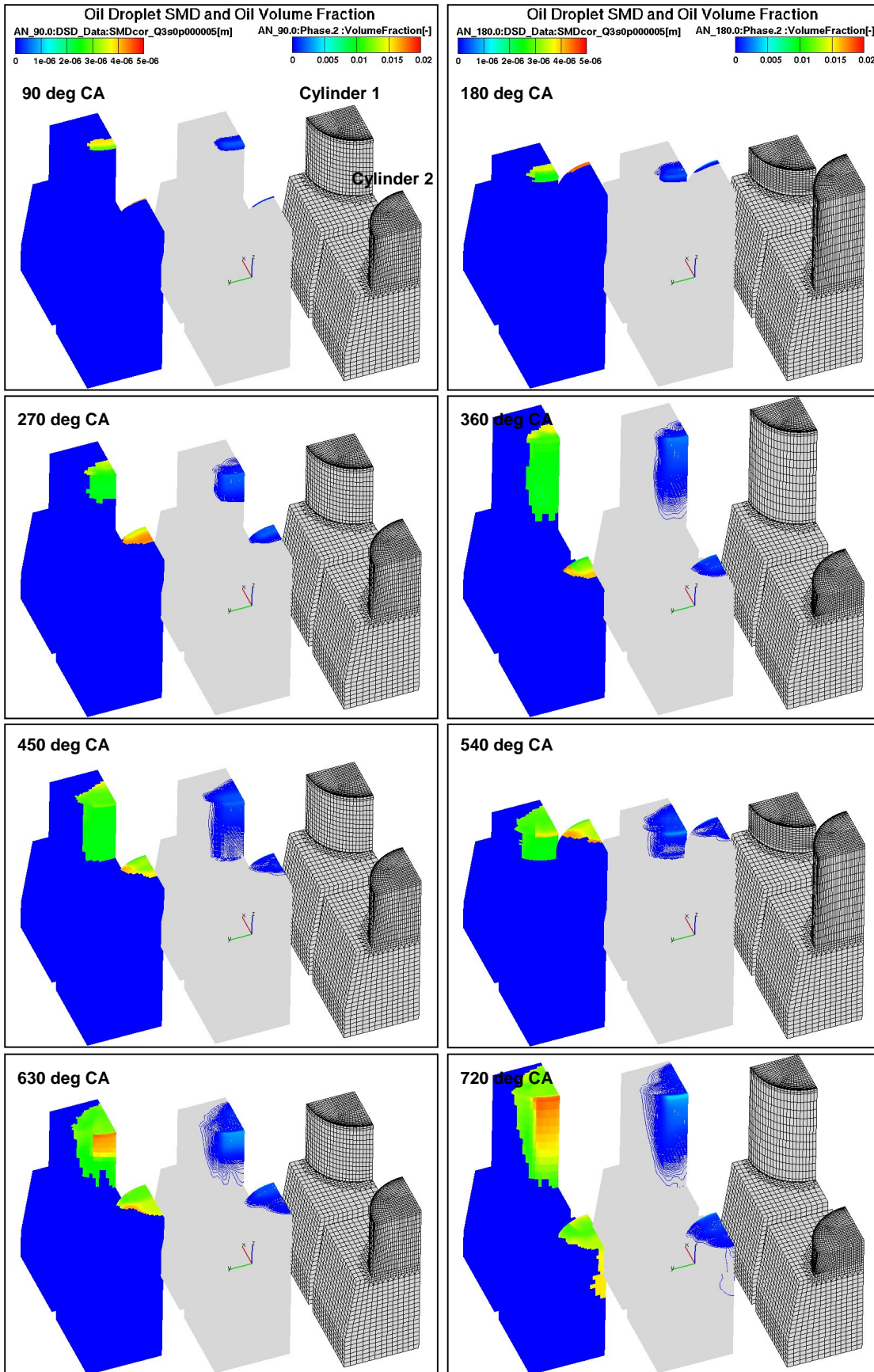
Figure 79: SMD and oil volume fraction at 90, 180, 270, 360, 450, 540, 630 and 720 deg CA

For cylinder 1, the largest droplets of the oil mist enter the crankcase between 630 and 720 deg CA, since there the droplet diameter curve of Figure 41 exhibits its maximum. At 720 deg CA, large oil mist droplets are deposited along the liner wall. In the following downward motion, these droplets are mixed with smaller droplets, and the local Sauter mean diameter decreases again.

The three-dimensional view shows very clearly that, after one simulated engine cycle, the oil droplets are only poorly distributed in the crankcase. The droplet clouds are mainly located in the regions underneath the pistons. Thus, the simulation has been performed for four further engine cycles from 720 to 3600 deg CA.

Figure 80 shows the oil volume fraction, the local droplet Sauter mean diameter, and the gas velocity vectors for the following engine cycles, each 90 deg CA before the end of the cycle, at 1350, 2070, 2790 and 3510 deg CA. Together with the plot at 630 deg CA in Figure 78, the evolution of the flow field at corresponding time steps over five engine cycles can be observed. With every engine cycle, the oil droplet cloud penetrates deeper into the crankcase. While at 630 deg CA the oil droplets are distributed only in the regions underneath the piston bottoms, at 3510 deg CA the oil is already distributed in the whole crankcase. The droplet Sauter mean diameter distribution is more homogeneous. Close to the blow-by inlet, the droplet diameter changes according to the curve in Figure 41. A certain distance away from the blow-by inlet, the droplet diameter distribution shows an almost homogeneous light green field, indicating an average droplet Sauter mean diameter of about 3.5 μm. This value can be interpreted as the time-dependent mean diameter of Figure 41.

It is very interesting to watch the evolution of the gas flow field illustrated in the vector plots. While there are obvious differences in the flow fields between 630 and 1350 deg CA, the differences between 1350 and 2070 deg CA are much smaller, and the vector plots at 2070, 2790 and 3510 deg CA are almost identical. The simulation was started with a flow field at rest, and hence some revolutions are required until the flow field is fully developed. This allows for the assumption that the gas flow field recurs periodically after three simulated engine cycles. However, it has to be considered that the gas velocity vectors are plotted on a coarser grid constituting a coarser flow field resolution. After three engine cycles, the oil droplets are not fully distributed in the crankcase. Hence, minor differences from cycle to cycle can be expected locally in regions which are just reached by the oil droplet cloud.
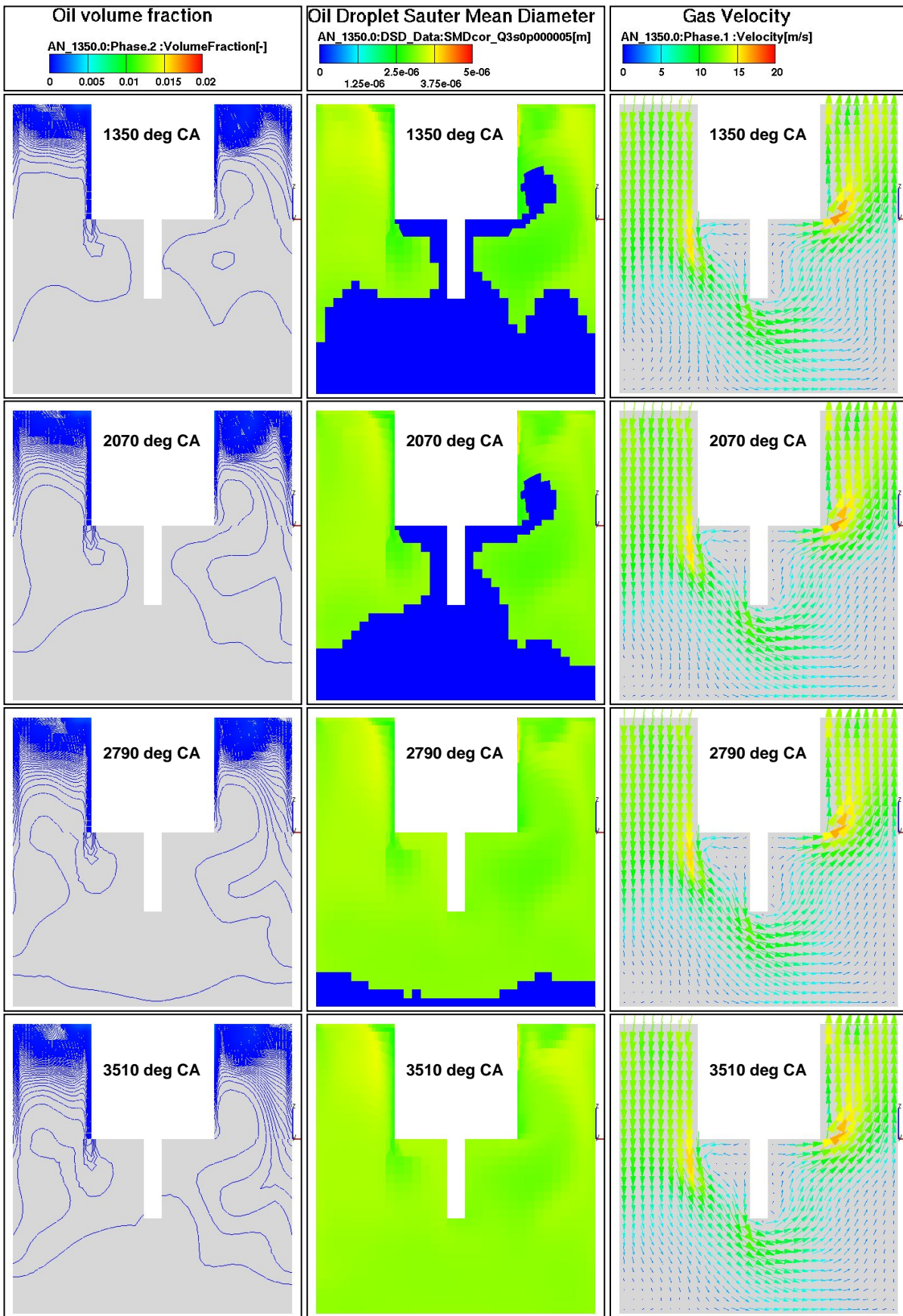
Figure 80: Oil volume fraction, local SMD, and gas velocity at 1350, 2070, 2790 and 3510 deg CA
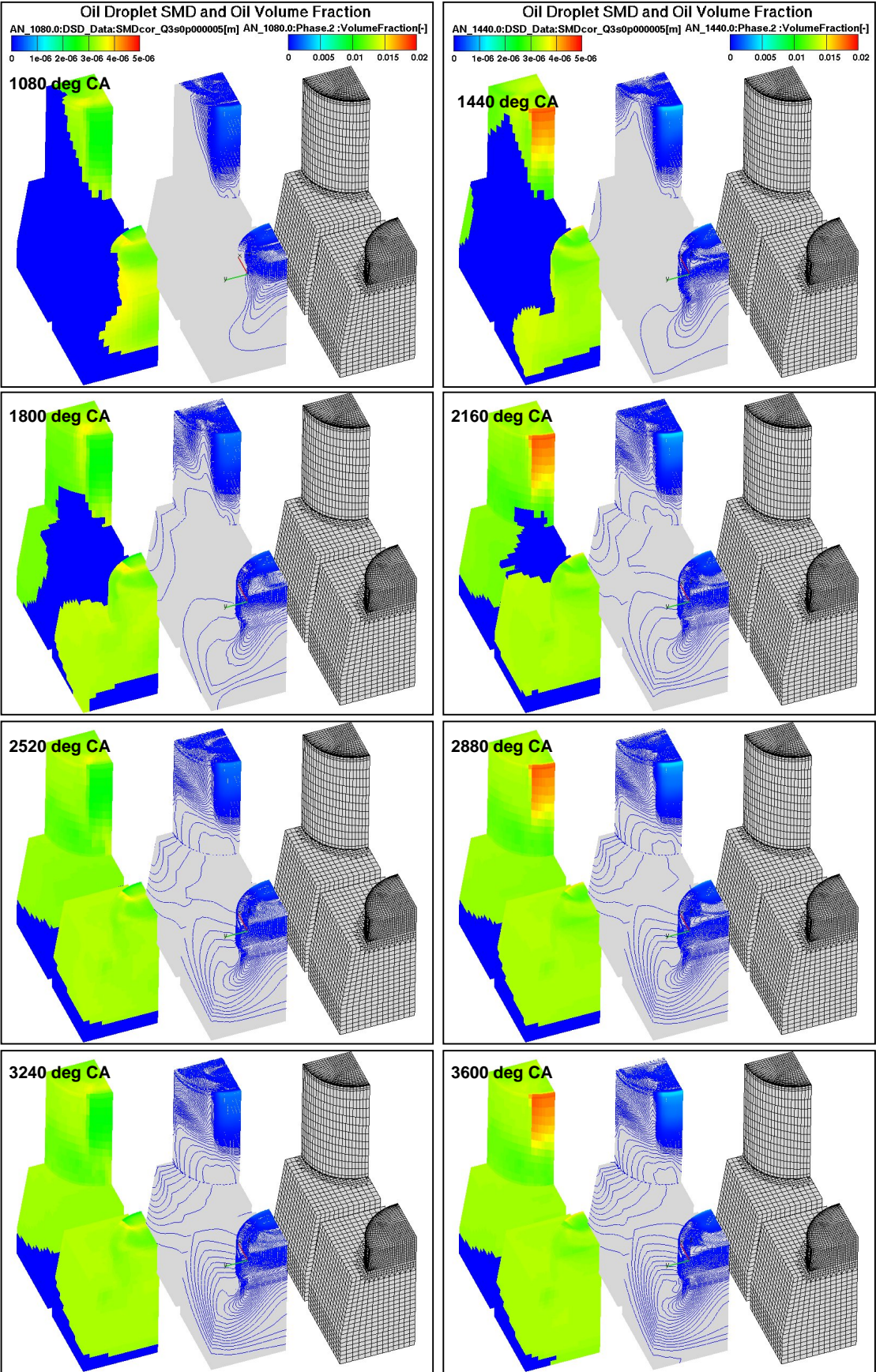
Figure 81: SMD and oil volume fraction at 1080, 1440, 1800, 2160, 2520, 2880, 3240 and 3600 deg CA

Figure 81 shows the three-dimensional view of the oil volume fraction and the local droplet Sauter mean diameter distributions at every 360 deg CA for the second to the fifth simulated engine cycle. The propagation and homogenisation of the oil droplet cloud are clearly visible. After three engine cycles, the oil droplet cloud has entered the crankcase for the most part. After five simulated engine cycles, the oil droplets are already distributed in the whole crankcase. Only in a small region at the bottom of the crankcase the oil volume fraction is less than $5 \cdot 10^{-6}$ and hence it is not visible in that plot.

Although the droplet cloud has reached almost the whole crankcase after five engine cycles, a homogeneous oil distribution is not reached in that time, since the oil concentration below the pistons is much higher than at the bottom of the crankcase. If a real engine runs at a certain operation point for a while, the gas and oil flow field in the crankcase reaches a quasi-steady state. The performed blow-by flow simulations do not reach this state. However, this is no weak point of the methodology; it is a matter of the computational effort. If the crankcase flow is simulated for several seconds, that means several hundred revolutions, the quasi-steady state would be reached, and the flow field would return every engine cycle.

Contrary to previous simulations published in [34] and [35], the total mass of atomised oil, determined by the oil strip thickness δ_{strip}, is much smaller in the current blow-by flow simulation. In the previous simulations, the strip thickness was estimated to be $1\,\mu m$. Measurements in [48] yielded a more precise estimation of the amount of oil passing the piston ring pack. The assumption of full atomisation of that oil mass yielded the applied value for the strip thickness δ_{strip} of $0.1\,\mu m$. The smaller amount of atomised oil mass in the current simulation is responsible for the retarded homogenisation of the oil in the crankcase. Furthermore, the influence of the oil droplets on the gas flow field is lower, since the drag forces in the computational cells are proportional to the number of droplets, and hence they are proportional to the atomised oil mass. However, the current blow-by simulation, which includes transport of the moments of the droplet size distribution and the application of a more accurate value for the strip thickness, yields more reliable results.

The blow-by flow simulations performed on the simple crankcase geometry over several engine cycles yielded some interesting information. Due to the transport of the moments of a droplet size distribution function it was possible to obtain a local droplet diameter distribution in an Eulerian-Eulerian multi-phase simulation. It could be shown that, at a certain distance away from the blow-by inlet, the local droplet Sauter mean diameter tends to an average value. Furthermore, the oil droplet concentration is not homogeneous after five

engine cycles. The gas flow field needs about three simulated engine cycles until it is fully developed with vanishing differences to the previous and the subsequent engine cycle.

5.3 Simulation of the Oil Disintegration on the Crankweb

The results of the simulation of the oil disintegration on the rotating crankweb are presented in this section. The simulation is performed on the computational mesh considering one half of a real 1-cylinder crankshaft, as represented in section 5.1. At first, an implementation test demonstrates the correct implementation of the model in the CFD code. Then the set-up of the CFD simulation is discussed, and finally the results of the simulation are presented.

5.3.1 Implementation Test

This section demonstrates that the correlations of the liquid disintegration model on the rotating disc are implemented correctly in the CFD code FIRE. For this purpose, the results for the mean droplet diameter and the radial velocity component in the CFD simulation are compared with manually calculated results. The droplet diameter and the radial velocity component, which depend on the corresponding disintegration regime, act as boundary conditions for the CFD simulation and are represented by the CFD post-processor. The correct implementation is demonstrated on two different operation points.
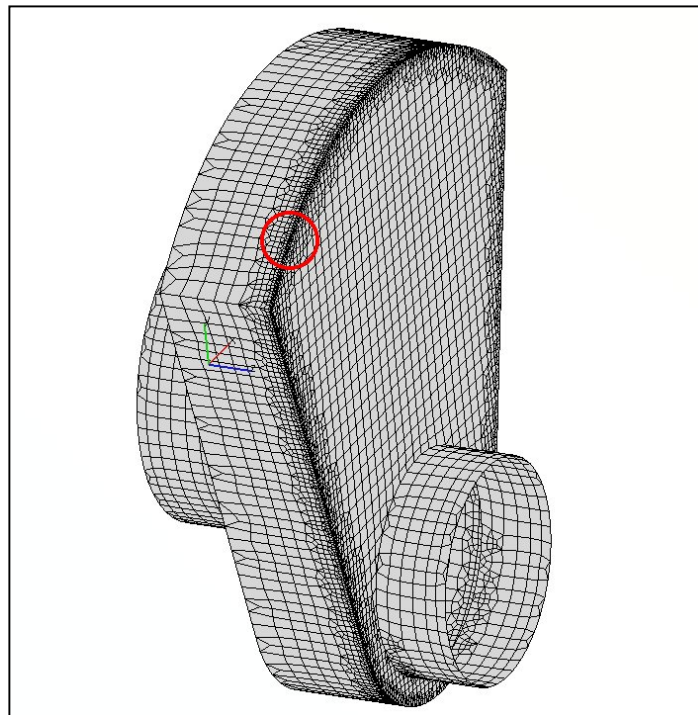

Figure 82: Region in the computational grid considered for the implementation test (red circle)

The implementation test is performed for the region at the crankweb edge, which is marked by the red circle in Figure 82. There the counter weight of the crankweb consists of a sector of a circular disc. The radius of the edge is 84 mm in that region. This means that the corresponding disc diameter for the determination of the disintegration regime is 168 mm.

The set-up of the test example is shown in Table 7. Two operation points have been chosen for this test to show the correct implementation of the correlations in different disintegration regimes. The only difference between Point 1 and Point 2 is the liquid volume flow rate on the crankweb. Similar to previous tests, the oil OMV Truck LD SAE 15W-40 is used as the engine oil. The liquid properties are deduced for an oil temperature of 100 °C. The ambient gas in the crankcase is air with a temperature of 100 °C.

			Point 1	Point 2
General calculation set-up	Rotational speed n	rpm	3000	3000
	Volume flow rate over crankweb	l/min	0.45	0.57
	Diameter of crankweb edge	m	0.168	0.168
	Model constant C_3 in Eq. (91)	-	2.55	2.55
Engine oil properties (OMV Truck LD SAE 15W-40)	Kinematic viscosity ν_d	m²/s	$14.9 \cdot 10^{-5}$	$14.9 \cdot 10^{-5}$
	Dynamic viscosity μ_d	Ns/m²	0.0123931	0.0123931
	Density ρ_d	kg/m³	831.75	831.75
	Surface tension σ	N/m	0.02561	0.02561
Ambient gas: air at 373 K	Pressure p	Pa	100 000	100 000
	Density ρ_c	kg/m³	0.93413	0.93413

Table 7: Set-up for CFD simulation for implementation test

The disintegration regimes are determined according to the correlations by Grave [42], which are represented in section 3.3.2. The droplet Sauter mean diameter, which depends on the disintegration regime, is calculated with the correlations of Hege [44], [45], and the adapted correlation from Walzel [87], which can be found in section 3.3.3.

In the first step of the implementation test, the disintegration regime is determined. Therefore the Weber number We of the rotary atomiser, the volume flow rate number $\dot{V}^*$, the square of the Ohnesorge number Z, and the fluid number K_F for both points are calculated in the first, second, third, and fourth columns of Table 8. All dimensions of Table 7 have to be inserted in SI-units. Only the volume flow rate number $\dot{V}^*$ is different for

the two data points. The other dimensionless numbers do not depend on the volume flow rate on the disc. The transition curves between the different disintegrations regimes are calculated in the fifth, sixth, and seventh columns of Table 8. Equation (77) determines the transition curve $x_{2,dr/\lg}$ between droplet and ligament disintegration, Equation (79) determines the transition curve $x_{2,\lg/sh}$ between ligament and sheet disintegration, and Equation (80) determines the transition curve $x_{2,atom}$ to the atomisation regime. The dimensionless coordinates of the disintegration regime map, x_1 and x_2, are calculated according to Equation (76) in the eighth and ninth columns of Table 8.

	1	2	3	4	5	6	7	8	9
Point	We	$\dot{V}^*$	Z	K_F	$x_{2,dr/\lg}$	$x_{2,\lg/sh}$	$x_{2,atom}$	x_1	x_2
1	$1.52 \cdot 10^7$	$3.85 \cdot 10^{-4}$	$4.29 \cdot 10^{-5}$	$6.03 \cdot 10^4$	10.52	95.80	152.9	0.0861	81.58
2	$1.52 \cdot 10^7$	$6.18 \cdot 10^{-4}$	$4.29 \cdot 10^{-5}$	$6.03 \cdot 10^4$	7.09	64.60	159.0	0,1091	81.58

Table 8: Calculation of disintegration regime

The values for x_2 are equal for both operation points, because the volume flow rate does not appear in the equation for x_2. Both values for $x_{2,atom}$ are greater than x_2, and hence the atomisation regime can be excluded. Furthermore, both values for $x_{2,dr/\lg}$ are smaller than x_2, and so the dropwise disintegration regime can also be excluded. The value for x_2 of Point 1 is greater than $x_{2,dr/\lg}$ and less than $x_{2,\lg/sh}$. Thus Point 1 belongs to the ligament disintegration regime. The value for x_2 of Point 2 is greater than $x_{2,\lg/sh}$, and consequently sheet disintegration is the expected regime for that operation point. For better illustration, Figure 83 shows the two operation points in the disintegration regime map.

The droplet diameter and the radial velocity component are calculated in Table 9. For ligament disintegration, the droplet diameter of Point 1 is calculated using Equation (90). The droplet diameter for sheet disintegration of Point 2 is determined by Equation (91). The oil film thickness δ is quoted as a matter of interest to represent the oil film thickness at the crankweb edge.

The detachment velocity exhibits of a radial and a circumferential component, as defined in Equation (161). The latter is determined by the radius of the crankweb edge and the rotational speed. The radial velocity component is calculated with Equation (164) for both disintegration regimes. Therefore the liquid rim thickness a and the distance between the ligaments l_{lig} are determined by Equations (67) and (71).
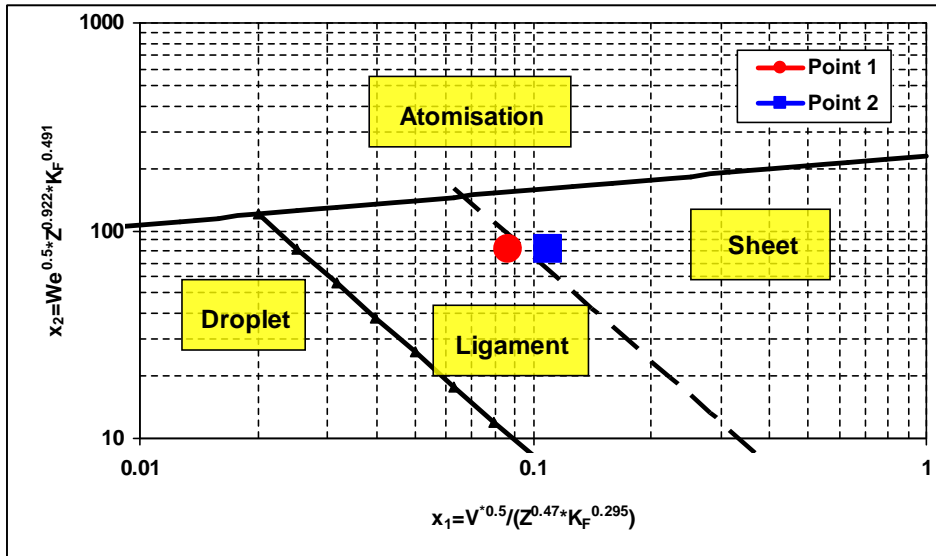
Figure 83: Disintegration regimes of the test points for implementation calculated according to Grave [42]

Point	regime	δ [μm]	d_d [μm]	a [μm]	l_{lig} [m]	U_r [m/s]
1	ligament	42.47	153.9	86.17	$5.23 \cdot 10^{-3}$	1.275
2	sheet	45.95	116.9	86.17	$5.23 \cdot 10^{-3}$	1.615

Table 9: Calculation of droplet diameters

Figure 84 shows the calculated boundary values in the CFD simulation for the droplet diameter and the radial velocity component for Point 1. Those values are calculated for every boundary face separately. This means that, for every boundary face, a corresponding rotary atomiser is determined to calculate the local droplet diameter, the components of the detachment velocity, and the liquid phase volume fraction. The colour bars are scaled for a very short data range, so that it is obvious that the results in the CFD simulation are equal to the results in Table 9. The small differences of the values between the faces result from the locally varying distance between face centre point and rotational axis. There are differences in the order of 0.1 mm resulting from the mesh generation process, which affect the local disc diameter of the corresponding rotary atomiser.

Figure 85 shows the local droplet diameters and the radial velocity components of the boundary faces for Point 2. Also there the CFD simulation shows the same values as the manually calculated values in Table 9.
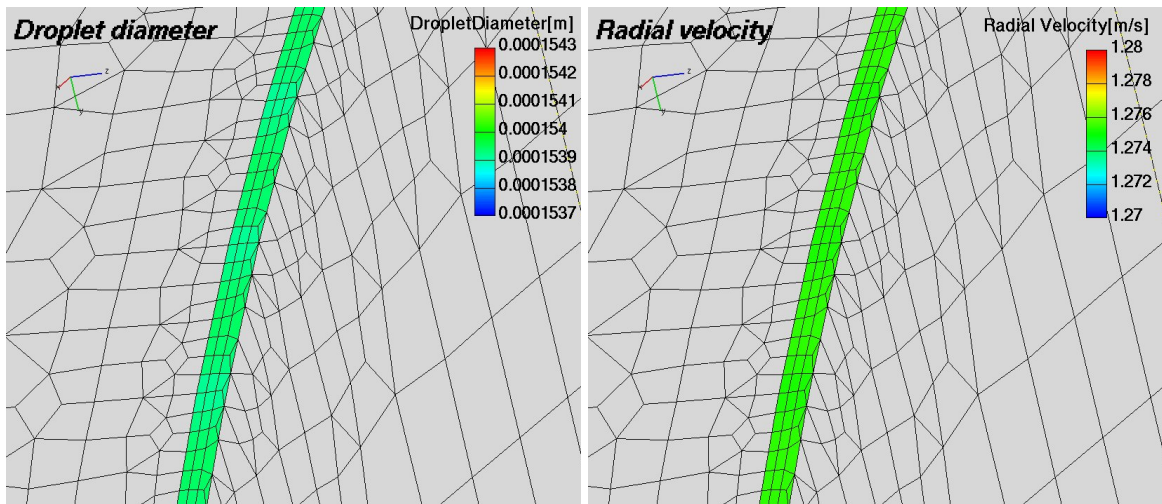
Figure 84: Droplet diameter and radial velocity at boundary condition of example Point 1
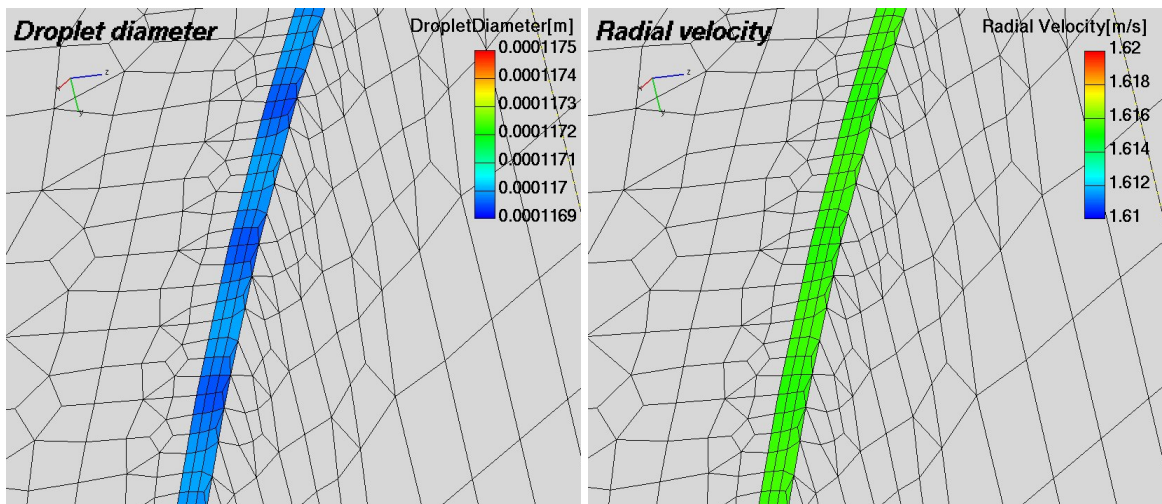

Figure 85: Droplet diameter and radial velocity at boundary condition of example Point 2

5.3.2 Set-up of the CFD Simulation

The set-up for the CFD simulation of the oil disintegration on the rotating crankweb is discussed in this section. The simulation is performed with exactly the same set-up as it was used in the implementation test of Point 1 in the previous section. A summary of the most important settings and parameters of the calculation is given in Table 10.

Similar to the simulation of the blow-by flow above, this simulation is performed with two phases. The gaseous phase is air, and the liquid phase is the engine oil OMV Truck LD SAE 15W-40 at 100 °C. The engine speed is 3000 rpm, and the calculation time step is determined by a crank angle step of 0.5 deg. The high number of computational cells causes high computational effort, and hence only one revolution of the crankshaft is simulated. At

simulation start, the flow field was at rest. The propagation of the oil droplets detaching from the rotating crankweb and the evolution of the gas flow field are the results of the simulation.

General calculation set-up	Rotational speed n	3000	rpm	
	Number of phases (gas and liquid)	2	-	Gas and liquid
	Time step	$2.78 \cdot 10^{-5}$	s	= 0.5 deg CA
	Simulated time	360	deg	One revolution
Oil disintegration model set-up	Volume flow rate over crankweb	0.45	l/min	
	Disintegration regime model	Grave	-	Equations (76), (79), (80)
	Droplet diameter correlation	Hege [44] and Walzel [87]	-	Equations (89), (90), (91)
	Model constant C_3	2.55	-	From Equation (91)
Droplet size distribution model set-up	Reference Sauter mean diameter	150	μm	Equation (120)
	Minimum Sauter mean diameter	50	μm	
	Maximum Sauter mean diameter	450	μm	
	Drag model	On	-	
	Collision model	Off	-	
Engine oil (OMV Truck LD SAE 15W-40) at 373 K	Kinematic viscosity ν_d	$14.9 \cdot 10^{-5}$	m²/s	
	Dynamic viscosity μ_d	0.0123931	Ns/m²	
	Density ρ_d	831.75	kg/m³	
	Surface tension σ	0.02561	N/m	
Ambient gas: air at 373 K	Pressure p	100 000	Pa	
	Density ρ_c	0.93413	kg/m³	

Table 10: Set-up for CFD simulation of the oil disintegration on the rotating crankweb

The oil flowing as a film on the crankweb is uniformly distributed, and it has a total volume flow rate of 0.45 litres per minute. This value is obtained from the volume flow rate curve in Figure 24, which results from a one-dimensional simulation of the lubricating oil circuit, as discussed in section 2.2. Uniform distribution means that the volume flow rate along the crankweb edge is not a function of the circumferential angle, and hence the inlet boundary conditions at the crankweb edge are determined by the correlations discussed in section 4.4.1.2. However, if the circumferential distribution of the oil volume flow rate along the crankweb edge is known, the simulation could be performed also with such a condition. Although both sides of the crankweb have sharp edges, from where the oil can detach, the oil

disintegration is only modelled on one side. This avoids a further increase of the number of computational cells, since there is no further grid refinement along the second edge required. The correlations of Grave [42] determine the disintegration regimes, and the correlations of Hege [44], as well as the adapted correlations from Walzel [87], determine the local Sauter mean diameters of the detached oil droplets.

The simulation is performed with transport of the moments of the droplet size distribution function. The reference Sauter mean diameter was set to 150 μm, representing an average value of the expected local droplet diameters detached from the crankweb edge. The minimum and maximum Sauter mean diameters are 50 μm and 450 μm. Hence, almost one order of magnitude in the range of the Sauter mean droplet diameter is covered by the transported droplet size distribution function. The drag force model determining the momentum exchange between the droplets and the gaseous phase is active. The collision model was deactivated, since, according to the photos in Figure 22 showing the oil disintegration in the different regimes, the droplet number density is small and collision has minor influence on the droplet flow.

The CPU time on a Linux workstation, 3.2 GHz in single processor mode, for the simulation of one revolution from 0 to 360 deg CA was about 110 hours. The moving mesh with unstructured computational cells and 36 rezones causes more solver iterations per time step than in the blow-by flow simulation, and hence the CPU time is disproportionately higher. For comparison: the simulation of the gas flow in the single-phase mode requires about 36 hours, while the two phase flow simulation with gas and oil, but without transport of the moments of the droplet size distribution function, requires about 72 hours.

5.3.3 CFD Simulation Results

The eagerly-awaited results of the CFD simulation in this thesis are presented in this section. At first the boundary conditions from the oil disintegration model at the crankweb edge are analysed, then the results of the overall flow field are presented at every 30 deg CA for the simulated revolution, and finally the gas flow field in a certain region is analysed in detail to demonstrate the complexity of the three-dimensional flow.

Figure 86 shows the local Sauter mean droplet diameter and the volume fraction of the liquid phase along the inlet boundary of the crankweb edge. Volume fraction and local SMD of the droplets at the boundary determine the boundary values for the transported moments Q_2 and Q_3. For an observer moving with the rotating crankshaft, the spatial distributions of the droplet SMD and the liquid volume fraction at the crankweb edge are steady. This means that, contrary to the blow-by flow simulation, the distributions do not change with time. If

the observer moves along the crankweb edge, droplet SMD and oil volume fraction change, since the conditions for each boundary face are calculated according to local "rotary atomisers".
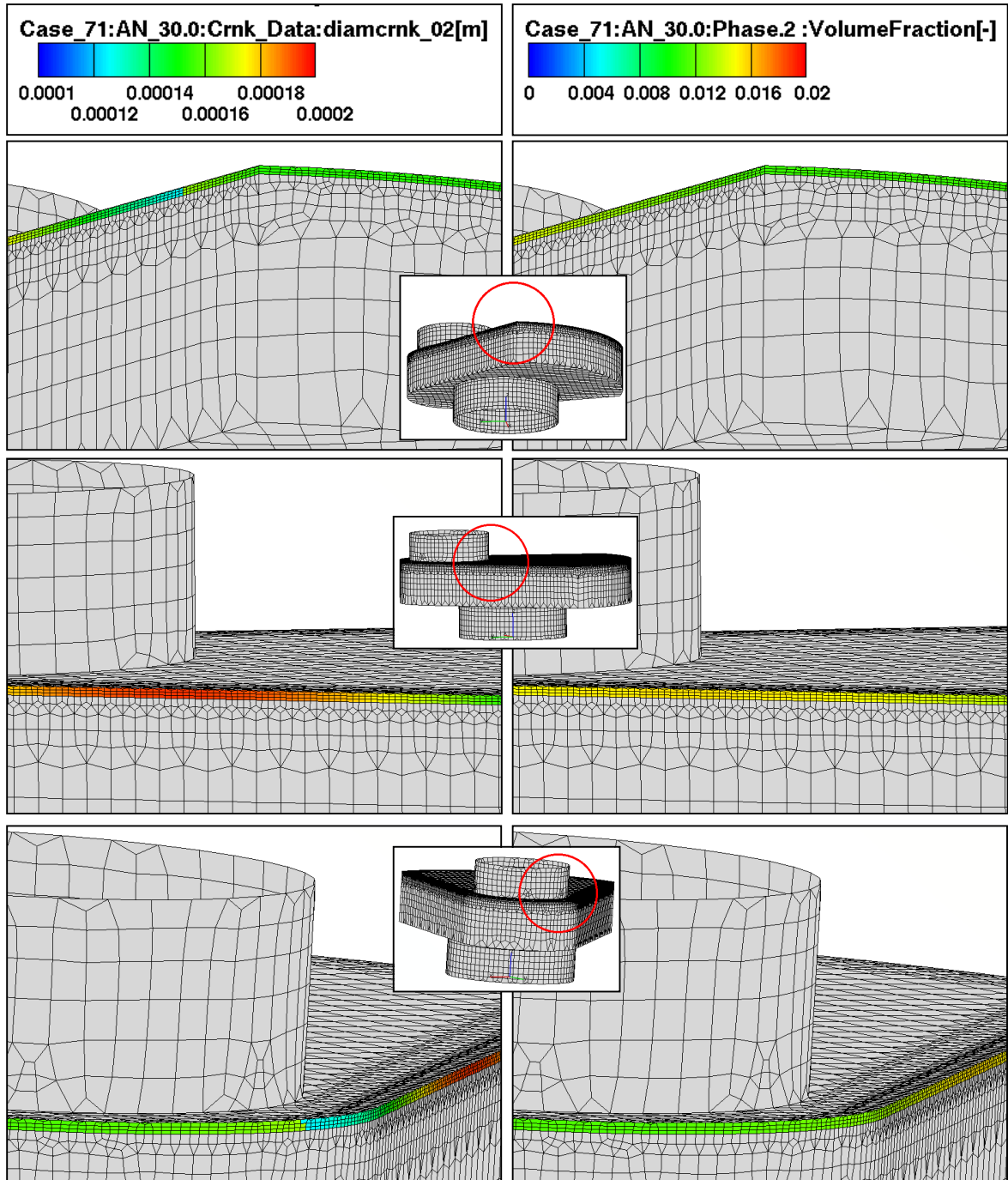

Figure 86: Local Sauter mean diameter and liquid phase volume fraction at detachment boundary

The droplet SMD at the boundary varies between approximately 120 and 190 μm. Two different disintegration regimes occur along the crankweb edge, sheet disintegration in the region where the radius of the crankweb is less than 73 mm, and ligament disintegration in

the other region. Dropwise disintegration does not occur, since the oil volume flow rate is too big for this regime. The abrupt jump from the larger to the smaller droplet diameters results from the transition between the two disintegration regimes. This effect can also be observed on the pink curve in Figure 67 right, where the droplet diameter curve for 100 °C oil temperature and 3000 rpm engine speed are drawn. The oil volume fraction along the inlet boundary varies between approximately 0.011 and 0.018.

Figures 87 and 88 show the gas velocity fields as vector plots in different cuts during one revolution. The plots in Figure 87 represent cuts perpendicular to the rotation axis in the middle of the crankweb. The plane representing the cuts in Figure 88 is determined by the cylinder axis and the rotational axis. Both vector plots of the gas velocity are interpolated onto a coarser grid to get a smooth vector distribution for showing the overall flow field.

From 0 to 180 deg CA, the piston moves downwards, pushing the gas from the piston bottom into the crankcase. During that time, the crank pin of the crankshaft moves along a circular curve from the top to the bottom position. From 180 to 360 deg CA, the piston moves upward again, and the gas is sucked back into the region underneath the piston. According to the kinematics of the crank drive, the piston velocity reaches the maximum values shortly before 90 deg CA and shortly after 270 deg. The plots show clearly that the highest gas velocities underneath the piston occur during those times. The highest gas velocities in the flow field occur when the gas flows around the sharp edge of the crankweb. Figure 87 shows that, at about 210 deg CA, the upward moving gas flow is superposed on the flow around the sharp edge of the crankweb, causing the maximum value in the flow domain of approximately 35 m/s.

The crankweb is not a circular disc, and hence the rotation of the crankshaft causes permanent displacement of the gas. The vector plots show clearly the regions where the gas is pushed away, indicated by vectors pointing out of the crankweb surface, when the crankweb covers new space of the flow domain. Apart from that, in regions where the crankweb sets space free, in the wake, the gas is sucked as it is indicated by vectors pointing to the crankweb surface. The periodically recurring displacement of the gas due to the piston motion as well as the permanent gas displacement due to the rotating crankshaft and the crank pin cause positive and negative pressures on the surface of the crank drive, which are responsible for the ventilation losses of the engine. The higher the engine speed, the higher the rate of the gas mass which is permanently displaced in the crankcase, and thus the higher the ventilation losses of the engine.
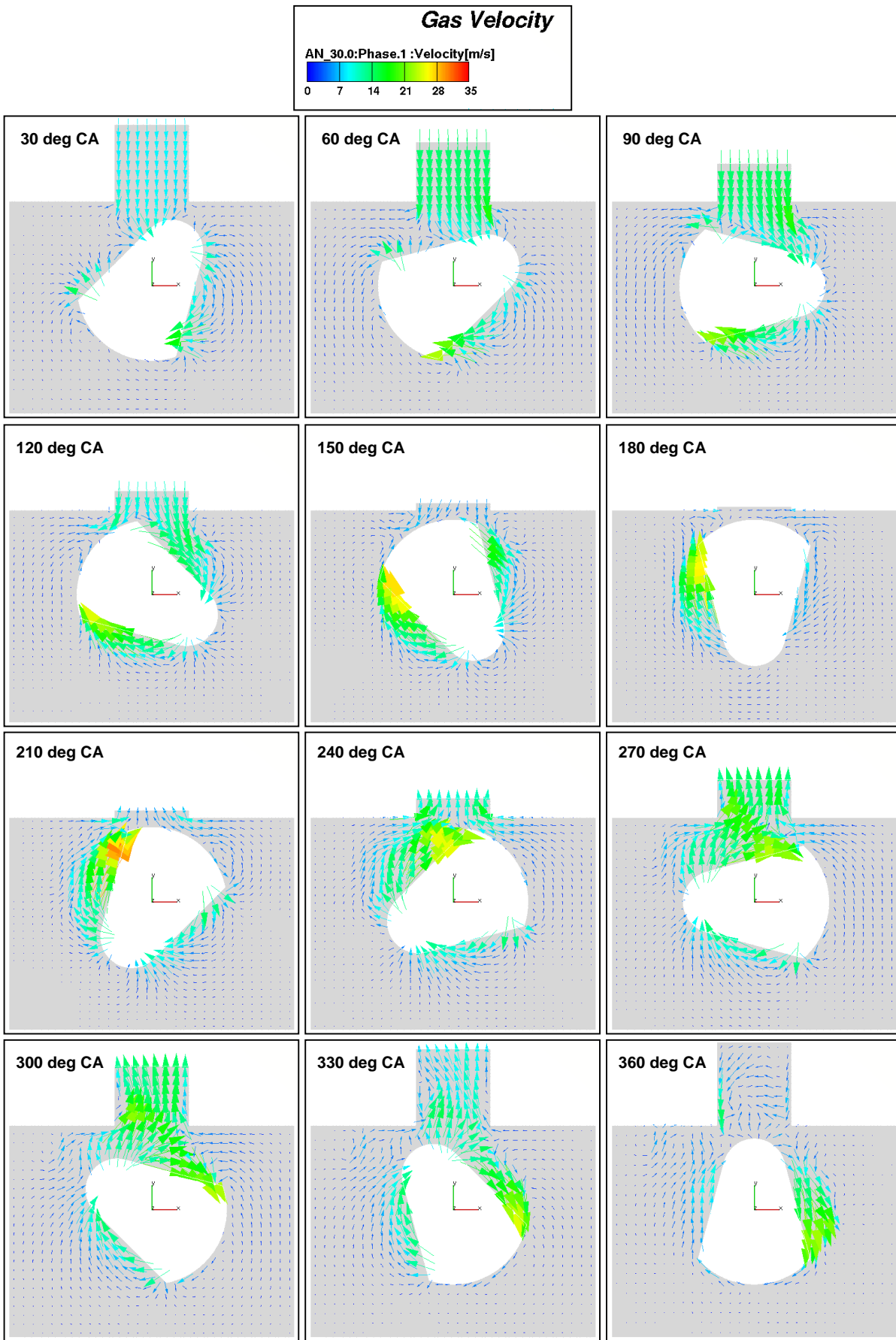
Figure 87: Gas velocity field in cuts perpendicular to the rotation axis in the middle of the crankweb
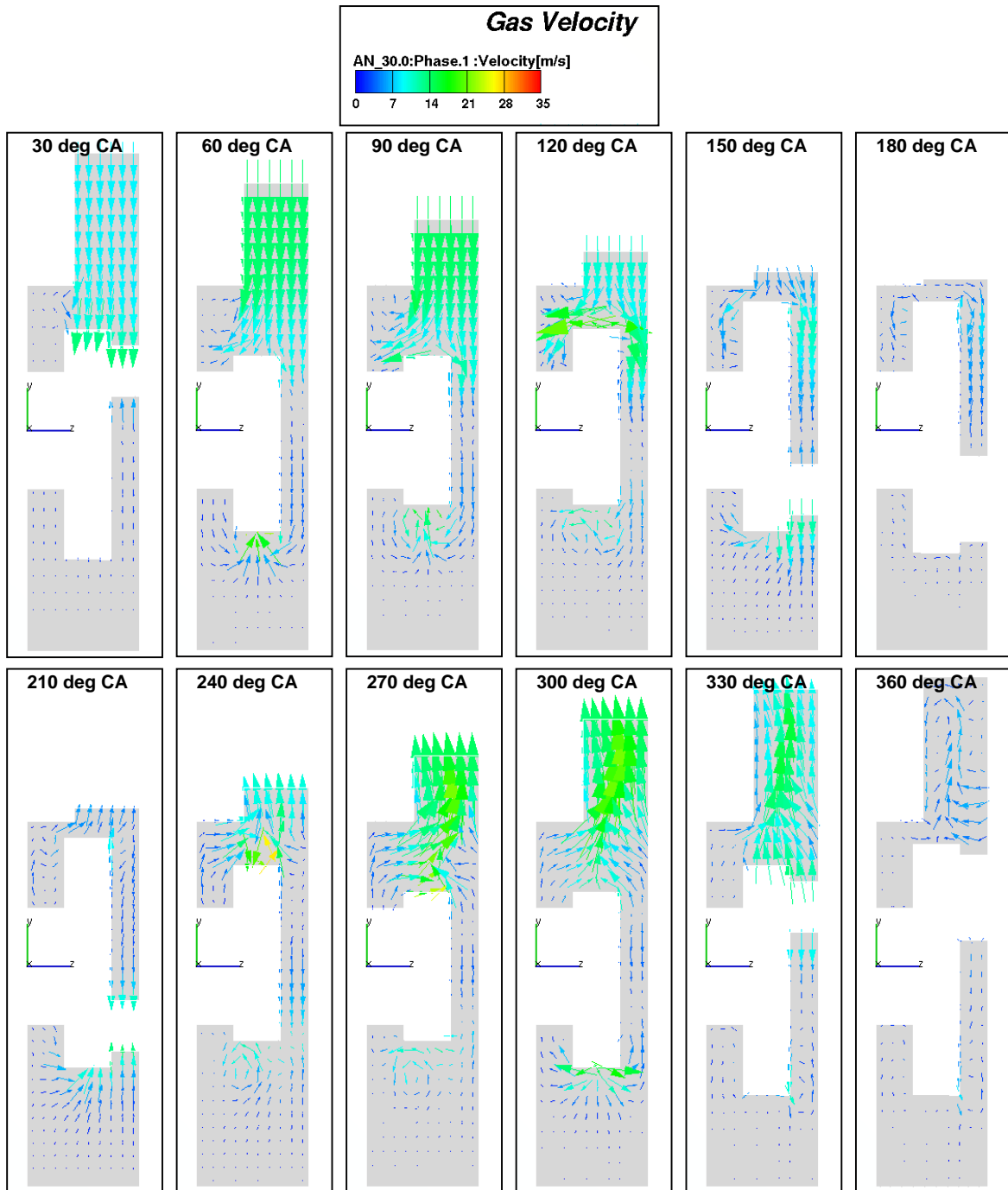
Figure 88: Gas velocity field during one revolution in cuts through cylinder axis and rotation axis

The gas flow is complex and fully three-dimensional. Especially at the dead centre positions at 180 and 360 deg CA, when the piston velocity is zero, the gas velocity field shows an interesting distribution. Although the spatial resolution of the vector plots in Figures 87 and 88 is much coarser than the mesh resolution, the complexity of the flow field is obvious. A further view of the gas velocity field in selected local regions will be shown and discussed in the plots of Figures 95 and 96 below.
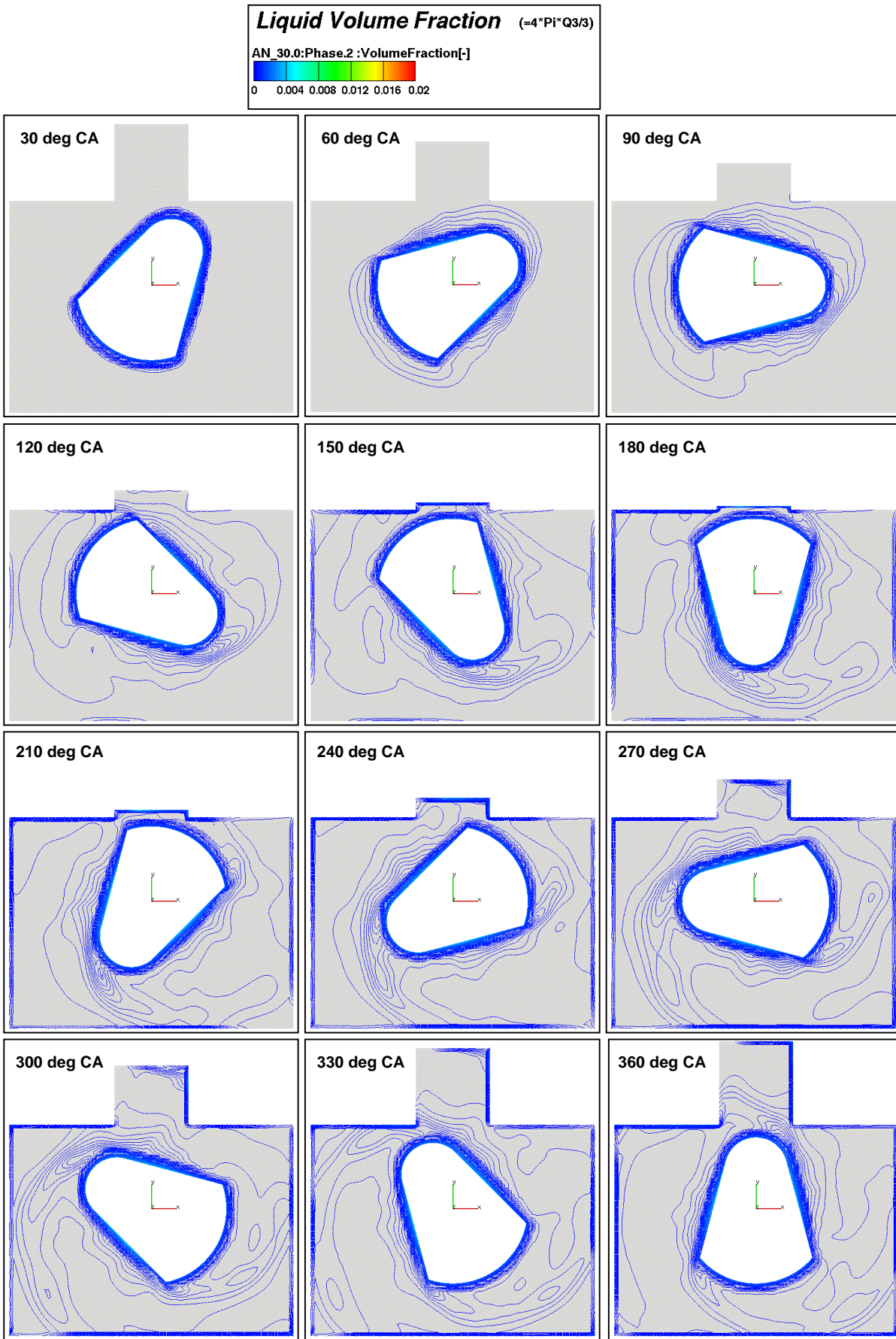
Figure 89: Liquid oil volume fraction during one revolution in cuts through the crankweb edge
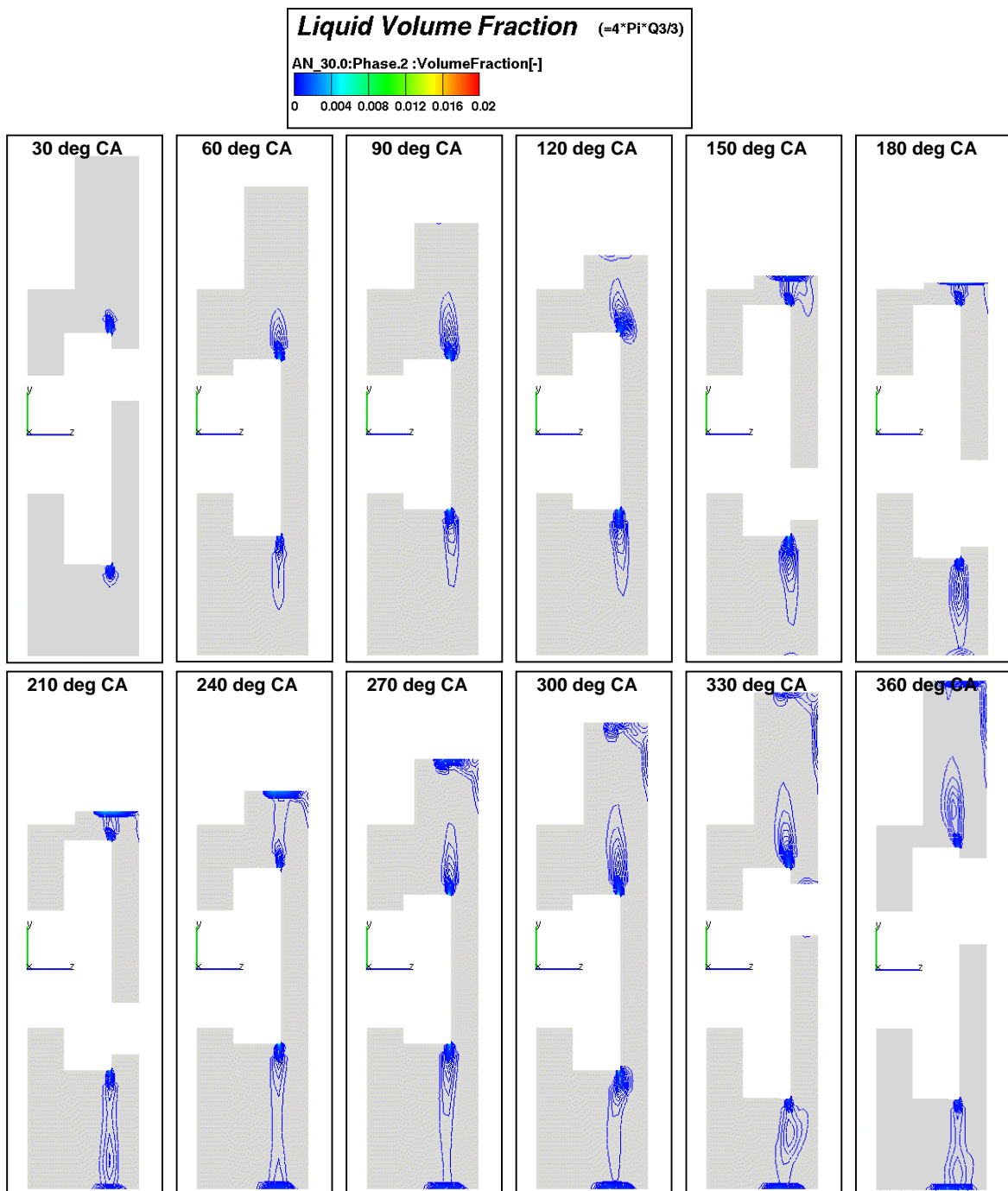
Figure 90: Liquid oil volume fraction during one revolution in cuts through cylinder axis and rotation axis

Figures 89 and 90 show the oil volume fraction distribution during one revolution. The plots in Figure 89 represent cuts perpendicular to the rotation axis through the inlet boundary along the crankweb edge. The plane representing the cuts in Figure 90 is exactly the same as shown for the gas velocity field in Figure 88. The oil volume fraction is drawn with isolines, where the minimum volume fraction is $5 \cdot 10^{-5}$. The simulation starts from rest at 0 deg CA,

where the piston is at the TDC and the crank pin is in its upper position. The oil droplet formation is plotted every 30 deg CA.

The plots in Figure 89 show the direction of the splash oil propagation within a plane perpendicular to the rotation axis. After entering the flow field, the droplets move to the outer wall on nearly straight trajectories. The flow direction is determined by the radial and the circumferential velocities at the detachment point on the crankweb edge, where the circumferential component is dominating. Due to drag forces the droplets slow down. For an observer rotating with the crankshaft, the droplets move away on an involute [44]. At 90 deg CA, first oil droplets reach the crankcase wall and accumulate close to the cylinder. At 120 deg CA, the oil droplets reach the bottom and the side wall of the crankcase. At 180 deg CA, the piston stays at the BDC, and the massive counter weight of the crankweb is located in the highest position causing a narrow gap between piston bottom and crankweb. Thus the oil accumulates at the piston bottom. From 180 to 360 deg CA, the piston moves upward pushing the accumulated oil also in the upward direction. Between 240 and 270 deg CA, the droplet cloud underneath the piston ruptures, since the piston is very fast there. At 360 deg CA, almost the whole crankcase wall in the considered plane is wetted by the engine oil. Apart from the cut through the crankweb edge, the amount of oil is rather small. The biggest part of the crankcase wall is not yet wetted by the oil after one revolution.

Figures 91 and 92 show the local Sauter mean diameter distribution of the splash oil droplets during one revolution. The SMDs of the droplets are plotted for regions where the liquid oil volume fraction is bigger than $5 \cdot 10^{-5}$. It is a remarkable result that, due to the transport of the moments Q_2 and Q_3, it is possible to obtain local Sauter mean droplet diameters in an Eulerian-Eulerian multi-phase simulation without segregation into droplet classes. As already mentioned above, the SMDs of the oil droplets disintegrating along the crankweb edge have values between 120 and 190 µm. In the flow field, SMDs outside this range exist. Different drag forces act in the momentum equations for the surface area-average and the mass-average velocities, $U_{d,2}$ and $U_{d,3}$. Hence the effect that small droplets slow down faster than large droplets is clearly visible. Especially in the figures for 90, 120, 150 and 180 deg CA one can see that there are large droplets at the front of the splash oil cloud, while the smaller droplets lag behind.
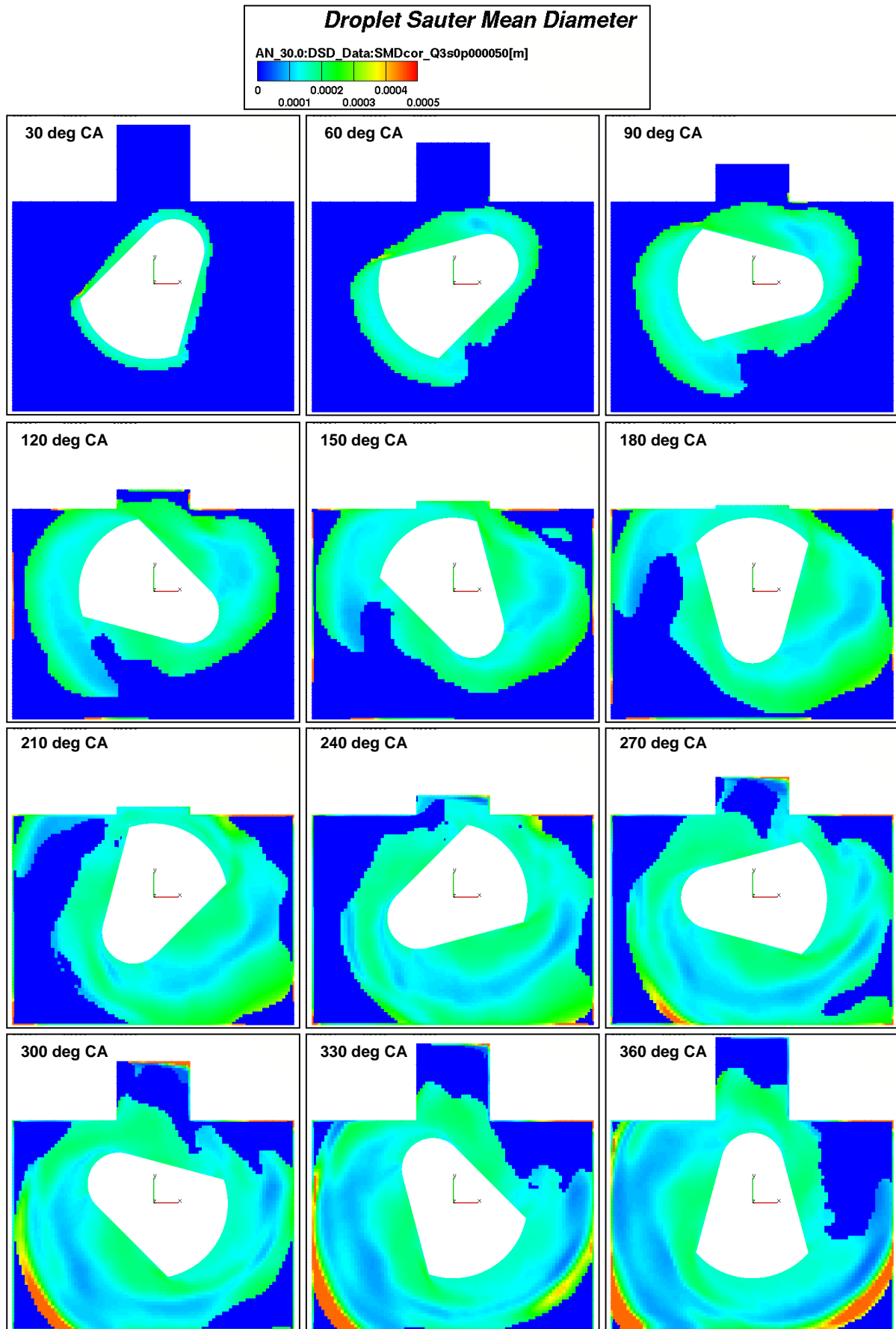
Figure 91: Spatial SMD distribution during one revolution (α_{min} =5·10^{-5}) in cuts through the crankweb edge
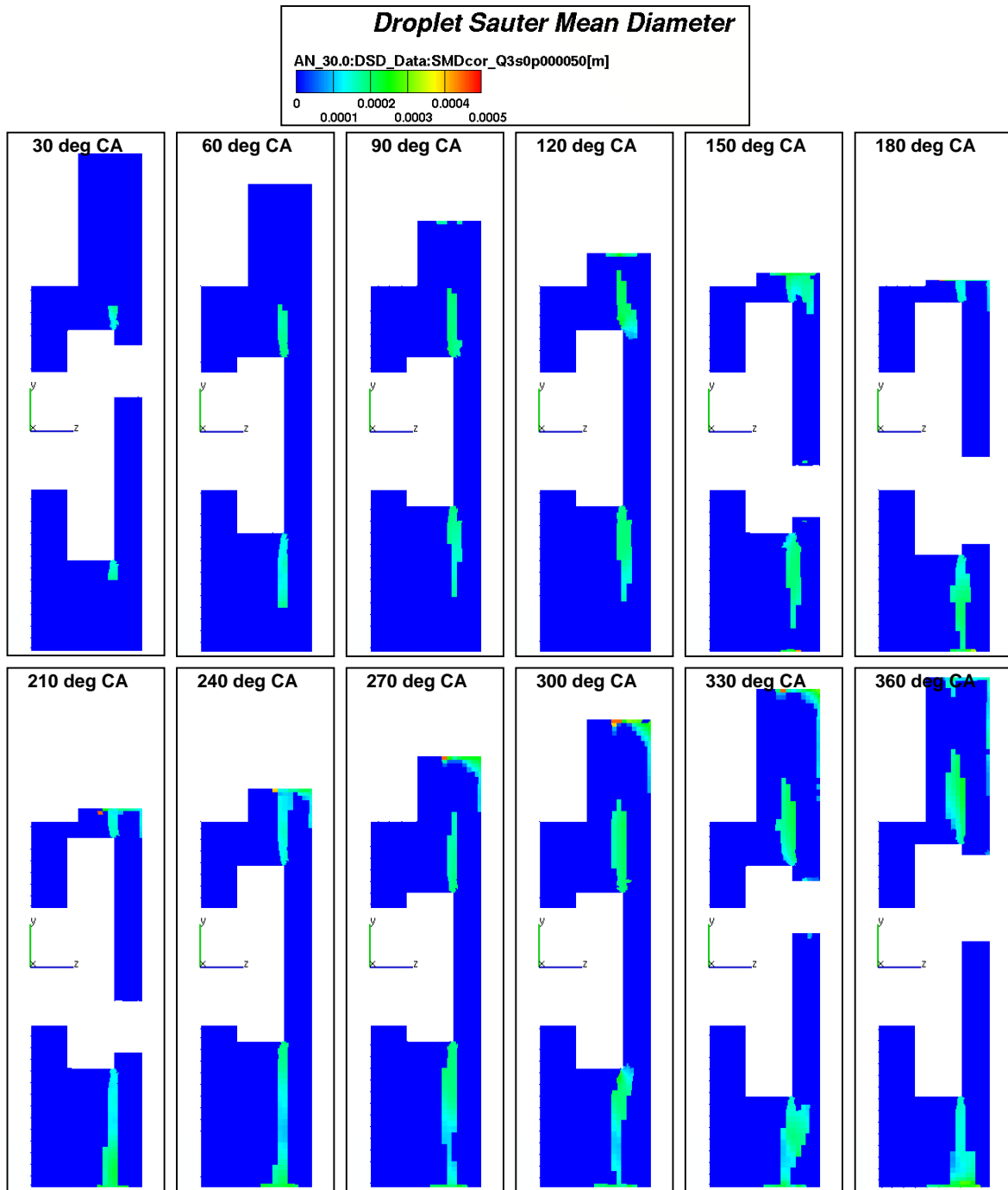
Figure 92: Spatial SMD distribution (α_{min} =5·10^{-5}) in cuts through cylinder axis and rotation axis

By considering the distributions of the velocities $U_{d,2}$ and $U_{d,3}$ in Figure 93, this effect is emphasised. Figure 93 shows the distributions of the gas velocity, the surface area-average velocity, and the mass-average velocity in the cut through the inlet boundary around the crankweb edge perpendicular to the rotation axis. The mass-average velocities at the front of the droplet cloud are higher than the surface area-average velocities, since the small droplets slow down faster than the large droplets. In the cuts of Figure 92, the radial propagation of

the droplets from the crankweb edge to the wall is shown. When inspecting those figures, it has to be taken into account that the circumferential velocity is the dominating velocity component. Thus the radial droplet propagation does not reflect the main flow direction of the droplets.

Figure 91 shows that, from 270 to 360 deg CA, the local SMD in some regions at the front of the droplet cloud reaches the maximum value of 450 μm. Especially in the regions where the droplets upstream have already reached the near-wall region, high values of the droplet SMD are visible. Large droplets reach the near-wall region first. That high SMD values are caused by separation of those "large" droplets due to the different velocity distributions of $U_{d,2}$ and $U_{d,3}$. One should keep in mind that the model of transport of the droplet size distribution was deduced for free droplet flow. There is no wall interaction model implemented. The oil droplets, which have reached the crankcase wall, are treated as a large number of accumulated droplets, and not as a wall film. Hence, in adjacent cells of the wall boundary, the SMD of the droplets loses its validity.

The gas velocity plots at every 90 deg CA in Figure 93 differ slightly from the plots in Figure 87, since the cuts through the three-dimensional flow field are positioned at different places. The cuts illustrated in Figure 93 are determined by a plane through the inlet boundary along the crankweb edge, while the cuts in Figure 87 are determined by a plane placed in the middle of the crankweb. The plots of the surface area-average and the mass-average velocities look similar. As discussed above, the mass-average velocity penetrates slightly faster, causing velocity values at the front of the droplet cloud which are higher than the surface area-average velocities there. The highest liquid velocity values occur at the circular shaped side of the crankweb. There the circumferential velocity is maximal, since this edge exhibits the largest distance from the rotary axis. At the crankweb edge from where the oil droplets detach, $U_{d,2}$ and $U_{d,3}$ are equal. The differences between the two velocities in the flow field are caused by the different drag forces on large and small droplets.

To demonstrate the complexity of the three-dimensional flow field, Figures 95 and 96 show the gas flow field at different times and in different cuts in the region underneath the piston. Figure 94 shows the positions of the three projected planes determining the cuts of Figure 95. The cut x-cut1 is positioned on the left-hand side of the cylinder axis, x-cut2 goes through the axis, and x-cut3 is positioned on the right-hand side of the cylinder axis. The plots in Figure 96 are determined by a cut through the boundary inlet at the crankweb edge perpendicular to the rotation axis. The resolution of the projected vector distributions in the plots is determined by the resolution of the computational mesh. Hence, it is much finer than previous vector plots, where the vectors were interpolated onto a coarser grid.
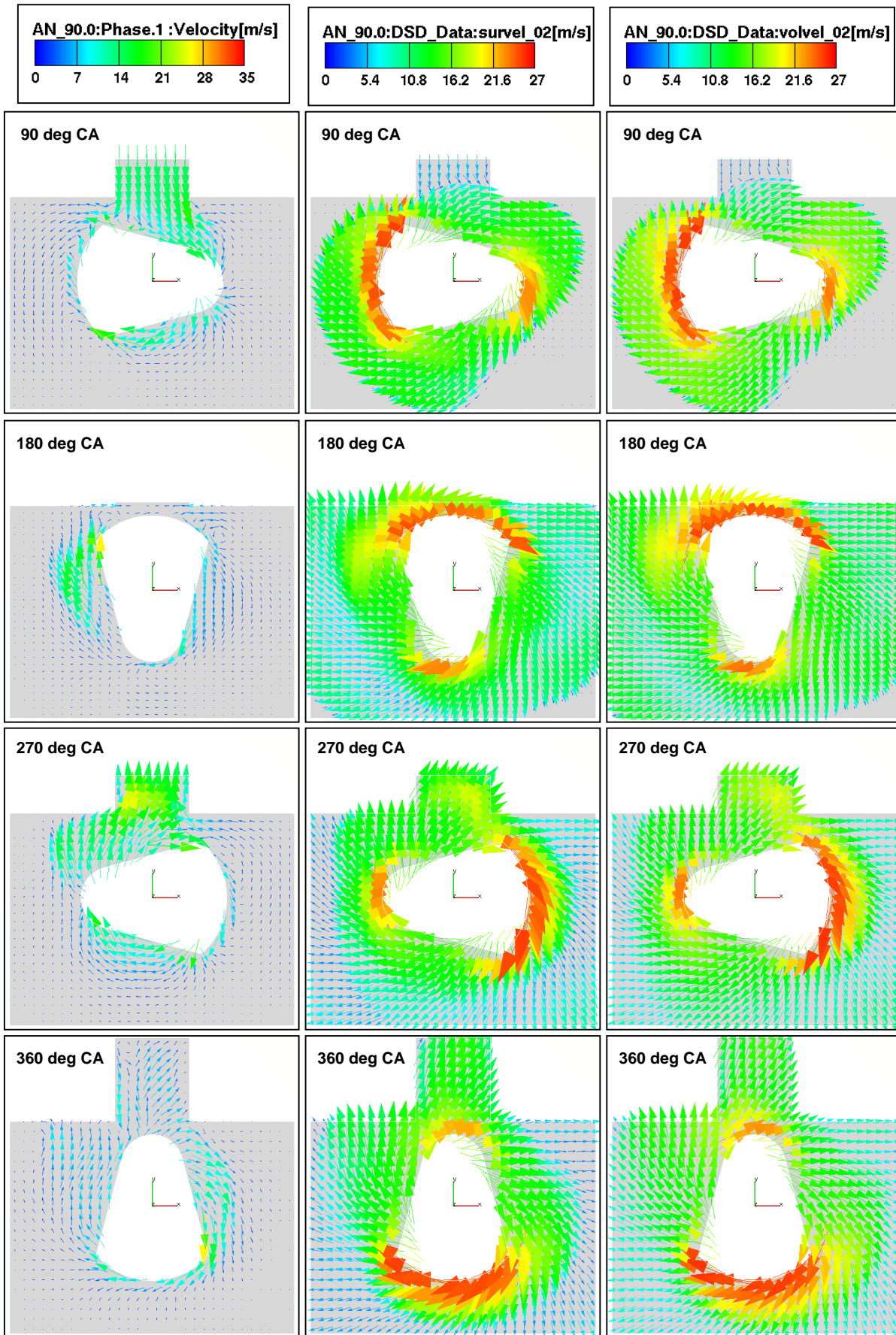
Figure 93: Gas, surface area-average, and mass-average velocity in cuts through the crankweb edge
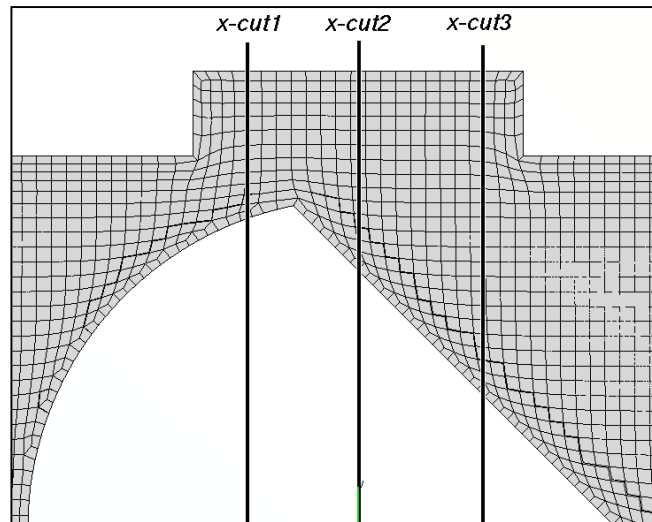
Figure 94: Additional cuts in the region underneath the piston

Figure 95 shows that, at 120 deg CA, the piston moves downward pushing gas into the crankcase, which has to evade the counter weights of the crankweb moving to its upper position. Locally there are high velocities of the flow around the crankweb, as it can be seen in x-cut1 and x-cut2. Furthermore, in x-cut2 and x-cut3 a clockwise rotating vortex can be detected on the left-hand side of the piston underneath the top of the crankcase wall. In Figure 96 it is interesting to see the gas flow around the crankweb, where the flow direction is aligned to the contour of the crankweb.

At 240 deg CA, the piston moves upward, sucking gas back from the crankcase, which creates high flow velocities in the regions where the flow is constricted. While underneath the piston the velocity vectors point more or less into the direction of the piston motion, x-cut2 shows an interesting velocity field. There is upward moving gas on the left and on the right-hand sides of the crankweb, and there is downward moving gas in the region above the middle of the crankweb. In Figure 96, high flow velocities of more than 30 m/s can be seen.

Figure 95: Detailed view of the gas flow field underneath the piston at different cuts
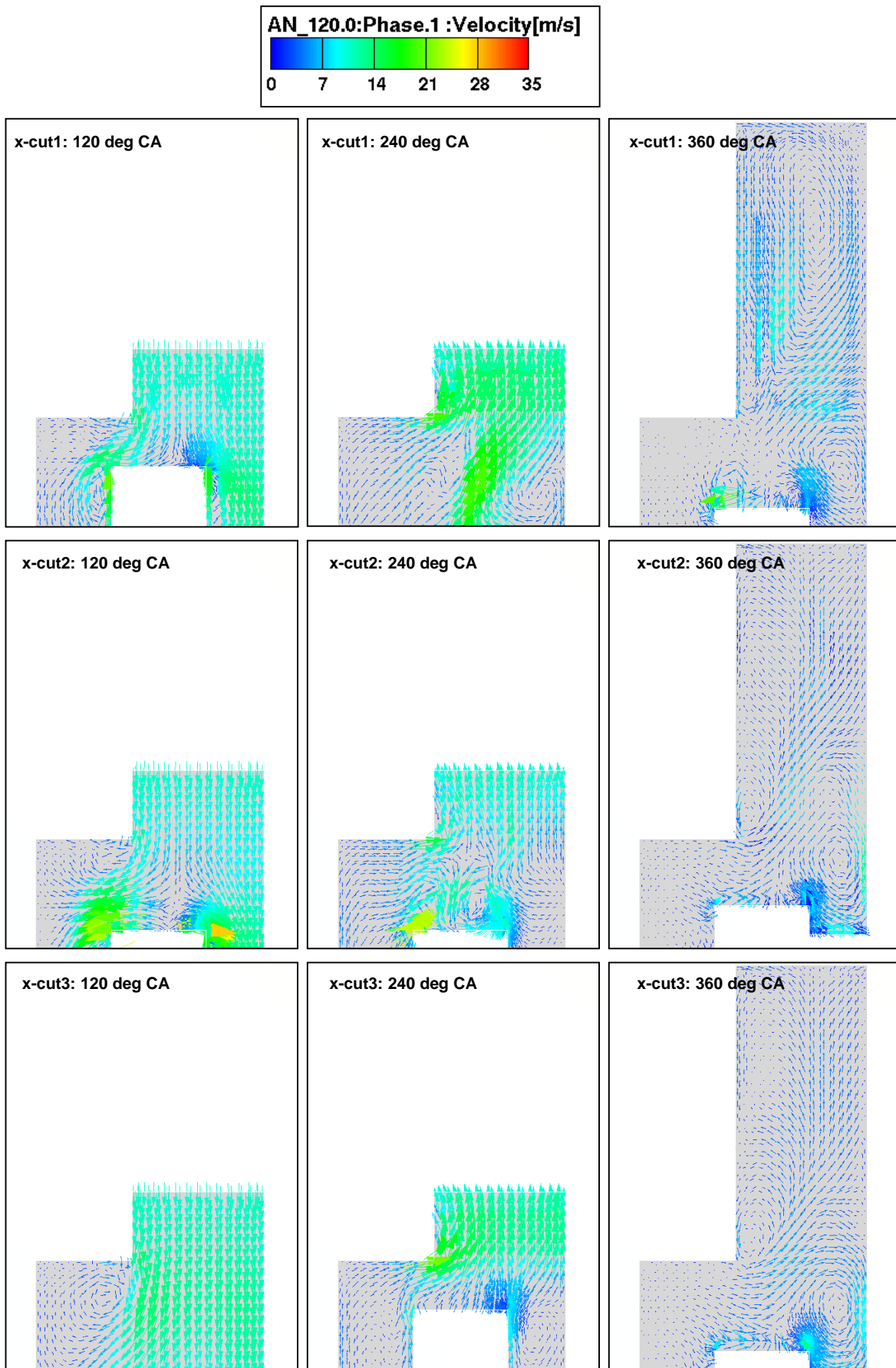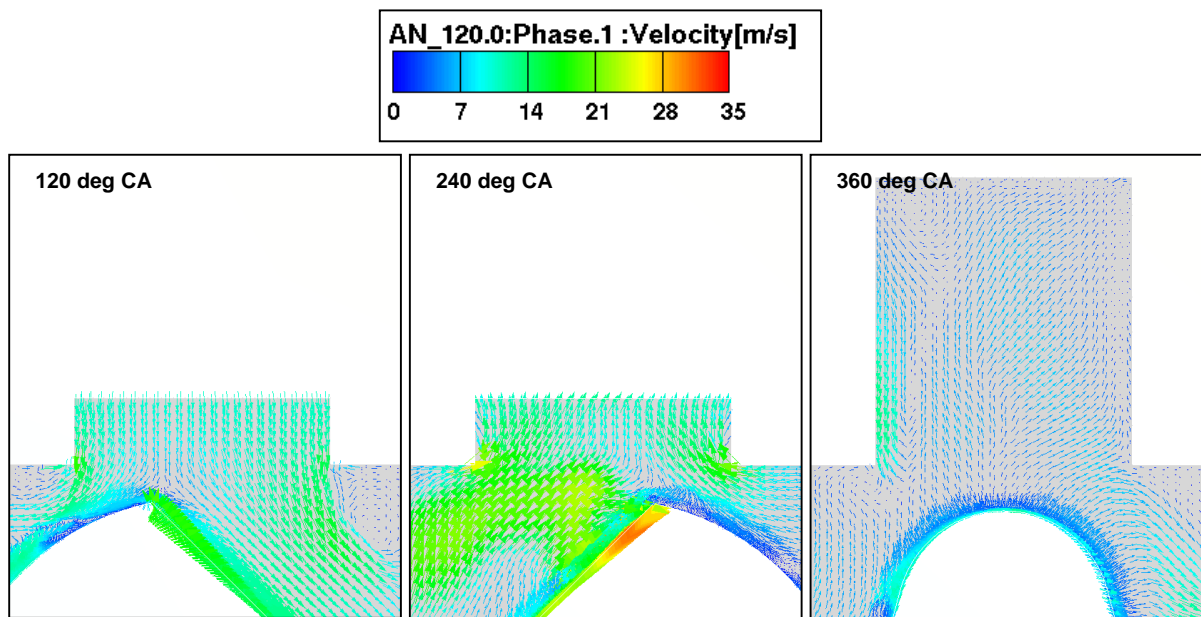
Figure 96: Detailed view of the gas flow field underneath the piston at different cuts

At 360 deg CA, the piston is at the TDC and its velocity is zero. Hence the upward moving gas is decelerated, causing a recirculation underneath the piston, as it is shown in Figure 95. The flow fields of the three cuts x-cut1, x-cut2 and x-cut3 look similar, as there is a counter-clockwise rotating vortex with up-streaming gas at the right-hand side of the cylinder, and downward streaming gas on the left-hand side. In the region near the crankweb edge, from where the oil droplets detach, a clockwise rotating vortex with high velocities close to the sharp edge can be observed. There the gas flow field is influenced by the droplet flow which pushes the gas locally. The plot in Figure 96 shows a slight upward motion of the gas. At the left-hand side, a weak counter-clockwise rotating vortex can be observed underneath the piston bottom. Furthermore, on the left-hand side, there is some gas moving downward along the liner wall.

The CFD simulations of the oil disintegration on the crankweb edge yielded a lot of interesting results. The gas flow field was analysed in general for the whole computational domain. The flow field in the region underneath the moving piston was discussed in detail for three different crank angle steps. The evolution of the liquid oil during one revolution was investigated. Furthermore, the transport of the moments of the droplet size distribution yielded the local Sauter mean diameter distribution of the detached oil droplets in the flow field.

The simulation shows the regions of the crankcase wall which are strongly wetted by the engine oil droplets. This is an important effect, since the splash oil in the crankcase has to

ensure enough oil on the liner wall for lubrication between piston, piston rings, and liner. Furthermore, the connector tube between crankcase and oil mist separator should not be attached in a region, which is strongly covered by the splash oil droplets. The oil could lead to plugging of the connector tube. Hence, the simulation can be used to determine an appropriate position for attaching the oil mist separator to the crankcase.

One should keep in mind that, as it was already mentioned in the discussion about the blow-by simulations, also here the quasi-steady state of the gas and oil flow field in the crankcase was not reached in the simulation. Therefore, the simulation of many more engine cycles is necessary. However, although only one revolution was simulated and the crank drive is still simplified, the simulation gave an idea about the complex three-dimensional flow field. This information helps to optimise the aerodynamic design of the crank drive, and consequently to reduce the ventilation losses and increase the engines efficiency. The pressure and shear stress fields on the surfaces of the crank drive can be obtained from the CFD simulation results. This enables the quantification of the ventilation losses in the crankcase, since they are determined by the resulting pressure and shear forces on the crankshaft, the conrod, and the piston.

The presented results are only a small part of the comprehensive results obtained by the CFD simulations. One could show much more results of the simulation, such as the fields for pressure, turbulent kinetic energy, and turbulence dissipation rate, to get a full comprehension of the complex and transient two-phase flow in the crankcase.

6 Conclusions and Further Work

This thesis deals with numerical simulations of the lubricating oil and air flows in the crankcase of an internal combustion engine. The Eulerian-Eulerian multi-phase approach has been applied for the CFD simulations with the commercial CFD code FIRE. The relevance of various physical processes and phenomena in the crankcase was estimated by determining dimensionless time scales. Blow-by, which is the leakage of the combustion gas into the crankcase, and oil disintegration on the rotating crankweb, have been indicated as important sources for the oil droplets in the crankcase. Separate models describe the formation process of the oil mist and the splash oil. Those models provide the boundary conditions for the CFD simulations of the gas flow field and the propagation of the oil droplets in the crankcase on simplified geometries. The moments of a given droplet size distribution function are transported to obtain the local Sauter mean diameter of the droplets. The gas mass flow rate due to blow-by is calculated by a zero-dimensional chamber model (also known as the labyrinth model). Correlations describing the atomisation of a liquid jet by a coaxial gas jet have been applied for modelling the engine oil atomisation due to the high-speed blow-by gas jets. The oil disintegration at the edge of the rotating crankweb is determined by an analogy to rotary atomisers, for which the correlations for the disintegrated oil mass flow rate and the droplet diameters are known. Variations of the parameters in the two models for the blow-by and the liquid disintegration on the crankweb have been performed to show the sensitivity of the models. The computational meshes for the CFD simulations are moving meshes including rezones. Separate CFD simulations for the blow-by and the oil disintegration on the rotating crankshaft have been performed. The blow-by flow simulation covers five engine cycles on a strongly simplified crankcase geometry. One revolution of the rotating crankweb is simulated on a simplified crankcase geometry with rotating crankshaft and a moving piston, but a neglected conrod.

6.1 Conclusions

The CFD simulations performed allow for the following conclusions.

1) It is possible to obtain reasonable results from CFD simulations of the complex and fully three-dimensional two-phase flow in the crankcase.

2) The liquid oil disintegration on the moving crank drive and the blow-by have been indicated as fast processes in the crankcase, which are relevant for simulations of one engine cycle.

3) Other processes in the crankcase, such as drip-off, wall film flow, and condensation of evaporated oil components, are slow processes with minor contributions to the

processes in a few engine cycles. Condensation of fuel components can be a fast process if the droplet diameter is very small (in the range of 1 μm).

4) Oil disintegration at the crank drive, and oil atomisation due to blow-by at the piston rings, are the major sources for the oil droplets in the crankcase.

5) The blow-by gas mass flow rate strongly depends on speed and load of the engine, since these parameters mainly influence the pressure differences in the spaces between the piston rings calculated with the chamber model.

6) Oil atomisation due to blow-by effects occurs in the small gaps around the piston ring pack. This process has been indicated as a source for the oil mist, producing particles with diameters of a few micrometers. The diameters mainly depend on the fluid properties and on the pressure and temperature conditions in the chambers. Measurements in the literature of the droplet size distribution of the oil mist in the crankcase have shown that there are droplet diameters which are even smaller (less than 1 μm). It can be assumed that condensation produces this important fraction of droplets in the oil mist.

7) Oil disintegration at the crank drive generates large droplet diameters determining the splash oil fraction of the oil droplets in the crankcase. The diameter of the disintegrated oil droplets depends on the disintegration regime, the fluid properties, the crankweb diameter, the rotational speed, and the oil volume flow rate.

8) By transporting the moments of a droplet size distribution function, the local Sauter mean diameter distribution can be obtained in an Eulerian-Eulerian multi-phase simulation without "segregation" into droplet size classes [13].

9) A CFD simulation started at rest takes about three engine cycles, until the gas flow field is fully developed and differences to the previous and the subsequent engine cycle are negligible small.

10) After a certain distance away from the blow-by inlet of the piston, the local Sauter mean diameter of the oil mist droplets tends to an average value. Furthermore, the CFD simulation has shown that the oil droplet concentration is not homogeneous after five simulated engine cycles.

11) The splash oil droplets resulting from the disintegration at the crank drive wet the liner wall. This effect ensures sufficient lubrication between liner and piston. The CFD simulation indicates the most wetted regions at the crankcase wall.

6.2 Further Work

The CFD simulations for blow-by and oil disintegration on the crankweb have been performed successfully in separate simulations, showing the effects independent from each other. In a next step, it is planed to combine the two models in one simulation. Although the moments of a droplet size distribution function would be transported, it would not be accurate to cover the fine oil mist droplets and the coarse splash oil by a single droplet size distribution function. Either the fine or the coarse droplets would be represented insufficiently. Hence, the simulation covering both phenomena, blow-by and oil disintegration on the crankweb, will be performed with two liquid phases, each transporting their own droplet size distribution function. The blow-by simulation has shown that several engine cycles are necessary for having a flow field which recurs for every further cycle. Hence, the simulation with both phenomena together should also be performed for more than one revolution. Since the computational time of the oil disintegration simulation for one revolution was very high, the simulation of several revolutions with the additional blow-by model requires powerful parallelisation of the models. Otherwise the CPU time would be too long for useful applications.

Furthermore the complexity, of the moving crankcase geometry will be increased. The applied meshing technique is able to generate computational meshes for arbitrary moving bodies. Using a real piston instead of the moving block, and applying a more detailed crankshaft geometry in an advanced crankcase, are the next steps. The oil disintegration will be applied on both edges of the crankweb. The long-term target of the crankcase simulations is to resolve the complete crank drive consisting of piston, crankshaft, and conrod. It is expected that, due to the complex motion of the conrod, the number of rezones as well as the total number of computational cells will be increased. However, the CPU costs and the time to be spent are the limiting factors for the further increase of the complexity of the mesh. The resolution of the crankcase geometry can only be as fine as acceptable with reasonable computational time, even with parallelised simulations. Performing simulations of several cycles on a real crankcase geometry with an expected number of one to two million computational cells will only be possible on MPI clusters with a sufficient number of CPUs.

7   References

[1]   Abbott C. E., "A Survey of Waterdrop Interaction Experiments," Reviews of Geophysics and Space physics 15 (3), 1997, pp. 363-374 (cited in [64]).

[2]   Abramzon B., Sirignano W. A., "Approximate Theory of a Single Droplet Vaporization in a Convective Field: Effects of Variable Properties, Stefan Flow and Transient Liquid Heating", Proceedings of the 2nd ASME-JSME Thermal Engineering Joint Conference, Honululu, Hawai, 1987, pp. 11-18.

[3]   Abramzon B., Sirignano W. A., "Droplet vaporization model for spray combustion calculations", Int. Journal Heat Mass Transfer, 1989, pp. 1605-1618.

[4]   AVL List GmbH, "BOOST User's Guide", Version 4.1 user manual, 2005, Graz, Austria.

[5]   AVL List GmbH, "CFD Solver v8.5 Theory", FIRE Version 8 user manual, 2006, Graz, Austria.

[6]   AVL List GmbH, "Multiphase Flow", FIRE Version 8 user manual, 2006, Graz, Austria.

[7]   AVL List GmbH, "CFD Workflow Manager v8.5 Users Guide", FIRE Version 8 user manual, 2006, Graz, Austria.

[8]   AVL List GmbH, "Bearing Analysis Module (EHD2)/(TEHD)", AVL EXCITE Version 6.1.1 user manual, 2005, Graz, Austria.

[9]   AVL List GmbH, "Piston Ring Dynamics and Lube Oil Consumption", AVL GLIDE Version 4.5.1 user manual, 2005, Graz.

[10] Avergård P., Lindström F., "Modelling of Crankcase Gas Behaviour in a Heavy-Duty Diesel Engine", Master thesis at Department of Automatic Control - Lund Institute of Technology, 2003, Lund, Sweden.

[11] Barris M., "Closed Crankcase Filtration: The Next Step in Diesel Engine Emissions Reduction", Feature article in Technology for clean air, October 2005, http://www.meca.org/page.ww?section=Resources&name=Feature+Article.

[12] Basshuysen R. v., Schäfer F., "Shell Lexikon Verbrennungsmotor", Ein Supplement von ATZ und MTZ – Folge 36 Heft 6, 1998, Vieweg , Wiesbaden, Germany.

[13] Beck J. C., "Computational Modelling of Polydisperse Sprays without Segregation into Droplet Size Classes", Ph.D. Thesis at UMIST, 2000, Manchester, United Kingdom.

[14] Beck J. C., Watkins A. P., "Simulation of Water and other Non-Fuel Sprays using a new Model", Atomisation and Sprays 13 (1), 2003, pp. 1-26.

[15] Berg E. v., Edelbauer W., Alajbegovic A., Tatschl R., "Coupled Calculation of Cavitating Nozzle Flow, Primary Diesel Fuel Break-up and Spray Formation with an Eulerian Multi-fluid-model", 9th International Conference on Liquid Atomisation and Spray Systems, 2003, Proc. 12-02.

[16] Bischof O. F., Tuomenoja H., "Messung von Blow-by-Gaspartikeln", MTZ Motortechnische Zeitschrift 7-8/2003 Jahrgang 64, 2003, pp. 586-591.

[17] Brauer H., "Grundlagen der Einphasen- und Mehrphasenströmungen", 1971, Verlag Sauerländer, Aarau und Frankfurt am Main, Germany.

[18] Brenn G., Kalenderski St., Ivanov I., "Investigation of the Stochastic Collisions of Drops produced by Rayleigh Breakup of two Laminar Liquid Jets", Physics of Fluids 9 (2), 1997, pp. 349-364.

[19] Brenn G., Valkovska D., Danov K. D., "The formation of satellite droplets by unstable binary drop collisions, " Physics of Fluids 13 (9), 2001, pp. 2463-2477.

[20] Brenn G., Hirschler T., Meile W., "Strömungslehre und Wärmeübertragung I", script to the lecture in fluid dynamics at the institute of fluid dynamics and heat transfer at Graz University of Technology, 2004.

[21] Brenn G., "Concentration Fields in Evaporating Droplets", Int. Journal Heat Mass Transfer 48 (2), 2005, pp. 395-402.

[22] Brenn G., Kolobaric V., "Satellite droplet formation by unstable binary drop collisions", Physics of Fluids 18 087101, 2006.

[23] Bukovnik S., Dörr N., Caika V., Bartz W., Loibnegger B., "Comparison of various Simulation Models for Combustion Engine Journal Bearings and the Influence of Oil Conditions", 2004 AIMETA International Tribology Conference, 2004, pp. 559-566.

[24] Chang H., Zhang Y., Chen L., "Gray forecast of Diesel engine performance based on wear", Applied Thermal Engineering 23, 2003, pp. 2285-2292.

[25] Clift R., Grace J. R., Weber M. E., "Bubbles, Drops and Particles", 1978, Academic press, San Diego, California.

[26] Crowe C., Sommerfeld M., Tsuji Y., "Multiphase Flows with Droplets and Particles", 1997, CRC Press, New York.

[27] Dhariwal H. C, "Control of Blow-by Emissions and Lubricating Oil Consumption in I.C. Engines", Energy Convers. Mgmt 38 (10-13), 1997, pp. 1267-1274.

[28] Di Felice R., "The Voidage Function for Fluid-Particle Interaction Systems", Int. Journal Multiphase Flow 20, 1994, pp. 159-159, (cited in [26]).

[29] Dörr N., Personal communication, Lubricant laboratory at AC²T research GmbH, 29.4.2004, Wr. Neustadt, Austria.

[30] Dörr N., Report of surface tension measurements, Lubricant laboratory at AC²T research GmbH, 2004, Wr.Neustadt, Austria.

[31] Drew D. A., Passman S. L, "Theory of Multi-component Fluids", 1998, Springer, New York.

[32] Dukowicz J.K., "A Particle Fluid Numerical Model for Liquid Sprays", J. Comp. Physics 35, 1980, pp. 229-253.

[33] Ebner H. W., Jaschek A. O., "Die Blow-by-Messung – Anforderungen und Messprinzipien", MTZ Motortechnische Zeitschrift 59 (1998) 2, pp. 90-95.

[34] Edelbauer W., Kratochwill H., Suffa M., "Numerische Simulation der Schmierölzerstäubung im Kurbelgehäuse eines Verbrennungsmotors", Proceeding of ÖTG Symposium, 2005, Graz, Austria, pp. 13-24.

[35] Edelbauer W., Kratochwill H., Brenn G., Tatschl R., "Basics of the Numerical Simulation of Oil Droplet Formation in the Crankcase of an IC Engine", Proceeding of 13th International Conference on Modelling Fluid Flow CMFF'06 (2), 2006, Budapest, Hungary, pp. 692-699.

[36] Ferziger J.H, Peric M., "Computational Methods for Fluid Dynamics", 1999, Springer, New York.

[37] Filter Manufacturers Council, "Positive Crankcase Ventilation", Technical Service Bulletin 94-2R1, November 2005, http://www.baldwinfilter.com/engineer/pdf/94-2R1.pdf.

[38] Flowmaster Ltd, Fluid flow analysis software, 2005, www.flowmaster.com.

[39] Fraser R. P., Eisenklam P., "Liquid Atomisation and the Drop Size of Sprays", Trans. Inst. Chem. Eng. 34, 1956, pp. 294-319.

[40] Fuchs W., Flowmaster calculation of lubricating oil circuit on 3.0 l V6 Diesel engine at AVL List GmbH, 2002, Graz, Austria.

[41] Fuchs W., Personal communication, AVL List GmbH engine research, 2004, Steyr, Austria.

[42] Grave B., "Die Flüssigkeitsablösung an rotierenden Zerstäuberscheiben", Dipl. -Arbeit am Lehrstuhl für Verfahrenstechnik der TU Berlin, 1967, Berlin (cited in [17]).

[43] Haldex AB (manufacturer of oil mist separators), "Haldex oil mist separator", advertising brochure, 2002, Stockholm, Sweden .

[44] Hege H., "Flüssigkeitsauflösung durch Schleuderscheiben", Chem. -Ing. -Tech. 36, 1964, pp. 52-59.

[45] Hege H., "Die Auflösung von Flüssigkeiten in Tropfen", Aufbereitungs-Technik Jahrgang 10 Heft 3, 1969, pp. 142-147.

[46] Hinze J. O., Milborn H., "Atomization of Liquids by Means of a Rotating Cup", J. Appl. Mech. 17-6, 1950, pp. 145-153 (cited in [17] and [57]).

[47] Kratochwill H., Project collaboration at AC²T research GmbH and AVL List GmbH, 2006, Graz, Austria.

[48] Lee P. M., Stark M. S., Wilkinson J. J., Priest M., Landsay Smith J. R., Taylor R. I. and Chung S., "The Study of the Residence Time and Flow Rate of Lubricating Oil through a Piston Ring Pack", IMechE Mission of Tribology Extended Abstract, School of Mechanical Engineering University of Leeds, 2004.

[49] Liu A.B., Mather D., Reitz R. D., "Modeling the Effects of Drop Drag and Breakup on Fuel Sprays", SAE 930072, 1993.

[50] Liu Z., Reitz R. D., "An Analysis of the Distortion and Breakup Mechanisms of High Speed Liquid Drops", Int. Journal Multiphase Flow 23 (4), 1997, pp. 631-650.

[51] Lee S. J., Lahey R. T Jr., Jones O. C. Jr., "The Prediction of Two-Phase Turbulence and Phase Distribution Phenomena Using a k-Epsilon Model", Japanese Journal Multiphase Flow 3 (4), 1989, pp. 335-368.

[52] Lopez de Bertodano M. A., "Two fluid model for two-phase turbulent jets", Nuclear Engineering and Design 179(1998), 1998, pp. 65-74.

[53] Mann+Hummel (manufacturer of automotive filters), "Mann-Filteringenieure berichten aus der Praxis", advertising brochure published in Mann+Hummel VKD 7032.1, 1989, Ludwigsburg, Germany.

[54] Mann+Hummel (manufacturer of automotive filters), "Mann-Filteringenieure berichten aus der Praxis", advertising brochure published in Mann+Hummel VKD 7033.1, 1989, Ludwigsburg, Germany.

7 References

[55] Mann+Hummel (manufacturer of automotive filters), "ProVent - Mann+Hummel Ölabscheider für geschlossene und offene Kurbelgehäuseentlüftung", 2005, http://www.mann-hummel.com/group/upload/doc/HBBRDM9eOK5.pdf.

[56] Mayer W. O. H., "Zur koaxialen Flüssigkeitszerstäubung im Hinblick auf die Treibstoffaufbereitung in Raketentriebwerken", 1993, DLR-FB 93-09, Germany.

[57] Mehrhardt E., "Zerstäubung von Flüssigkeiten mit rotierenden Scheiben. Flüssigkeitsauflösung, Tropfengrößen und Tropfengrößenverteilungen", Dissertation vom Fachbereich 10 Verfahrenstechnik der TU Berlin, 1978, Berlin.

[58] Meinig U., Pietschner S., May T, "Kurbelgehäuse-Entlüftung aktueller und zukünftiger Fahrzeugmotoren- Teil 1: Aktuelle Entlüftungssysteme", Motortechnische Zeitschrift MTZ 10/2004 Jahrgang 65, 2004, pp. 768-777.

[59] Michaelides E. E., "Particles, Bubbles & Drops - Their Motion, Heat and Mass Transfer", 2006, World Scientific, Singapore.

[60] Miyachika M., Hirota T., Kashiyama K., "A Consideration on Piston Second Land Pressure and Oil Consumption of Internal Combustion Engine", SAE 840099, 1984.

[61] Moshammer T., Mayr F., "Simulationstechnische Optimierung der Getriebeölversorgung zur Minimierung der Füllmenge und Reduktion der Wärmeentwicklung", Proceedings of the ÖTG Symposium, 2005, Graz, Austria, pp. 25-42.

[62] Orthaber G. C., "Berechnungsverfahren für Ölverbrauch und Blow-by zwischen Kolben, Kolbenringen und Zylinderlaufbuchse", Ph.D. Thesis at Graz University of Technology, 1992, Graz, Austria.

[63] O'Donnell B. J., Helenbrook B. T., "Drag on Ellipsoids at Finite Reynolds Number", 9th International Conference on Liquid Atomisation and Spray Systems, 2003, Proc. 13-14.

[64] Orme M., "Experiments on Droplet Collisions, Bounce, Coalescences and Disruption", Progress Energy Combustion Science 23, 1997, pp. 65-79.

[65] O'Rourke P. J., "Collective Drop Effects on Vaporizing Liquid Sprays", Ph. D. Thesis, Los Alamos Lab. Report LA-9069 T, 1981, (cited in [56]).

[66] O'Rourke P. J, Amsden A. A., "The TAB Method for Numerical Calculation of Spray Droplet Breakup", SAE 872089, 1987.

[67] Patankar S. V., "Numerical Heat Transfer and Fluid Flow", 1980, McGraw Hill, London.

[68] Pischinger R., "Thermodynamik", script to the lecture in thermodynamics at the institute for internal combustion engines and thermodynamic at Graz University of Technology, 1989.

[69] Pope S. B., "PDF Methods for Turbulent Reactive Flows", Prog. Energy Combust. Sci. 11, 1985, pp. 119-192.

[70] Post S. L., Abraham J., "Modeling the Outcome of Drop–Drop Collisions in Diesel Sprays", Int. Journal Multiphase Flow 28, 2002, pp. 997–1019.

[71] Putnam A. A., "An integrable form of the drop drag coefficient", American Rocket Society Journal 31, 1961, pp. 1467-1468 (cited in [26]).

[72] Reeks M. W., "On a kinetic equation for the transport of particles in turbulent flows", Physics of Fluids A 3 (3), 1991, pp 446-456.

[73] Reid R. C., Prausnitz J. M., Poling B. E, "The Properties of Gases & Liquids", 1988, McGraw-Hill, Singapore.

[74] Qian J, Law C. K., "Regimes of coalescence and separation in droplet collision", J. Fluid Mech. 331, 1997, pp. 59-80.

[75] Sauter H., Trautmann P., "Messung und Abscheidung von Ölnebelaerosolen aus der Kurbelgehäuseentlüftung von Verbrennungsmotoren – Teil 1: Messung der Tropfengrößenverteilung und der emittierten Ölmenge", MTZ Motortechnische Zeitschrift 61 (2000) 12, 2000, pp. 874-878.

[76] Sauter H., Trautmann P., Abendschein M., "Messung und Abscheidung von Ölnebelaerosolen aus der Kurbelgehäuseentlüftung von Verbrennungsmotoren – Teil 2: Konzepte zur Abscheidung von Öltröpfchen bei der Kurbelgehäuseentlüftung", MTZ Motortechnische Zeitschrift 62 (2001) 1, 2001, pp. 80-83.

[77] Sauter H., Brodesser K., Brüggemann D., "Highly Effective Oil Mist Separator for Crankcase Ventilation", Special print from Motortechnische Zeitschrift MTZ worldwide 3/2003 64, 2003, pp. 1-7.

[78] Schaflinger U., "Strömungslehre und Wärmeübertragung I", script to the lecture in fluid dynamics at the institute of fluid dynamics and heat transfer at Graz University of Technology, 1999.

[79] Schiller L., Naumann A. Z., Ver. Deut. Ing 77, 1933, pp. 318-320 (cited in [25]).

[80] Siemiet D., "Developmental Testing of Automotive Oil Separators in the PCV System", 2005, www.testing-expo.com/usa/04conf/pres_testing/siemiet.pdf.

7 References

[81] Stöcker H., "Taschenbuch mathematischer Formeln und moderner Verfahren", 1995, Harri Deutsch, Frankfurt am Main, Germany.

[82] Totten G. E., "Handbook of Hydraulic Fluid Technology", 1999, Marcel Dekker, New York.

[83] Tritthart P., Personal communication, AVL List GmbH engine research, 10.5.2004, Graz, Austria.

[84] Troxler P., "Cool design at Harley-Davidson Motor Company", 2006, http://www.cd-adapco.com/press_room/dynamics/19/harley.html.

[85] Tomberger C., "Conversion of an Eulerian Primary Break-up Model based on Turbulent Diffusion into a Non-Homogeneous Multiphase Formulation", diploma thesis at FH Joanneum Graz, 2004, Graz, Austria.

[86] Varga C. M., Lasheras J. C., Hopfinger E. J., "Atomization of a Small-Diameter Liquid Jet by a High-Speed Gas Stream", 9th International Conference on Liquid Atomisation and Spray Systems, 2003, Proc. 03-05.

[87] Walzel P., "Auslegung von Einstoffdruckdüsen", Chem.-Ing.-Tech. 54, 1982, pp. 312-328.

[88] Yeaple F., "Fluid Power Design Handbook", 1996, Marcel Dekker, New York.

8 Appendix

8.1 Condensation on a Single Droplet

This section contains the derivations and the calculation of the characteristic process time due to condensation performed in section 2.4. The condensation and evaporation of the single-component droplet is described with the model of [2] and [3], which has been applied for the following calculation.

As shown in Equation (13) in section 2.4, the mass transfer rate due to condensation or evaporation of a single droplet depends on the droplet radius r_{drop}, the gas mixture density $\overline{\rho}_{gas}$ in the vapour film around the droplet, the binary diffusion coefficient $\overline{D}_Y$, the modified Sherwood number Sh^*, and the Spalding mass transfer number B_M, which is defined in Equation (14). The higher the difference of the vapour mass fraction Y between the droplet surface and the ambient gas, the higher is the condensation or evaporation mass transfer rate. Per definition, $\dot{m}_{drop}$ is negative for condensation, and positive for evaporation, since for condensation the vapour mass fraction on the droplet surface Y_S is smaller than the vapour mass fraction in the ambient gas Y_{amb}.

The vapour mass fraction can be expressed as a function of the partial pressures, as done in the equation

$$Y_S = \frac{p_{sat}}{p}\frac{M_{vap}}{M} = \frac{p_{sat}}{p}\frac{M_{vap}}{\left(\dfrac{p_{sat}}{p}M_{vap} + \dfrac{p_{air}}{p}M_{air}\right)} = \frac{p_{sat}}{p_{sat} + \left(p - p_{sat}\right)\dfrac{M_{air}}{M_{vap}}} \quad . \tag{186}$$

Hence, it depends on the saturation pressure of the liquid, the total gas pressure, and the molecular weight of the vapour and the carrier gas, which in the present case is air here. For the following considerations it is convenient to introduce the saturation ratio S, which is defined by

$$S = \frac{p_{vap}}{p_{sat}(T)} \quad . \tag{187}$$

S is the ratio of the partial pressure of the fuel vapour contained in the ambient gas, and the saturation pressure of the fuel at the ambient temperature. If S is given, the vapour mass fraction in the ambient gas is determined by

$$Y_{amb} = \frac{p_{sat}\, S}{p_{sat}\, S + \left(p - p_{sat}\, S\right)\dfrac{M_{air}}{M_{vap}}} \; . \tag{188}$$

Vice versa, if Y_{amb} is given, S is determined. If the droplet and the ambient gas have the same temperature, saturation ratios greater than unity are required for condensation.

The heat transfer rate into the droplet is described by the equation

$$\overset{\circ}{H}_{drop} = \overset{\circ}{m}_{drop}\left[\frac{\overline{c}_{P,vap}\left(T_{amb} - T_S\right)}{B_T} - L(T_S)\right] . \tag{189}$$

Depending on the latent heat L of the liquid, the Spalding heat transfer number B_T, and the temperature difference between the droplet surface and the ambient carrier gas, the heat transfer rate can be positive or negative. Per definition, heat transferred from the ambient gas into the droplet is positive. The heat transfer number B_T is a function of B_M and the exponent ϕ_{BT}, as shown in the equation

$$B_T = \left(1 + B_M\right)^{\phi_{BT}} - 1 \quad with \quad \phi_{BT} = \phi_{BT}\left(B_M, B_T, Re, Pr, Sc, Le\right) . \tag{190}$$

The exponent ϕ_{BT} itself is a function of B_T and this is why Equation (190) has to be solved iteratively. This makes the model computationally more expensive than simpler models.

The heat transfer across the liquid surface of the droplet normally leads to a temperature change of the droplet. In the easiest way the rapid mixing model is applied, where uniform temperature distribution in the droplet is assumed. This means that the heat transfer into the droplet causes the same temperature increase on the droplet surface as well as in the core of the droplet. Thus this model is also called infinite conductivity model. It is satisfied by a vanishingly small Biot number of the droplet. The equations

$$\overset{\circ}{H}_{drop} = m_{drop}\, c_{P,liq}\, \frac{dT_S}{dt} \; , \tag{191}$$

and

$$\frac{dT_S}{dt} = \frac{3\, \overset{\circ}{H}_{drop}}{4\pi\, r_{drop}^{3}\, \rho_{liq}\, c_{P,liq}} \tag{192}$$

determine the heat transfer rate into the droplet and the temperature change of the droplet.

To obtain the characteristic process time for condensation, Equation (13) of section 2.4 for $\overset{\circ}{m}_{drop}$ can be transformed into Equation (15) for $\overset{\circ}{d}_{drop}$. After separation of time and diameter, the equation can be integrated. The characteristic process time is defined as the time required

by a droplet for growing due to condensation from the certain diameter $d_{drop,1}$ to the diameter $d_{drop,2}$. In a simplified case, where the droplet temperature and the vapour mass fraction of the ambient gas are almost constant, the gas density in the film $\bar{\rho}_{gas}$, and the binary diffusion coefficient $\bar{D}_Y$ can also be kept constant. To keep the modified Sherwood number Sh^* constant, non-moving droplets with a droplet Reynolds number of zero have to be assumed for this simplified case. Then the condensation time results from integrating over the droplet diameter only, and is proportional to the square of the droplet diameter, as it is expressed by

$$
t_{cond} = \int_{d_{drop,1}}^{d_{drop,2}} \frac{-d_{drop}\,\rho_{liq}}{2\,\bar{\rho}_{gas}\,\bar{D}_Y\,Sh^*\,\ln(1+B_M)}dd_{drop} \approx
$$
$$
\approx -\frac{\rho_{liq}}{4\,\bar{\rho}_{gas}\,\bar{D}_Y\,Sh^*\,\ln(1+B_M)}\left(d_{drop,1}^2 - d_{drop,2}^2\right) \cong d_{drop,2}^2 - d_{drop,1}^2 \ .
$$

(193)

This is the well known d^2-law, which provides a good possibility to control the numerically calculated results.

The calculation of the characteristic process time for condensation has been done numerically with an explicit time integration of Equation (13) and (189). The program is simple, but it is able to treat evaporation and condensation at varying temperatures of the droplet. The temperature change of the droplet is determined by Equation (192). The gas properties in the film around the droplet, consisting of vapour and carrier gas, are calculated at an average temperature and an average vapour mass fraction, which are interpolated as proposed in [2] and [3]. The liquid in the calculation is N-dodecane ($C_{12}H_{26}$), which is a common model fluid for characterisation of Diesel fuel. Therefore, all required fluid properties depending on temperature and pressure were available. Useable correlations for the determination of the binary diffusion coefficient, the saturation pressure, the latent heat, the liquid density, the specific heat capacity of the vapour, the thermal conductivity of the vapour, and the dynamic viscosity of the vapour have been applied from [73].

The conditions of the condensation calculation and the fluid properties are listed in Table 11. An ambient pressure of 100 000 Pa and an ambient temperature of 373 K are conditions, which can occur in the crankcase during ordinary operation of the engine. A constant supersaturation of one percent (S =1.01) at constant ambient gas temperature has been applied for the calculation. So a continuous condensation is guaranteed. Nevertheless, in the real crankcase it is expected that condensation occurs when hot crankcase gas, which contains a considerable amount of vapour, is mixed with crankcase gas from colder regions. The gases mix, and due to the lower temperature of the mixture, the saturation ratio would become locally greater than one. Hence condensation is initiated. The aim of the calculations

performed here is not to deal with the exact conditions in the crankcase. It is rather to get a feeling for the relevant processes and their time scales.

Two calculations with different initial droplet diameters of 1 μm and 10 μm have been applied. At the beginning of the calculation, the temperature of the droplet and the ambient gas are exactly the same. The time for increasing the droplet diameter by a factor of 1.5 is the searched process time for condensation. Thus, the relative gain of liquid mass due to condensation is equal for both calculations, where the droplet growths from 10 μm to 15 μm and from 1 μm to 1.5 μm are simulated.

General calculation set-up	Pressure p	100 000	Pa
	Temperature T	373	K
	Saturation ratio S	1.01	-
	Initial droplet diameter $d_{drop,1}$	10/1	μm
	Relative velocity droplet-gas U	0	m/s
Fluid properties of N-dodecane at 373 K (calculated from [73])	Molecular weight of fuel M_{vap}	170.36	kg/kmol
	Density ρ_{liq}	734	kg/m³
	Specific heat capacity $c_{P,liq}$	2424.2	J/kgK
	Latent heat L	313898	J/kg
	Saturation pressure p_{sat}	2013	Pa
	Dynamic viscosity μ_{vap}	$5.69 \cdot 10^{-6}$	Ns/m²
	Thermal conductivity k_{vap}	0.0132	W/mK
	Specific heat capacity $c_{P,vap}$	1984.0	J/kgK
Fluid properties of air at 373 K	Molecular weight of gas M_{air}	29.8	kg/kmol
	Density ρ_{air}	0.961	kg/m³
	Dynamic viscosity μ_{air}	$22.38 \cdot 10^{-6}$	Ns/m²
	Thermal conductivity k_{air}	0.0316	W/mK
	Specific heat capacity $c_{P,air}$	1011.9	J/kgK
Mixture properties at 373 K	Binary diffusion coefficient D_Y	$7.86 \cdot 10^{-6}$	m²/s

Table 11: Fluid properties from [73] and conditions for the condensation calculation

The results are shown in Figure 97, where droplet temperature and diameter are drawn versus time in a logarithmic scale. The temperature of the droplet reaches very soon a constant temperature, which is slightly higher than the ambient gas temperature. At that temperature there is an energy balance. The heat gain of the droplet due to the latent heat of

the vapour is as big as the heat loss of the droplet due to the temperature difference between droplet surface and ambient gas. Due to the constant saturation ratio, the droplet diameter continuously increases. The droplet with 10 μm initial diameter takes 1.8195 s for growing to 15 μm. The second droplet with 1 μm initial diameter is approximately hundred times faster for the same relative mass gain, since it takes 0.0178 s for growing to 1.5 μm. This is a remarkable result, if one considers that the mass of the 10 μm droplet is thousand times bigger than the mass of the 1 μm droplet. This means that for the condensation of a certain amount of vapour mass, a single droplet with an initial diameter of 10 μm takes about hundred times longer than 1000 droplets with an initial diameter of 1 μm. To obtain the dimensionless time scales for condensation, $\tau_{cond-fuel1}$ and $\tau_{cond-fuel2}$ for Table 2 in section 2.4, the values for the condensation time have to be divided by the reference time of Equation (2).
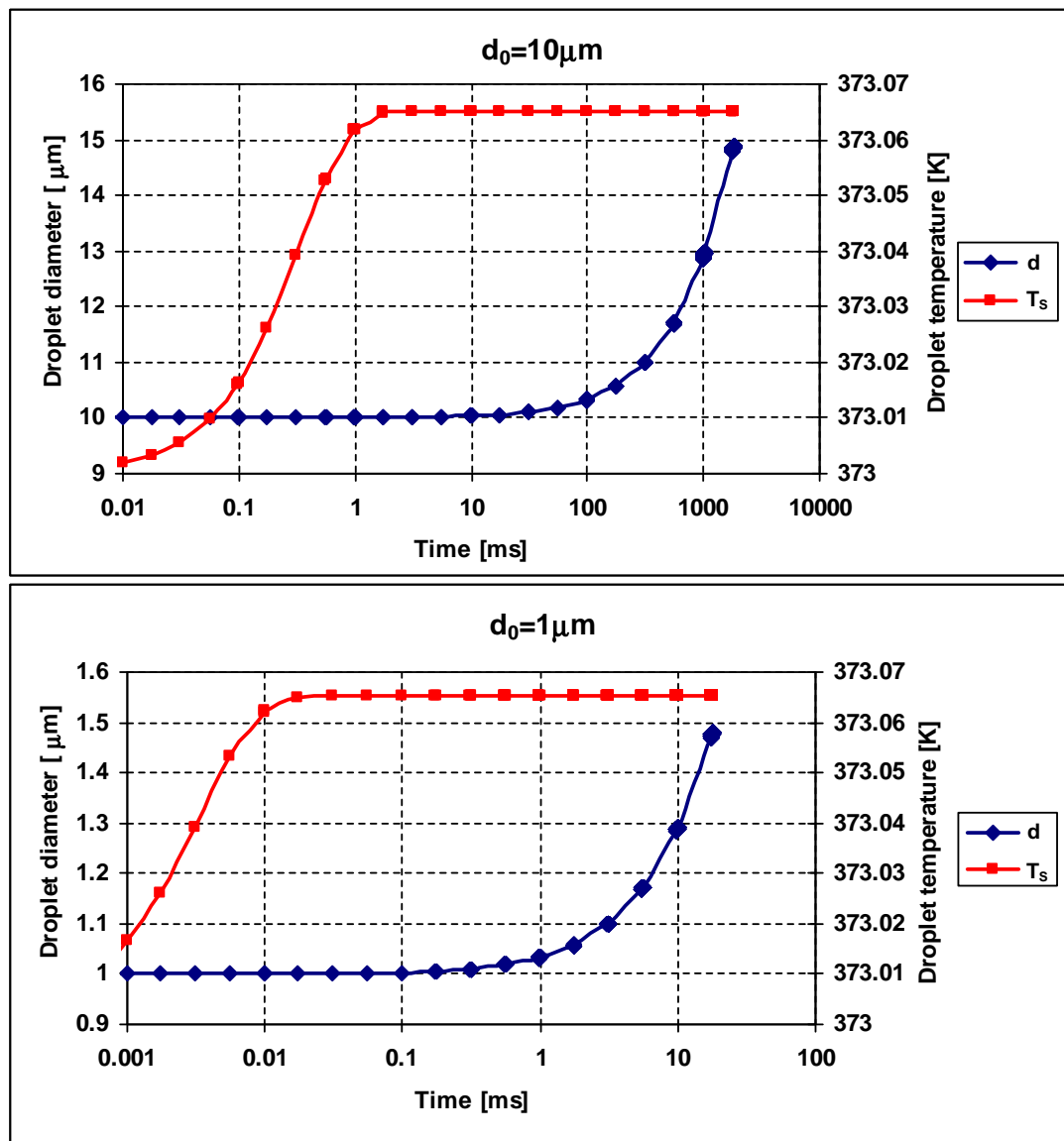

Figure 97: Droplet growth of N-dodecane from 10 to 15 μm (top), and 1.0 to 1.5 μm (bottom)

For engine oil it is more difficult to determine the time scales for condensation, since there is no reasonable single-component alternative fluid available. But such a fluid with its properties is required for the calculation of the time required for condensation. Engine oils consist of many different hydrocarbons with 20 to 35 carbon atoms. In [73], fluid property correlations are provided for hydrocarbons with less than twenty carbon atoms. For this reason, it was decided to estimate the condensation time for engine oil by comparison with the performed condensation of N-dodecane.

In the following considerations, subscript 1 stands for the fuel N-dodecane, and subscript 2 for engine oil. Building the ratio between the condensation times of fuel and engine oil according to Equation (193) leads to the relation

$$\frac{t_{cond,1}}{t_{cond,2}} = \frac{\dfrac{\rho_{liq,1}}{4\,\overline{\rho}_{gas,1}\,\overline{D}_{Y,1}\,Sh_1^*\,\ln(1+B_M)_1}\left(d_{drop,2}^2 - d_{drop,1}^2\right)_1}{\dfrac{\rho_{liq,2}}{4\,\overline{\rho}_{gas,2}\,\overline{D}_{Y,2}\,Sh_2^*\,\ln(1+B_M)_2}\left(d_{drop,2}^2 - d_{drop,1}^2\right)_2} \quad . \tag{194}$$

After simplification, the following equation can be obtained:

$$\frac{t_{cond,1}}{t_{cond,2}} = \frac{\rho_{liq,1}}{\rho_{liq,2}}\frac{\overline{\rho}_{gas,2}}{\overline{\rho}_{gas,1}}\frac{\overline{D}_{Y,2}}{\overline{D}_{Y,1}}\frac{Sh_2^*}{Sh_1^*}\frac{\ln(1+B_M)_2}{\ln(1+B_M)_1} \quad \text{with} \quad \frac{\overline{\rho}_{gas,2}}{\overline{\rho}_{gas,1}}\cdot\frac{Sh_2^*}{Sh_1^*}\approx 1 \tag{195}$$

The ratio between the process times of condensation for fuel and engine oil depends on the ratios of the liquid densities, the gas densities in the vapour film covering the droplet, the binary diffusion coefficients, the modified Sherwood numbers, and the logarithmic value of the Spalding mass transfer number.

Assuming unity of the second and the fourth factor in Equation (195) leads to a further simplification. With increasing number of carbon atoms, the diffusion coefficient decreases [62]. Hence, the third term of Equation (195) has to be less than unity, since oil has a higher number of carbon atoms than Diesel fuel. Consequently one can say that the ratio of the process times for condensation has to be greater than the ratio of the liquid densities and the ratio of the logarithmic values of the Spalding mass transfer number, as expressed by the following inequality

$$\frac{t_{cond,1}}{t_{cond,2}} > \frac{\rho_{liq,1}}{\rho_{liq,2}}\frac{\ln(1+B_M)_2}{\ln(1+B_M)_1} \quad . \tag{196}$$

The term $\ln(1+B_M)$ can be interpreted as the driving force of the condensation. For estimation of the condensation time, special attention has to be paid to this term. Inserting Equations (14), (186), and (188) into this term leads to

$$\ln(1 + B_M) = \ln\left(1 + \frac{Y_S - Y_{amb}}{1 - Y_S}\right) = \ln\left(\frac{1 - Y_{amb}}{1 - Y_S}\right) = \ln\left[\frac{1 - \dfrac{p_{sat}\, S}{p_{sat}\, S + (p - p_{sat}\, S)\dfrac{M_{air}}{M_{vap}}}}{1 - \dfrac{p_{sat}}{p_{sat} + (p - p_{sat})\dfrac{M_{air}}{M_{vap}}}}\right]. \qquad (197)$$

Further simplification leads to

$$\ln(1 + B_M) = \ln\left[\frac{1 - \dfrac{p_{sat}}{p}\, S \quad \dfrac{p_{sat}}{p} + \left(1 - \dfrac{p_{sat}}{p}\right)\dfrac{M_{air}}{M_{vap}}}{1 - \dfrac{p_{sat}}{p} \quad \dfrac{p_{sat}}{p}\, S + \left(1 - \dfrac{p_{sat}}{p}\right)S\, \dfrac{M_{air}}{M_{vap}}}\right]. \qquad (198)$$

The driving force of condensation $\ln(1 + B_M)$ depends on the saturation ratio, the saturation pressure, and the ratio of the molecular weights of air and vapour. In Figure 98, the absolute values of $\ln(1 + B_M)$ for engine oil with a molecular weight ten times greater than air are shown. With increasing saturation pressure p_{sat}, the condensation driving force increases significantly. The ambient pressure p is kept constant.
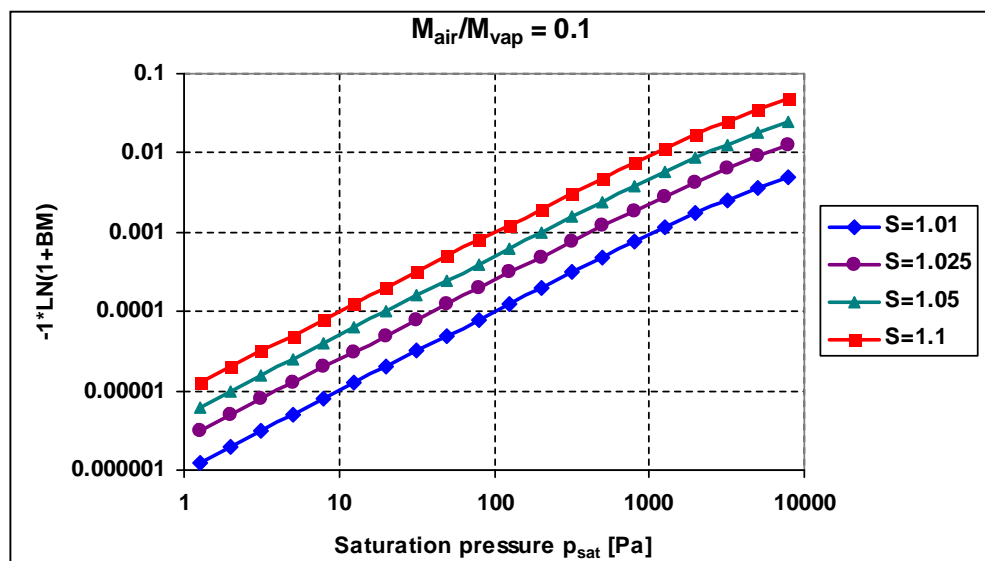

Figure 98: Driving force of condensation for different saturation ratios

To obtain the condensation driving force ratio, which is the second term on the right-hand side of Equation (196), the values of $\ln(1 + B_M)$ for N-dodecane and engine oil are taken from the calculations shown in the Figures 99 and 100. It is assumed that the engine oil has the same molecular weight as $C_{30}H_{62}$. N-dodecane has a saturation pressure of approximately 2000 Pa at 373 K. This leads to a value for $\ln(1 + B_M)$ of $-1.0634 \cdot 10^{-3}$ at a

saturation ratio of 1.01 (Figure 99). According to [88] and [82], the saturation pressure of petroleum oil is about 50 Pa at 373 K. Hence, the value of $\ln(1 + B_M)_2$ is $-7.067 \cdot 10^{-5}$ (Figure 100). Inserting these values and the liquid density ratio into Equation (196) leads to the result that the ratio of $t_{cond,1} / t_{cond,2}$ must be greater than 0.0553. In other words, the estimated condensation time for engine oil is at least eighteen times longer than the condensation time for fuel. Multiplying $\tau_{cond-fuel,2}$ of 0.89 in Table 2 by eighteen leads to the value of 16.05 for $\tau_{cond-oil}$. This is why the condensation of engine oil is assigned to the slow processes.
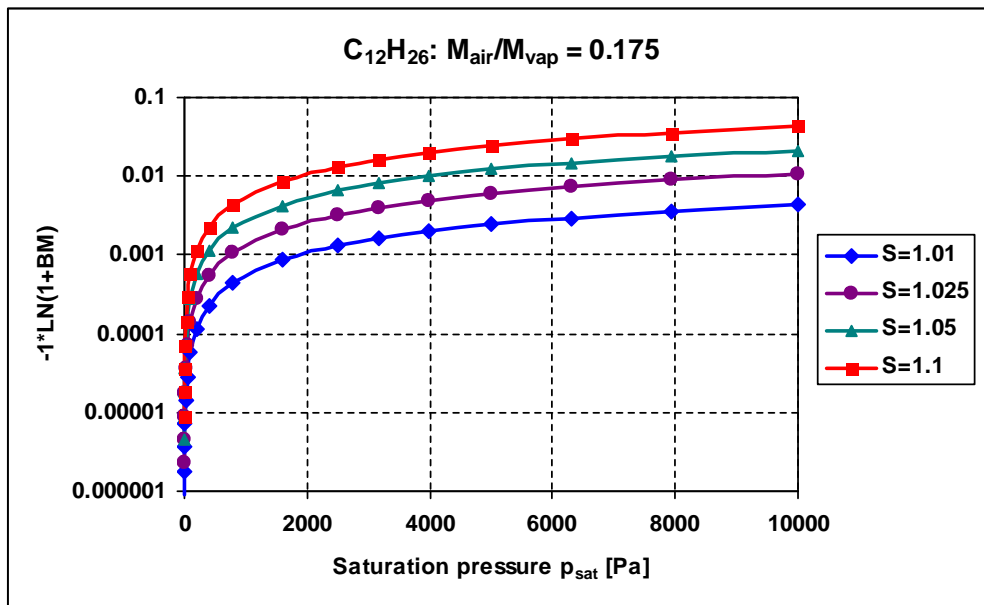

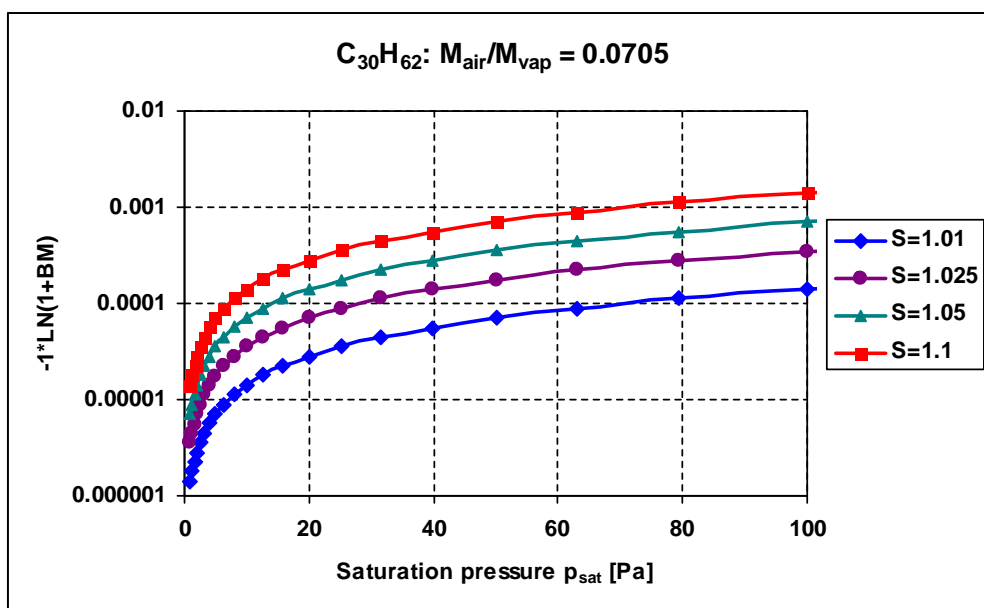Figure 99: Driving force of condensation for fuel (N-dodecane)

Figure 100: Driving force of condensation for engine oil fluid

8.2 Liquid Disintegration on Rotating Discs

8.2.1 Range of the Measurements

In section 3.3, different correlations from the literature for the droplet diameters and the disintegration regimes on rotary atomisers are compared. Those correlations, which are based on measurements, are valid in a certain ranges of the relevant process parameters. To compare them with the conditions in the crankcase, the experimental data range is shown here.

Table 12 shows the varied parameters of the experiments of Hege [44], [45]. The applied disc diameters of these experiments occur at crankshafts of common passenger car combustion engines. The Froude number, defined in Equation (68), varies from 10 to 1000. This is equivalent to a variation of the rotational speed from 669 to 6687 rpm for a disc with the diameter of 200 mm. The surface tension against air, and the liquid density of the experimental fluids are slightly larger than typical values for the surface tension and density of common engine oils. The experimental range of the oil viscosity covers the viscosity values of lubrication oil in an engine running at operation temperature. Cold engine oils at room or even lower temperatures have a higher viscosity.

Disc diameters	m	0.05, 0.07, 0.14
Froude number	-	10 - 1000
Surface tension	N/m	0.0343-0.0736
Liquid density	kg/m³	931.95 – 1226.25
Kinematic viscosity	m²/s	$1 \cdot 10^{-6} – 70 \cdot 10^{-6}$

Table 12: Range of the liquid disintegration experiments of Hege [44]

Grave [42] performed measurements on water, and two different types of oil. The fluid properties are shown in Table 13. The oil viscosities of Oil 1 and Oil 2 are equivalent to the oil viscosities of typical engine oils (e.g. SAE 10W-30) at 70 °C and 35 °C. There is no information about the rotational speeds and the volume flow rates available.

8 Appendix

Fluid	Temperature [°C]	Liquid Density [kg/m³]	Dynamic viscosity [Ns/m²]	Surface tension [N/m]
Oil 1	25	880	0.01926	0.0298
Oil 2	25	871	0.0798	0.0312
Water	15	999	0.0015	0.0741
Disc diameters [m]	0.13, 0.19, 0.28			

Table 13: Range of the liquid disintegration experiments of Grave [42]

Mehrhardt [57] performed measurements on water and three different types of oil, as shown in Table 14. The viscosity of Oil 1 is lower than the viscosity of lubrication oil operated in the temperature range of a combustion engine. The oil viscosity of Oil 3 is, e.g. equivalent to the oil viscosity of SAE 10W-30 at 15 °C. The experimental data range of the angular speeds and the volume flow rates cover the operation conditions in the crankcase.

Fluid	Temperature [°C]	Liquid Density [kg/m³]	Dynamic viscosity [Ns/m²]	Surface tension [N/m]
Oil 1	22	858	0.0014	0.0295
Oil 2	20	861	0.0722	0.032
Oil 3	22	880	0.2345	0.0326
Water	20	998	0.001	0.0726
Disc diameters [m]	0.13, 0.19, 0.25			
Angular speed [rad/s]	60.3 - 1090			
Volume flow rate [m³/s]	$0.23 \cdot 10^{-6}$ - $144 \cdot 10^{-6}$			

Table 14: Range of the liquid disintegration experiments of Mehrhardt [57]

The varied fluid properties and the operation conditions of the rotary atomiser experiments, such as density, viscosity, rotational speed, and volume flow rate, cover the expected conditions in the crankcase quite well. Only the surface tension against air is not fully covered by the experiments of Hege, Grave, and Mehrhardt. At higher oil temperatures in the engine, the surface tension against air can become less than the minimum value in Table 14, which is 0.0295 N/m. This extrapolation should be kept in mind.

- 182 -

8.2.2 Droplet Diameter at Sheet Disintegration

The droplet diameter correlations of Hege [44], as discussed in section 3.3.3, are valid for dropwise and ligament disintegration. Hence, an appropriate correlation for sheet disintegration is required. Walzel [87] compared different designs and disintegration regimes of single substance pressure jets. He derived a correlation for the droplet diameters from the disintegration of liquid lamellas, valid for fan-shaped and hollow-conical jets. Furthermore, he compared different correlations from the literature. A general relation for the Sauter mean diameter is given by the equation

$$\frac{d_{32,d}}{d_{ref}} = C_3 \left(\frac{\kappa_{lam}}{We_{ref}} \right)^{\frac{1}{3}} \left(\frac{\rho_c}{\rho_d} \right)^{-\frac{1}{6}} \; . \tag{199}$$

This equation results from the assumption that, the droplet diameter is proportional to the square of the product between wave length of the fastest growing wave obtained from a linear stability analysis, and the thickness of the lamella at the point of disintegration. Nevertheless, this correlation has been derived and validated for fan-shaped or hollow-conical jets. One should keep in mind that this correlation creates an error, if it is applied for the sheet disintegration regime of rotary atomisers, since there are large circumferential velocity components. Hence, it can be expected that the model parameter has to be adjusted.

d_{ref} is the reference diameter, which is originally determined as the diameter of the inflow jet. κ_{lam} is the lamella number depending on the design of the single substance pressure jet, and We_{ref} is the characteristic Weber number. ρ_d and ρ_c are the densities of the liquid and the gaseous phases. The recommended value of the model parameter C_3 is 1.13. To adapt the droplet diameter correlation for the sheet disintegration on rotary atomisers, the used dimensions have to be transferred. The reference diameter d_{ref} is determined by the volume flow rate and the inflow velocity U, as shown in the correlations

$$d_{ref} = \left(\frac{4 \dot{V}}{\pi U} \right)^{\frac{1}{2}} \quad and \quad U = \frac{1}{2} d_{disc} \omega \; . \tag{200}$$

At the fan-shaped jet, this inflow velocity is approximately equal to the velocity of the lamella at the point of disintegration. At rotary atomisers the dominant velocity component of the disintegration is the circumferential velocity at the disc edge. Hence, it is reasonable to take this value for U.

The lamella number, as described by the equation

$$\kappa_{lam} = \frac{1}{2\pi} \; , \tag{201}$$

is originally defined for cylindrical colliding plates. There the jet enters the centre of the plate, is redirected, and forms the lamella. This design is most similar to the sheet disintegration regime of a rotary atomiser. Walzel [87] defined this lamella number to compare different designs of the single substance pressure jets.

Equation (199) is valid for $10^3 \le We_{ref} \le 10^5$, where the reference Weber number is defined by the equation

$$We_{ref} = \frac{d_{ref} U^2 \rho_d}{\sigma} = 2 \frac{\rho_d}{\sigma} U^{\frac{3}{2}} \left(\frac{\dot{V}}{\pi} \right)^{\frac{1}{2}} \; . \tag{202}$$

The final correlation for the Sauter mean diameter of Equation (91) in section 3.3.3 is provided by the substitution of the Equations (200), (201), and (202) into the Equation (199), and it yields

$$
\begin{aligned}
d_{32,d} &= C_3 \, d_{ref} \left(\frac{1}{2\pi} \frac{\sigma}{d_{ref} U^2 \rho_d} \right)^{\frac{1}{3}} \left(\frac{\rho_c}{\rho_d} \right)^{-\frac{1}{6}} = C_3 \left(\frac{1}{2\pi} \frac{4\dot{V}}{\pi U} \frac{\sigma}{U^2 \rho_d} \right)^{\frac{1}{3}} \left(\frac{\rho_c}{\rho_d} \right)^{-\frac{1}{6}} = \\
&= 0.5874 \frac{C_3}{U} \left(\frac{\dot{V}\sigma}{\rho_d} \right)^{\frac{1}{3}} \left(\frac{\rho_c}{\rho_d} \right)^{-\frac{1}{6}} = 1.1747 \, C_3 \frac{1}{d_{disc}\omega} \left(\frac{\rho_d}{\rho_c} \right)^{\frac{1}{6}} \left(\frac{\sigma\dot{V}}{\rho_d} \right)^{\frac{1}{3}} \; .
\end{aligned}
\tag{203}
$$